

**BRIDGING LENGTH AND TIME SCALES BY  
AFM-BASED NANOTRIBOLOGY:  
APPLICATIONS TO NANOSTRUCTURED CERAMICS  
AND POLYMER SURFACES**

**Ewa Tocha**

This research was supported by the Dutch Technology Foundation STW (Project no. TFC.5287), and the European Office of Aerospace Research & Development (EOARD) of US-AF.

Members of the Committee:

Chairman:	Prof. Dr. Ir. L. Lefferts	University of Twente
Secretary:	Prof. Dr. Ir. A. Blik	University of Twente
Promotor:	Prof. Dr. G.J. Vancso	University of Twente
Assistant-promotor:	Dr. H. Schönherr	University of Twente
Referee:	Dr. Ir. T.H. Oosterkamp	University of Leiden
Members:	Prof. Dr. N.D. Spencer	ETH Zürich, Switzerland
	Prof. Dr. Ing. D.H.A. Blank	University of Twente
	Prof. Dr. Ir. D.J. Schipper	University of Twente
	Prof. Dr. Ir. J.W.M. Noordermeer	University of Twente

Bridging length and time scales by AFM-based nanotribology: Applications to nanostructured ceramics and polymer surfaces

By Ewa Tocha

Ph.D. Thesis, University of Twente, Enschede, The Netherlands, 2006.

ISBN 90-365-2345-1

Copyright © 2006 by E. A. Tocha

Cover design by Alicja Grudnowska and Grzegorz Bielak.

All rights reserved.

Printed by PrintPartners Ipskamp, Enschede, The Netherlands, 2006.

**BRIDGING LENGTH AND TIME SCALES BY  
AFM-BASED NANOTRIBOLOGY:  
APPLICATIONS TO NANOSTRUCTURED CERAMICS  
AND POLYMER SURFACES**

PROEFSCHRIFT

ter verkrijging van  
de graad van doctor aan de Universiteit Twente,  
op gezag van de rector magnificus,  
prof. dr. W.H.M. Zijm,  
volgens besluit van het College voor Promoties  
in het openbaar te verdedigen  
op donderdag 27 april 2006 om 16.45 uur

door

**Ewa Agnieszka Tocha**

geboren op 5 juli 1976

te Gdynia, Polen

Dit proefschrift is goedgekeurd door:

Promotor: Prof. Dr. G.J. Vancso

Assistent-promotor: Dr. H. Schönherr

*Mojemu mężowi Grzesiowi*



# Contents

<b>Chapter 1. Significance of nanotribology and its application</b>	<b>1</b>
1.1. Micrometer scale tribology	1
1.2. Nanometer scale tribology	2
1.3. Concept of this Thesis	3
1.4. References	7
<b>Chapter 2. Tribology from single asperity to multi asperity contacts</b>	<b>9</b>
2.1. Fundamentals of tribology	10
2.1.1. <i>Definition of friction</i>	10
2.1.2. <i>Early observations of friction</i>	11
2.1.3. <i>Multiple and single asperity tribology</i>	12
2.2. Surface forces and adhesion	13
2.2.1. <i>Elementary forces</i>	13
2.2.2. <i>Adhesion and capillary forces</i>	15
2.3. Elastic continuum contact mechanics	17
2.3.1. <i>Hertz model</i>	17
2.3.2. <i>Johnson, Kendall and Roberts (JKR) model</i>	18
2.3.3. <i>Derjaguin, Muller, Toporov (DMT) model</i>	19
2.3.4. <i>Greenwood and Williamson model of multiasperity contact</i>	20
2.4. Modern concepts of friction	20
2.4.1. <i>Interfacial friction</i>	21
2.4.2. <i>Friction on the atomic scale</i>	24
2.4.3. <i>Friction anisotropy</i>	25
2.4.4. <i>Effects of chemistry and environment on friction</i>	26
2.4.5. <i>Velocity effects in nanotribology</i>	27
2.5. Theoretical models and numerical simulations of friction	28
2.5.1. <i>Cobblestone model</i>	28
2.5.2. <i>Simple analytical models of friction on the atomic scale</i>	29
2.5.3. <i>Molecular dynamics</i>	31
2.6. Measuring friction: from micro- to nanotribology	32
2.6.1. <i>Pin-on-disc instrument</i>	33
2.6.2. <i>Surface forces apparatus</i>	34
2.6.3. <i>Lateral force microscopy</i>	35

2.7. Concluding remarks	38
2.8. References	41
<b>Chapter 3. Quantification of friction forces in lateral force microscopy</b>	<b>47</b>
3.1. Introduction	48
3.2. Determination of cantilever spring constants	51
3.2.1. <i>Calibration according to elasticity theory</i>	51
3.2.2. <i>Calibration according to finite element modeling</i>	53
3.3. Calibration of the lateral photodiode sensitivity	54
3.4. Probe tip characterization	58
3.4.1. <i>Characterization of the tip apex</i>	58
3.4.2. <i>Tip wear</i>	60
3.5. Conclusions	63
3.6. Experimental	63
3.6.1. <i>Calibration procedure</i>	63
3.6.2. <i>Tip wear test</i>	64
3.6.3. <i>Wear-resistant coating for AFM tips</i>	65
3.7. Appendix	66
3.7.1. <i>Non-uniform thickness of a Si<sub>3</sub>N<sub>4</sub> cantilever</i>	66
3.7.2. <i>Error analysis of the two-step calibration technique</i>	66
3.7.3. <i>Monitoring of tip wear in situ</i>	69
3.7.4. <i>XRD of Al<sub>2</sub>O<sub>3</sub> coated Si tip</i>	70
3.8. References	71
<b>Chapter 4. Fabrication, validation and application of a new universal calibration specimen for the calibration of friction forces in AFM</b>	<b>75</b>
4.1. Introduction	76
4.2. Wedge calibration method	77
4.3. Fabrication of the universal calibration specimen	79
4.4. Comparison of the direct method and the two-step approach	81
4.5. Discussion of the factors that affect the direct wedge calibration method	83
4.5.1. <i>Wedge calibration on differently sloped surfaces</i>	84
4.5.2. <i>Effect of laser light interference</i>	85
4.5.3. <i>Tip position relative to the cantilever's main axis</i>	86
4.5.4. <i>Tips with flat apex</i>	87



---

4.5.5. <i>Additional sample tilt</i>	88
4.5.6. <i>Different feedback settings</i>	89
4.5.7. <i>Repositioning of the laser beam on the cantilever</i>	89
4.6. Experimental results for nanotribology on Si(100), PMMA and micropatterned SAMs	90
4.7. Conclusions	93
4.8. Experimental	94
4.8.1. <i>Materials and sample preparation</i>	94
4.8.2. <i>Fabrication of the universal calibration specimen</i>	95
4.8.3. <i>Calibration procedures</i>	95
4.8.4. <i>Lateral force measurements</i>	95
4.9. Appendix	97
4.9.1. <i>Error analysis for the wedge calibration method</i>	97
4.9.2. <i>The improved wedge calibration method for specimens with two (non-zero) slopes</i>	97
4.10. References	99
<b>Chapter 5. Development of a high velocity accessory for atomic force microscopy-based friction measurements</b>	<b>101</b>
5.1. Introduction	102
5.2. Experimental setup	103
5.2.1. <i>Instrumental design</i>	103
5.2.2. <i>Data acquisition</i>	106
5.2.3. <i>Calibration</i>	107
5.3. Experimental results and discussion	110
5.4. Conclusions	112
5.5. Appendix	113
5.6. References	116
<b>Chapter 6. Effects of grain size and humidity on nanotribological properties of nanostructured ZrO<sub>2</sub></b>	<b>119</b>
6.1. Introduction	120
6.2. Morphology	122
6.3. Film characterization	124
6.4. Nanotribology – results and discussion	125

---

6.4.1. <i>Effect of humidity</i>	127
6.4.2. <i>Effect of grain size</i>	128
6.5. Conclusions	130
6.6. Experimental	130
6.6.1. <i>Materials</i>	130
6.6.2. <i>AFM</i>	131
6.6.3. <i>X-ray photoelectron spectroscopy (XPS)</i>	131
6.6.4. <i>Contact angle measurements</i>	132
6.7. Appendix	133
6.8. References	134

**Chapter 7. Nano- and microtribology of low friction wear-resistant ceramics:**

<b>From micro- to nanotribology</b>	<b>137</b>
7.1. Introduction	138
7.2. Morphology of 3Y-TZP doped with CuO	140
7.3. Microtribology of 3Y-TZP doped with CuO	142
7.4. Nanotribology of 3Y-TZP doped with CuO	143
7.5. Comparative discussion of micro- and nanotribology on CuO doped 3Y-TZP	148
7.6. Concluding remarks	151
7.7. Experimental	152
7.7.1. <i>Materials and sample preparation</i>	152
7.7.2. <i>AFM</i>	153
7.7.3. <i>Pin-on-disc measurements</i>	154
7.8. Appendix	155
7.9. References	157

**Chapter 8. Tribology from the nano- to the mesoscale: Probing polymer relaxations at the surface of PMMA films by high velocity AFM**

8.1. Introduction	160
8.2. Nanotribology on PMMA films	164
8.2.1. <i>Effect of temperature</i>	165
8.2.2. <i>Effect of different tip radii</i>	167
8.3. Conversion of scanning velocity to frequency	170
8.4. Effect of sample-tip contact pressure on relaxation processes	171

8.5. Construction of a mastercurve for observed surface relaxations via the time-temperature superposition principle	172
8.6. Conclusions	174
8.7. Experimental	175
8.7.1. <i>Materials and sample preparation</i>	175
8.7.2. <i>Lateral force measurements</i>	175
8.8. Appendix	177
8.9. References	178
<b>Outlook</b>	<b>181</b>
<b>Summary</b>	<b>185</b>
<b>Samenvatting</b>	<b>189</b>
<b>Acknowledgments</b>	<b>193</b>
<b>Curriculum Vitae</b>	<b>195</b>
<b>Publications</b>	<b>195</b>



# Chapter 1

## Significance of nanotribology and its application

Tribology is the study of adhesion, friction, lubrication and wear of surfaces in relative motion. Despite its important role for a large range of technological processes, as well as for everyday life, a fundamental understanding of friction has not yet emerged.<sup>1</sup> Tribology remains as important today as it was in ancient times in the fields of physics, chemistry, mechanics, geology, biology and engineering. Our everyday life is strongly affected by phenomena related to friction, wear and lubrication. Friction plays an important role since it largely determines energy dissipation and, together with wear, determines the lifetime and reliability of devices, instrumentation, *etc.* Sometimes high friction is used to our advantage, such as in the brakes in our cars or the soles of our shoes. In other instances, such as the sliding of the piston against the cylinder in our car engine, lower friction is desirable.

### 1.1. Micrometer scale tribology

The demand for the control of friction has been the motivation for tribological studies for centuries. However, until the 1950's technological advances have been made mainly empirically.<sup>1</sup> Three phenomenological macroscopic friction laws were formulated: (i) friction force is independent of the apparent area of contact, (ii) friction force is proportional to the applied load, and (iii) friction force is independent of velocity. The modern study of friction started in 1950's, when a research group at Cambridge headed by Bowden and Tabor made an important discovery.<sup>2</sup> They found that friction is independent of the *apparent* (macroscopic) contact area, but is proportional to the *true* contact area. The vast majority of surfaces is not atomically flat. When two such surfaces touch, contact between them takes place only at the exposed asperities. Consequently, the importance of investigating single asperity contacts in fundamental tribological studies has been recognized.

## 1.2. Nanometer scale tribology

Since the advent of new experimental techniques, such as the friction force microscope (FFM),<sup>3-5</sup> the surface forces apparatus (SFA),<sup>6-8</sup> and the quartz crystal microbalance (QCM),<sup>9,10</sup> friction of single asperity contacts can be studied. A new field has emerged, which is called tribology on the nanometer scale or *nanotribology*.<sup>4</sup> The experimental “single asperity” techniques have provided insights into many tribological phenomena that were not accessible before.<sup>11</sup>

The studies of single asperity friction force often reveal behavior that is markedly different from that obtained on the macroscopic scale.<sup>10,12</sup> In contrast to microtribology, wear-less interfacial friction can be observed.<sup>13,14</sup> Friction of a single asperity contact is proportional to the contact area. Thus, for a spherical probe on a flat surface a 2/3 power law behavior of friction force vs. load is expected according to continuum contact mechanics (e.g. using the Hertz or the Johnson-Kendall-Roberts, JKR, model).<sup>13,14</sup> This behavior has been indeed observed.<sup>13,15</sup> Moreover, for single asperity contacts friction force may depend on velocity.<sup>16</sup> Thus the classical laws are not applicable on the nanometer scale. However, for multiasperity contact the linearity of the second law (*ii*) can be recovered through the statistical average over all contacts, assuming a certain height distribution of the contacting asperities.<sup>17</sup>

Furthermore, new phenomena were revealed on the atomic scale, such as lateral forces exhibiting stick-slip behavior with the atomic or molecular lattice periodicity,<sup>18,19</sup> and a new mechanism of friction, superlubricity.<sup>20</sup> The ultralow friction observed in the presence of the latter mechanism was attributed to lattice incommensurability between the contacting surfaces. Friction anisotropy was observed for different molecular/atomic orientations and structures of the corresponding surfaces.<sup>21,22</sup> Besides the orientation effect, the chemical environment and the chemical identity of species at the interface also determine friction forces.<sup>23-25</sup>

It is the main challenge of modern tribology to develop a fundamental understanding of friction, which allows one to bridge the different length (and time) scales and to properly relate the atomistic processes with macroscopically observed phenomena.<sup>26,27</sup> The ability of controlling friction will be highly advantageous in new technological developments, such as magnetic storage devices, and applications, such as in microelectromechanical systems (MEMS) and nanoelectromechanical systems (NEMS),<sup>28</sup> biosystems,<sup>29</sup> and many others.

However, the necessary bridge between micro- and nanotribology, as well as atomistic and continuum models, has not yet been addressed convincingly. Systematic studies that bridge the gap between the scale of microscopic friction and nanometer scale tribology are still missing.

---

This shortcoming can in parts be attributed to the fact that the instruments for nano- and microtribology operate on different time and length scale regimes. The most prominent instrument for performing nanotribological studies is atomic force microscope (AFM), since it is suitable for the detection of friction forces of nanometer scale contacts of real surfaces with high spatial resolution under pressures of up to several GPa. The main drawbacks of this instrument are difficulties with reliable friction force calibration and a very restricted range of velocities as compared to velocities that are relevant for real processes and applications.<sup>4</sup>

### 1.3. Concept of this Thesis

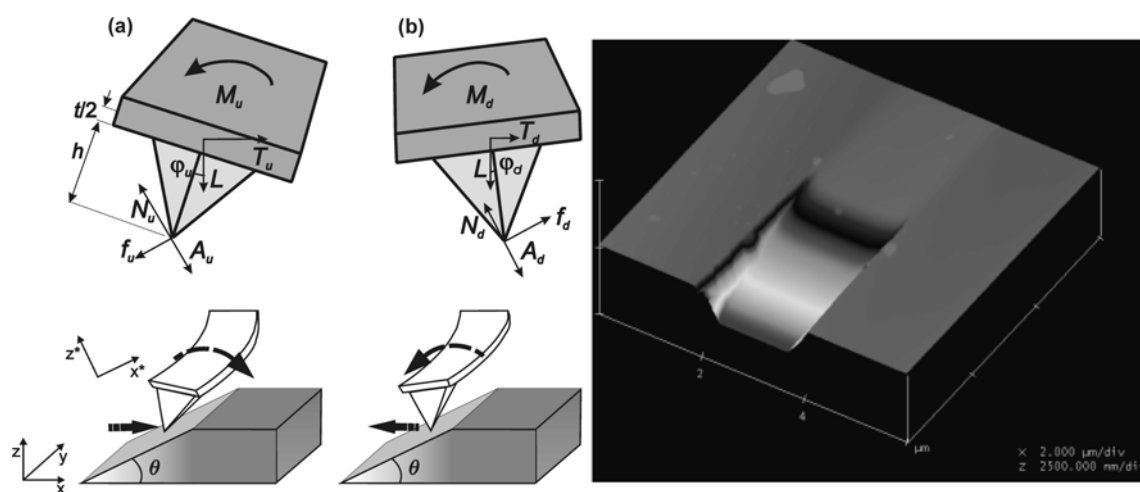
The objective of this Thesis is to provide the necessary platform development for quantitative nanotribology, including the reliable calibration of friction forces, the technical development of a high velocity accessory and full environmental control for atomic force microscopy, which allows one to perform nanotribological studies that are complementary to microtribology. Expanding on these advances, the experimental work in this Thesis aimed at the quantification of nanoscale friction of a wide range of materials and the elucidation of the effects of nanostructure, environment and velocity on friction.

Chapter 2 provides the background for this Thesis and presents an overview of modern concepts of tribology. The aspects summarized range from single asperity to multi asperity friction, including energy dissipation processes, interfacial friction, atomic scale friction, friction anisotropy, velocity dependence, as well as effects of chemistry and environment. Both experimental and computational results are reviewed and instruments for micro- and nanotribology are discussed.

The most important issues for quantitative friction force measurements, including friction force calibration, tip apex characterization, and tip stability, are discussed and critically tested using a variety of lateral force microscopy (LFM) probes. In particular, the frequently applied technique for friction quantification, the two-step calibration method, is experimentally tested for V-shaped and single beam cantilevers and its accuracy is estimated. The crucial parameters limiting this accuracy are identified. Finally, the wear-resistance of different tips is investigated and a method for improving the wear-resistance of LFM probe tips is developed.

In Chapter 4 the fabrication, validation and application of a new, universally applicable standard specimen for a direct calibration method (the wedge calibration method, as originally introduced by Ogletree, Carpick, and Salmeron *Rev. Sci. Instrum.* **1996**, *67*, 3298 – 3306 and later improved by Varenberg, Etsion, and Halperin *Rev. Sci. Instrum.* **2003**, *74*, 3362-3367) are

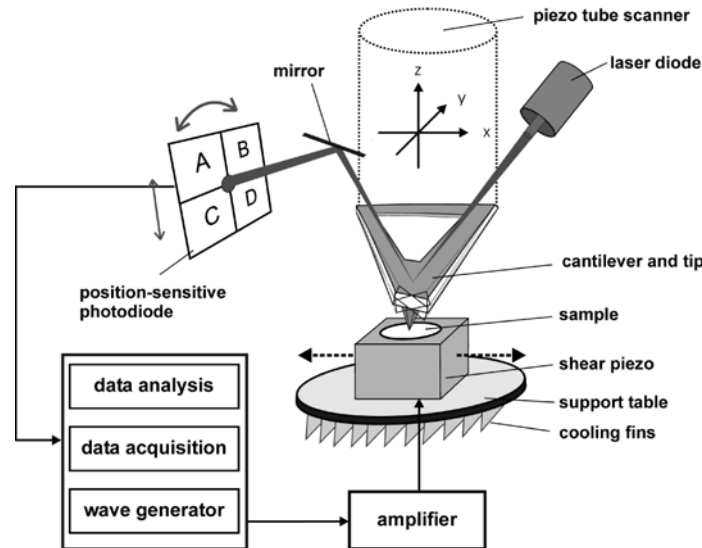
described. This calibration platform (specimen + method, see Scheme 1-1) overcomes the mentioned limitations of the two-step procedure and enables calibration of all types of LFM probe cantilevers with an error of  $\sim 5\%$ . The quantification of friction forces obtained on this universal standard specimen using the direct method is critically tested for various types of  $\text{Si}_3\text{N}_4$  integrated cantilever-tip assemblies. As demonstrated for oxidized Si(100), thin films of poly(methyl methacrylate) (PMMA), and micropatterned self-assembled monolayers (SAMs) on gold, this calibration allows one to perform quantitative nanotribology.



Scheme 1-1. (left) Schematic illustration of the torsion of a LFM cantilever while (a) sliding up and (b) sliding down on a sloped surface (in the  $x$  direction). (right) AFM height image of the lateral force calibration specimen fabricated using focused ion beam (FIB) milling.<sup>30</sup>

In chapter 5, the development of a high velocity accessory for friction force measurements in controlled environment (0 - 40% relative humidity (RH) and 0 - 40°C) is described, covering the velocity range between nm/s and several mm/s (Scheme 1-2). The design and calibration of the accessory, as well as validation measurements at high velocities, are discussed, followed by a report of novel nanotribology data acquired on thin polymer films and oxidized Si(100).





Scheme 1-2. Schematic of the high velocity AFM set-up comprised of a commercial stand-alone AFM, the high velocity accessory and peripheral devices for accessory operation, data acquisition and signal processing (the components are not shown to scale).<sup>31</sup>

The nanotribological properties of ultrathin nanostructured tetragonal  $ZrO_2$  coatings on oxidized Si(100), which can be used as protective coatings owing to improved material properties, were assessed by AFM-based friction force microscopy under full environmental control, as discussed in Chapter 6. In addition to validating nanotribology on ceramic coatings by AFM, the effects of grain size and humidity on the friction coefficient are investigated. In comparison with the reference sample of Si(100) with native oxide layer, ultrathin nanostructured  $ZrO_2$  coatings show a significantly reduced friction coefficient under all conditions.

In Chapter 7, the process of third body formation in 3Y-TZP (3 mol% yttria-stabilized tetragonal zirconia) ceramics doped with CuO is studied at different length scales as a function of sliding distance in pin-on-disc tests. The morphology and nanotribology of the tracks are analyzed by AFM. During the initial sliding in the microtribology experiments, the layer of surface contaminations is removed and wear of high asperities occurs. On these surfaces, very similar trends are observed in both nano- and microtribology. Challenges of bridging the gap between nano- and microtribology, such as understanding the influence of humidity on nanotribology, sample heterogeneity and experiments using the same probe material as in microtribology tests, are discussed as well.

The characterization and control of surface dynamics become increasingly important for advanced applications, such as NEMS, protective coatings, adhesives and lubricants. In Chapter 8, macromolecular relaxations of PMMA at the surface of  $\sim 120$  nm thick films are examined quantitatively by high velocity AFM over a broad range of frequencies (1 Hz to  $10^7$  Hz) using

distinctive velocity (from 0.3  $\mu\text{m/s}$  to 1 mm/s) and temperature (from  $-3^\circ\text{C}$  to  $26^\circ\text{C}$ ) ranges, as well as probe tips with different radii (20 nm to 870 nm). Friction data acquired at different temperatures and velocities are corrected for the effect of tip-sample contact pressure and are successfully shifted to yield one mastercurve (Figure 1-1). The  $\alpha$  and  $\beta$  relaxation processes of PMMA are identified in the Hz and MHz regime, respectively ( $T_{\text{ref}} = 26^\circ\text{C}$ ) and the corresponding activation energies of the relaxation processes are determined. These activation energies are found to be significantly lower and the relaxation frequencies of the processes are noticeably higher with respect to reported values for bulk PMMA.

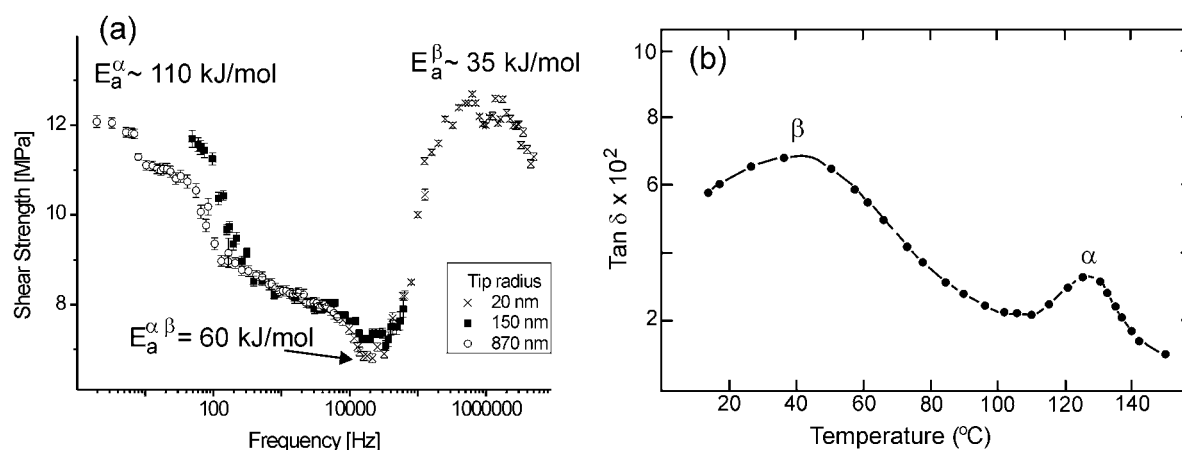


Figure 1-1 (a) Mastercurve of shear strength vs. frequency for PMMA film obtained by LFM ( $T_{\text{ref}} = 26^\circ\text{C}$ ). (b) Temperature dependence of the dielectric loss tangent at 28 Hz for conventional PMMA (after reference 32).

---

## 1.4. References

- 1 Dowson, D. *History of Tribology*. Professional Engineering Publishing: London, 1998.
- 2 Bowden, F. P.; Tabor, D. *Brit. J. Appl. Phys.* **1966**, *17*, 1521-1544.
- 3 Gnecco, E. In *Encyclopedia of Nanoscience and Nanotechnology*, Nalwa, H. S., Ed. American Scientific Publishers: Stevenson Ranch, 2004; Vol. 7, p 879-898.
- 4 Carpick, R. W.; Salmeron, M. *Chem. Rev.* **1997**, *97*, 1163-1194.
- 5 Marti, O. In *Handbook of Micro/Nano Tribology*, Bhushan, B., Ed. CRC Press: New York, 1999; p 81-144.
- 6 Homola, A. M.; Israelachvili, J. N.; McGuiggan, P. M.; Gee, M. L. *Wear* **1990**, *136*, 65-83.
- 7 Luengo, G.; Heuberger, M.; Israelachvili, J. *J. Phys. Chem. B* **2000**, *104*, 7944-7950.
- 8 Yoshizawa, H.; Chen, Y. L.; Israelachvili, J. *J. Phys. Chem.* **1993**, *97*, 4128-4140.
- 9 Krim, J. *Langmuir* **1996**, *12*, 4564-4566.
- 10 Krim, J. *Scient. Am.* **1996**, *October*, 2-8.
- 11 Meyer, E.; Overney, R. M.; Dransfeld, K.; Gyalog, T. *Nanoscience: Friction and Rheology on the Nanometer Scale*. World Scientific: Singapore, 1998.
- 12 Gao, J. P.; Luedtke, W. D.; Gourdon, D.; Ruths, M.; Israelachvili, J. N.; Landman, U. *J. Phys. Chem. B* **2004**, *108*, 3410-3425.
- 13 Schwarz, U. D.; Allers, W.; Gensterblum, G.; Wiesendanger, R. *Phys. Rev. B* **1995**, *52*, 14976-14984.
- 14 Schwarz, U. D.; Zwörner, O.; Köster, P.; Wiesendanger, R. *Phys. Rev. B* **1997**, *56*, 6987-6996.
- 15 Carpick, R. W.; Agrait, N.; Ogletree, D. F.; Salmeron, M. *Langmuir* **1996**, *12*, 3334-3340.
- 16 Gnecco, E.; Bennewitz, R.; Gyalog, T.; Loppacher, C.; Bammerlin, M.; Meyer, E.; Güntherodt, H. J. *Phys. Rev. Lett.* **2000**, *84*, 1172-1175.
- 17 Greenwood, J. A.; Williamson, J. B. P. *Proc. R. Soc. London A* **1966**, *295*, 300-319.
- 18 Mate, C. M.; McClelland, G. M.; Erlandsson, R.; Chiang, S. *Phys. Rev. Lett.* **1987**, *59*, 1942-1945.
- 19 Vancso, G. J.; Forster, S.; Leist, H. *Macromolecules* **1996**, *29*, 2158-2162.
- 20 Dienwiebel, M.; Verhoeven, G. S.; Pradeep, N.; Frenken, J. W. M.; Heimberg, J. A.; Zandbergen, H. W. *Phys. Rev. Lett.* **2004**, *92*, 126101.
- 21 Park, J. Y.; Ogletree, D. F.; Salmeron, M.; Ribeiro, R. A.; Canfield, P. C.; Jenks, C. J.; Thiel, P. A. *Science* **2005**, *309*, 1354-1356.
- 22 Liley, M.; Gourdon, D.; Stamou, D.; Meseth, U.; Fischer, T. M.; Lautz, C.; Stahlberg, H.; Vogel, H.; Burnham, N. A.; Duschl, C. *Science* **1998**, *280*, 273-275.
- 23 Frisbie, C. D.; Rozsnyai, L. F.; Noy, A.; Wrighton, M. S.; Lieber, C. M. *Science* **1994**, *265*, 2071-2074.
- 24 Vancso, G. J.; Hillborg, H.; Schönherr, H. *Adv. Polym. Sci* **2005**, *182*, 55-129.
- 25 Marti, A.; Hahner, G.; Spencer, N. D. *Langmuir* **1995**, *11*, 4632-4635.
- 26 Urbakh, M.; Klafter, J.; Gourdon, D.; Israelachvili, J. *Nature* **2004**, *430*, 525-528.
- 27 Robbins, M. O.; Smith, E. D. *Langmuir* **1996**, *12*, 4543-4547.
- 28 Cagin, T.; Che, J. W.; Gardos, M. N.; Fijany, A.; Goddard, W. A. *Nanotechnology* **1999**, *10*, 278-284.
- 29 Granick, S.; Lin, Z.; Bae, S. C. *Nature* **2003**, *425*, 467-468.
- 30 Tocha, E.; Schönherr, H.; Vancso, G. J. *Langmuir* **2006**, *22*, 2340-2350.

- 31 Tocha, E.; Stefański, T.; Schönherr, H.; Vancso, G. J. *Rev. Sci. Instrum.* **2005**, *76*, 083704.
- 32 McCrum, N. G.; Read, B. E.; Williams, G. *Anelastic and Dielectric Effects in Polymeric Solids*. John Wiley & Sons: London, 1967.

# Chapter 2

## **Tribology from single asperity to multi asperity contacts**

*This chapter serves as a background and a general overview of modern concepts of friction. The aspects summarized range from single asperity to multi asperity friction, including energy dissipation processes, interfacial friction, atomic scale friction, friction anisotropy, velocity dependence, as well as effects of chemistry and environment. Both experimental and computational results are reviewed and instruments for micro- and nanotribology are discussed.*

## 2.1. Fundamentals of tribology

Tribology is the science and technology of interacting surfaces in relative motion. The word tribology originated from the Greek word *tribos*, meaning rubbing.<sup>1</sup> Research in tribology, which includes studies of friction, wear and lubrication, has been most often motivated by the need to reduce energy losses and material degradation in moving mechanical devices. All complex phenomena that occur between interacting surfaces, including the formation of interfacial bonds, adhesion, structural rearrangements in solids and liquid phases during shear, hydrodynamics and rheology of lubrication films, are in the focus in tribology. However, despite the heavy volume of work performed so far,<sup>2,3</sup> a fundamental understanding of tribological processes does not exist. It could be said that friction itself is one of the most common, yet most poorly understood physical phenomena.

### 2.1.1. Definition of friction

When a lateral force, or shear stress, is applied to two surfaces in adhesive contact, the surfaces initially remain “pinned” to each other until some critical shear force is reached. At this point, the surfaces begin to slide past each other either smoothly or in jerks. The friction force needed to initiate sliding from the rest position is known as the *static friction force*, denoted by  $F_s$  (see Figure 2-1). The force needed to maintain smooth sliding is referred to as the *kinetic* or *dynamic friction force*, denoted by  $F_k$  or  $F_f$ . In general,  $F_s > F_k$ .<sup>4</sup> Two sliding surfaces may also move in regular jerks, known as “stick-slip” sliding, which is discussed in more detail in Section 2.4.2. The friction force between two bodies in the absence of lubrication is often called *dry friction*.

In the most common situation *normal friction* (kinetic friction accompanied by wear and/or plastic deformation) takes place when two rough surfaces slide with respect to each other. The surface asperities may deform elastically or plastically. When a strong force is applied to the surfaces, damage (or wear) of the shearing substrates occurs. Under certain conditions (low load, completely elastic interactions, smooth tip shape, atomically flat substrate, unreactive surfaces, *etc.*) a single-asperity contact may be formed and wear-less friction can be observed. This situation is often referred to as *interfacial* or *boundary friction* (Section 2.4.1).<sup>5</sup> In this regime it has been observed that friction is proportional to the contact area. This type of friction can be probed using the surface force apparatus (SFA) or atomic force microscopy (AFM)<sup>6</sup> (the differences between the instruments are described in detail in Section 2.6).

A general form of the normal friction force (also called lateral force) is given by:<sup>7</sup>

$$F_f = \mu F_N = \mu(L + A) \quad (\text{Eq. 2-1})$$

where  $\mu$  is the friction coefficient and  $F_N$  denotes the *normal force*, which is calculated as the sum of externally applied load  $L$  and the contribution from *adhesion forces* or *adhesion*  $A$  (the maximum force needed to separate two bodies).

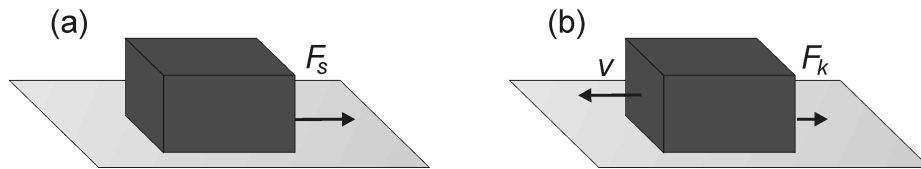


Figure 2-1. (a) The friction force needed to initiate sliding from rest is known as the *static friction force*, denoted by  $F_s$ . (b) The force needed to maintain smooth sliding is referred to as the *kinetic* or *dynamic friction force*, denoted by  $F_k$  or  $F_f$ .  $v$  stands for velocity.

### 2.1.2. Early observations of friction

Since prehistoric times humans have attempted to use and understand friction. By 200,000 B.C.E., Neanderthals had achieved a clear mastery of friction, generating fire by the rubbing of wood on wood and by the striking of flint stones. Significant tribological advances occurred 5,000 years ago in Egypt. Lubricated wooden sledges were developed for the transportation of large stone statues and blocks used for the construction of the pyramids. Classical tribology began 500 years ago, when Leonardo da Vinci made quantitative studies of the problem of friction. Da Vinci made two important observations: friction force (*i*) does not depend on the contact area and (*ii*) is proportional to the applied load. He introduced, for the first time, the concept of coefficient of friction as the ratio of the friction force to normal force. Da Vinci's work had no historical influence, because his observations remained unpublished for hundreds of years. In the 17<sup>th</sup> century, Guillaume Amontons rediscovered the laws of friction after he studied dry sliding between two flat surfaces. The third law of friction that states that friction is independent of velocity is attributed to Charles – Augustin de Coulomb.<sup>1,8</sup>

Based on the studies by Amontons and Coulomb, three laws of friction have been formulated:

1. *The friction force is independent of the apparent area of contact.*
2. *The friction force ( $F_f$ ) is proportional to the applied load ( $L$ ):  $F_f = \mu L$ . The ratio  $L/F_f$  is called coefficient of friction  $\mu$ . It's value is usually larger for static friction than for kinetic friction ( $\mu_s > \mu_k$ ).*
3. *Kinetic friction is independent of the velocity.*

These three macroscopic phenomenological laws of friction are still not fully understood in terms of the corresponding fundamental microscopic processes. However, these laws apply surprisingly well on the macroscopic scale for dry friction.

### 2.1.3. Multiple and single asperity tribology

The modern study of friction started in 1950's, when Bowen and Tabor presented a simple model of friction on the micrometer scale.<sup>9</sup> They found that friction force, although independent of apparent microscopic contact area, is in fact proportional to the true contact area ( $A_R$ ). Surfaces are rough on the microscopic scale, hence the microscopic irregularities of the surfaces touch and push into one another (Figure 2-2). The real area of contact is therefore a few orders of magnitude smaller than the apparent area of contact. In the Bowen and Tabor model, the friction force between two unlubricated (dry) surfaces arises from two main factors (Eq. 2-2). The first, and usually the most important factor is the interaction between the asperities of the contacting surfaces. It is assumed that this part of the friction force is proportional to both the real area of contact  $A_R$  and the interfacial shear strength  $\tau^*$ . The second factor, called the deformation term  $D$ , arises from the ploughing, grooving or cracking of one surface by asperities on the other surface. .

$$F_f = \tau^* A_R + D \quad (\text{Eq. 2-2})$$

Since the friction force is proportional to the real area of contact, as is adhesion (see Section 2.2.2), and since the energy loss in the friction mechanism is ascribed to plastic deformation of the asperities, the model is often called *adhesion model* or *plastic junction model*.<sup>9</sup>

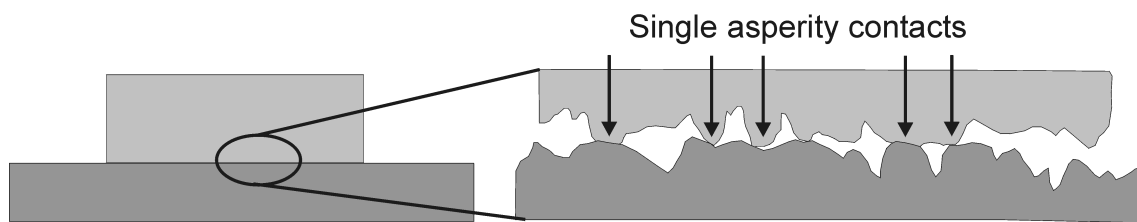


Figure 2-2. Surfaces are rough on the microscopic scale. The irregularities of the surfaces touch and push into one another. The real area of contact is a few orders of magnitude smaller than the apparent area of contact.

For purely plastic deformation, the area of contact  $A_R$  is proportional to the load<sup>10</sup> (which simplifies Eq. 2-2 to the second law by Amontons). However, totally plastic deformation during sliding provokes huge damage in a short time, which is usually not observed. Thus, elastic



processes must play an important role in friction processes and other dissipation mechanisms must exist, which do not change the structure of the surfaces in contact.<sup>9</sup>

Different length scales are relevant for microscopic experiments. The surface roughness will determine the size of the asperities. The smallest asperities are plastically deformed at very low loads, whereas larger asperities are still in the elastic regime (interfacial friction). On the micrometer scale the friction force has contributions from different phenomena, such as wear-less friction, plastic deformation of asperities, lateral forces to move debris particles, viscous forces and ploughing terms.<sup>7</sup>

To understand the behavior of such a complex contact, it is hence desirable to learn about the properties of single asperity contacts under conditions of interfacial friction. In this case, the friction force was found to be proportional to the real area of contact, hence in good agreement with the Bowden and Tabor model. As will be shown in Section 2.3, a non-linear friction force – load dependence is expected for single asperity contacts, which is in contradiction to Amontons' friction law. This is further detailed in section 2.4.1.

## **2.2. Surface forces and adhesion**

The interactions between the contacting asperities mentioned in the context of the adhesion model (section 2.1.3) are determined by interatomic/intermolecular forces between the atoms or molecules (functional groups) on the contacting surfaces. To provide a basis for further in depth discussions the most important types of surface forces are described in this section.

### *2.2.1. Elementary forces*

A number of attractive and repulsive forces operate between surfaces and particles, such as long-ranged (van der Waals, electrostatic, magnetic forces) and short-ranged forces (due to chemical and metallic bonding).<sup>11</sup> The intermolecular force  $F(r)$ , can be described by an interaction potential as a function of the intermolecular distance  $r$ , defined as a negative derivative of the interaction potential  $w(r)$ :  $F(r) = -dw(r)/dr$ . An interaction potential of two molecules, which includes a repulsive and an attractive term, was proposed by Mie

$$w(r) = -\frac{A}{r^n} + \frac{B}{r^m} \quad (\text{Eq. 2-3})$$

where  $(n, m)$  are integers. For  $(6, 12)$  we obtain the well-known Lennard-Jones potential (Figure 2-3).

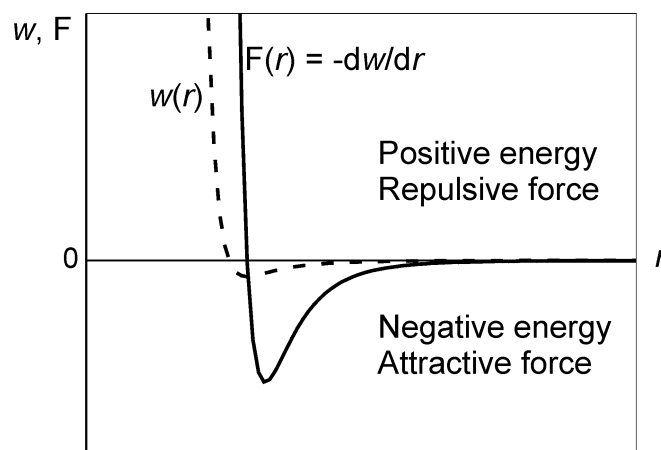


Figure 2-3. Lennard-Jones potential  $w(r)$  and force  $F(r)$  between two atoms as a function of separation distance  $r$ . Attractive forces possess per definition a negative sign.

The van der Waals forces encompass three forces of different origin. The dominant contribution is the dispersion, or *London* force, due to nonzero instantaneous dipole moments of all atoms and molecules. The second contribution is the *Keesom* force, which originates from the attraction between rotating permanent dipoles. The interaction between rotating permanent dipoles and the polarizability of all atoms and molecules generates the third contribution, the *Debye* force. The interaction potential between atoms and molecules of each force is a function of  $1/r^6$ . The van der Waals interaction potential between two bodies (*i.e.* an AFM tip and the sample surface) is usually given in terms of the *Hamaker* constant,  $A$ , as  $w(r)_{\text{sphere-planar surface}} = -AR/6r$  and  $w(r)_{\text{two planar surfaces}} = -A/12\pi r^2$  for sphere-planar surface and planar-planar surface, respectively.<sup>12</sup>  $r$  denotes the separation distance and  $R$  is the sphere radius. The van der Waals forces can be attractive (in vacuum and air) or repulsive only in some cases between dissimilar bodies interacting in solution.<sup>11,13</sup> The sign of Hamaker constant characterizes the type of van der Waals interactions.

In *vacuum*, the two main long-ranged interactions are the attractive van der Waals and electrostatic (coulombic) forces, while at smaller separations of the surfaces – corresponding to molecular contacts at a separation of  $\sim 0.2$  nm – additional attractive forces can come into play, such as covalent and metallic bonding forces. These attractive forces are stabilized by the hard-core repulsion and together they determine the surface and interfacial energies, as well as the strength of material and adhesive junctions.

When exposed to *vapors* (*e.g.*, atmospheric air containing water or organic molecules), two solid surfaces in or close to contact will generally have a surface layer of chemisorbed or physisorbed molecules, or a capillary condensed liquid bridge between them. These effects can drastically

modify adhesion (see also Section 2.2.2). In the case of capillary condensation the additional Laplace pressure or attractive “capillary” force between the surfaces may render the adhesion stronger than in inert gas or vacuum.

When totally immersed in a *liquid*, the force between two surfaces is once again completely modified from that in vacuum or air (vapor). The van der Waals attraction is generally reduced, but other forces can now arise, which can qualitatively change both the range and even the sign of the interaction. The overall attraction can be either stronger or weaker than in the absence of the intervening liquid medium. For example, the overall attraction is stronger in the case of two hydrophobic surfaces in water, but weaker for two hydrophilic surfaces. Since a number of different forces may be operating simultaneously in solution, the overall force law is not generally monotonically attractive, even at long range: it can be repulsive, oscillatory, or the force can change sign at some finite surface separation. In such cases, the potential energy minimum, which determines the adhesion force or energy, occurs not at true molecular contact, but at some small distance farther out.<sup>4</sup>

### 2.2.2. Adhesion and capillary forces

Adhesion between two surfaces is established by intermolecular forces.<sup>14</sup> Quantitatively, thermodynamic adhesion is expressed in terms of the change of Helmholtz  $\Delta F$  free energy in the process of joining two surfaces:  $\Delta F = \gamma_{ij} - \gamma_{iv} - \gamma_{jv}$ , where  $v$  stands for vapor,  $\gamma_{ij}$ ,  $\gamma_{iv}$ , and  $\gamma_{jv}$  are the interfacial and surface free energies of the  $ij$ ,  $iv$ , and  $jv$  interfaces, respectively.  $\Delta F$  is the equivalent to the thermodynamic work of adhesion  $W$ . In non-equilibrium processes, the so-called *adherence*<sup>15</sup> is used instead of the typically not measured thermodynamic adhesion; the value of (practical) work of adhesion is often higher than the reversible thermodynamic work of adhesion.

Different contributions are involved in adhesion force. These include the same type of forces as are responsible for the cohesions of solids, such as electrostatic, quantum-mechanical, polarization and van der Waals forces. Adhesion force, as the term used here, is the maximum force needed to separate two bodies. In an AFM force analysis experiment (see Section 2.6.3), the maximum negative force upon separation of the tip and sample is often denoted as the pull-off force.<sup>4</sup> The pull-off force is a function of the local radius of curvature, the equilibrium interatomic distance, the reduced elastic modulus of the tip and the sample (Eq. 2-8), as well as the practical work of adhesion. One may calculate the surface or interfacial energy  $\gamma$  from the pull-off force experiment, using the models described in next Section. If the maximum force

observed upon tip-sample approach in a force experiment (pull-on force) in the absence of cantilever instabilities is the same as the pull-off force, there is no *adhesion hysteresis*.<sup>4</sup> Adhesion hysteresis is the energy dissipated during loading-unloading cycles of force experiment, and is proportional to the area between loading and unloading curves. The most likely mechanism responsible for the adhesion hysteresis for systems in non-equilibrium thermodynamical conditions,<sup>16</sup> such as viscoelastic materials (does not hold for solid-solid contacts), was attributed to the interdigitation (*i.e.* thermally activated interdiffusion, interpenetration, entanglements, or molecular reorganization) of chains or molecular groups across the interface once they have come into contact.<sup>17,18</sup>

When considering the adhesion of two solid surfaces or particles in air or in a liquid, the important role of capillary forces (*i.e.* forces arising from the Laplace pressure of curved menisci which have formed as a consequence of the condensation of a liquid between and around two adhering surfaces) needs to be considered. The adhesion force  $F_a$  between a spherical particle of radius  $R$  and a flat surface of the same material in an inert atmosphere is:

$$F_a = -4\pi R\gamma_{SV} \quad (\text{Eq. 2-4})$$

but in an atmosphere containing a condensable vapor, the above equation becomes replaced by:

$$F_a = -4\pi R(\gamma_{LV} \cos\theta + \gamma_{SL}) \quad (\text{Eq. 2-5})$$

where  $\gamma_{SV}$ ,  $\gamma_{LV}$ , and  $\gamma_{SL}$  are solid-vapor, liquid-vapor surface energy (surface tension) and solid-liquid interfacial energy, respectively,  $\theta$  denotes the contact angle of the liquid on the surface (Figure 2-4). The first term of Eq. 2-5 is due to the Laplace pressure of the meniscus and the second is due to the direct adhesion of the two contacting solids with the liquid. It was observed that capillary forces can often largely determine the adhesion of the two surfaces in vapor.<sup>4,11,19</sup> Fisher and Israelachvili<sup>20</sup> measured the adhesion forces between curved mica surfaces in various vapors such as cyclohexane and benzene and found that  $F_a = -4\pi R\gamma_{LV}\cos\theta$  is already valid once the relative vapor pressures exceed 0.1 - 0.2, corresponding to meniscus radii of only 0.5 nm.

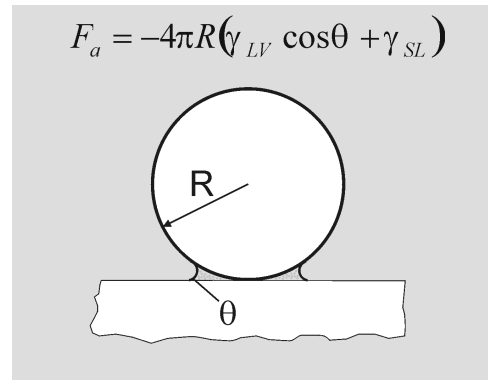


Figure 2-4. Sphere on flat in an atmosphere containing vapor “capillary condensed” around the contact zone.  $\theta$  denotes the contact angle of the liquid on the surface.

### 2.3. Elastic continuum contact mechanics

In macroscopic contacts, the interface consists of many micrometer and submicrometer size asperities, where real contact occurs. Contact continuum mechanics describe the elastic deformation of single asperities. All theories described below are based on the following assumptions: the deformations are purely elastic, the contacting materials are elastically isotropic, Young’s modulus and Poisson’s ratio are not load dependent, the atomic structure is not considered, and the contact radius  $a$  is small compared to the radius  $R$  of the sphere.

#### 2.3.1. Hertz model

The Hertz theory<sup>21</sup> assumes that no attractive forces act between the two materials. For a sphere-sphere contact, the contact area  $A_R$  depends on load  $L$ :

$$A_R = \pi \left( \frac{R \cdot L}{K} \right)^{\frac{2}{3}} \quad (\text{Eq. 2-6})$$

$$\frac{1}{R} \equiv \frac{1}{R_1} + \frac{1}{R_2} \quad (\text{Eq. 2-7})$$

$$K \equiv \frac{4}{3} \left( \frac{1-\nu_1^2}{E_1} + \frac{1-\nu_2^2}{E_2} \right)^{-1} \quad (\text{Eq. 2-8})$$

where  $R$  is the composite radius and  $R_1, R_2$  are the radii of curvature of the lower and upper body, respectively,  $K$  is the reduced elastic modulus,  $E_1, E_2$  and  $\nu_1, \nu_2$  are the Young’s moduli and Poisson’s ratios for the lower and upper body, respectively (Figure 2-5).

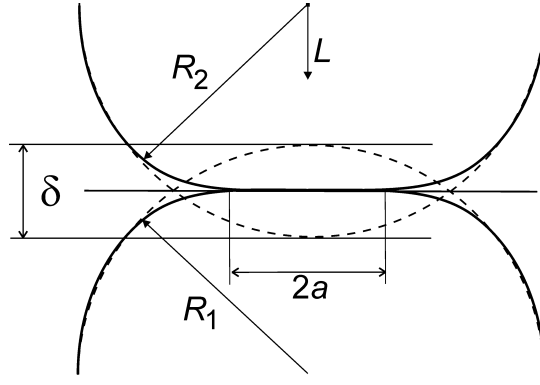


Figure 2-5. Geometry of a contact between two elastic spheres ( $R_1$  and  $R_2$ ) under applied load  $L$  for the Hertz theory.  $a$  denotes the contact radius,  $\delta$  is the indentation depth.

### 2.3.2. Johnson, Kendall and Roberts (JKR) model

The JKR model<sup>22,23</sup> is the extension of the Hertz model, in which the work of adhesion  $\gamma$  is taken into account.<sup>24</sup> It assumes that the adhesive forces are confined to the inside of the contact area. The contact area is described by:

$$A(L) = \pi \left( \frac{R}{K} \right)^{\frac{2}{3}} \left( L + 3\pi\gamma R + \sqrt{6\pi\gamma RL + (3\pi\gamma R)^2} \right)^{\frac{2}{3}} \quad (\text{Eq. 2-9})$$

Even at zero applied load there is a finite contact area of  $A_R(0) = \pi(6\pi\gamma R^2/K)^{2/3}$ . Hence, load has to be applied to break the contact. In the limit of work of adhesion equal zero ( $\gamma \rightarrow 0$ ) and also for large forces compared to  $\gamma R$ , the JKR result coincides asymptotically with the Hertzian result. The derivative of  $A_R$  with respect to load yields the minimum for the contact area (area at pull-off, see Section 2.6.3 for AFM pull-off force), which can be transformed to equation:

$$F_{\text{pull-off}}^{\text{JKR}} = -\frac{3}{2}\pi R W_{12} \quad (\text{Eq. 2-10})$$

The work of adhesion  $\gamma = W_{12}$  can be expressed as a function of the surface energies of the tip  $\gamma_1$ , the sample  $\gamma_2$ , and the corresponding interfacial energy  $\gamma_{12}$ :

$$W_{12} = \gamma_1 + \gamma_2 - \gamma_{12} \quad (\text{Eq. 2-11})$$

The JKR model can be applied when the surface forces are short range in comparison to the elastic deformations they cause (*i.e.* compliant materials, strong adhesion force, large tip radii).

### 2.3.3. Derjaguin, Muller, Toporov (DMT) model

The DMT model<sup>25-28</sup> includes adhesion outside the contact area by considering long-range attractive forces of van der Waals type. Maugis<sup>29</sup> provided an analytical solution for the model. In this case, the real area of contact  $A_R$  varies with load  $L$  in a simple fashion:

$$A_R = \pi \left[ \frac{R}{K} (L + 2\pi R\gamma) \right]^{\frac{2}{3}} \quad (\text{Eq. 2-12})$$

The pull-off force is given by:

$$F_{\text{Pull-off}}^{\text{DMT}} = -2\pi R W_{12} \quad (\text{Eq. 2-13})$$

The JKR and DMT models apply for two extreme cases: for compliant materials with large, short-range attractive forces and for stiff materials with small, long-range attractive forces, respectively. The parameter  $\lambda$  is used to determine which of the two models is most appropriate.

$$\lambda = \left( \frac{9RW_{12}^2}{4\pi K^2 z_o^3} \right)^{\frac{1}{3}} \quad (\text{Eq. 2-14})$$

where  $z_o$  is the equilibrium separation between the contacting surfaces. If  $\lambda > 5$ , the JKR theory should be valid, while for  $\lambda < 0.1$  the DMT theory should describe the relation between  $A_R$  and  $L$ .<sup>30,31</sup> The most frequently used description covering the JKR – DMT transition regime is the Maugis-Dugdale (MD) theory.<sup>29</sup> The model is relatively difficult to use because it is presented in two coupled analytical equations that must be solved numerically through iteration.

Recently, Carpick, Ogletree and Salmeron,<sup>32</sup> as well as Schwarz,<sup>33</sup> proposed a general analytical model for the elastic deformation of an adhesive contact in the intermediate regime between JKR and DMT limits as an alternative.

The application of the elastic contact continuum models for viscoelastic materials is limited. For instance, the models can be used only for materials that possess a glass transition temperature well below ambient temperature. For a viscoelastic material the size of the contact zone depends on the loading history. Several attempts have been made to modify the JKR theory with some relaxation functions. A combination model of classical JKR theory with a fracture mechanics model of crack initiation and growth in linear viscoelastic materials has been proposed by Johnson.<sup>34,35</sup> The major assumption of the model is that viscoelastic effects are limited to the periphery of the contact. Longer-range creep effects are ignored. Hui *et al.*<sup>36-38</sup> extended the JKR

theory for the contact radius which is a non-decreasing function of time (describing the bonding process). The presented models are complex and often necessitate the use of numerical calculations.

#### 2.3.4. Greenwood and Williamson model of multiasperity contact

Realistic surface interactions are influenced by not only the nominal apparent or contact areas  $A_n$ , but also by the individual asperity/roughness interactions. Greenwood and Williamson modeled surface roughness using a statistical model, where the roughness of two approaching surfaces is combined into an infinitely smooth surface and a surface with spherically shaped asperities having a uniform mean radius  $R$  and following a Gaussian height distribution. A linear dependence between the real contact area and the applied load was obtained independently of the mode of deformation of the asperities (*i.e.* whether it is elastic, plastic or something in-between) or the shape of asperities.<sup>39-41</sup> In this case, the Greenwood model leads to Amontons' law, as well as to the plastic junction model (Section 2.1.3).

### 2.4. Modern concepts of friction

Most frictional energy is dissipated as heat.<sup>42</sup> Neither the macroscopic nor microscopic mechanisms of energy dissipation have been fully explained. Two basic issues, the nature of friction and the energy dissipation at the fundamental level, are in the focus of present studies.<sup>43,44</sup> Different types of excitations, such as atomic and molecular excitation modes (vibrations and rotations), electron-hole excitations, collisions with impurities, phonons,<sup>45,46</sup> are responsible for the energy dissipation. Each process has an associated characteristic lifetime.<sup>47</sup> Electronic excitations, for example, have characteristic times on the order of femtoseconds; the typical lifetime of phonons is measured in picoseconds.<sup>43</sup> Other excitations to consider are soft phonon modes (*i.e.* modes of very low frequency), such as molecular displacements, rotations and liberations, which are particularly important in polymeric materials and films of organic molecules. Other excitations give rise to conformational changes of the molecules through the creation of gauche defects.<sup>48</sup> These various excitation modes determine the viscoelastic behavior of materials. Typical lifetimes of these modes can be in range of  $10^{-6} - 10^3$  s, depending strongly on temperature.<sup>49</sup> Because this lifetime can be comparable to sliding times in friction experiments (AFM, SFA), viscoelastic excitations can give rise to velocity dependent effects in friction and adhesion hysteresis that is observed in the formation and rupture of contacts.<sup>48</sup>



### 2.4.1. Interfacial friction

Interfacial friction, which can be probed using AFM<sup>50,51</sup> and SFA,<sup>52,53</sup> (Section 2.6) usually implies a single asperity contact, where no damage occurs to the contacting surfaces (wear-less regime). In general, the interfacial friction force of surfaces sliding smoothly past each other is given by:

$$F_f = \tau A_R \quad (\text{Eq. 2-15})$$

where  $\tau$  is the interfacial shear strength. The shear strength may depend on the applied pressure ( $P$ ) as observed experimentally on GeS using a Si tip in air (Figure 2-6)<sup>50</sup>

$$\tau = \tau_0 + \alpha P \quad (\text{Eq. 2-16})$$

$$F_f = \tau_0 A_R + \alpha L \quad (\text{Eq. 2-17})$$

where  $\tau_0$  and  $\alpha$  are assumed to be constant. The second term is proportional to the applied load as in Amontons' law for normal friction, but it has a different origin, since it does not require any interfacial adhesion nor the shearing of adhesive junctions.<sup>19</sup> Depending on whether the friction force  $F_f$  is dominated by the first or the second term (Eq. 2-17), one may refer to the friction as adhesion controlled or load controlled, respectively.<sup>4</sup> The most likely mechanism of energy dissipation in the low load regime (adhesion controlled friction) is the thermalization of phonons<sup>54</sup> generated in the contact zone during sliding. At higher loads different modes of energy dissipation may activate higher stresses, such as molecular deformation.<sup>55</sup>

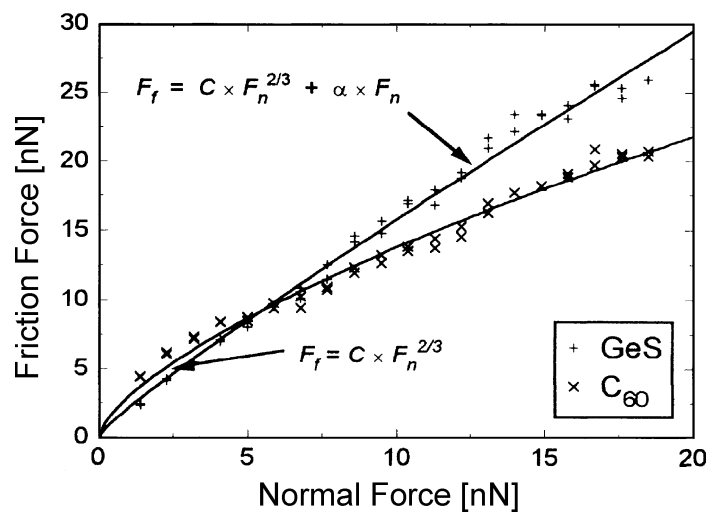


Figure 2-6. Friction force vs. normal force dependence for GeS and  $C_{60}$  obtained using a Si tip. Single asperity contacts were observed for  $C_{60}$  and GeS with a  $F_f \sim (F_N)^{2/3}$  law as well as a linear trend  $F_f \sim F_N$  due to shear strength dependence on pressure (after reference 50).

Most single asperity contacts show a nonlinear friction force – load dependence. In SFA experiments, the local contact geometry between the two mica cylinders is equivalent to the contact of a sphere and a flat surface (see Section 2.6.2).<sup>5</sup> The resulting contact area (as well as friction force) has been described using Hertz<sup>53,56</sup> or JKR<sup>16,57</sup> models. However, in AFM analysis, only tips with a spherical tip apex resulted in a  $F_f \sim (F_N)^{2/3}$  law.<sup>58</sup> Even small deviations from spherical shape produced deviations from the 2/3-power law. Using tips as provided by the manufacturers resulted in force laws of  $F_f \sim (F_N)^m$  with  $0.4 < m < 1.2$  at low loads due to the undefined tip/sample contact geometry. Moreover, AFM tips may be rough on the nanometer scale. Putman *et al.*<sup>59</sup> observed single to multi asperity transition between Si<sub>3</sub>N<sub>4</sub> tip and mica by changing environmental conditions from ambient to N<sub>2</sub> or Ar gas conditions. In ambient, the friction force – load curves showed Hertzian behavior. The same tip revealed a linear dependence under gaseous conditions. The result was explained by the tip being smoothed by the condensed water film, which led to single asperity contact at high humidities and to a multi asperity contact at low humidities. Single asperity contact has been observed for various systems, including mica,<sup>60-62</sup> diamond,<sup>58,63</sup> amorphous carbon,<sup>51</sup> C<sub>60</sub>,<sup>50</sup> glass<sup>64</sup> showing Hertzian,<sup>50</sup> JKR,<sup>60</sup> DMT<sup>63,65</sup> or MD<sup>66</sup> contact area – load dependences.

Frictional damage can have many causes, such as adhesive tearing at high loads or overheating at high sliding speeds. Once damage occurs, there is a transition from interfacial to normal friction,<sup>4,5</sup> as the surfaces become forced apart by the torn out asperities (wear particles). The friction changes rapidly from single asperity behavior to a behavior that obeys Amontons' law. Further, the sliding proceeds smoothly with the surfaces separated by wear debris of dimensions 100 to 1,000 Å. In contrast to interfacial friction, the values of friction coefficient for mica during normal friction were found to be insensitive to the ambient atmospheric conditions, or even immersing in a liquid.<sup>5</sup> Thus, the mechanism and factors, which determine normal friction behavior, must be different from those that govern interfacial friction.

Israelachvili *et al.*<sup>18,67</sup> reported that the absolute magnitude of adhesion is not directly correlated with the friction force values, as the above equations suggest. For instance, they found that mica separated by one or two layers of cyclohexane exhibits high friction, but low adhesion energy. By contrast, two mica surfaces in humid air show low friction but high adhesion energy. However, the authors suggested that the *adhesion hysteresis* is in close relation with friction. Israelachvili's theory is based on studies of particular molecular structures, such as long hydrocarbon chain molecules.

Israelachvili *et al.*<sup>18,53,68,69</sup> proposed a new approach to rationalize friction forces for confined liquids, lubricants and polymers, which can undergo first-order transitions and become “glassy” depending on the sliding conditions (load, velocity and temperature, see Figure 2-7). They found two extreme behaviors of confined layers, called solidlike and liquidlike, which can be captured in *friction phase diagrams*.<sup>18</sup> Solidlike films are characterized by stick-slip behavior (see Section 2.4.2). Above some critical velocity, smooth friction proceeds. Usually the friction force decreases slightly with increasing velocity. In contrast, the friction force of liquidlike layers is lower and more like of viscous liquid flowing between the surfaces. In the analysis of energy dissipation in confined layers versus the shear rate, a nonmonotonic change of friction was ascribed to the existence of characteristic relaxation times in the confined molecules. The maximum value of friction force can be expected when the time of observation is comparable with a characteristic relaxation time at the interface. This state, which occurs between the solidlike and liquidlike states, was called by the authors the amorphous state. Moreover, the phases (solidlike, amorphous, liquidlike) could be changed by varying the atmosphere, temperature, velocity or related parameters.<sup>57</sup> However, the velocity range accessible with conventional SFA and AFMs is limited to the range of nm/s to  $\mu\text{m/s}$ , which is often insufficient to provide relevant friction force data captured under realistic conditions. An approach to circumvent this problem of limited velocities is the combination of an AFM with a high frequency actuator for lateral displacement (Chapter 5).<sup>70</sup>

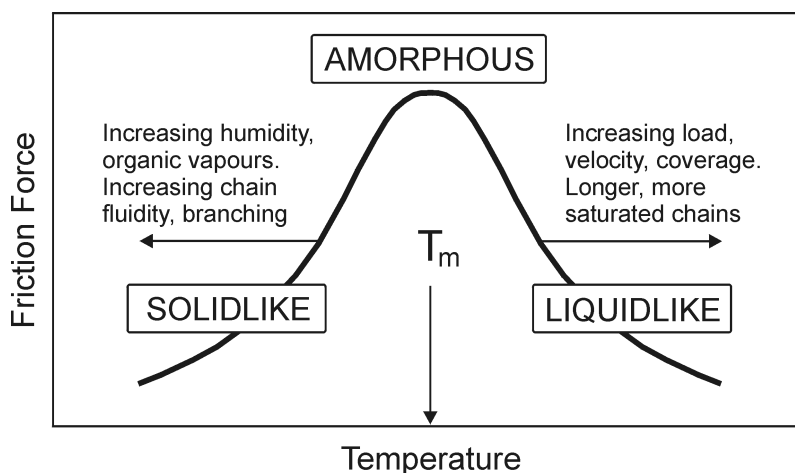


Figure 2-7. Schematic friction phase diagram representing the trends observed in the interfacial friction of confined liquids, lubricants and polymers. The arrows indicate the direction in which the whole bell-shaped curve shifts when the load, velocity, *etc.*, are increased (after reference 18).

### 2.4.2. Friction on the atomic scale

Pioneering work on atomic-scale friction was performed by Mate *et al.* using AFM (Figure 2-8).<sup>71</sup> They observed, for a tungsten tip sliding on graphite surface, lateral forces exhibiting stick-slip behavior with the lattice periodicity. The stick-slip phenomenon was first formulated by Tomlinson<sup>72</sup> in 1929 (see Section 2.5.2). At the contact interface of the tip and sample, atoms move in stick-slip motion over the surface, jumping from one potential minimum of the tip-sample interaction to the next one.<sup>60</sup> When the scan direction is reversed (retrace), the signal polarity changes sign and the stick-slip process has opposite polarity.<sup>73</sup> The maximum and average value of the stick-slip sawtooth modulation can be related to micrometer scale values of static and dynamic friction force, respectively.<sup>74</sup> The area enclosed by the lateral force curve (trace-retrace, called friction loop) has the dimensions of energy and its value represents the energy dissipated during each scanning cycle.<sup>56,73</sup> The height of the interaction potential was found to increase proportionally to the applied external load.<sup>75</sup>

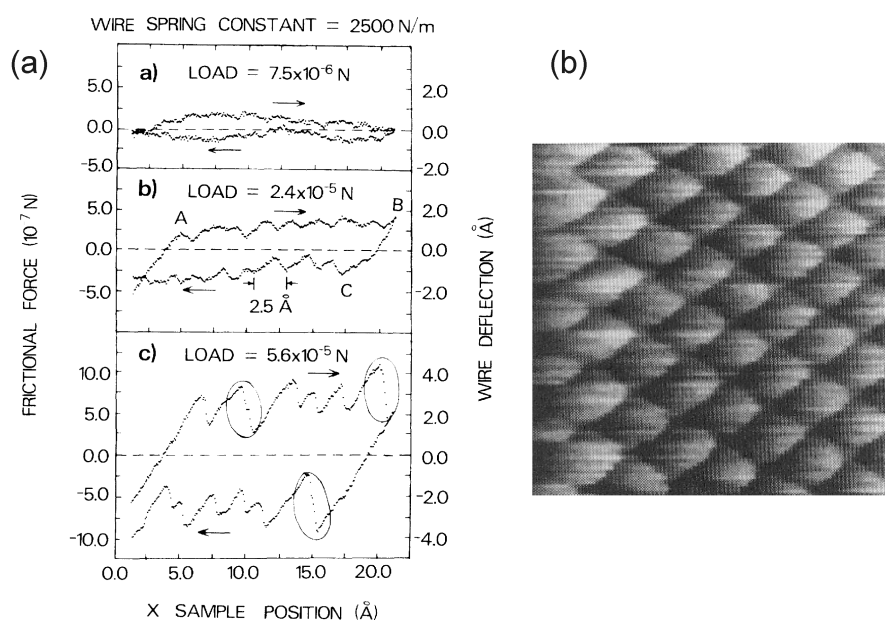


Figure 2-8. (a) Variation of the lateral force between a tungsten tip and graphite surface as the tip is scanned laterally over the surface. Three of these so-called friction loops are shown for different loading forces. The lower curve clearly shows the typical stick-slip behavior. (b) Two-dimensional map of the lateral force recorded as the tip is moved 2 nm from left to right. The spatial variation of the lateral force has the periodicity of the HPOG (highly oriented pyrolytic graphite) (after reference 71).

If the sample is scanned slowly in the direction perpendicular to the fast scan which corresponds to the acquisition of the friction loops, two-dimensional maps of the lateral force are obtained.<sup>73</sup> The “atomically resolved” friction maps (images) show potential minima, but not the atomic

positions.<sup>76</sup> The two dimensional stick-slip effects observed in experimental friction maps<sup>77,78</sup> were reproduced in simulations, where the tip trajectories may have straight or zig-zag stick-slip shape.<sup>79</sup>

Atomic scale friction on ionic crystals (NaF, AgBr, NaCl, and KBr)<sup>80-83</sup> was systematically studied by Meyer and coworkers with an ultra high vacuum-AFM (UHV-AFM). Atomic stick-slip was also revealed on Cu(111) and Cu(100),<sup>84</sup> diamond,<sup>85</sup> MoS<sub>2</sub>,<sup>78,86</sup> and mica.<sup>60,62,87</sup> In contrast to microscopic stick-slip behavior,<sup>18,88,89</sup> the observation of the atomic scale stick-slip phenomena was independent on the cantilever stiffness.<sup>84</sup> Moreover stick-slip behavior on the molecular scale was observed on oriented PTFE films,<sup>90</sup> if the scanning was performed at an angle significantly different from zero with respect to the chain direction. If scanning was performed in the chain direction, smooth sliding was obtained, revealing friction anisotropy (see Section 2.4.3).

As another example of atomic scale friction phenomena a new mechanism of friction, superlubricity, has been postulated based on atomistic theory.<sup>91</sup> Friction forces vanish, when the surfaces that are sliding against each other are incommensurate.<sup>92</sup> For example, the ultralow friction of graphite was revealed by AFM and attributed to incommensurability between rotated graphite layers (graphite surface and a graphite flake attached to the AFM tip).<sup>93</sup> A transition from stick-slip to continuous sliding in atomic friction, which was observed for NaCl surfaces, coincides with the onset of a new regime of ultra low friction force.<sup>94</sup> This ultra low friction was attributed to absence of mechanical instabilities and was controlled by variations of applied load on the contact, which changes the atomic corrugation potential.

### 2.4.3. Friction anisotropy

The following examples demonstrate that the tip-sample frictional interaction can depend upon the molecular/atomic orientation and structure of the interface in a measurable fashion by AFM. The role of the sliding direction in friction processes was observed by Hirano *et al.*<sup>91</sup> in the contact of two mica sheets with different orientations. The friction forces were anisotropic with respect to the lattice misfit angle, *i.e.* the forces increased when commensurate contact of the surfaces was approached and decreased when incommensurate contact of the surfaces was approached. Different molecular alignments of an organic bilayer film, as reported by Overney *et al.*,<sup>74</sup> lead to a significant change of friction forces. An impressive example of friction anisotropy was found for a thiolipid monolayer on mica by Gourdon *et al.*<sup>95,96</sup> These authors observed a flower-shaped structure, formed by domains with different molecular orientation.

The dependence of friction force on scanning direction suggested that molecules possess a radial tilt, which is directed towards the center of the ‘flower’.

A transition from anisotropic to isotropic friction was observed for an Al-Ni-Co quasicrystal and a thiol-passivated TiN tip after oxidation of the surface.<sup>97</sup> Other studies unveiled anisotropic friction at the surface of lamellar polymer crystals (see Figure 2-9), including poly(oxymethylene)<sup>98,99</sup> and polyethylene,<sup>99,100</sup> as well as on oriented PTFE and PE films.<sup>90,99</sup>

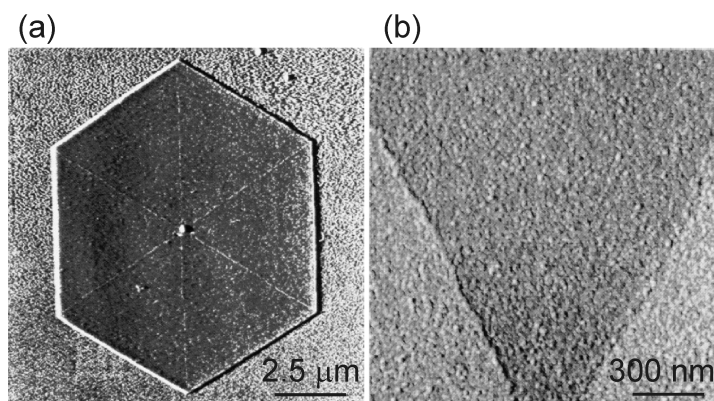


Figure 2-9. Lamellar crystals of poly(oxymethylene) with clearly resolved chain fold domains at the surface of the lamellae defined by the diagonals and the edges of the crystals. The frictional force within the domains, obtained in AFM experiments, was found to depend on the relative scan direction (after reference 98).

#### 2.4.4. Effects of chemistry and environment on friction

Besides atomic orientation effects, the role of the chemical environment and the chemical identity plays a role at the interface in determining friction. The sensitivity of lateral forces to chemical diversity can be also exploited to achieve surface chemical imaging using AFM. Marti *et al.*<sup>101,102</sup> have shown that changes in pH can affect friction. These authors measured lateral forces between a Si<sub>3</sub>N<sub>4</sub> tip and a flat SiO<sub>2</sub> sample immersed in solution. Variations in the pH changed the degree of protonation of hydroxyl (OH) groups on the tip and sample surfaces. This affected the interaction forces between tip and sample and the resultant dependence of friction upon load varied with pH. The measured friction forces and adhesion hysteresis were highly correlated in accordance with Israelachvili's theory.<sup>4</sup>

Binggeli *et al.*<sup>103</sup> studied changes in frictional forces under variable electrochemical conditions. The authors measured frictional forces between a tip and a graphite surface in an electrolyte solution as a function of the electro-chemical potential. They found that there was a dependence of the friction force at graphite step edges. In a certain potential range, friction was strongly enhanced at step edges. Higher friction at step edges was also observed on NaCl.<sup>104</sup> In particular

this topographic effect, influenced by several factors, such as variations in contact area, differences in van der Waals, capillary and electrostatic forces, contaminants, can be explained in terms of increased energy barriers at the steps, known as Schwoebel barriers.

The connection between chemical nature, adhesion and friction has been established by Frisbie *et al.*,<sup>105</sup> who demonstrated different adhesion between surfaces (tip and substrate) coated with molecules exposing a variety of end groups. The adhesive forces between self-assembled monolayer coated tip and sample surfaces probed in ethanol were found to be in the order  $\text{COOH}/\text{COOH} > \text{CH}_3/\text{CH}_3 > \text{COOH}/\text{CH}_3$ . The trend in adhesive forces was consistent with the interactions between hydrophilic groups that can form hydrogen bonds, which were stronger than between hydrophobic groups. The frictional forces were observed to change in the same order. Green *et al.*<sup>106</sup> reported similar effects with a large variety of functional groups at the end of molecules of similar length (15 carbon atoms) attached to one or both surfaces (COOH, CH<sub>2</sub>OH, COOCH<sub>3</sub>, CH<sub>2</sub>Br, CH<sub>3</sub> terminations). The frictional forces ranked in the same order given above and showed a clear correlation with the surface energy as measured by macroscopic methods, such as water contact angle. Moreover, the terminal functional groups can affect the wettability of the surface.<sup>107</sup> Under conditions of high humidity, the frictional force for hydrophilic surfaces decreases due to the lubricating effect of water, whereas for hydrophobic surfaces, the friction force increases by increased adhesion in the contact zone.

As shown above there is an interplay between friction and chemistry and vice versa. On the one hand, the chemical environment and chemical identity can determine the friction. On the other hand, friction influences chemical reactions occurring at the interface and stimulates the formation of surface layers for different kind of materials (called tribochemistry).<sup>108,109</sup> For instance, Carpick *et al.*<sup>60</sup> observed a scanning induced reduction of the tip-sample adhesion and friction for Pt-mica system in UHV. These interfacial changes were attributed to either structural or chemical changes in the surface of the Pt tip.

#### **2.4.5. Velocity effects in nanotribology**

The velocity effects in friction force were studied by AFM only recently. Zwörner *et al.*<sup>110</sup> observed that friction between silicon tips and diamond, graphite or amorphous carbon is constant with scan velocities of several  $\mu\text{m/s}$ . Gourdon *et al.*<sup>95</sup> explored a range of velocities from 0.01 to 50  $\mu\text{m/s}$  and found a critical velocity of 3.5  $\mu\text{m/s}$  (for a thiolipid monolayer on mica), which discriminates between an increasing friction force and constant friction force regime. A clear observation of a logarithmic dependence of friction force on the micrometer

scale was reported by Bouhacina *et al.*,<sup>111</sup> who studied friction of triethoxysilane molecules and polymers grafted on silica with sliding velocity up to 300  $\mu\text{m/s}$ . The result was explained with a thermally activated Eyring model.<sup>112</sup> The first measurements on the atomic scale were performed by Bennowitz *et al.*<sup>82,84</sup> on copper and sodium chloride. In both cases a logarithmic increase of friction force on velocity was revealed (for velocities up to 1  $\mu\text{m/s}$ ). This result was attributed to thermal activation of the irreversible jumps leading to the hysteretic behavior of lateral forces.<sup>82</sup> Higher values of velocities were not explored due to the limited range of the scan frequencies of AFM.

The dependence of friction force on increasing velocity is ultimately related to the materials and the environment in which the measurements are performed. In humid environment, Riedo *et al.*<sup>64,113</sup> observed that the surface wettability has an important role. Friction force decreases logarithmically with increasing velocity on hydrophilic surfaces, and the rate of the decrease depends strongly on humidity. By contrast, a logarithmic increase of friction force as a function of velocity was found on partly hydrophobic surfaces. These results were interpreted considering the thermally activated nucleation of water bridges between tip and sample asperities.<sup>114,115</sup>

### **2.5. Theoretical models and numerical simulations of friction**

At both macroscopic and molecular levels, friction can be described as the dissipation of energy. The goal of molecular-level experiments is to determine the mechanisms of energy dissipation and to correlate the energy loss to molecular events. At surface separations below a few nanometers, continuum approaches break down and molecular or atomistic models need to be considered to explain friction processes.

#### **2.5.1. Cobblestone model**

A simple model that relies on surface energy and shear strength in the absence of wear is the so-called *Cobblestone model*, which was first proposed by Tabor<sup>116</sup> and later described by Israelachvili and coworkers.<sup>4</sup> In this model, the values of the interfacial shear strength and coefficient of friction are calculated in terms of the energy needed to overcome the attractive intermolecular forces and compressive externally applied load as one surface is raised and then slides across the molecular asperities of the other (Figure 2-10).



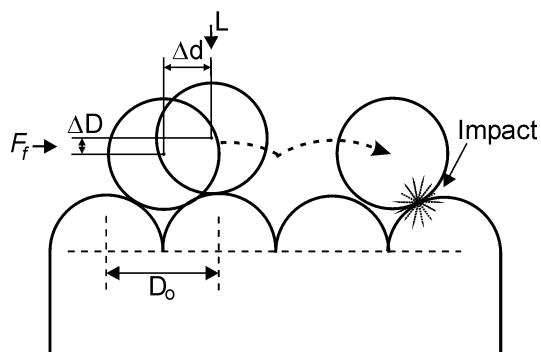


Figure 2-10. Schematic representation of events occurring during sliding motion of an AFM tip over an ordered surface (*i.e.* atomic surface, molecules ordered into solidlike film, or polymer crystal) when a lateral force  $F_f$  is applied.  $\Delta D$ ,  $\Delta d$  denote the vertical and lateral displacement of the tip, respectively.  $D_0$  denotes the lattice constant.

Surfaces sliding with respect to one another are considered in a similar fashion to the wheels of a cart rolling over a cobblestone street. If at rest, the wheels will be settled into the grooves between the cobblestones. To initiate motion, a lateral force is required to lift the wheels out of the grooves and over the cobblestones. In this model, the force of gravity replaces the attractive surface forces. For an atomically smooth sample, the cobblestones could represent the atomic corrugation, and the wheels the outermost atom(s) of the AFM tip. Energy is dissipated by liberation of heat (phonons, sound waves, *etc.*) each time a wheel (outermost atom(s) of the tip) hits the next cobblestone. The model predicts that the interfacial shear strength is linearly proportional to the interfacial surface energy.<sup>19</sup>

### 2.5.2. Simple analytical models of friction on the atomic scale

The first attempt to explain friction on the atomic level was given by Tomlinson in his pioneering work in 1929.<sup>72</sup> He considered the surface atoms as single independent oscillators that are “plucked” by the atoms of the other surface. Plucking is possible only if the sliding brings surface atoms into metastable states from which they suddenly jump into a more stable one. Each plucked surface atom vibrates. This approach has been used by Mc Clelland *et al.*,<sup>117</sup> Zhong and Tomanek *et al.*,<sup>118,119</sup> Colchero and Marti *et al.*<sup>73</sup> and others, to model the friction measured in AFM experiments. In recent developments of the model, the AFM tip is considered to be a single atom or at least a single entity without internal degrees of freedom (multiple atom tips have been also considered).<sup>120</sup> A periodic interaction potential<sup>79</sup> between the tip and sample is given by the sum of the cantilever spring potential and the interaction potential with the lattice periodicity (Figure 2-11).<sup>121</sup> The potential amplitude increases for increasing load. When scanning, the lateral displacement between the lever and the sample is increased. Initially, the tip

resides in a potential minimum that is determined by the tip-sample interaction. Finite static friction due to the interaction inhibits sliding of the tip, and so elastic energy is built up in the cantilever and in elastic deformation of the tip and the sample themselves.<sup>122</sup> Relative slip between tip and sample takes place when a critical point is reached and the elastic strain energy eliminates the potential minimum. Then the system relaxes, releasing the energy excess and the tip finds a new potential minimum, one unit cell further. The energy is dissipated via phonons generated in this process.

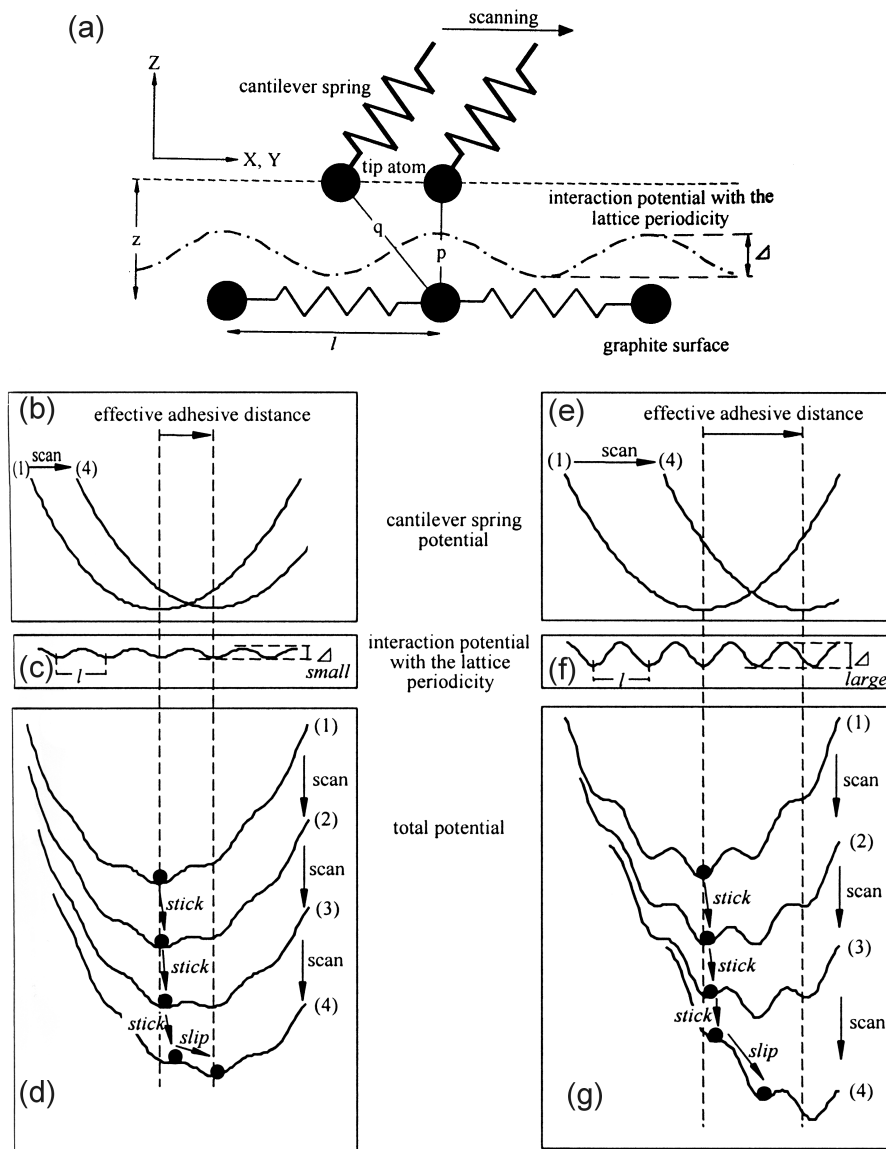


Figure 2-11. (a) A simple one-dimensional model of a single-atom tip and atomically flat surface. (b)-(g) the relation of the effective adhesive distance and amplitude of the interaction potential. (left) and (right) show the two limiting cases with a small and a large amplitude of the interaction potential  $\Delta$ , respectively; (d) and (g) show the sum of the cantilever spring potential (b) and (e), and the interaction potential between the tip and the surface (c) and (f). (1)-(4) represents the evolution of the total potential by the scanning from (1) to (4) (after reference 79).

Weiss and Elmer<sup>123</sup> proposed a model, which takes the coupling between surface atoms into account by introducing nearest-neighbor interactions of the oscillators. The so-called Frenkel-Kontorova-Tomlinson (FKT) model assumes two rigid sliding bodies, where the layer of surface atoms of one body is modeled by two kinds of springs, a nearest neighbor spring and a spring, which couples each particle/atom to the body. The behavior of the system strongly depends on the strength of the interaction between the sliding surfaces and the commensurability of the surface lattices. A decrease in friction was predicted with decreasing commensurability.<sup>124</sup> This phenomenon was verified experimentally on graphite (Section 2.4.2).<sup>93</sup>

A model which goes beyond the FKT model has been introduced by Sokoloff.<sup>125,126</sup> Instead of one layer it has several layers coupled harmonically. Urbakh and coworkers studied the origin and transitions of stick-slip friction of a particle that interacts with two periodic potentials. Three regimes were identified: (i) stick-slip motion, (ii) intermittent stick-slip characterized by force fluctuations, and (iii) sliding which occurs above a critical velocity.<sup>127-129</sup> The authors revealed that the presence of roughness between two surfaces separated by a thin liquid film increases interfacial friction and can lead to time dependence of the friction.<sup>130</sup> Modification of friction was achieved by manipulating the normal response or by using an electrolytic environment.<sup>131-134</sup>

### 2.5.3. Molecular dynamics

In molecular dynamics (MD) simulations, the Newtonian equations of motion are solved numerically for a system containing up to tens of thousands of particles. The interaction forces are described by sophisticated model potentials that can go beyond the predictions of the simple analytical models. MD simulations allow one to investigate temperature and sliding velocity effects, *etc.*, and visualize molecular (atomic) events by video animations.<sup>43</sup> Simulations and theoretical calculations of tribosystems have been largely realized through advances in computer technologies, which allowed an increase number of atoms within the contact and a greater specification of parameters within the system.

An early example of MD calculations of frictional contact between solid surfaces was performed by Landman and coworkers,<sup>135</sup> who studied dynamics of wear and transfer of material in the sliding contact. Marti *et al.*<sup>136</sup> modeled (in two dimensions) the behavior of the atoms forming the end of the tip, as well as those of the probed surface, during contact. These authors used an additive interaction (van der Waals type) and a hexagonal structure. They could show that atoms move without deformation of the end of the tip and the surface. As they are displaced from their equilibrium position, they quickly come back to their position, leading to dissipation of energy

---

that is transmitted to the whole crystal by atomic vibrations (phonon generation). In addition, Glosli *et al.*<sup>137</sup> and Harrison also visualized the trajectories of atoms and molecules (hydrocarbon chains) at the interface during wear-less sliding. They observed friction resulting from two mechanisms, a continuous energy dissipation similar to that of liquid viscosity and a discontinuous plucking motion. Furthermore, the relation between strain release taking place during the shearing of molecularly thin hydrocarbon films and heat flow were simulated. Sorensen *et al.*<sup>138</sup> studied tip-surface contacts of copper atoms. Kinetic friction was caused by atomic-stick slip, which occurred by nucleation and subsequent motion of dislocations. Depending on crystal orientation and load, frictional wear was revealed. Robbins and coworkers studied energy dissipation mechanisms during the rupture of thin adhesive bonds,<sup>139</sup> the effect of third bodies in the contact on static friction,<sup>140</sup> stick-slip motion that involves shear-melting transitions and recrystallization of thin fluid films.<sup>141,142</sup> An increase of static friction in the vicinity of defects was observed by Sololov.<sup>143</sup> Recent simulations<sup>144,145</sup> and experimental results<sup>146,147</sup> demonstrated that oscillations of the normal load could lead to a transition from a state of high friction stick-slip dynamics to a low friction smooth sliding state. Manipulation by mechanical excitations, when applied at high frequency, amplitude and direction, pull the molecules out of their energy minima and thereby reduce friction (at other frequencies or amplitudes the friction can be increased).<sup>148</sup>

In general, complementary AFM experiments and MD simulations now facilitate the study of contact areas of similar dimensions (since MD recently increased the number of atoms or molecules involved in the contact), but still differ drastically in the time scale of the measurements. MD simulations are currently limited to timescales no greater than tens of nanoseconds and length scales of tens of nanometers, which are insufficient for analyzing many tribological systems.<sup>148</sup>

### **2.6. Measuring friction: from micro- to nanotribology**

Friction, adhesion and wear need to be understood at the fundamental level in terms of chemical bonding and the elementary processes that are involved in the excitation and dissipation energy modes.<sup>2</sup> The macro/microscopic scale, multi-asperity experiments are performed using a tribometer. The recent development of new techniques allows one to probe friction of single asperity contacts. Two instruments, namely the SFA and the AFM, that can probe single asperity friction, are among the most prominent instruments for performing micro- and nanotribological studies.<sup>149</sup> However, both instruments work in different regimes of contact pressure and time scale (Table 2-1). For the development of appropriate theories and simulations

for applications, it is necessary to conduct micro- and nanoscale friction measurements under similar environmental conditions (temperature and humidity), at the relevant velocities, *i.e.*, mm/s to m/s, with similar composition of the probe-substrate interface.

Table 2-1. Comparison of the typical range of contact area, applied load, pressure and velocity for AFM, SFA and tribometer.<sup>7,150</sup>

	AFM	SFA	pin-on-disc tribometer
Contact area [m <sup>2</sup> ]	10 <sup>-16</sup> (*)	10 <sup>-8</sup>	10 <sup>-5</sup> (**)
Load [N]	0 – 10 <sup>-7</sup>	10 <sup>-2</sup> – 10 <sup>-1</sup>	10 <sup>-3</sup> – 10 <sup>3</sup>
Pressure [Pa]	0 – 10 <sup>10</sup>	0 – 10 <sup>8</sup>	10 <sup>8</sup> – 10 <sup>9</sup>
Velocity [m/s]	10 <sup>-8</sup> – 10 <sup>-5</sup>	10 <sup>-9</sup> – 10 <sup>-4</sup>	10 <sup>-3</sup> – 1

(\*) depends on tip size, (\*\*) depends on ball size.

### 2.6.1. Pin-on-disc instrument

In a classical tribometer experiment a slider is moved along a surface. The most common arrangement is the pin-on-disc experiment (see Figure 2-12), where a pin slides over a rotating disc. During the experiment, the friction forces between the slider and the sample are measured using different sensors, such as resistance strain gauges (or capacitance) sensors that detect the deformations of elastic joints holding a very stiff arm. The friction force is measured as a function of normal force and the friction coefficient  $\mu$  is calculated as the ratio of the friction force  $F_f$  divided by the normal force  $F_N$ .

Several methods can be used to measure wear rates, *i.e.* the weight loss or weight gain of the slider and/or the disc or an in-situ technique based on height displacement, where a laser displacement sensor measures the vertical displacement of the pin arm in respect to the rotating disc. Environmental control can be performed by placing the tribometer in a climate chamber. Typical pin materials are alumina, zirconia and silicon nitride.<sup>7</sup>

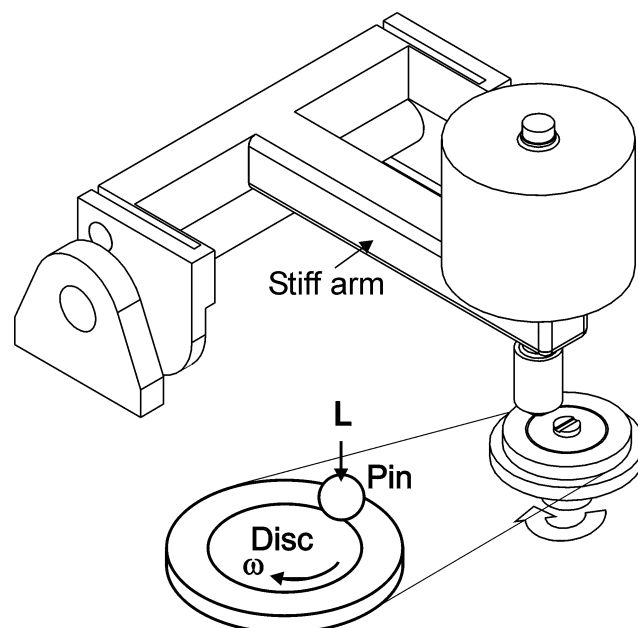


Figure 2-12. Schematic of pin-on-disc tribometer.

### 2.6.2. Surface forces apparatus

Tabor, Winterton and Israelachvili<sup>151,152</sup> developed the SFA for measuring van der Waals forces between mica surfaces. Later, the apparatus was extended to study shear forces.<sup>5</sup> In SFA, two crossed mica cylinders are approached towards each other and the distance between the two surfaces is controlled by the combination of micrometer screws, a differential spring mechanism and a piezoelectric crystal transducer (Figure 2-13). The surface separation is measured with accuracy of better than 1 Å by an optical technique using multiple beam interference fringes of equal chromatic order (FECO). The shapes of the interference FECO provide a continuous, direct visualization of the surface profiles, *i.e.* their shapes and elastic or viscoelastic deformations.<sup>6,7</sup> The area of contact of the contacting surfaces under applied load can be precisely measured. Lateral motion of one of the cylinders with respect to the other one is performed by piezoelectric bimorphs attached to the double-cantilever spring. The friction force is detected using resistance or semiconductor strain gauges attached to the spring in form of Wheatstone bridge that measures the relative lateral displacement of the surfaces (cylinders). SFA can be performed in liquid or in a controlled environment.<sup>7</sup>

The limits of the instrument are that the lateral resolution is in the range of several micrometers, UHV measurements are extremely difficult and substrates are restricted to mica with coated or adsorbed layers (polymers, surfactants or lipid layers, *etc.*).

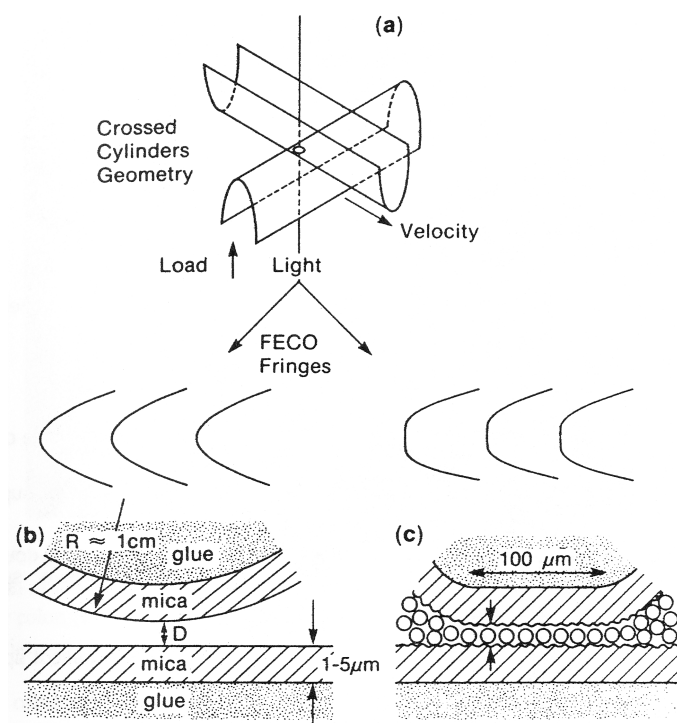


Figure 2-13. Schematic of the configuration of a SFA: (a) cross-cylinders of mica sheets, showing the formation of the contact area. Schematic of the fringes of equal chromatic order (FECO) observed when the two mica surfaces are (b) separated by distance  $D$  and (c) are flattened with a monolayer of liquid between them (after reference 5).

### 2.6.3. Lateral force microscopy

The AFM has been used to study interactions between surfaces with nanometer resolution. The force microscope, in which both normal and lateral forces are measured simultaneously, is often called friction force microscope (FFM) or lateral force microscope (LFM).<sup>153,154</sup> In AFM contact mode a sharp tip (typical radius of 10 – 100 nm, typical probe material Si and Si<sub>3</sub>N<sub>4</sub>) mounted to the end of a flexible cantilever (normal spring constant of  $k_N = 0.01 - 1$  N/m) is brought into contact with the surface. While scanning either by the tip or by the sample, forces acting between atoms of the AFM tip and atoms of the sample surface will result in deflection of the cantilever. The cantilever bends vertically (*i.e.* towards or away from the sample) in response to attractive and/or repulsive forces acting on the tip (see Section 2.2). The deflection of the cantilever is measured in order to obtain surface topography of the scanned sample (“constant height mode”). When the sample is scanned in “constant force mode”, a feedback loop maintains preset scanning parameters to keep the vertical deflection of the cantilever constant and a topographic image can be obtained by plotting the feedback signal (Figure 2-14). The deflection is proportional to the normal load applied to the tip by the cantilever.<sup>155</sup>

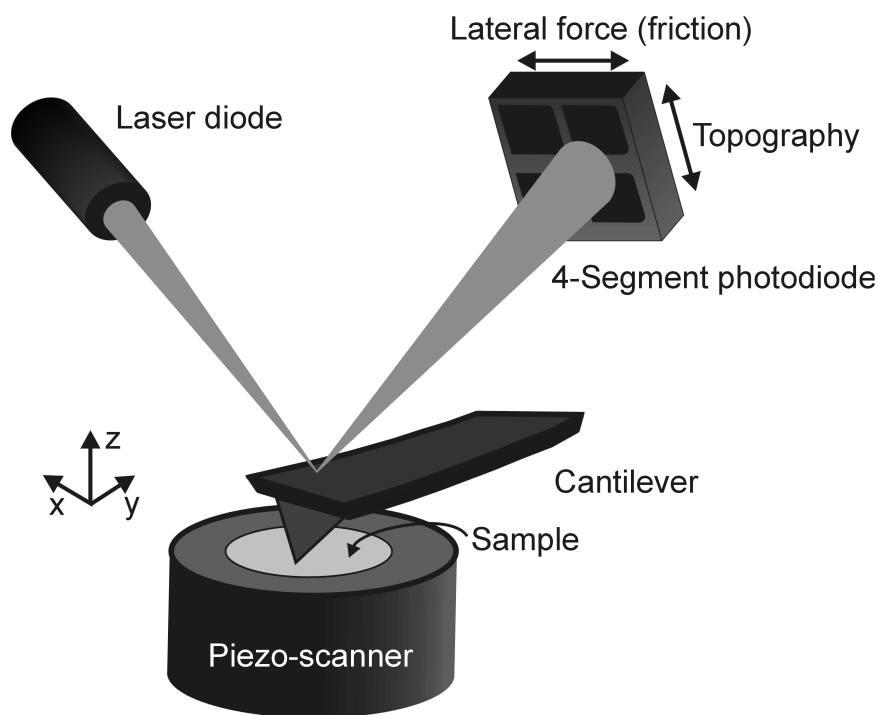


Figure 2-14. Schematic diagram of contact mode AFM.

When the sample is scanned perpendicular to the main cantilever axis in constant force mode, lateral forces acting on the tip result in twisting of the cantilever.<sup>156</sup> The magnitude of the cantilever torsion (lateral deflection) is proportional to the friction forces of the tip-sample contact. Simultaneous measurement of normal and lateral deflections can be performed using several techniques, including a four-segment photodiode (also called optical beam deflection method),<sup>157</sup> dual fiber interferometer,<sup>117,158</sup> capacitance<sup>159</sup> and piezoresistive sensors.<sup>160</sup> The optical deflection method as the most frequently utilized technique to monitor forces in AFM is based on detection of laser beam position reflected from the back of the cantilever into a position sensitive four-segment photodiode. The voltages measured on the four segment photodiode in normal and lateral direction are defined as the difference voltage between top and bottom photodiode output:<sup>156</sup>  $\Delta U_N = ((A+B)-(C+D))/(A+B+C+D)$  and difference voltage between left and right photodiode output:  $\Delta U_L = ((A+C)-(B+D))/(A+B+C+D)$ , and are labeled *difference normal signal* and *difference friction signal*, respectively. The method, in fact, measures the deflection angles and bending angles of the cantilever, which for small angles is linearly proportional to the cantilever deflections (normal and lateral, respectively).

The interactions between the tip and the sample surface can be measured using the force spectroscopy mode.<sup>161,162</sup> In the experiment the sample is moved up and down (in and out of contact with the tip). The obtained force-displacement curve (“force curve”) is shown in Figure 2-15(a).



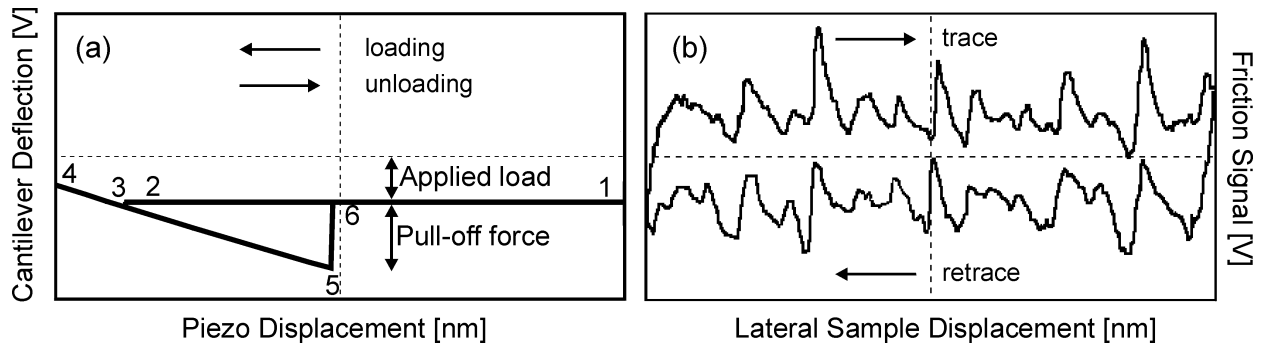


Figure 2-15. (a) Typical force-displacement curve for adhesive contact, (b) typical friction loop.

During the approach (loading) part (position 1 – 2), no interactions occur between the tip and the sample surface. As the tip-surface distance becomes sufficiently small, the gradient of the attractive force overcomes the cantilever spring constant and brings the tip in contact with the sample surface (position 3). Further approaching causes a deflection of the cantilever (position 3 – 4). The unloading part of the force-displacement curve starts from position 4, the deflection of the cantilever is decreased as the sample surface retracts from the tip. When the sample surface is further withdrawn from the tip, the cantilever is deflected owing to adhesive forces. At position 5, the elastic force in the cantilever overcomes the force gradient and the tip snaps off from the surface (position 6). From position 6 to 1, the cantilever returns to its equilibrium position. The adhesion between tip and sample is characterized by the so-called pull-off or pull-out force (snap off).

Lateral forces acting on the cantilever tip in a direction perpendicular to the cantilever main axis will twist the cantilever.<sup>156</sup> Typical AFM friction measurements are recorded in form of friction loops, as shown in Figure 2-15(b). In the friction loop, the difference friction signal (also called friction signal) is plotted against the trace (forward scan) and retrace (backward scan) lateral sample displacement. At the beginning of each trace and retrace, the sample remains in static contact until the shear force increases and overcomes the static friction force. The signal changes sign for the retrace in respect to trace scan. For a given load (normal force), the friction force can be determined as a half of the difference between the corresponding friction signals for trace and retrace scans.

The friction loop may contain information originating from topography features.<sup>103</sup> Most of this topographic component (*i.e.* the local slope of the sample surface)<sup>163</sup> is removed from the difference friction signals by the subtracting procedure. However, thermal drift and hysteresis in the lateral scan system may prevent an exact match of trace and retrace data. For quantitative analyses a correction (off-set) of trace and retrace data may be required. The friction force can

also be determined from trace and retrace lateral force images, as the difference image (also called friction map). By creating histograms of the force maps, the friction forces can be quantified.<sup>164</sup>

In order to obtain quantitative data from force microscopy, a reliable and accurate force calibration must be performed.<sup>165</sup> This requires, among other the calibration of the normal and lateral force constants of the cantilevers and of the photodiode sensitivity.<sup>166</sup> Normal force calibration is well established. Several methods can be used, such as the thermal fluctuation method,<sup>167-169</sup> the reference lever<sup>170</sup> or the added mass technique.<sup>171</sup> However, the calibration of the lateral forces is still a challenge. This issue will be addressed in detail in Chapters 3 and 4.

### **2.7. Concluding remarks**

In the previous sections different theoretical approaches, *i.e.* atomistic and continuum approaches, have been discussed. A gap can be identified between molecular or atomistic models on the one hand, and continuum (*e.g.* contact mechanics) approaches that describe the deformation between elastic single asperities on the other hand. Consequently, fundamental aspects of friction and the mechanisms of energy dissipation are poorly understood on a first principles level. Multi-level experiments (from micrometer to nanometer scale) are clearly required to advance the understanding of tribology. The goal of the multi-level experiments is to determine the mechanism of friction, which is partly based on the atomic-scale phenomena at the sliding interface, and to correlate the corresponding processes to the macroscopic scale frictional behavior. The necessary bridge between micro- and nanotribology, as well as atomistic and continuum models has not yet been addressed convincingly. Both experimental (tribology) and theoretical (simulations) approaches suffer from limitations that prevent a unified understanding.

As has been discussed in Section 2.6, new experimental techniques, such as SFA and AFM, allow one to study friction processes from micrometer length scales down to molecular levels. Thus, in principle, it should be feasible to bridge these different length scales regimes. However, the link between micro- and nanotribology is not yet established, since the instruments work on different time scale and length scale regimes (Figure 2-16). In addition, each method possesses its own limitations. For instance, SFA is limited to studies of a very narrow range of model surfaces (*i.e.* mica and thin films coated on mica). AFM does not suffer from this limitation, as the technique is capable to probe real surfaces and to map friction forces with high spatial resolution. The main drawbacks of AFM compared to SFA, however, are difficulties with

reliable friction force calibration and absence of knowledge of the contact area.<sup>172</sup> Furthermore, both instruments possess a restricted range of velocities as compared to velocities that are relevant for real processes and applications.

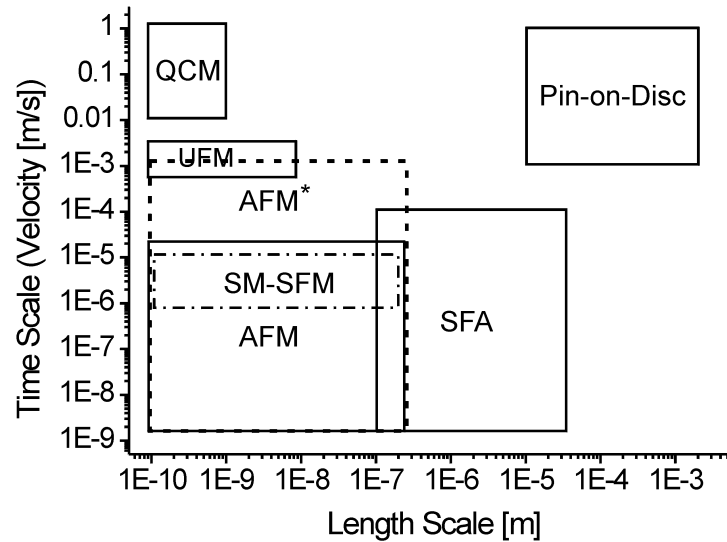


Figure 2-16. Time and length scales (contact length) of the experimental techniques for nano- and microtribology. AFM\* stands for the instrument with increased range of velocity (see also Chapter 5),<sup>70</sup> UFM represents ultrasonic force microscopy and acoustic force microscopy,<sup>173,174</sup> SM-SFM correspond to shear modulation scanning force microscopy,<sup>175-177</sup> and QCM stands for quartz crystal microbalance.<sup>44,178</sup>

MD simulations have been shown to complement experimental data. In the context of bridging time and length scales, also MD simulations are limited. Timescales no greater than tens of nanoseconds and length scales of tens of nanometers at the most can be simulated at present, which is still insufficient. Consequently, the comparison of experimental and theoretical results is difficult and little connection has been achieved so far.

It is evident that several main shortcomings must be addressed in order to bridge the gap between experimental techniques for micro- and nanotribology and thereby to allow also the development of testing of unified theoretical treatments. The most prominent instrument for performing nanotribological studies is the AFM, since it is suitable to detect friction forces of nanometer-scale contacts of real surfaces with high spatial resolution under pressures of several GPa. As shown in this Thesis, the reliable quantification of friction forces (Chapters 3 and 4), the control of environmental factors (humidity and temperature) and the extension of the range of scan velocities to 2 mm/s (Chapter 5) of the AFM technique allow one to perform nanotribology studies complementary to microtribology. With these distinctive advances,

nanoscale friction of different types of surfaces can be quantitatively determined on a wide range of materials and conditions. The data acquired on soft condensed matter (polymer films, see Chapter 8), as well as inorganic materials (nanostructured ceramics, see Chapter 6) show the influence of environmental conditions, velocity and nanostructure on friction force. Finally, these advances are the basis for the comparison of nano- and microtribological data for ceramics (Chapter 7). With an increase of computing power, simulations of a wide range of realistic friction processes on different systems and length scales will eventually be possible. A combination of these developments may provide the link between atomistic and continuum approaches.

---

## 2.8. References

- 1 Dowson, D. *History of Tribology*. Professional Engineering Publishing: London, 1998.
  - 2 Dedkov, G. V. *Phys. Stat. Sol.* **2000**, *179*, 3-75.
  - 3 Gnecco, E.; Bennewitz, R.; Gyalog, T.; Meyer, E. *J. Phys.-Condes. Matter* **2001**, *13*, R619-R642.
  - 4 Israelachvili, J. N.; Berman, A. D. In *Handbook of Micro/Nano Tribology*, Bhushan, B., Ed. CRC Press: New York, 1999; p 371-432.
  - 5 Homola, A. M.; Israelachvili, J. N.; McGuiggan, P. M.; Gee, M. L. *Wear* **1990**, *136*, 65-83.
  - 6 SFA and AFM are among the most prominent instruments for performing micro- and nanotribological studies. While the SFA is limited to mica as a substrate and affords atomic resolution only in the vertical direction and has limited lateral resolution (several micrometers), AFM is suitable to detect friction forces with atomic resolution in all three dimensions of nanometer-scale contacts of real surfaces under pressures of several GPa.
  - 7 Meyer, E.; Overney, R. M.; Dransfeld, K.; Gyalog, T. *Nanoscience: Friction and Rheology on the Nanometer Scale*. World Scientific: Singapore, 1998.
  - 8 Krim, J. *Scient. Am.* **1996**, *October*, 2-8.
  - 9 Bowden, F. P.; Tabor, D. *Brit. J. Appl. Phys.* **1966**, *17*, 1521-1544.
  - 10 If the deformation is totally plastic, the asperities are compressed until the pressure becomes equal to a certain yield pressure  $p^*$ , which is usually smaller than the yield pressure of the bulk material.
  - 11 Israelachvili, J. *Intermolecular and Surface Forces*. 2<sup>nd</sup> ed.; Academic Press: London, 1997.
  - 12 The Hamaker constant can either be measured or calculated in terms of the dielectric properties and refractive indices of the materials using Lifshitz theory.
  - 13 Burnham, N. A.; Kulik, A. In *Handbook of Micro/Nano Tribology*, Bhushan, B., Ed. CRC Press: New York, 1999; p 247-272.
  - 14 Ghatak, A.; Vorvolakos, K.; She, H. Q.; Malotky, D. L.; Chaudhury, M. K. *J. Phys. Chem. B* **2000**, *104*, 4018-4030.
  - 15 Vancso, G. J.; Hillborg, H.; Schönherr, H. *Adv. Polym. Sci* **2005**, *182*, 55-129.
  - 16 Luengo, G.; Pan, J. M.; Heuberger, M.; Israelachvili, J. N. *Langmuir* **1998**, *14*, 3873-3881.
  - 17 This increases the number and/or strength of the contact bonds between the molecular groups of the two contacting surfaces.
  - 18 Yoshizawa, H.; Chen, Y. L.; Israelachvili, J. *J. Phys. Chem.* **1993**, *97*, 4128-4140.
  - 19 Israelachvili, J. N. In *Fundamentals of Friction: Macroscopic and Microscopic Processes*, Singer, I. L.; Pollock, H. M., Eds. Kluwer: Dordrecht, 1992; p 351-396.
  - 20 Fisher, L. R.; Israelachvili, J. *Colloids Surf.* **1981**, *3*, 303-319.
  - 21 Hertz, H. *J. Reine Angew. Math.* **1882**, *92*, 156-171.
  - 22 Johnson, K. L. *Proc. R. Soc. London Ser. A-Math. Phys. Eng. Sci.* **1997**, *453*, 163-179.
  - 23 Johnson, K. L. *Langmuir* **1996**, *12*, 4510-4513.
  - 24 The work of adhesion is defined as the energy per unit area to separate two flat surfaces in vacuum from contact to infinity.
  - 25 Muller, V.; Derjaguin, B. V.; Toporov, Y. P. *Colloid. Surf.* **1983**, *7*, 251-259.
  - 26 Derjaguin, B. V.; Muller, V.; Toporov, Y. P. *J. Colloid Interface Sci.* **1980**, *73*, 293-294.
  - 27 Derjaguin, B. V.; Muller, V.; Toporov, Y. P. *J. Colloid Interface Sci.* **1978**, *67*, 378-379.
  - 28 Derjaguin, B. V.; Muller, V.; Toporov, Y. P. *J. Colloid. Interface Sci.* **1978**, *53*, 314.
-

- 29 Maugis, D. J. *Colloid Interface Sci.* **1992**, *150*, 243-269.
- 30 Greenwood, J. A. *Proc. R. Soc. London Ser. A-Math. Phys. Eng. Sci.* **1997**, *453*, 1277-1297.
- 31 Tabor, D. J. *Colloid Interface Sci.* **1977**, *58*, 2-13.
- 32 Carpick, R. W.; Ogletree, D. F.; Salmeron, M. J. *Colloid Interface Sci.* **1999**, *211*, 395-400.
- 33 Schwarz, U. D. *J. Colloid Interface Sci.* **2003**, *261*, 99-106.
- 34 Johnson, K. L. In *Microstructure and Microtribology of Polymer Surfaces*, Tsukruk, V. V.; Wahl, K. J., Eds. American Chemical Society: Washington, 2000; ACS Symp. Ser.; Vol. 741, p 24-41.
- 35 Giri, M.; Bousfield, D. B.; Unertl, W. N. *Langmuir* **2001**, *17*, 2973-2981.
- 36 Hui, C. Y.; Baney, J. M.; Kramer, E. J. *Langmuir* **1998**, *14*, 6570-6578.
- 37 Lin, Y. Y.; Hui, C. Y.; Baney, J. M. *J. Phys. D-Appl. Phys.* **1999**, *32*, 2250-2260.
- 38 Lin, Y. Y.; Hui, C. Y. *J. Polym. Sci. Pt. B-Polym. Phys.* **2002**, *40*, 772-793.
- 39 Greenwood, J. A.; Williamson, J. B. P. *Proc. R. Soc. London A* **1966**, *295*, 300-319.
- 40 Greenwood, J. A.; Tripp, J. H. *Trans. ASME Ser. E, J. Appl. Mech.* **1967**, *34*, 153-159.
- 41 Greenwood, J. A. *Trans. ASME Ser. F, J. Lubrication Technol.* **1967**, *89*, 81-91.
- 42 If friction processes generate heat, they are irreversible and cannot be treated by classical thermodynamics. If, however, each step in sliding interaction is executed with infinite slowness and with the two couples always in equilibrium (never an unbalanced force), then the process may be considered reversible. In such quasistatic process, sliding can be achieved with zero friction.
- 43 Singer, I. L. *J. Vac. Sci. Technol. A-Vac. Surf. Films* **1994**, *12*, 2605-2616.
- 44 Krim, J. *Am. J. Phys.* **2002**, *70*, 890-897.
- 45 Phonons are the mechanical vibration of an atomic lattice.
- 46 Dransfeld, K.; L. Jie In *Forces in Scanning Probe Methods*, Güntherodt, H. J., Ed. Kluwer Academic Publishers: Dordrecht, 1995; p 273-283.
- 47 This is the time it takes for the excitation to decay back to the original or ground state.
- 48 Salmeron, M.; Kopta, S.; Barrena, E.; Ocal, C. In *Fundamentals of Tribology and Bridging the Gap between Macro- and Micro/Nanoscales*, Bhushan, B., Ed. Kluwer Academic Publishers: Dordrecht, 2001; p 41-52.
- 49 McCrum, N. G.; Read, B. E.; Williams, G. *Anelastic and Dielectric Effects in Polymeric Solids*. John Wiley & Sons: London, 1967.
- 50 Schwarz, U. D.; Allers, W.; Gensterblum, G.; Wiesendanger, R. *Phys. Rev. B* **1995**, *52*, 14976-14984.
- 51 Schwarz, U. D.; Zwörner, O.; Köster, P.; Wiesendanger, R. *Phys. Rev. B* **1997**, *56*, 6987-6996.
- 52 Disadvantages of the SFA method are the lack of spacial resolution, and its limitation to mica or thin films on mica substrates.
- 53 Ruths, M.; Alcantar, N. A.; Israelachvili, J. N. *J. Phys. Chem. B* **2003**, *107*, 11149-11157.
- 54 Phonons exist in crystalline as well as amorphous materials, see: Pelous, J.; Levelut, C. In *Encyclopedia of Materials: Science and Technology*, Buschow, J. K. H.; Cahn, R. W.; Flemings, M. C.; Ilshner, B.; Kramer, E. J.; Mahajan, S.; Veyssi re, P., Eds. Elsevier Science Ltd.: Amsterdam, 2001; p 242-251.
- 55 Barrena, E.; Kopta, S.; Ogletree, D. F.; Charych, D. H.; Salmeron, M. *Phys. Rev. Lett.* **1999**, *82*, 2880.
- 56 Gao, J. P.; Luedtke, W. D.; Gourdon, D.; Ruths, M.; Israelachvili, J. N.; Landman, U. *J. Phys. Chem. B* **2004**, *108*, 3410-3425.
- 57 Yamada, S.; Israelachvili, J. *J. Phys. Chem. B* **1998**, *102*, 234-244.

- 
- 58 Schwarz, U. D.; Zwörner, O.; Köster, P.; Wiesendanger, R. *J. Vac. Sci. Technol. B* **1997**, *15*, 1527-1530.
- 59 Putman, C. A. J.; Igarashi, V.; Kaneko, R. *Appl. Phys. Lett.* **1995**, *66*, 3221-3223.
- 60 Carpick, R. W.; Agrait, N.; Ogletree, D. F.; Salmeron, M. *Langmuir* **1996**, *12*, 3334-3340.
- 61 Kaneko, R. *Tribol. Lett.* **2000**, *9*, 89-96.
- 62 Hu, J.; Xiao, X. D.; Ogletree, D. F.; Salmeron, M. *Surf. Sci.* **1995**, *327*, 358-370.
- 63 Enachescu, M.; van den Oetelaar, R. J. A.; Carpick, R. W.; Ogletree, D. F.; Flipse, C. F. J.; Salmeron, M. *Phys. Rev. Lett.* **1998**, *81*, 1877-1880.
- 64 Riedo, E.; Pallaci, I.; Boragno, C.; Brune, H. *J. Phys. Chem. B* **2004**, *108*, 5324-5328.
- 65 Enachescu, M.; van den Oetelaar, R. J. A.; Carpick, R. W.; Ogletree, D. F.; Flipse, C. F. J.; Salmeron, M. *Tribol. Lett.* **1999**, *7*, 73-78.
- 66 Lantz, M. A.; O Shea, S. J.; Welland, M. E.; Johnson, K. L. *Phys. Rev. B* **1997**, *55*, 10776-10785.
- 67 Golan, Y.; Drummond, C.; Israelachvili, J.; Tenne, R. *Wear* **2000**, *245*, 190-195.
- 68 Berman, A. D.; Ducker, W. A.; Israelachvili, J. N. *Langmuir* **1996**, *12*, 4559-4563.
- 69 Luengo, G.; Heuberger, M.; Israelachvili, J. *J. Phys. Chem. B* **2000**, *104*, 7944-7950.
- 70 Tocha, E.; Stefański, T.; Schönherr, H.; Vancso, G. J. *Rev. Sci. Instrum.* **2005**, *76*, 083704.
- 71 Mate, C. M.; McClelland, G. M.; Erlandsson, R.; Chiang, S. *Phys. Rev. Lett.* **1987**, *59*, 1942-1945.
- 72 Tomlinson, G. A. *Philos. Mag.* **1929**, *7*, 905-939.
- 73 Colchero, J.; Meyer, E.; Marti, O. In *Handbook of Micro/Nano Tribology*, Bhushan, B., Ed. CRC Press: New York, 1999; p 273-333.
- 74 Overney, R. M.; Takano, H.; Fujihira, M.; Paulus, W.; Ringsdorf, H. *Phys. Rev. Lett.* **1994**, *72*, 3546-3549.
- 75 Riedo, E.; Gnecco, E.; Bennewitz, R.; Meyer, E.; Brune, H. *Phys. Rev. Lett.* **2003**, *91*, 084502.
- 76 Hölscher, H.; Schwarz, U. D. *Z. Metallk.* **2001**, *92*, 1040-1045.
- 77 Fujisawa, S.; Kizuka, T. *Tribol. Lett.* **2003**, *15*, 163-168.
- 78 Fujisawa, S.; Kishi, E.; Sugawara, Y.; Morita, S. In *Forces in Scanning Probe Methods*, Güntherodt, H. J., Ed. Kluwer Academic Publishers: Dordrecht, 1995; p 313-318.
- 79 Morita, S.; Sugawara, Y.; Yokoyama, K.; Fujisawa, S. In *Fundamentals of Tribology and Bridging the Gap between Macro- and Micro/Nanoscales*, Bhushan, B., Ed. Kluwer Academic Publishers: Dordrecht, 2001; p 83-101.
- 80 Howald, L.; Haefke, H.; Lüthi, R.; Meyer, E.; Gerth, G.; Rudin, H.; Güntherodt, H. J. *Phys. Rev. B* **1994**, *49*, 5651-5656.
- 81 Lüthi, R.; Meyer, E.; Haefke, H.; Howald, L.; Gutmannsbauer, W.; Guggisberg, M.; Bammerlin, M.; Güntherodt, H. J. *Surf. Sci.* **1995**, *338*, 247-260.
- 82 Gnecco, E.; Bennewitz, R.; Gyalog, T.; Loppacher, C.; Bammerlin, M.; Meyer, E.; Güntherodt, H. J. *Phys. Rev. Lett.* **2000**, *84*, 1172-1175.
- 83 Lüthi, R.; Meyer, E.; Bammerlin, M.; Howald, L.; Haefke, H.; Lehmann, T.; Loppacher, C.; Güntherodt, H. J.; Gyalog, T.; Thomas, H. *J. Vac. Sci. Technol. B* **1996**, *14*, 1280-1284.
- 84 Bennewitz, R.; Gyalog, T.; Guggisberg, M.; Bammerlin, M.; Meyer, E.; Güntherodt, H. J. *Phys. Rev. B* **1999**, *60*, R11301-R11304.
- 85 Fujisawa, S.; Kishi, E.; Sugawara, Y.; Morita, S. *Phys. Rev. B* **1995**, *51*, 7849-7857.
- 86 Morita, S.; Fujisawa, S.; Sugawara, Y. *Surf. Sci. Rep.* **1996**, *23*, 1-41.
- 87 Kopta, S.; Salmeron, M. *J. Chem. Phys.* **2000**, *113*, 8249-8252.
-

- 
- 88 In SFA, stick-slip behavior depends on the inertia (mass and stiffness) of the system and measuring apparatus. A transition to smooth sliding is observed for stiff springs or above critical velocity.
- 89 Robbins, M. O.; Thompson, P. A. *Science* **1991**, *253*, 916-916.
- 90 Vancso, G. J.; Forster, S.; Leist, H. *Macromolecules* **1996**, *29*, 2158-2162.
- 91 Hirano, M.; Shinjo, K. *Wear* **1993**, *168*, 121-125.
- 92 Two surfaces are incommensurate, when the surface lattices are not in perfect registry.
- 93 Dienwiebel, M.; Verhoeven, G. S.; Pradeep, N.; Frenken, J. W. M.; Heimberg, J. A.; Zandbergen, H. W. *Phys. Rev. Lett.* **2004**, *92*, 126101.
- 94 Socoliuc, A.; Bennewitz, R.; Gnecco, E.; Meyer, E. *Phys. Rev. Lett.* **2004**, *92*, 134301.
- 95 Gourdon, D.; Burnham, N. A.; Kulik, A.; Dupas, E.; Oulevey, F.; Gremaud, G. *Tribol. Lett.* **1997**, *3*, 317-324.
- 96 Liley, M.; Gourdon, D.; Stamou, D.; Meseth, U.; Fischer, T. M.; Lautz, C.; Stahlberg, H.; Vogel, H.; Burnham, N. A.; Duschl, C. *Science* **1998**, *280*, 273-275.
- 97 Park, J. Y.; Ogletree, D. F.; Salmeron, M.; Ribeiro, R. A.; Canfield, P. C.; Jenks, C. J.; Thiel, P. A. *Science* **2005**, *309*, 1354-1356.
- 98 Nisman, R.; Smith, P.; Vancso, G. J. *Langmuir* **1994**, *10*, 1667-1669.
- 99 Vancso, G. J.; Schönherr, H. In *Microstructure and Microtribology of Polymer Surfaces*, Tsukruk, V. V.; Wahl, K. J., Eds. American Chemical Society: Washington, 2000; ACS Symp. Ser.; Vol. 741, p 317-335.
- 100 Smith, P. F.; Nisman, R.; Ng, C.; Vancso, G. J. *Polym. Bull.* **1994**, *33*, 459-464.
- 101 Marti, A.; Hahner, G.; Spencer, N. D. *Langmuir* **1995**, *11*, 4632-4635.
- 102 The authors also attempt to correlate the observed friction with adhesion hysteresis.
- 103 Binggeli, M.; Christoph, R.; Hintermann, H.-E. *Tribol. Lett.* **1995**, *1*, 13-21.
- 104 Meyer, E.; Lüthi, R.; Howald, L.; Bammerlin, M.; Guggisberg, M.; Güntherodt, H. J. *J. Vac. Sci. Technol. B* **1996**, *14*, 1285-1288.
- 105 Frisbie, C. D.; Rozsnyai, L. F.; Noy, A.; Wrighton, M. S.; Lieber, C. M. *Science* **1994**, *265*, 2071-2074.
- 106 Green, J. B. D.; McDermott, M. T.; Porter, M. D.; Siperko, L. M. *J. Phys. Chem.* **1995**, *99*, 10960-10965.
- 107 Liu, Y. H.; Evans, D. F.; Song, Q.; Grainger, D. W. *Langmuir* **1996**, *12*, 1235-1244.
- 108 Fischer, T. M. In *Fundamentals of Friction: Macroscopic and Microscopic Processes*, Singer, I. L.; Pollock, H. M., Eds. Kluwer: Dordrecht, 1992; p 299-312.
- 109 Hsu, S. M.; Zhang, J.; Yin, Z. F. *Tribol. Lett.* **2002**, *13*, 131-139.
- 110 Zwörner, O.; Holscher, H.; Schwarz, U. D.; Wiesendanger, R. *Appl. Phys. A-Mater. Sci. Process.* **1998**, *66*, S263-S267.
- 111 Bouhacina, T.; Aime, J. P.; Gauthier, S.; Michel, D.; Heroguez, V. *Phys. Rev. B* **1997**, *56*, 7694-7703.
- 112 Eyring, H. *J. Chem. Phys.* **1935**, *3*, 107-115.
- 113 Riedo, E.; Levy, F.; Brune, H. *Phys. Rev. Lett.* **2002**, *88*, 185505.
- 114 Riedo, E.; Gnecco, E. *Nanotechnology* **2004**, *15*, S288-S292.
- 115 Szoszkiewicz, R.; Riedo, E. *Phys. Rev. Lett.* **2005**, *95*, 135502.
- 116 Tabor, D. *Microscopic Aspects of Adhesion and Lubrication*. Societe de Chimie Physique Ed.: Paris, 1982; p 651.
- 117 McClelland, G. M.; Glosli, J. N. In *Fundamentals of Friction: Macroscopic and Microscopic Processes*, Singer, I. L.; Pollock, H. M., Eds. Kluwer: Dordrecht, 1992; p 405-425.
-



- 
- 118 Zhong, W.; Tomanek, D. *Phys. Rev. Lett.* **1990**, *64*, 3054-3057.
- 119 Overney, G.; Zhong, W. Q.; Tomanek, D. *J. Vac. Sci. Technol. B* **1991**, *9*, 479-482.
- 120 Gyalog, T.; Thomas, H. Z. *Phys. B-Condens. Mat.* **1997**, *104*, 669-674.
- 121 Since typical AFM scanning velocities are much smaller than the sound velocities of the materials, the scanning process is carried out adiabatically, *i.e.* the system is assumed to be in equilibrium at each step of the simulation.
- 122 The total energy of the system consists of the interaction energy and the elastic energy stored in the lever and the contacting materials.
- 123 Weiss, M.; Elmer, F. J. *Phys. Rev. B* **1996**, *53*, 7539-7549.
- 124 Gyalog, T.; Thomas, H. *Europhys. Lett.* **1997**, *37*, 195-200.
- 125 Sokoloff, J. B. *Phys. Rev. B* **1993**, *47*, 6106-6109.
- 126 Sokoloff, J. B. *Phys. Rev. B* **1995**, *52*, 7205-7214.
- 127 Rozman, M. G.; Urbakh, M.; Klafter, J. *Phys. Rev. Lett.* **1996**, *77*, 683-686.
- 128 Rozman, M. G.; Urbakh, M.; Klafter, J. *Phys. Rev. E* **1996**, *54*, 6485-6494.
- 129 Rozman, M. G.; Urbakh, M.; Klafter, J. *Physica A* **1998**, *249*, 184-189.
- 130 Daikhin, L.; Urbakh, M. *Phys. Rev. E* **1994**, *49*, 1424-1429.
- 131 Daikhin, L. I.; Urbakh, M. *Phys. Rev. E* **1999**, *59*, 1921-1931.
- 132 Zaloj, V.; Urbakh, M.; Klafter, J. *Phys. Rev. Lett.* **1999**, *82*, 4823-4826.
- 133 Klafter, J.; Rozman, M. G.; Zaloj, V.; Urbakh, M. *Abstr. Pap. Am. Chem. Soc.* **1999**, *218*, U454-U454.
- 134 Porto, M.; Zaloj, V.; Urbakh, M.; Klafter, J. *Tribol. Lett.* **2000**, *9*, 45-54.
- 135 Landman, U.; Lüdtke, W. D.; Ringer, E. M. In *Fundamentals of Friction: Macroscopic and Microscopic Processes*, Singer, I. L.; Pollock, H. M., Eds. Kluwer: Dordrecht, 1992; p 463-508.
- 136 Marti, O.; Colchero, J.; Mlynek, J. In *Nanosources and Manipulation of Atoms under High Fields and Temperatures: Applications*, Binh, V. T.; Garcia, N.; Dransfeld, K., Eds. Kluwer Academic Publishers: Dordrecht, 1993; Series E, Applied Sciences; p 253-269.
- 137 Glosli, J. N.; McClelland, G. M. *Phys. Rev. Lett.* **1993**, *70*, 1960-1963.
- 138 Sorensen, M. R.; Jacobsen, K. W.; Stoltze, P. *Phys. Rev. B* **1996**, *53*, 2101-2113.
- 139 Baljon, A. R. C.; Robbins, M. O. *Science* **1996**, *271*, 482-484.
- 140 He, G.; Muser, M. H.; Robbins, M. O. *Science* **1999**, *284*, 1650-1652.
- 141 Cieplak, M.; Smith, E. D.; Robbins, M. O. *Science* **1994**, *265*, 1209-1212.
- 142 Thompson, P. A.; Robbins, M. O. *Science* **1990**, *250*, 792-794.
- 143 Sokolov, I. Y. *Tribol. Lett.* **2002**, *12*, 131-134.
- 144 Gao, J. P.; Lüdtke, W. D.; Landman, U. *J. Phys. Chem. B* **1998**, *102*, 5033-5037.
- 145 Rozman, M. G.; Urbakh, M.; Klafter, J. *Phys. Rev. E* **1998**, *57*, 7340-7343.
- 146 Heuberger, M.; Drummond, C.; Israelachvili, J. *J. Phys. Chem. B* **1998**, *102*, 5038-5041.
- 147 Cochard, A.; Bureau, L.; Baumberger, T. *Trans. ASME* **2003**, *70*, 220-226.
- 148 Urbakh, M.; Klafter, J.; Gourdon, D.; Israelachvili, J. *Nature* **2004**, *430*, 525-528.
- 149 An additional instrument that can probe single asperity friction is Quartz Crystal Microbalance (QCM) (reference 44 and 178). However, it possesses a limited range of substrates (*i.e.* atomically thin layer adsorbed onto the QCM Au electrode), and has very different time scale of pico- to nanosecond, as compared to AFM, SFM and tribometer. This instrument will not be described here.
-

- 150 Feldman, K.; Fritz, M.; Hahner, G.; Marti, A.; Spencer, N. D. *Tribol. Int.* **1998**, *31*, 99-105.
- 151 Israelachvili, J. N.; Tabor, D. *Proc. R. Soc. Lond.* **1972**, *A331*, 19-38.
- 152 Tabor, D.; Winterton, R. H. S. *Proc. R. Soc. Lond.* **1969**, *A312*, 435-450.
- 153 Overney, R.; Meyer, E. *MRS Bull.* **1993**, *18*, 26-34.
- 154 Liu, Y. H.; Wu, T.; Evans, D. F. *Langmuir* **1994**, *10*, 2241-2245.
- 155 Marti, O. In *Handbook of Micro/Nano Tribology*, Bhushan, B., Ed. CRC Press: New York, 1999; p 81-144.
- 156 Perry, S. S. *MRS Bull.* **2004**, *29*, 478-483.
- 157 Meyer, G.; Amer, N. M. *Appl. Phys. Lett.* **1990**, *57*, 2089-2091.
- 158 Rugar, D.; Mamin, H. J.; Guethner, P. *Appl. Phys. Lett.* **1989**, *55*, 2588-2590.
- 159 Kalus, J.; Neubauer, G.; Schmelzer, U. *Rev. Sci. Instrum.* **1990**, *61*, 3384-3389.
- 160 Kassing, R.; Rangelow, I. W.; Oesterschulze, E.; Stuke, M. *Appl. Phys. A-Mater. Sci. Process.* **2003**, *76*, 907-911.
- 161 Cappella, B.; Dietler, G. *Surf. Sci. Rep.* **1999**, *34*, 1-104.
- 162 Butt, H. J.; Cappella, B.; Kappl, M. *Surf. Sci. Rep.* **2005**, *59*, 1-152.
- 163 The reaction force from a tilted surface (with respect to the horizontal) will impose a lateral force on the tip, even in a case of zero friction.
- 164 Hammerschmidt, J. A.; Gladfelter, W. L.; Haugstad, G. *Macromolecules* **1999**, *32*, 3360-3367.
- 165 Carpick, R. W.; Salmeron, M. *Chem. Rev.* **1997**, *97*, 1163-1194.
- 166 Schwarz, U. D.; Köster, P.; Wiesendanger, R. *Rev. Sci. Instrum.* **1996**, *67*, 2560-2567.
- 167 Levy, R.; Maaloum, M. *Nanotechnology* **2002**, *13*, 33-37.
- 168 Ma, H. L.; Jimenez, J.; Rajagopalan, R. *Langmuir* **2000**, *16*, 2254-2261.
- 169 Butt, H. J.; Jaschke, M. *Nanotechnology* **1995**, *6*, 1-7.
- 170 Tortonese, M.; Kirk, M. *Proc. SPIE* **1997**, *3009*, 53-60.
- 171 Cleveland, J. P.; Manne, S.; Bocek, D.; Hansma, P. K. *Rev. Sci. Instrum.* **1993**, *64*, 403-405.
- 172 The contact area between the AFM tip and the sample can be determined using an indirect method of the lateral stiffness measurements of the contact. The knowledge of the elastic contacts of the materials is required (see reference 60 and Carpick, R. W.; Ogletree, D. F.; Salmeron, M. *Appl. Phys. Lett.* **1997**, *70*, 1548-1550). Enachescu *et al.* (reference 63 and 65) performed contact conductance experiments between the conductive tungsten-carbide AFM tip and the doped diamond sample, which provided a direct information of the contact area.
- 173 Yamanaka, K.; Tomita, E. *Jpn. J. Appl. Phys. Part 1 - Regul. Pap. Short Notes Rev. Pap.* **1995**, *34*, 2879-2882.
- 174 Scherer, V.; Arnold, W.; Bhushan, B. *Surf. Interface Anal.* **1999**, *27*, 578-587.
- 175 Reinstadtler, M.; Rabe, U.; Scherer, V.; Hartmann, U.; Goldade, A.; Bhushan, B.; Arnold, W. *Appl. Phys. Lett.* **2003**, *82*, 2604-2606.
- 176 Overney, R. M.; Buenviaje, C.; Luginbuhl, R.; Dinelli, F. *J. Therm. Anal.* **2000**, *59*, 205-225.
- 177 Kawagishi, T.; Kato, A.; Hoshi, Y.; Kawakatsu, H. *Ultramicroscopy* **2002**, *91*, 37-48.
- 178 Krim, J. *Langmuir* **1996**, *12*, 4564-4566.

# Chapter 3

## Quantification of friction forces in lateral force microscopy\*

*In this Chapter, the most important issues for quantitative friction force measurements, including friction force calibration, tip apex characterization, and tip stability, as well as critical tests using a variety of LFM probes, are discussed. A general relation between photodiode lateral sensitivity  $S_L$  and photodiode normal sensitivity  $S_N$  was derived, that takes the laser spot asymmetry for different types of cantilevers into account, as well as AFM instrument specific amplification factors. In particular, the most often applied technique for friction quantification, the two-step calibration method, was experimentally tested and the corresponding errors were estimated. It was found that the final friction calibration factors  $\alpha_i$  cannot be obtained with high accuracy according to this procedure. Relative errors  $\delta\alpha_i$  of 45 - 50% and 35 - 40% were observed for V-shaped and single beam cantilevers, respectively. The uncertainties in the cantilever materials properties and thickness, as well as in the lateral photodiode sensitivity, were identified as crucial parameters that inherently limit the accuracy of this method. The shortcomings of the two-step friction force calibration method thus severely limit quantitative nanotribology and demand the development of an improved universal calibration platform, as described in Chapter 4. Finally, the wear-resistance of different tips was investigated and a method for improving the tip stability, by applying wear-resistant  $Al_2O_3$  coatings by pulsed laser deposition, was developed.*

---

\* Parts of this work were published in the following article: Tocha, E.; Schönherr, H.; Vancso, G. J. *Langmuir* **2006**, *22*, 2340-2350.

### 3.1. Introduction

Despite recent experimental<sup>1-3</sup> and theoretical<sup>4-6</sup> progress in tribology, the understanding of the fundamentals of friction and the underlying tribological processes on different length and time scales is still limited, as has been discussed in detail in Chapter 2. In addition to its fundamental relevance, tribology has represented, and will continue to represent, a crucial area for applications in which moving mechanical objects are in physical contact. For example, highly advanced microelectromechanical systems (MEMS) and nanoelectromechanical (NEMS) applications, as well as high-density data storage devices, for instance, require minimized friction forces.<sup>7-11</sup> In these systems the contacting parts approach the nanometer length scale regime, in which single asperity friction may ultimately play a decisive role. On the other hand, investigations of the transition from single (nanoscale) asperity to multiple asperity contacts hold the promise to understand and predict tribological behavior based on first principles. Hence much effort has been invested to unravel and quantify tribological phenomena also on nanometer length scales, for instance using lateral force microscopy (LFM).<sup>12-16</sup>

LFM is also widely used in nanoscience and nanotechnology-related surface characterization, primarily in the localized compositional mapping of patterned surfaces fabricated, *e.g.* by soft or scanning probe lithographic approaches.<sup>17-19</sup> Central to the approach is the observation that self-assembled monolayers (SAMs) on solid supports exhibit a different friction force contrast compared to the bare substrates, or compared to similar layers that expose different headgroups.<sup>20,21</sup>

A reliable quantification of the surface composition based on any LFM approach requires the rigorous determination of the friction coefficient (lateral forces depend on normal forces, see Chapter 2, Sections 2.3 and 2.4) under carefully controlled conditions (medium, temperature, %RH - if applicable). However, the *quantitative* determination of friction forces remains a significant challenge in LFM, primarily because of difficulties with the calibration of the instrument and the force probe utilized. As one fundamental requirement the symmetrical shape of the probe tip apex has been identified. Moreover, as discussed in Chapter 2, friction force is directly proportional to the contact area for single asperity contacts.<sup>22,23</sup> Therefore, a well-characterized, stable tip shape is required for quantitative nanotribology.<sup>24</sup>

The optical detection method is the most frequently utilized technique to monitor forces in AFM (Chapter 2, Section 2.6.3).<sup>25</sup> The deflection of a cantilever (both in horizontal and vertical direction) is measured with a position sensitive detector. The required calibration of this system

involves the conversion of the lateral force signal (difference output voltage) of the four-segment photodiode detector to values of absolute lateral force. Despite the number of different calibration approaches proposed,<sup>26-39</sup> no universally applicable method has emerged yet that provides a precise calibration of various AFM cantilever probes independent of lever geometry and tip radius. In addition, many of the existing methods suffer from large errors and poor reproducibility.<sup>15,16</sup>

The various calibration techniques proposed can be grouped into (i) reference methods,<sup>40</sup> (ii) two-step<sup>29,34,37</sup> and (iii) direct (single step)<sup>28,35,38</sup> procedures. A new universal calibration platform based on a direct method will be introduced in Chapter 4.

One of the *reference methods*, which is called “blind calibration”,<sup>40</sup> is based on the normalization of the friction coefficient  $\mu_{\text{standard}}$  measured on a standard sample. This method relies on the knowledge of the corresponding value of the absolute friction coefficient. A clean reference sample,<sup>41</sup> such as Si(100), has been reported to provide reproducible calibration under well-controlled environmental and scanning conditions. However, any contamination or poorly defined tip apex material<sup>24</sup> may lead to systematic errors since in this case the reference value for the absolute friction coefficient  $\mu_{\text{standard}}$  may not be correct.

The *two-step procedures*, which are the most often used methods, rely on estimates of (i) the lateral spring constant  $k_L$  of the cantilever (calculated from the cantilever geometry, dimensions and material properties, *i.e.* Young's modulus and Poisson's ratio, as well as the tip height)<sup>42</sup> and of (ii) the photodiode lateral sensitivity  $S_L$  (the parameter that relates the lateral photodiode voltage signal to the cantilever twist angles). The calculation of the lateral force is carried out analogously to the calculation of the normal force  $F_N$ , which is quantified using the value of normal spring constant  $k_N$  of the cantilever and normal photodiode sensitivity  $S_N$ .<sup>37</sup> The normal and lateral forces acting on the cantilever can be expressed as:

$$F_N = k_N S_N \Delta U_N \quad (\text{Eq. 3-1})$$

$$F_L = k_L S_L \Delta U_L = \alpha \cdot \Delta U_L \quad (\text{Eq. 3-2})$$

where  $\alpha$  denotes the lateral calibration factor, which transforms the measured lateral difference signal [V] into friction force [nN].

The spring constants of single beam cantilevers are *easily* accessible as these levers can be modeled using elasticity theory, if isotropic deformation mechanics can be assumed.<sup>43,44,45</sup> For V-shaped cantilevers the spring constants can be estimated using the parallel beam

approximation,<sup>34,36,46,47</sup> complex analytical models<sup>33,39,48</sup> or finite element analysis (FEA).<sup>49-51</sup> However, the accuracy of the chosen method relies on the precision of the determination of the cantilever dimensions and the corresponding material properties (*vide infra*).<sup>49</sup> For Si<sub>3</sub>N<sub>4</sub> cantilevers, the material properties are not well defined and may vary significantly<sup>34</sup> due to differences of the chemical vapor deposition (CVD) processes.<sup>52,53</sup> By contrast, for Si cantilevers the materials properties are known, thus the thickness of the cantilever can be obtained from a measurement of its resonance frequency.<sup>54</sup> However, the application of Si probes is often limited in nanotribology due to insufficient wear-resistance of the tip. Additionally, some types of cantilevers are coated with a reflective coating (*e.g.* gold or aluminum), which may influence the cantilever stiffness.<sup>50,55,56</sup>

The lateral photodiode sensitivity  $S_L$  can be obtained via different approaches. An experimental method is based on the reflection of the laser light of the AFM optical detection system inside the AFM from a mirror inserted into the beam path.<sup>26,31,32,57</sup> This mirror is tilted in a controlled way by a stepper motor. The corresponding photodiode output voltage is then measured as a function of tilt angle. Alternatively, the lateral sensitivity can be determined by recording the output signal, while the photodiode position is manually moved by a known distance.<sup>29,37</sup> The sensitivity  $S_L$  can also be obtained from measurements of the vertical and lateral cantilever deflections as a result of a force applied to a lever attached to the cantilever.<sup>28,58</sup> Finally, the initial slope of the friction loop<sup>59,60,61</sup> has been analyzed based on the assumption that tip is initially pinned to the surface upon reversal of the piezo scan direction.<sup>62,27,63</sup>  $S_L$  can also be estimated from the normal sensitivity  $S_N$  and the cantilever geometry (assuming a symmetrical shape of the laser beam on the cantilever).<sup>30</sup>

As the values of  $S_N$  and  $S_L$  are very sensitive to the position of the laser beam on the cantilever apex<sup>37,48,64</sup> and the corresponding spot shape,<sup>65</sup> the sensitivities must be determined for each cantilever and also for each position of the laser beam on the cantilever.<sup>66,67</sup>

The large errors associated with the two-step approach are related to the limited accuracy of determination of both  $k_L$  and  $S_L$ . The reported discrepancy between results on the same systems studied under identical conditions can be as large as one order of magnitude.<sup>15,16</sup>

In this Chapter, the most important issues for quantitative friction force measurements, including friction force calibration, tip apex characterization, and tip stability are discussed and critically tested using a variety of LFM probes. In particular, the most often applied technique for friction quantification, the two-step calibration method, is experimentally tested and its accuracy is estimated. The crucial parameters limiting this accuracy are identified. Finally, the

---

wear-resistance of different tips is investigated and a method for improving the tip stability is developed.

### 3.2. Determination of cantilever spring constants

The calibration of cantilever spring constants has represented a central problem for quantitative nanotribology by AFM, as reviewed *e.g.* by Salmeron *et al.*<sup>68</sup> To confirm this assertion the most frequently applied (two-step calibration) approach was first experimentally tested and critically discussed in terms of accuracy and limitations. For this purpose, and also for the quantitative comparison of the two-step friction force calibration approach with the direct wedge method (Chapter 4), several V-shaped (labeled A, B, C, D) and single beam (labeled E, F, G, H) cantilevers with different spring constants were selected.

#### 3.2.1. Calibration according to elasticity theory

The force constants of single beam cantilevers (normal spring constant  $k_N$ , torsional spring constant  $k_\varphi$ , and lateral spring constant  $k_L$ ) were calculated from continuum elasticity mechanics of isotropic solids.<sup>44,45</sup>

$$k_N = \frac{Ewt^3}{4l^3} \quad (\text{Eq. 3-3})$$

$$k_\varphi = \frac{Gwt^3}{3l} \quad (\text{Eq. 3-4})$$

$$k_L = \frac{k_\varphi}{h^2} = \frac{Gwt^3}{3lh^2} \quad (\text{Eq. 3-5})$$

with cantilever length  $l$ , cantilever thickness  $t$ , cantilever width  $w$ , tip height  $h$ , Young's modulus  $E$ , Poisson's ratio  $\nu$ , and shear modulus  $G = E / 2(1+\nu)$ .<sup>69</sup>

The spring constants of V-shaped cantilevers were obtained from two different analytical approaches (*i.e.* the approaches by Sader *et al.*<sup>39</sup> and Neumeister *et al.*,<sup>33</sup> respectively, using simplified cantilever shapes).<sup>70</sup> The accuracy of the method to calculate the spring constants of single beam and V-shaped cantilevers is related to the precision of the determination of the cantilever dimensions, mainly the thickness, as well as of the material properties.<sup>45</sup> For Si cantilevers<sup>71</sup> the material properties (Young's modulus and Poisson's ratio) are known in any crystal orientation.<sup>72,73</sup> By contrast, the material properties of the Si<sub>3</sub>N<sub>4</sub> cantilevers<sup>74</sup> are not well defined and may vary significantly<sup>34</sup> due to differences of the CVD processes.<sup>52,53</sup> For instance,

Young's moduli and Poisson's ratios of  $\text{Si}_3\text{N}_4$  cantilevers in the range of 120 - 200 GPa and 0.22 - 0.27, respectively, have been reported.<sup>75</sup> To illustrate the impact of these uncertainties on the results of the two-step calibration procedure, the normal spring constants  $k_N$  of V-shaped and single beam  $\text{Si}_3\text{N}_4$  cantilevers were calculated for several values of the Young's modulus. In Figure 3-1, the calculated values of  $k_N$  are contrasted with the values of  $k_N$  determined experimentally using the reference lever method (see also Table 3-1).<sup>76</sup>

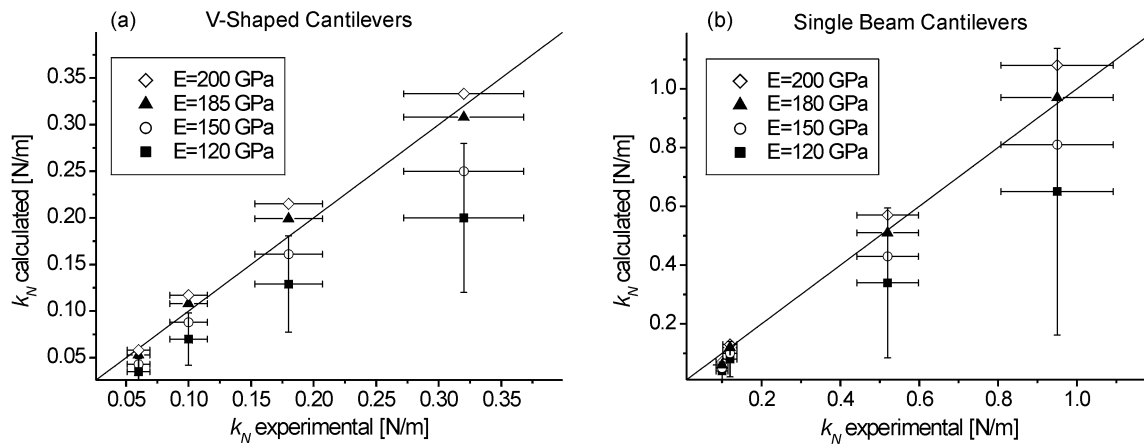


Figure 3-1. Plot of calculated normal spring constants (for different values of the Young's modulus) vs. experimentally determined spring constants, (a) for V-shaped and (b) for single beam  $\text{Si}_3\text{N}_4$  cantilevers. The solid lines correspond to unity slope.

In general, a linear dependence of  $k_N$  (calculated) vs.  $k_N$  (experimental) was observed. The calculated values for  $k_N$  increased with increasing Young's modulus. From linear least squares fits,  $185 \pm 15$  GPa and  $180^{77} \pm 40$  GPa were obtained for the values of the Young's moduli for V-shaped and single beam cantilevers, respectively. Despite the different sources of the cantilevers, these values are to within the error virtually identical. These values were used in the subsequent calculations (Table 3-1).

Moreover, the cantilever thickness may not be uniform. For instance, the single beam cantilevers analyzed in this study were found (by SEM, see Appendix 3.7.1) to possess non-uniform thicknesses. The value of the thickness decreased nonlinearly from the apex to the base from  $0.9 \mu\text{m}$  to  $0.7 \mu\text{m}$ . In this case, equations 3-3 to 3-5 do not provide quantitative force constants, but only a rough approximation. Furthermore, without precise knowledge of the thickness and its variation along the cantilever the force constants cannot be modeled quantitatively even with FEA.



Table 3-1. Normal and lateral spring constants determined using the method by Sader *et al.*<sup>39</sup> for V-shaped (A, B, C, and D) and single beam (E, F, G, and H) Si<sub>3</sub>N<sub>4</sub> cantilevers, respectively.

	V-shaped <sup>*,39</sup>				Single beam <sup>**</sup>			
	A	B	C	D	E	F	G	H
$k_N$ [N/m] <sup>#</sup>	0.32 ± 0.05	0.10 ± 0.01	0.18 ± 0.03	0.06 ± 0.01	0.12 ± 0.02	0.95 ± 0.014	0.10 ± 0.01	0.52 ± 0.08
$k_N$ calculated [N/m]	0.31 ± 0.12	0.11 ± 0.04	0.20 ± 0.08	0.05 ± 0.02	0.12 ± 0.09	0.97 ± 0.73	0.06 ± 0.05	0.51 ± 0.38
$k_L$ calculated [N/m]	210 ± 80	230 ± 90	150 ± 60	120 ± 50	180 ± 160	360 ± 320	90 ± 80	180 ± 160

<sup>#</sup> determined according to the reference lever approach,<sup>76</sup> \* $E=185$  GPa, \*\* $E=180$  GPa

### 3.2.2. Calibration according to finite element modeling

The spring constants of V-shaped cantilevers were determined by FEA using the actual cantilever shapes (Figure 3-2) and the same values of materials properties as for the calculated force constants (Section 3.2.1). The results obtained for the normal and lateral force constants using the analytical approaches on the one hand, and from FEA on the other hand, were found to be in good agreement to within an error of 10% (Table 3-2). Hence, in our subsequent analysis, only values calculated using the Sader approach were used.

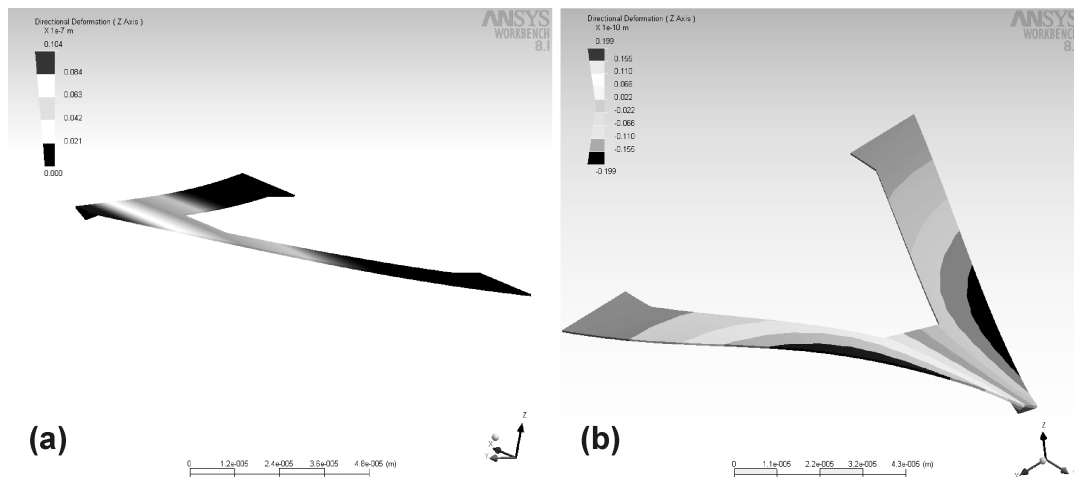


Figure 3-2. (a) Normal deflection and (b) torsion of a V-shaped cantilever modeled for the actual probe shapes using FEA. The images show the cantilever deformation after applying: (a) normal and (b) lateral force to the tip. The grey scale represents the magnitude of the deformation.

Table 3-2. Normal and lateral spring constant for a V-shaped cantilever calculated according to Sader *et al.*<sup>39</sup> and Neumeister *et al.*,<sup>33</sup> as well as using FEA modeling.<sup>49,50</sup>

calculated according to	$k_N$ [N/m]	$k_L$ [N/m]
Sader	0.17	109
Neumeister	0.16	104
FEA	0.19	123

### 3.3. Calibration of the lateral photodiode sensitivity

The photodiode response to the bending, or the twist angle, of the cantilever, which corresponds to the movement of the laser spot in the photodiode in normal and lateral directions, respectively, is expressed by the photodiode sensitivities in normal and lateral direction ( $S_N$  and  $S_L$ ).  $S_N$  can be readily obtained from a force displacement curve acquired on a hard substrate in the linear compliance region, where the tip and the piezo are in hard wall contact and move together.<sup>37</sup> The relation between  $S_N$  and  $S_L$  is obtained from an analysis of the laser beam path reflected from the cantilever.<sup>29</sup> Assuming equal bending and torsion angles of the cantilever, this will result in equal displacement of the reflected laser beam on the photodiode in normal and lateral directions, respectively (Eq. 3-6).

$$\Phi_N = \varphi = \frac{1}{2O}n \quad (\text{Eq. 3-6})$$

with bending angle  $\Phi_N$ , torsion angle  $\varphi$ , length of the laser beam optical path from the cantilever apex to the photodiode  $O$ , and displacement of the laser beam on the photodiode  $n$ . The bending angle function  $\Phi_N$  is defined as the first derivative of the bending function<sup>29</sup>  $z(x)$  of the cantilever ( $\Phi_N(x) = dz(x)/dx$ ).

For symmetrical laser spot shapes equal bending and torsion angles result consequently in identical changes in the output voltages  $U_N$  and  $U_L$ . However, in most cases the laser spot shape is elliptical, rectangular or even trapezoidal.

The effect of an unsymmetrical laser spot size was taken into account using a correction factor  $R$ , which characterizes the aspect ratio of the beam ( $R =$  the ratio of the beam height to the beam width).  $R$  was experimentally determined by image analysis of photographs of the actual laser spot shape, as described below.<sup>78</sup> The vertical and horizontal length of each spot was revealed

from a cross-sectional analysis of the photographs.  $R$  was found to be 0.45 - 0.77 and also to depend on the cantilever shape and the laser beam position on the cantilever (Figure 3-3).

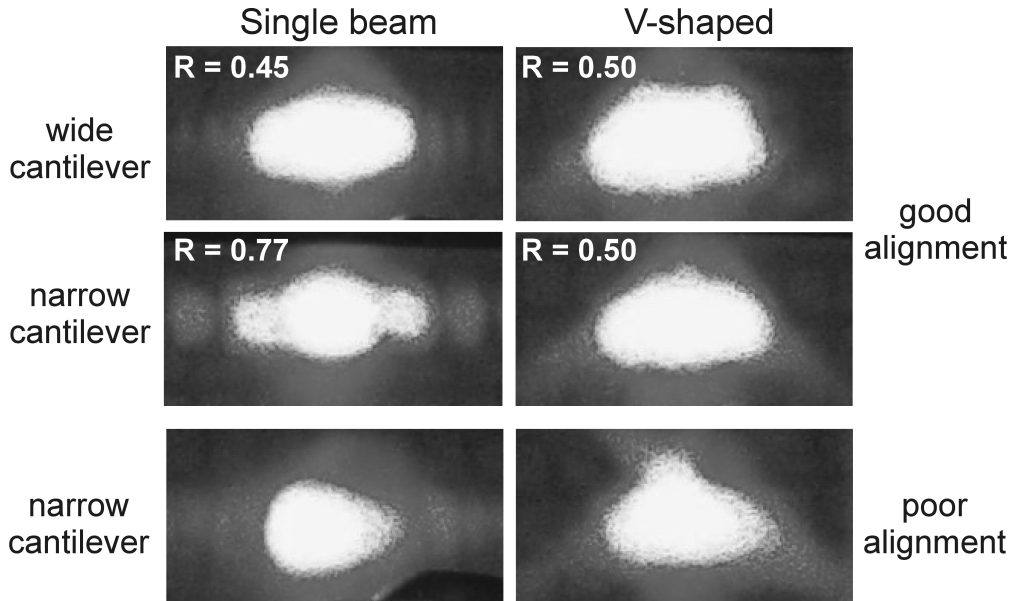


Figure 3-3. Digital photographs of laser light reflected off the cantilever as detected on a piece of paper inserted into the path of the light in front of the photodiode. The asymmetry of the laser beam reflected from various types of cantilevers is obvious: left – single beam, and right - V-shaped. The two images in the bottom row display the effect of poor alignment of the laser on the cantilever. The values of  $R$  were determined by an image analysis of these photographs as described in the Experimental Section.

For single beam cantilevers the beam shape is nearly elliptical, with an aspect ratio of 0.77 and 0.45 for narrow and wide cantilevers, respectively. By contrast, for V-shaped cantilevers, the beam shape depends strongly on the laser beam position on the cantilever apex and may vary from elliptical to trapezoidal shape, with little variation between cantilevers with narrow and wide legs ( $R = 0.43 - 0.50$ ).<sup>79</sup>

For identical small displacements  $n$  of the laser beam in normal and lateral directions (see Figure 3-4(b) and (c)) with respect to the center position on the four-segment photodiode, the relation between the measured output voltages can be approximated as:

$$\Delta U_L = R \cdot \Delta U_N \quad (\text{Eq. 3-7})$$

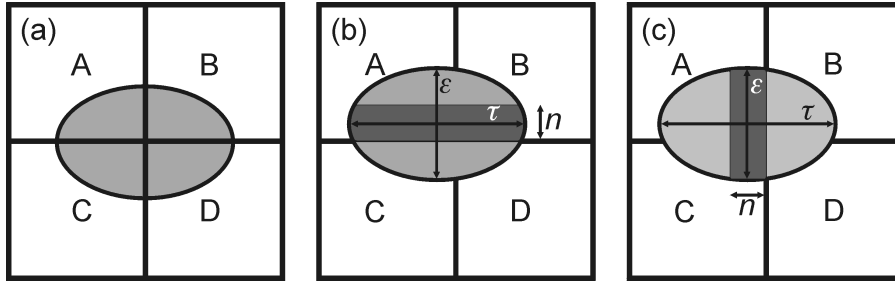


Figure 3-4. Different laser beam positions on the four segment photodiode (A, B, C, and D represent the four segments of photodiode output voltage): (a) in the center, (b) and (c) shifted by a small displacement of  $n$  in normal and lateral directions. The asymmetry of the laser beam shape is expressed by aspect ratio  $R = \varepsilon/\tau$ . The voltage measured on the four segment photodiode in normal and lateral direction are defined as the difference voltage between top and bottom photodiode output:  $\Delta U_N = ((A+B)-(C+D))/(A+B+C+D)$  and difference voltage between left and right photodiode output:  $\Delta U_L = ((A+C)-(B+D))/(A+B+C+D)$ , respectively. The dark colored areas in (b) and (c) illustrate the effect of identical small displacement  $n$  from the center position in normal and lateral direction, on measured values of the output voltages: (a)  $\Delta U_N = \Delta U_L = 0$ , (b)  $\Delta U_N \approx n\tau$ , and (c)  $\Delta U_L \approx n\varepsilon$ .

Using the bending angle functions for single beam and V-shaped cantilevers, the relation between bending angle  $\Phi_N$  and displacement  $z$  at the laser beam position on the cantilever can be established:

$$\Phi_N = \frac{P}{l^*} z \quad (\text{Eq. 3-8})$$

where  $P$  is a constant (proportionality factor), which is specific for each type of cantilever and  $l^*$  is the cantilever length ( $l^*$  is measured from the cantilever base to the position of the laser beam on the cantilever apex). For both types of cantilevers the constants were calculated from the bending functions, as well as from FEA modeling. The influence of the laser position on the cantilever was also taken into account. The values of  $P$  were equal to  $1.5 \pm 0.1$  and  $2.5 \pm 0.5$  for single beam and V-shaped cantilevers, respectively. In the case of V-shaped cantilevers, the value of  $P$  will strongly diverge when moving the beam from the cantilever apex towards its base. Furthermore, the relation between output voltages and sensitivities for normal and lateral direction can be expressed from Eq. 3-1 and 3-2, respectively:

$$z = S_N \cdot \Delta U_N \quad (\text{Eq. 3-9})$$

$$x = S_L \cdot \Delta U_L \quad (\text{Eq. 3-10})$$

where  $x$  denotes a lateral displacement of the tip.

Since the lateral signal measured is amplified by a factor  $a$  in some AFM systems (*e.g.* for a DI Multimode NanoScope III:  $a_{DI} = 4.1$ , for a Molecular Imaging PicoSPM:  $a_{MI} = 5.3$ ) this must also be considered. Thus, from equations (Eq. 3-6) to (Eq. 3-10), a general relation between  $S_L$  and  $S_N$ , taking the spot asymmetry and different type of cantilever into account, is expressed as:

$$S_L = \frac{P}{aR} \frac{h}{l^*} S_N \quad (\text{Eq. 3-11}).$$

Table 3-3. Values of  $S_L$ , laser beam aspect ratio and the corresponding calibration factor  $\alpha$  determined using the two-step approach for V-shaped (A, B, C, and D) and single beam (E, F, G, and H)  $\text{Si}_3\text{N}_4$  cantilevers, respectively.

	V-shaped <sup>*,39</sup>				Single beam <sup>**</sup>			
	A	B	C	D	E	F	G	H
$S_L$ [nm/V]	1.60 ± 0.24	1.60 ± 0.24	1.60 ± 0.24	1.40 ± 0.21	0.82 ± 0.12	0.93 ± 0.14	0.51 ± 0.08	0.55 ± 0.08
laser beam aspect ratio	0.50 ± 0.05	0.50 ± 0.05	0.43 ± 0.04	0.50 ± 0.05	0.45 ± 0.04	0.45 ± 0.04	0.77 ± 0.08	0.77 ± 0.08
$\alpha$ cal [nN/mV]	0.34 ± 0.18	0.37 ± 0.20	0.23 ± 0.12	0.16 ± 0.08	0.14 ± 0.13	0.33 ± 0.30	0.04 ± 0.04	0.10 ± 0.09

\* $E=185\text{GPa}$ , \*\* $E=180\text{ GPa}$

The error analysis for the two-step method was performed as described in the Appendix 3.7.2. The calculated spring constants  $k_L$  are loaded with large relative errors of 40 - 45% and 30 - 35% (assuming uniform thickness) for V-shaped and single beam  $\text{Si}_3\text{N}_4$  cantilevers, respectively, due to the uncertainty in materials properties<sup>29,33,49</sup> and cantilever thickness (*vide supra*). For non-uniform thicknesses of the cantilevers the relative errors can exceed 75 - 90% for single beam cantilevers.

In addition to the inherent errors in the values of  $k_L$  and the lateral photodiode sensitivity  $S_L$ , which is very sensitive to laser intensity fluctuations, interference effects, the position of the laser beam on the cantilever apex, and the thermal stability of the AFM set up, are additional significant sources of error in the two-step calibration approach. Therefore, the final friction calibration factors  $\alpha_i$  cannot be obtained with high accuracy according to this two-step procedure; relative errors  $\delta\alpha_i$  are 45 - 50% and 35 - 40% for V-shaped and single beam cantilevers, respectively.

It is clear based on the analysis shown above that the two-step approach leads inevitable to errors of at least 35%. The variations of the corresponding spring constants and friction coefficients reported in the literature for identical levers (V-shaped) and tip – sample combinations ( $\text{Si}_3\text{N}_4$  – alkanethiol monolayers on Au (111)),<sup>15,16</sup> respectively, can be in parts attributed to these large errors, as well as to irreproducibilities due to poorly defined materials properties and low precision in the determination of the cantilever thickness and the lateral photodiode sensitivity. The magnitude of the errors is not acceptable for quantitative nanotribology. Thus, in order to be able to address the nanotribological properties of nanostructured ceramics, as well as those of polymers, *etc.* (Chapters 6 - 8), an accurate calibration procedure is clearly required. As shown in Chapter 4, a universal platform has been developed that overcomes these limitations. This platform enables one to conveniently perform quantitative nanotribological measurements for a wide range of materials and applications.

### 3.4. Probe tip characterization

In addition to accurate estimates of the calibration factors  $\alpha_i$  (see above and Chapter 4), the geometry and the chemical composition of the tip material are of crucial importance in nanotribology. The friction force is directly proportional to the tip-sample contact area, for an elastic, wear-less single asperity contact. Moreover, the friction force in AFMs is determined as the difference between the corresponding trace and retrace scans (as described in detail in Chapter 2); consequently the same contact area between the tip and the sample for corresponding trace and retrace scans is necessary. Therefore, for quantitative nanotribology, stable probes with symmetrical tip apex, are required.<sup>23,24</sup>

#### 3.4.1. Characterization of the tip apex

The shape and size of the probe apex can be characterized using several *in situ*<sup>80-85</sup> and *ex situ*<sup>24,84-86</sup> methods. The *in situ* methods rely on the analysis of convoluted AFM topography images<sup>87,88,89</sup> obtained on samples with well-characterized geometrical features. As a standard, a sample with individual monodisperse spherical particles<sup>80</sup> with defined diameter  $H$  (Figure 3-5), can be used for the analysis of the tip apex shape and its radius  $r$ .

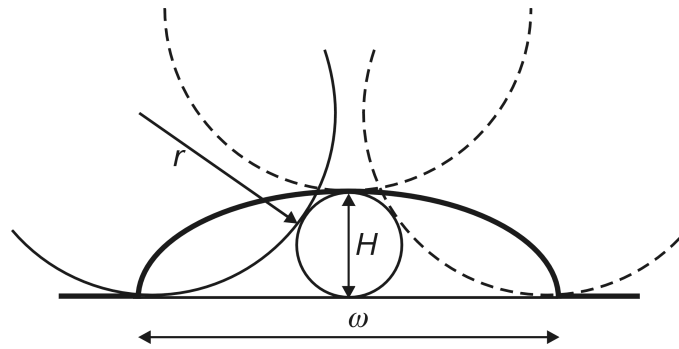


Figure 3-5. A schematic of tip-sample convolution of a spherical particle with diameter  $H$ , imaged with a spherical AFM tip with radius  $r$ .  $\omega$  denotes the apparent width of the particle.

Assuming a spherical tip and a spherical particle, the tip radius  $r$  can be calculated according to Pythagora's law as:

$$r = \frac{\omega^2}{8H} \quad (\text{Eq. 3-12}).$$

Another method is based on the analysis of images obtained by scanning a sample with much sharper structures than the tip itself, resulting in so-called tip imaging. Different well-defined morphological features can be used, such as pin-like structures<sup>81-84</sup> or gratings with microfabricated arrays of sharp tips (see Figure 3-6).<sup>85</sup>

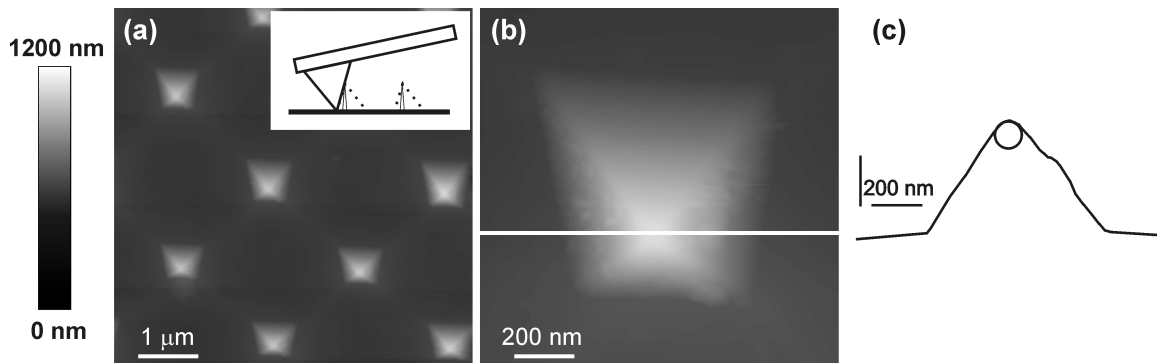


Figure 3-6. (a) AFM "tip imaging" showing the geometry of the AFM tip, obtained by scanning an array of sharp spikes; the inset illustrates the schematic of tip imaging, (b) tip image on a single sharp spike with white line corresponding to cross-sectional analysis (c). The tip radius is  $\sim 55 \text{ nm} \pm 10 \text{ nm}$ . The accuracy is determined by the radius of the spike (nominally below 10 nm).

Various *ex situ* techniques for tip characterization, such as SEM<sup>84,85</sup> and TEM,<sup>24,86</sup> provide detailed information about the probe shape, size and its quality. However, the tip can be easily contaminated during the characterization, *e.g.* with traces of vacuum pump oil. Thus, the tip analysis according to these methods can be performed only after the nanotribology examination.

### 3.4.2. Tip wear

To ensure the required spherical shape of the tip apex and the absence of wear, which both would render AFM-based nanotribology difficult or even impossible, the stability of several AFM probe tips was tested on a hard nanostructured ZrO<sub>2</sub> sample (see also Chapter 6). The examined tip was scanned on the zirconia sample in the same area for a number of images under various applied loads. Sharp morphological features on the sample (zirconia aggregates) gave rise to tip images (see Appendix 3.7.3). These images were used to monitor the tip wear *in situ*. The progress of the tip wear was measured as apparent “tip area” for the same features normalized to the starting value as a function of scanning time. Figure 3-7(a) shows the relative tip area vs. scanning time for Si<sub>3</sub>N<sub>4</sub> tips produced by different manufacturers (single beam and V-shaped cantilevers purchased from Olympus and Veeco, respectively). The relative tip area for the tip integrated with the single beam cantilever rapidly increases as a function of scanning time. The tip wore severely without applying any external load (initial normal force ~ 14 nN). SEM images of the tip captured before and after the wear experiments showed significant tip degradation as a result of the wear test (Figure 3-7(b) and (c)). By contrast, for the tip integrated with the V-shaped cantilever mild wear was observed at the initial scanning stage. Further, even with significantly increased load this tip remained stable. These results show that the same type of material may have very different wear, and likely other properties (see Appendix 3.7.3).<sup>90</sup>

This particular example of a severely worn tip reveals that both tip-sample contact area and the tip height are affected by the tip degradation, which will directly change the value of the lateral spring constant (Eq. 3-5). Therefore, quantitative nanotribology cannot be performed under these conditions.

The tip stability can be significantly improved by applying a wear-resistant coating on the tip.<sup>91</sup> One of the possible materials that could be utilized as a coating is  $\alpha$ -Al<sub>2</sub>O<sub>3</sub>, which is known as a hard and wear-resistant material. Moreover,  $\alpha$ -Al<sub>2</sub>O<sub>3</sub> is widely used as a pin material in microtribology tests. In particular, it has been used in the ceramic tribosystems discussed in Chapter 7. In the context of this work, it is desirable to realize an identical tribosystem using AFM tips for nanoscopic investigations. As shown below, this can be obtained by applying new tip coating procedures.



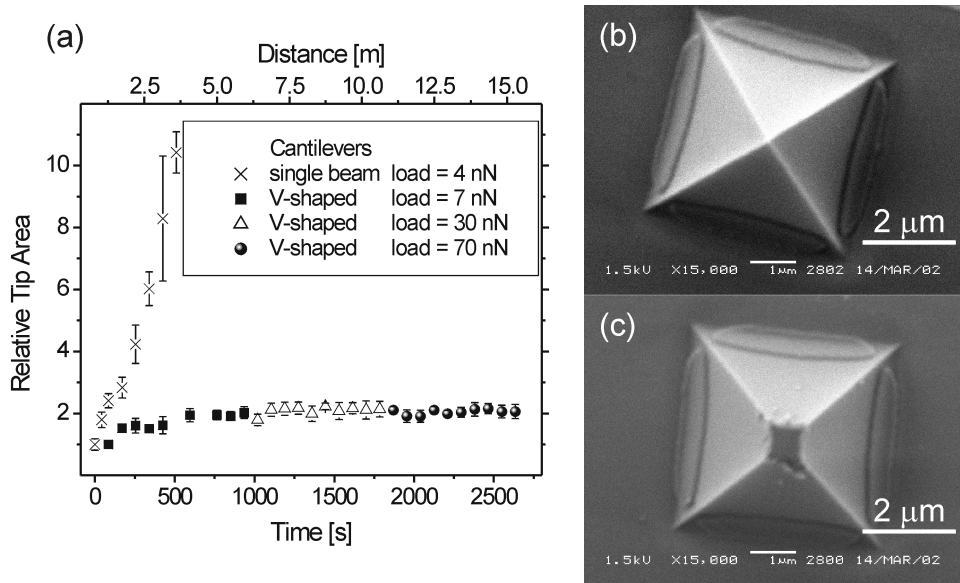


Figure 3-7. (a) Tip stability test of two  $\text{Si}_3\text{N}_4$  AFM probes (single beam cantilever and V-shaped cantilever) performed on hard nanostructured  $\text{ZrO}_2$  sample under different load conditions. SEM images of the single beam cantilever tip (b) before and (c) after the wear test.

For these experiments Si probes were chosen, since they are high temperature resistant and have better defined material properties as compared to  $\text{Si}_3\text{N}_4$  cantilevers. The deposition of a wear-resistant  $\text{Al}_2\text{O}_3$  coating was performed using pulsed laser deposition (PLD), which provides high quality homogeneous layers.<sup>92</sup> Figure 3-8 shows SEM images of (a) an uncoated and (b) a coated Si tip captured after PLD and subsequent annealing at  $1000^\circ\text{C}$ . The uncoated tip possessed a smooth surface, whereas the coated one was covered with a layer of fine grains.

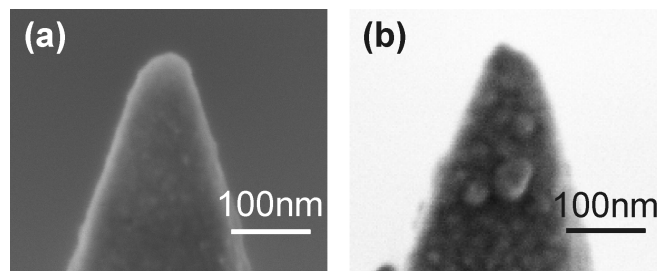


Figure 3-8. High resolution SEM images of (a) an uncoated Si tip and (b) a Si tip coated with a 26 - 29 nm thick  $\text{Al}_2\text{O}_3$  film.

The composition of the coating was further investigated by energy dispersive X-ray (EDX) analysis, which was performed on the tip apex (Figure 3-9). In addition to a signal originating from the underlying Si, clear evidence for the presence of Al and O was revealed. The also detected C originates likely from airborne contaminations.

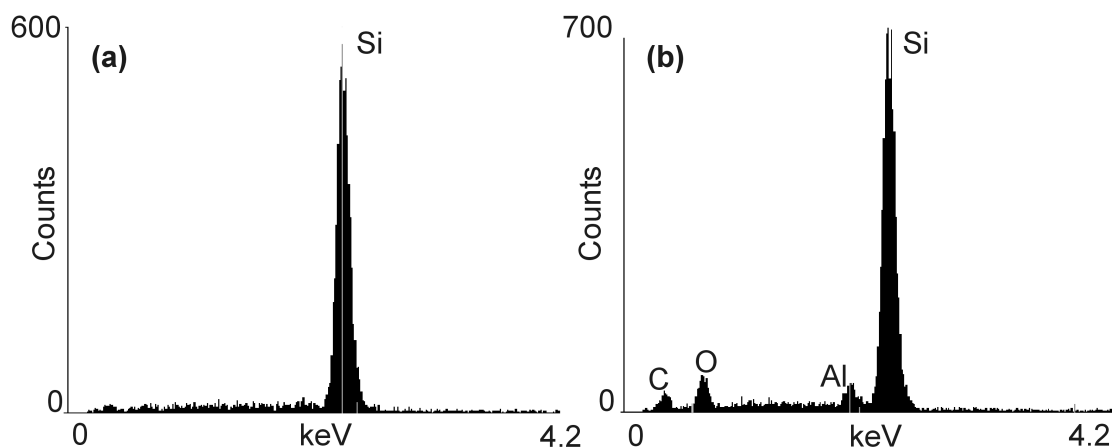


Figure 3-9. EDX analysis captured at the apex of (a) an uncoated Si tip and (b) a Si tip coated with 26 - 29 nm  $\text{Al}_2\text{O}_3$ .

The obtained coating was also characterized by X-ray diffraction (XRD) (see Appendix 3.7.4). In the analysis, only  $\gamma\text{-Al}_2\text{O}_3$  was detected. The  $\alpha$  structure was not observed.

The wear-resistance of the uncoated and  $\text{Al}_2\text{O}_3$  coated tips was tested subsequently on the hard nanostructured  $\text{ZrO}_2$  sample under different applied loads. The tip radii (30 nm) and the initial adhesion force (12 nN) for both probes were comparable. Figure 3-10 shows the relative tip area for both coated and uncoated probes as a function of time. The uncoated Si tip already started to wear at low applied external loads (12 nN). By contrast, the coated tip remained stable for applied loads up to 55 nN. It can be seen that the  $\gamma\text{-Al}_2\text{O}_3$  film is a very effective wear-resistant coating for Si probes.

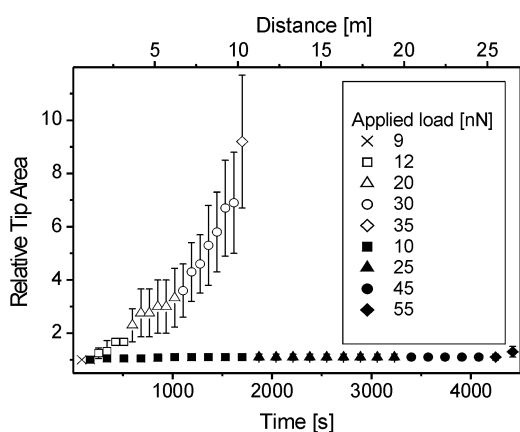


Figure 3-10. Tip stability test of the  $\text{Al}_2\text{O}_3$  coated and uncoated Si probes (solid and open symbols, respectively), performed on hard nanostructured  $\text{ZrO}_2$  sample under different load conditions.

Several attempts made to obtain  $\alpha$ -Al<sub>2</sub>O<sub>3</sub> coatings on Si tips, *e.g.*, by performing the PLD of Al<sub>2</sub>O<sub>3</sub> at ultra high temperature (1150°C) or by using Cr<sub>2</sub>O<sub>3</sub> as a template layer,<sup>93,94</sup> have failed so far. However, it is likely that by further optimalization of the deposition process, an even better wear-resistant  $\alpha$ -Al<sub>2</sub>O<sub>3</sub> coating for Si AFM tips may be obtained.

### 3.5. Conclusions

A general relation between photodiode lateral sensitivity  $S_L$  and photodiode normal sensitivity  $S_N$  was derived that takes the laser spot asymmetry for different types of cantilevers, as well as AFM instrument specific amplification factors, into account. As shown, the two-step calibration method for Si<sub>3</sub>N<sub>4</sub> cantilevers may be highly inaccurate due to the inherent errors in the calculation of  $k_L$  originating from poorly defined materials properties and insufficient precision in determination of the value of cantilever thickness. Moreover, the lateral photodiode sensitivity  $S_L$  is an additional significant source of error in the two-step calibration approach. Therefore, the final friction calibration factors  $\alpha_i$  cannot be obtained with high accuracy according to this procedure; relative errors  $\delta\alpha_i$  are 45 - 50% and 35 - 40% for V-shaped and single beam cantilevers, respectively. The low accuracy of the two-step friction force calibration method will very likely cause poor reproducibility of nanotribological measurements performed with different cantilevers. This result necessitates the development of the universal calibration platform described in Chapter 4, which provides access to *quantitative* friction forces. Finally, the wear-resistance of Si tips was significantly improved by applying a thin wear-resistant Al<sub>2</sub>O<sub>3</sub> coating by PLD.

### 3.6. Experimental

#### 3.6.1. Calibration procedure

The calibration of friction force was achieved by (i) calculating the cantilevers' spring constants based on their geometry, dimensions and material properties, and (ii) by determining the lateral photodiode sensitivities for individual cantilevers.

The force constants of single beam cantilevers (OMCL-RC800PSA series, Olympus, Tokyo, Japan) were calculated from continuum elasticity mechanics of isotropic solids (Eq. 3-3 to 3-5). For V-shaped cantilevers (Model NP, Veeco Nano Probe, Santa Barbara, CA) the force constants were calculated according to two different analytical approaches, *i.e.* by Sader *et al.*<sup>39</sup> and by Neumeister *et al.*<sup>33</sup> The spring constants were additionally determined using a finite element analysis (FEA) by Dr. Rihard Pasaribu and Prof. dr. ir. Dik Schipper (Tribology Group,

University of Twente). The simulation of the cantilevers bending and torsion was carried out using plate elements in the ANSYS Workbench 8.1 (Canonsburg, PA) software package, with different numbers of elements.<sup>49,50</sup> The dimensions of the cantilevers were obtained from scanning electron microscopy (SEM) images (JSM 5600 LV, Jeol, Tokyo, Japan operated at 2 kV) by Clemens Padberg (Department of Materials Science and Technology of Polymers, University of Twente). The cantilevers thicknesses were determined from high resolution SEM images (HR LEO 1550 FEG SEM, Oberkochen, Germany, operated at a voltage of 0.5 kV) by Dr. Nina Demkina (Department of Materials Science and Technology of Polymers, University of Twente).

The lateral photodiode sensitivity was estimated from the analysis of the reflected laser beam path as described in reference 29. The laser spot asymmetry was corrected based on the analysis of the shape of the laser spot for each cantilever, as established from the analysis of a series of photographs of the beam projection on a piece of paper inserted into the beam path in front of the photodiode (Figure 3-3). The photographs were taken with a digital camera (Konica-Minolta Dimage Z3, Tokyo, Japan) using different exposure times and aperture settings. The aspect ratios of the laser spots were determined from the photographs obtained, as proportion of vertical to horizontal spot length using Scion image software.<sup>95</sup>

### 3.6.2. Tip wear test

The wear-resistance of several different probes was investigated, including V-shaped (Model NP, Veeco Nano Probe, Santa Barbara, CA) and single beam (OMCL-RC800PSA series, Olympus, Tokyo, Japan) Si<sub>3</sub>N<sub>4</sub> cantilevers, as well as single beam Si cantilevers (NSC36, MikroMasch, Tallin, Estonia) with and without tip Al<sub>2</sub>O<sub>3</sub> coating (see Section 3.6.3). The tip wear tests were performed on the nanostructured zirconia samples (grain size 12 nm) (see Chapter 6). The tested tip was scanned on the zirconia sample in the same area for a number of images under various applied loads. Sharp morphological features on the sample (zirconia aggregates) showed tip images, which were used to monitor the tip wear *in situ*. The progress of the tip wear was measured as apparent “tip area” for the same features normalized to the starting value. The tips apexes were characterized before and after the wear tests using a calibration grating (silicon grating TGT1, NT-MDT, Moscow, Russia) and determined from SEM images (JSM 5600 LV, Jeol, Tokyo, Japan, operated at a voltage of 1.5 - 2 kV) by Clemens Padberg (Department of Materials Science and Technology of Polymers, University of Twente).

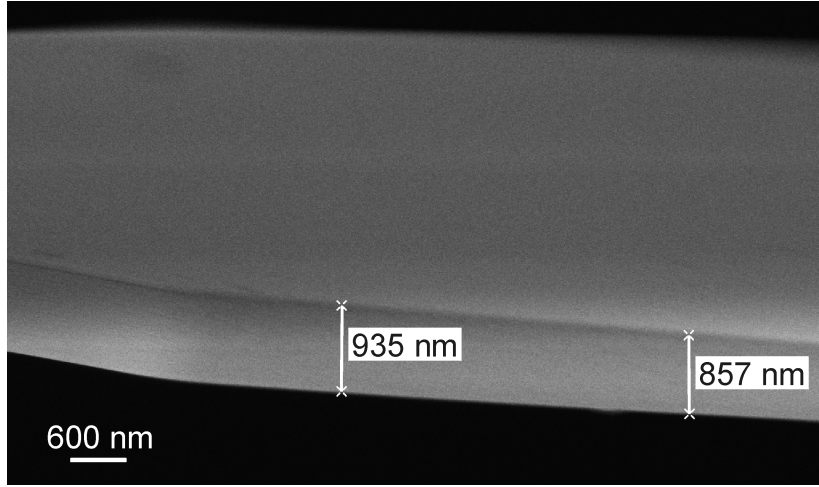
### 3.6.3. *Wear-resistant coating for AFM tips*

The Al<sub>2</sub>O<sub>3</sub> films were grown on the commercial n-type (100) Si AFM probes with native oxide layer and Al reflecting coating (NSC36, MikroMasch, Tallin, Estonia) using a pulsed laser deposition (PLD) system<sup>92,96</sup> by Joska Broekmaat (Low Temperature Division Group, University of Twente) and Dr. ing. Guus Rijnders and Prof. dr. ing. Dave Blank (Inorganic Materials Science Group, University of Twente). Before the deposition the probes were immersed in 69% HNO<sub>3</sub> for 20 minutes in order to remove contaminations. The PLD process was performed using a KrF excimer laser ( $\lambda = 248$  nm) with a laser energy density of 3 J/cm<sup>2</sup>. The base pressure in the deposition chamber was  $2 \times 10^{-6}$  mbar in the load lock system. In one deposition two AFM probes were mounted on a thermo-coax heater 40 mm from the single-crystalline Al<sub>2</sub>O<sub>3</sub> target doped with 0.145% Ti. The deposition took place in Ar atmosphere with  $3 \times 10^{-3}$  mbar pressure at a temperature of 500°C, measured inside the heater block with a K-type thermocouple (maximum heating/cooling rates were used). The target was ablated for 400 pulses at 5 Hz resulting in the film thickness of 26 – 29 nm. Subsequently, the probes were annealed at 1000°C for 6 hours in N<sub>2</sub> atmosphere.

The thin films produced by PLD were characterized by high resolution SEM (HR LEO 1550 FEG SEM, Oberkochen, Germany, operated at a voltage of 0.5 kV) and energy dispersive X-ray analysis (EDX) (Model Vantage, Thermo NORAN Instruments, Tallahassee, FL) at the Central Materials Analysis Laboratory (MESA<sup>+</sup> Institute for Nanotechnology, University of Twente) and X-ray diffraction (XRD) by Joska Broekmaat (Low Temperature Division Group, University of Twente).

### 3.7. Appendix

#### 3.7.1. Non-uniform thickness of a $\text{Si}_3\text{N}_4$ cantilever



Appendix 3-1. High resolution SEM image of  $\text{Si}_3\text{N}_4$  single beam cantilever. The thickness of the cantilever decreases non-uniformly from the apex to the base.

#### 3.7.2. Error analysis of the two-step calibration technique

The errors of the normal and lateral spring constants ( $\delta k_N$  and  $\delta k_L$ ) for V-shaped and single beam cantilevers (for isotropic materials and uniform cantilever thickness), as well as the errors of the lateral photodiode sensitivities ( $\delta S_L$ ), were calculated by the error propagation according to Gauss:

$$\delta k_N^V = \sqrt{\left(\frac{\partial k_N}{\partial E} \delta E\right)^2 + \left(\frac{\partial k_N}{\partial t} \delta t\right)^2 + \left(\frac{\partial k_N}{\partial l} \delta l\right)^2 + \left(\frac{\partial k_N}{\partial \Delta l} \delta \Delta l\right)^2 + \left(\frac{\partial k_N}{\partial d} \delta d\right)^2 + \left(\frac{\partial k_N}{\partial b} \delta b\right)^2}$$

(Eq. 3-13)

$$\delta k_L^V = \sqrt{\left(\frac{\partial k_L}{\partial E} \delta E\right)^2 + \left(\frac{\partial k_L}{\partial t} \delta t\right)^2 + \left(\frac{\partial k_L}{\partial l} \delta l\right)^2 + \left(\frac{\partial k_L}{\partial \Delta l} \delta \Delta l\right)^2 + \left(\frac{\partial k_L}{\partial d} \delta d\right)^2 + \left(\frac{\partial k_L}{\partial b} \delta b\right)^2 + \left(\frac{\partial k_L}{\partial v} \delta v\right)^2 + \left(\frac{\partial k_L}{\partial h} \delta h\right)^2}$$

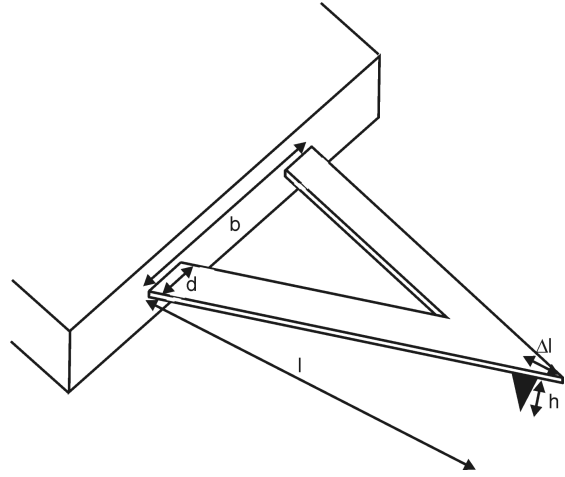
(Eq. 3-14)

where:

$$k_N = \frac{Et^3 d}{2\sqrt{B}(l - \Delta l)^3 C} \quad (\text{Eq. 3-15})$$

$$B = 1 + \frac{b^2}{4l^2} \quad (\text{Eq. 3-16})$$

$$\text{and } C = 1 + \frac{4d^3}{B^{\frac{3}{2}} b^3} \quad (\text{Eq. 3-17})$$



Appendix 3-2. Schematic diagram of V-shaped cantilever plates used for the spring constants calculations, showing dimensions.

Partial derivatives of  $k_N^V$ :

$$\frac{\partial k_N}{\partial E} = \frac{t^3 d}{2\sqrt{B}(l - \Delta l)^3 C} \quad (\text{Eq. 3-18})$$

$$\frac{\partial k_N}{\partial t} = \frac{3Et^2 d}{2\sqrt{B}(l - \Delta l)^3 C} \quad (\text{Eq. 3-19})$$

$$\frac{\partial k_N}{\partial l} = \frac{Et^3 db^2}{8B^{\frac{3}{2}}(l - \Delta l)^3 l^3 C} - \frac{3Et^3 d}{2\sqrt{B}(l - \Delta l)^4 C} - \frac{3Et^3 d^4}{2B^3(l - \Delta l)^3 bl^3 C^2} \quad (\text{Eq. 3-20})$$

$$\frac{\partial k_N}{\partial \Delta l} = \frac{3Et^3 d}{2\sqrt{B}(l - \Delta l)^4 C} \quad (\text{Eq. 3-21})$$

$$\frac{\partial k_N}{\partial d} = \frac{Et^3}{2\sqrt{B}(l - \Delta l)^3 C} - \frac{6Et^3 d}{B^2(l - \Delta l)^3 b^3 C^2} \quad (\text{Eq. 3-22})$$

$$\frac{\partial k_N}{\partial b} = -\frac{Et^3 db}{8B^{\frac{3}{2}}(l - \Delta l)^3 l^2 C} + \frac{3Et^3 d^4(b^2 + 4Bl^2)}{2B^3(l - \Delta l)^3 b^4 l^2 C^2} \quad (\text{Eq. 3-23})$$

and

$$k_L = \frac{Et^3 d}{3h^2 l(1+\nu)J} \quad (\text{Eq. 3-24})$$

$$J = 1 + \frac{d}{b} \left( 2 \log \left( \frac{2dl}{b\Delta l} \right) - 2 - \frac{3b^2}{8l^2 B} \right) \quad (\text{Eq. 3-25})$$

Partial derivatives of  $k_L^V$ :

$$\frac{\partial k_L}{\partial E} = \frac{t^3 d}{3h^2 l(1+\nu)J} \quad (\text{Eq. 3-26})$$

$$\frac{\partial k_L}{\partial t} = \frac{Et^2 d}{h^2 l(1+\nu)J} \quad (\text{Eq. 3-27})$$

$$\frac{\partial k_L}{\partial l} = -\frac{Et^3 d}{3h^2 l^2(1+\nu)J} - \frac{Et^3 d^2}{3h^2 l^2 b(1+\nu)J^2} \left( 2 + \frac{3b^2}{4l^2 B} - \frac{3b^4}{16l^4 B^2} \right) \quad (\text{Eq. 3-28})$$

$$\frac{\partial k_L}{\partial \Delta l} = -\frac{2Et^3 d^2}{3h^2 l b \Delta l(1+\nu)J^2} \quad (\text{Eq. 3-29})$$

$$\frac{\partial k_L}{\partial d} = -\frac{Et^3}{3h^2 l(1+\nu)J} - \frac{Et^3 d}{3h^2 l b(1+\nu)J^2} \left( 2 \log \left( \frac{2dl}{b\Delta l} \right) - \frac{3b^2}{8l^2 B} \right) \quad (\text{Eq. 3-30})$$

$$\frac{\partial k_L}{\partial b} = -\frac{Et^3 d^2}{3h^2 l b^2(1+\nu)J^2} \left( -2 \log \left( \frac{2dl}{b\Delta l} \right) - \frac{3b^2}{8l^2 B} + \frac{3b^4}{16l^4 B^2} \right) \quad (\text{Eq. 3-31})$$

$$\frac{\partial k_L}{\partial \nu} = -\frac{Et^3 d}{3h^2 l(1+\nu)^2 J} \quad (\text{Eq. 3-32})$$

$$\frac{\partial k_L}{\partial h} = -\frac{2Et^3 d}{3h^3 l(1+\nu)J} \quad (\text{Eq. 3-33})$$

The errors of  $k_N$ ,  $k_L$  for single beam cantilevers and the photodiode lateral sensitivity were calculated according to:

$$\delta k'_N = \sqrt{\left( \frac{k_N}{E} \delta E \right)^2 + \left( \frac{3k_N}{t} \delta t \right)^2 + \left( \frac{k_N}{w} \delta w \right)^2 + \left( \frac{3k_N}{(l-\Delta l)} \delta l \right)^2 + \left( \frac{3k_N}{(l-\Delta l)} \delta \Delta l \right)^2} \quad (\text{Eq. 3-34})$$



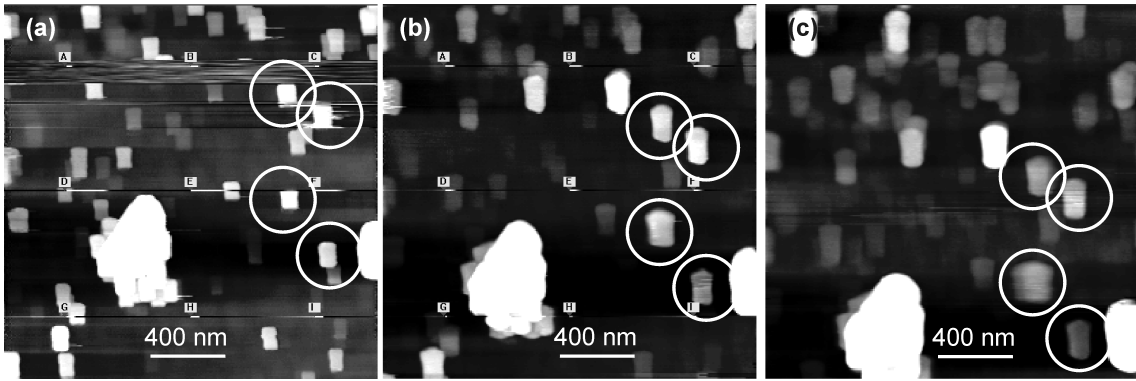
$$\delta k_L^I = \sqrt{\left(\frac{k_L}{E} \delta E\right)^2 + \left(\frac{3k_L}{t} \delta t\right)^2 + \left(\frac{k_L}{w} \delta w\right)^2 + \left(\frac{k_L}{(l-\Delta l)} \delta l\right)^2 + \left(\frac{k_L}{(l-\Delta l)} \delta \Delta l\right)^2 + \left(\frac{k_L}{v} \delta v\right)^2 + \left(\frac{2k_L}{h} \delta h\right)^2}$$

(Eq. 3-35)

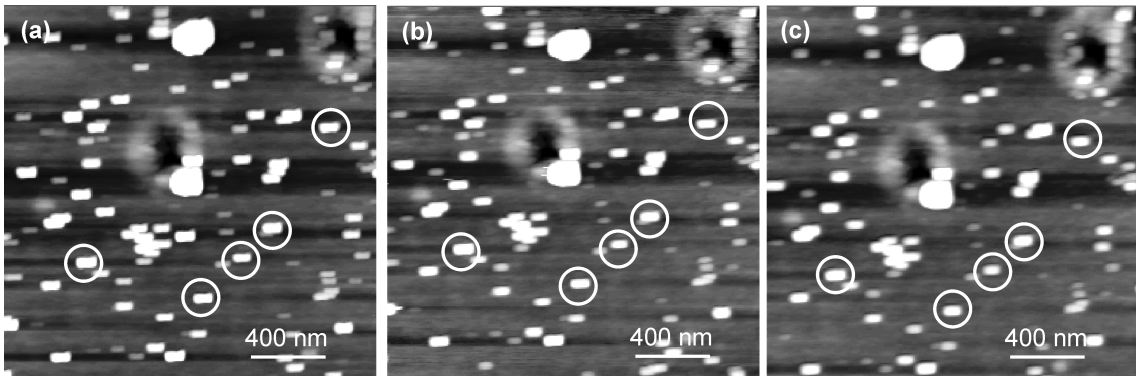
$$\delta S_L = \sqrt{\left(\frac{S_L}{R} \delta R\right)^2 + \left(\frac{S_L}{P} \delta P\right)^2 + \left(\frac{S_L}{h} \delta h\right)^2 + \left(\frac{S_L}{l} \delta l\right)^2 + \left(\frac{S_L}{S_N} \delta S_N\right)^2}$$

(Eq. 3-36)

### 3.7.3. Monitoring of tip wear in situ

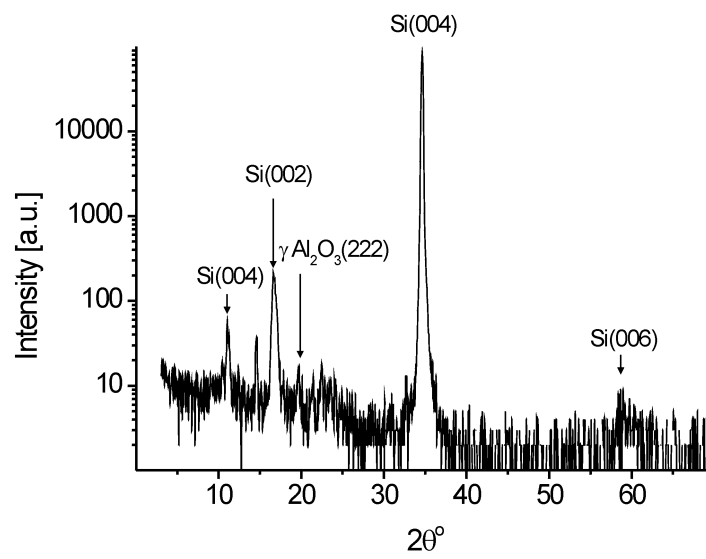


Appendix 3-3. AFM topography images of a hard nanostructured  $ZrO_2$  sample obtained by single beam  $Si_3N_4$  AFM probe revealing a progress of the tip wear, captured after: (a) 40 s, (b) 255 s, and (c) 510 s of scanning under external load of 4 nN. Sharp morphological features on the sample (zirconia aggregates) showed tip images, which were used to monitor the progress of the tip wear *in situ*, measured as apparent “tip area” for the same features (white circles) normalized to the starting value.



Appendix 3-4. AFM topography images of a hard nanostructured  $ZrO_2$  sample obtained by V-shaped  $Si_3N_4$  AFM probe revealing a progress of the tip wear, captured after: (a) 40 s, (b) 1360 s, and (c) 2210 s of scanning under external loads of 7 nN, 30 nN, and 70 nN, respectively. Sharp morphological features on the sample (zirconia aggregates) showed tip images, which were used to monitor the progress of the tip wear *in situ*, measured as apparent “tip area” for the same features (white circles) normalized to the starting value.

3.7.4. XRD of  $\text{Al}_2\text{O}_3$  coated Si tip



Appendix 3-5. XRD spectrum of Si tip coated with  $\text{Al}_2\text{O}_3$ , showing peaks from Si and  $\text{Al}_2\text{O}_3$ .<sup>97</sup>

---

### 3.8. References

- 1 Maeda, N.; Chen, N. H.; Tirrell, M.; Israelachvili, J. N. *Science* **2002**, *297*, 379-382.
- 2 Raviv, U.; Giasson, S.; Kampf, N.; Gohy, J. F.; Jerome, R.; Klein, J. *Nature* **2003**, *425*, 163-165.
- 3 Park, J. Y.; Ogletree, D. F.; Salmeron, M.; Ribeiro, R. A.; Canfield, P. C.; Jenks, C. J.; Thiel, P. A. *Science* **2005**, *309*, 1354-1356.
- 4 Urbakh, M.; Klafter, J.; Gourdon, D.; Israelachvili, J. *Nature* **2004**, *430*, 525-528.
- 5 Mosey, N. J.; Muser, M. H.; Woo, T. K. *Science* **2005**, *307*, 1612-1615.
- 6 Goldenberg, C.; Goldhirsch, I. *Nature* **2005**, *435*, 188-191.
- 7 Cagin, T.; Che, J. W.; Gardos, M. N.; Fijany, A.; Goddard, W. A. *Nanotechnology* **1999**, *10*, 278-284.
- 8 Maboudian, R.; Carraro, C. *Annu. Rev. Phys. Chem.* **2004**, *55*, 35-54.
- 9 Wang, W. Y.; Wang, Y. L.; Bao, H. F.; Xiong, B.; Bao, M. H. *Sens. Actuator A-Phys.* **2002**, *97-8*, 486-491.
- 10 Dürig, U.; Cross, G.; Despont, M.; Drechsler, U.; Häberle, W.; Lutwyche, M. I.; Rothuizen, H.; Stutz, R.; Widmer, R.; Vettiger, P.; Binnig, G. K.; King, W. P.; Goodson, K. E. *Tribol. Lett.* **2000**, *9*, 25-32.
- 11 King, W. P.; Kenny, T. W.; Goodson, K. E.; Cross, G.; Despont, M.; Dürig, U.; Rothuizen, H.; Binnig, G. K.; Vettiger, P. *Appl. Phys. Lett.* **2001**, *78*, 1300-1302.
- 12 Zhang, Q.; Archer, L. A. *Langmuir* **2005**, *21*, 5405-5413.
- 13 Liu, Y. H.; Wu, T.; Evans, D. F. *Langmuir* **1994**, *10*, 2241-2245.
- 14 Li, L. Y.; Yu, Q. M.; Jiang, S. Y. *J. Phys. Chem. B* **1999**, *103*, 8290-8295.
- 15 Lio, A.; Charych, D. H.; Salmeron, M. *J. Phys. Chem. B* **1997**, *101*, 3800-3805.
- 16 McDermott, M. T.; Green, J. B. D.; Porter, M. D. *Langmuir* **1997**, *13*, 2504-2510.
- 17 Kumar, A.; Whitesides, G. M. *Appl. Phys. Lett.* **1993**, *63*, 2002-2004.
- 18 Piner, R. D.; Zhu, J.; Xu, F.; Hong, S. H.; Mirkin, C. A. *Science* **1999**, *283*, 661-663.
- 19 Wilbur, J. L.; Biebuyck, H. A.; Macdonald, J. C.; Whitesides, G. M. *Langmuir* **1995**, *11*, 825-831.
- 20 There are abundant reports in the literature, which show that there may not be a simple relationship between friction forces for systems with nominally identical surface chemistry, such as well-defined monolayers terminated by identical functional groups [a] reference 15, [b] Schönherr, H.; Vancso, G. *J. Mater. Sci. Eng. C* **1999**, *8-9*, 243-249. In these cases contributions of different modes of energy dissipation are thought to affect the tribological behavior. For example, AFM friction experiments using (unmodified) silicon nitride tips performed on silane-based SAMs on mica [a] and organosulfur-based SAMs on Au(111) [b] show this pronounced effect. In addition, Bar *et al.* ([c] Bar, G.; Rubin, S.; Parikh, A. N.; Swanson, B. I.; Zawodzinski, T. A.; Whangbo, M. H. *Langmuir* **1997**, *13*, 373-377) showed that monolayer systems with non-detectable surface coverage differences may exhibit friction force contrast.
- 21 As reported in (Schönherr, H.; Hruska, Z.; Vancso, G. *J. Macromolecules* **2000**, *33*, 4532-4537) normal force measurements in chemical force microscopy utilizing chemically modified AFM probe tips allow one to vary and control the intermolecular interactions between the functional groups exposed on the tip and on the sample surface systematically. Thereby these spatially different interactions can be detected in normal force measurements, thus providing access to variations in, e.g., surface chemistry averaged over the tip - sample contact area.
- 22 Enachescu, M.; van den Oetelaar, R. J. A.; Carpick, R. W.; Ogletree, D. F.; Flipse, C. F. J.; Salmeron, M. *Tribol. Lett.* **1999**, *7*, 73-78.
- 23 Schwarz, U. D.; Zwörner, O.; Köster, P.; Wiesendanger, R. *Phys. Rev. B* **1997**, *56*, 6987-6996.

- 
- 24 Schwarz, U. D.; Zwörner, O.; Köster, P.; Wiesendanger, R. *J. Vac. Sci. Technol. B* **1997**, *15*, 1527-1530.
- 25 In this Chapter, only force calibration of AFM with optical detection technique is addressed. For AFMs with different type of forces monitoring (e.g. using independent detection of vertical and lateral forces by cantilever assembly with piezoresistive sensors, see Chui, B. W.; Kenny, T. W.; Mamin, H. J.; Terris, B. D.; Rugar, D. *Appl. Phys. Lett.* **1998**, *72*, 1388-1390) the calibration will rely on different approaches, not discussed here.
- 26 Bogdanovic, G.; Meurk, A.; Rutland, M. W. *Colloid Surf. B-Biointerf.* **2000**, *19*, 397-405.
- 27 Cain, R. G.; Biggs, S.; Page, N. W. *J. Colloid Interface Sci.* **2000**, *227*, 55-65.
- 28 Feiler, A.; Attard, P.; Larson, I. *Rev. Sci. Instrum.* **2000**, *71*, 2746-2750.
- 29 Liu, E.; Blanpain, B.; Celis, J. P. *Wear* **1996**, *192*, 141-150.
- 30 Lüthi, R.; Meyer, E.; Haefke, H.; Howald, L.; Gutmannsbauer, W.; Guggisberg, M.; Bammerlin, M.; Güntherodt, H. J. *Surf. Sci.* **1995**, *338*, 247-260.
- 31 Marti, O.; Colchero, J.; Mlynek, J. In *Nanosources and Manipulation of Atoms under High Fields and Temperatures: Applications*, Binh, V. T.; Garcia, N.; Dransfeld, K., Eds. Kluwer Academic Publishers: Dordrecht, 1993; p 253-269.
- 32 Meurk, A.; Larson, I.; Bergström, L. *Mat. Res. Soc. Symp. Proc.* **1998**, *522*, 427-432.
- 33 Neumeister, J. M.; Ducker, W. A. *Rev. Sci. Instrum.* **1994**, *65*, 2527-2531.
- 34 Noy, A.; Frisbie, C. D.; Rozsnyai, L. F.; Wrighton, M. S.; Lieber, C. M. *J. Am. Chem. Soc.* **1995**, *117*, 7943-7951.
- 35 Ogletree, D. F.; Carpick, R. W.; Salmeron, M. *Rev. Sci. Instrum.* **1996**, *67*, 3298-3306.
- 36 Sader, J. E. *Rev. Sci. Instrum.* **1995**, *66*, 4583-4587.
- 37 Schwarz, U. D.; Köster, P.; Wiesendanger, R. *Rev. Sci. Instrum.* **1996**, *67*, 2560-2567.
- 38 Varenberg, M.; Etsion, I.; Halperin, G. *Rev. Sci. Instrum.* **2003**, *74*, 3362-3367.
- 39 Sader, J. E. *Rev. Sci. Instrum.* **2003**, *74*, 2438-2443.
- 40 Buenviaje, C. K.; Ge, S. R.; Rafailovich, M. H.; Overney, R. M. *Mat. Res. Soc. Symp. Proc.* **1998**, *522*, 187-192.
- 41 Cleaning via subsequent sonification in acetone and methanol, rinsing with water and heating above 1000°C.
- 42 The mechanical properties are implicitly assumed to be isotropic, which is strictly speaking only correct for amorphous materials.
- 43 This assumption may not be appropriate for single crystalline materials, such as Si cantilevers. More complex tensor analysis will provide more accurate values of the spring constants.
- 44 Beer, F. P.; Johnston, E. R. *Mechanics of Materials*. McGraw-Hill: New York, 1981.
- 45 Landau, L. D.; Lifshitz, E. M. *Theory of Elasticity*. Pergamon Press: Oxford, 1986; Vol. 7.
- 46 Albrecht, T. R.; Akamine, S.; Carver, T. E.; Quate, C. F. *J. Vac. Sci. Technol. A-Vac. Surf. Films* **1990**, *8*, 3386-3396.
- 47 Sader, J. E.; White, L. *J. Appl. Phys.* **1993**, *74*, 1-9.
- 48 Warmack, R. J.; Zheng, X. Y.; Thundat, T.; Allison, D. P. *Rev. Sci. Instrum.* **1994**, *65*, 394-399.
- 49 Clifford, C. A.; Seah, M. P. *Nanotechnology* **2005**, *16*, 1666-1680.
- 50 Hazel, J. L.; Tsukruk, V. V. *Thin Solid Films* **1999**, *339*, 249-257.
- 51 Labardi, M.; Allegrini, M.; Salerno, M.; Frediani, C.; Ascoli, C. *Appl. Phys. A-Mater. Sci. Process.* **1994**, *59*, 3-10.
-

- 
- 52 Kieseewetter, L.; Zhang, J. M.; Houdeau, D.; Steckenborn, A. *Sens. Actuator A-Phys.* **1992**, *35*, 153-159.
- 53 Schneider, D.; Tucker, M. D. *Thin Solid Films* **1996**, *291*, 305-311.
- 54 Nonnenmacher, M.; Greschner, J.; Wolter, O.; Kassing, R. *J. Vac. Sci. Technol. B* **1991**, *9*, 1358-1362.
- 55 Gibson, C. T.; Weeks, B. L.; Abell, C.; Rayment, T.; Myhra, S. *Ultramicroscopy* **2003**, *97*, 113-118.
- 56 Sader, J. E.; Larson, I.; Mulvaney, P.; White, L. R. *Rev. Sci. Instrum.* **1995**, *66*, 3789-3798.
- 57 Putman, C.; Igarashi, M.; Kaneko, R. *Jpn. J. Appl. Phys. Part 2 - Lett.* **1995**, *34*, L264-L267.
- 58 Attard, P. *J. Adhes. Sci. Technol.* **2002**, *16*, 753-791.
- 59 see, e.g.: Overney R.M.; Takano H.; Fujihira M.; Paulus W.; Ringsdorf H.; *Phys. Rev. Lett.* **1994**, *72*, 3546-3549.
- 60 Vezenov, D. V.; Noy, A.; Lieber, C. M. *J. Adhes. Sci. Technol.* **2003**, *17*, 1385-1401.
- 61 Fujisawa, S.; Kishi, E.; Sugawara, Y.; Morita, S. *Appl. Phys. Lett.* **1995**, *66*, 526-528.
- 62 This approach may be highly inaccurate, if the tip-sample contact stiffness is not significantly larger than the lateral stiffness of the cantilever. Nonlinearity of the piezo may also lead to erroneous results.
- 63 Carpick, R. W.; Ogletree, D. F.; Salmeron, M. *Appl. Phys. Lett.* **1997**, *70*, 1548-1550.
- 64 Proksch, R.; Schaffer, T. E.; Cleveland, J. P.; Callahan, R. C.; Viani, M. B. *Nanotechnology* **2004**, *15*, 1344-1350.
- 65 D'Costa, N. P.; Hoh, J. H. *Rev. Sci. Instrum.* **1995**, *66*, 5096-5097.
- 66 Gibson, C. T.; Watson, G. S.; Myhra, S. *Wear* **1997**, *213*, 72-79.
- 67 Burnham, N. A.; Chen, X.; Hodges, C. S.; Matei, G. A.; Thoreson, E. J.; Roberts, C. J.; Davies, M. C.; Tendler, S. J. B. *Nanotechnology* **2003**, *14*, 1-6.
- 68 Carpick, R. W.; Salmeron, M. *Chem. Rev.* **1997**, *97*, 1163-1194.
- 69 These equations are applicable only for cantilevers with uniform thickness.
- 70 Compare the simplified and the real cantilever shapes in Appendix 3-2 and Figure 3-2, respectively.
- 71 The application of Si probes in nanotribology is often limited due to its insufficient wear-resistance.
- 72 Wortman, J. J.; Evans, R. A. *J. Appl. Phys.* **1965**, *36*, 153-156.
- 73 The values of Young's modulus in the [100], [110] and [111] directions are  $E[100] = 130$  GPa,  $E[110] = 168$  GPa, and  $E[111] = 187$  GPa, respectively (see reference 72).
- 74 The stability of the  $\text{Si}_3\text{N}_4$  cantilevers usually is much higher than Si cantilevers.
- 75 Data provided by the probe manufacturer.
- 76 Tortonese, M.; Kirk, M. *Proc. SPIE* **1997**, *3009*, 53-60.
- 77 Due to large errors in the calculated value of the normal spring constant as a result of differences in the cantilever thickness, this value may not be accurate.
- 78 This is not required if the wedge calibration method is used, and was done solely to characterize the best possible calibration using the two-step approach.
- 79 The observed significant differences in shapes and aspect ratios of reflected laser beams from various cantilevers are due to different shapes and sizes of the cantilever apex relative to the diameter of the laser beam at this position.
- 80 Ramirez-Aguilar, K. A.; Rowlen, K. L. *Langmuir* **1998**, *14*, 2562-2566.
- 81 Atamny, F.; Baiker, A. *Surf. Sci.* **1995**, *323*, L314-L318.
- 82 Montelius, L.; Tegenfeldt, J. O. *Appl. Phys. Lett.* **1993**, *62*, 2628-2630.
-

- 83 Montelius, L.; Tegenfeldt, J. O.; Vanheeren, P. *J. Vac. Sci. Technol. B* **1994**, *12*, 2222-2226.
- 84 Bao, G. W.; Li, S. F. Y. *Talanta* **1998**, *45*, 751-757.
- 85 Bykov, V.; Gologanov, A.; Shevyakov, V. *Appl. Phys. A-Mater. Sci. Process.* **1998**, *66*, 499-502.
- 86 Lantz, M. A.; O'Shea, S. J.; Welland, M. E.; Johnson, K. L. *Phys. Rev. B* **1997**, *55*, 10776-10785.
- 87 AFM topography images are always convoluted images in which the actual surface profile is convoluted with the shape of the probe tip utilized.
- 88 Markiewicz, P.; Goh, M. C. *J. Vac. Sci. Technol. B* **1995**, *13*, 1115-1118.
- 89 Markiewicz, P.; Goh, M. C. *Rev. Sci. Instrum.* **1995**, *66*, 3186-3190.
- 90 The differences in materials properties originate from the CVD fabrication process of the probes.
- 91 Salvadori, M. C.; Fritz, M. C.; Carraro, C.; Maboudian, R.; Monteiro, O. R.; Brown, I. G. *Diam. Relat. Mat.* **2001**, *10*, 2190-2194.
- 92 Blank, D. H. A.; Koster, G.; Rijnders, G.; van Setten, E.; Slycke, P.; Rogalla, H. *J. Cryst. Growth* **2000**, *211*, 98-105.
- 93 Andersson, J. M.; Czigany, Z.; Jin, P.; Helmersson, U. *J. Vac. Sci. Technol. A* **2004**, *22*, 117-121.
- 94 Jin, P.; Xu, G.; Tazawa, M.; Yoshimura, K.; Music, D.; Alami, J.; Helmersson, U. *J. Vac. Sci. Technol. A-Vac. Surf. Films* **2002**, *20*, 2134-2136.
- 95 [www.scioncorp.com](http://www.scioncorp.com), freeware: Scion Image Beta 4.02 for Windows 95 to XP.
- 96 Blank, D. H. A.; Rijnders, G.; Koster, G.; Rogalla, H. *J. Electroceram.* **2000**, *4*, 311-318.
- 97 Ladd, M. F. C.; Palmer, R. A. *Structure determination by X-ray crystallography*. Plenum Press: New York, 1993.

# Chapter 4

## Fabrication, validation and application of a new universal calibration specimen for the calibration of friction forces in AFM\*

*In this Chapter, a new calibration standard is introduced for a direct calibration method (the wedge calibration method, as originally introduced by Ogletree, Carpick, and Salmeron Rev. Sci. Instrum. 1996, 67, 3298 - 3306 and later improved by Varenberg, Etsion, and Halperin Rev. Sci. Instrum. 2003, 74, 3362-3367), which overcomes the limitations of the two-step friction force calibration procedures discussed in Chapter 3. The fabrication, validation and application of this new, universally applicable standard specimen that enables one to accurately calibrate all types of AFM cantilevers and tips for quantitative friction force measurements are reported. The Si(100) calibration standard, which exhibits 30 and 50  $\mu\text{m}$  wide notches with tilt angles  $\theta$  between  $20^\circ$  and  $35^\circ$  with respect to the wafer surface, was fabricated by focused ion beam (FIB) milling. The quantification of friction forces obtained on this universal standard specimen using the direct method was critically tested for various types of  $\text{Si}_3\text{N}_4$  integrated cantilever-tip assemblies. The error in the calibration factors obtained was found to be ca. 5%, which is a significant improvement compared to errors of 30 - 50% observed for the often applied two-step calibration procedures of cantilever lateral force constant and photodiode sensitivity (Chapter 3). As demonstrated for oxidized Si(100), thin films of poly(methyl methacrylate) (PMMA), and micropatterned self-assembled monolayers (SAMs) on gold, the calibration of various V-shaped and single beam cantilevers based on the application of the new universal standard in conjunction with the direct wedge method proposed, allows one to conveniently perform quantitative nanotribological measurements for a wide range of materials and applications.*

---

\* Parts of this work were published in the following article: Tocha, E.; Schönherr, H.; Vancso, G. J. *Langmuir* **2006**, *22*, 2340-2350.

## 4.1. Introduction

Various *single step procedures* have been reported in the literature, which overcome the limitations of the two-step friction force calibration procedures discussed in Chapter 3. These methods allow one to perform a direct calibration of friction forces.<sup>1-5</sup> One of these procedures is the application of a turning moment to a cantilever using an attached lever.<sup>1-3</sup> However, this approach is typically difficult to perform and can be considered very time consuming. As a viable alternative, Ogletree *et al.*<sup>4</sup> introduced the so-called wedge calibration method, which was later improved by Varenberg *et al.*,<sup>5</sup> who took the contribution of adhesion into account. In this Chapter the wedge calibration method is exclusively discussed, and will be denoted as *the direct method* in the following sections. A detailed description of the wedge calibration procedure can be found in Section 4.2.<sup>6</sup> This method is the only technique, which accounts for all the effects of the shape of the laser beam and its position on the cantilever, and is therefore the most commonly accepted method.

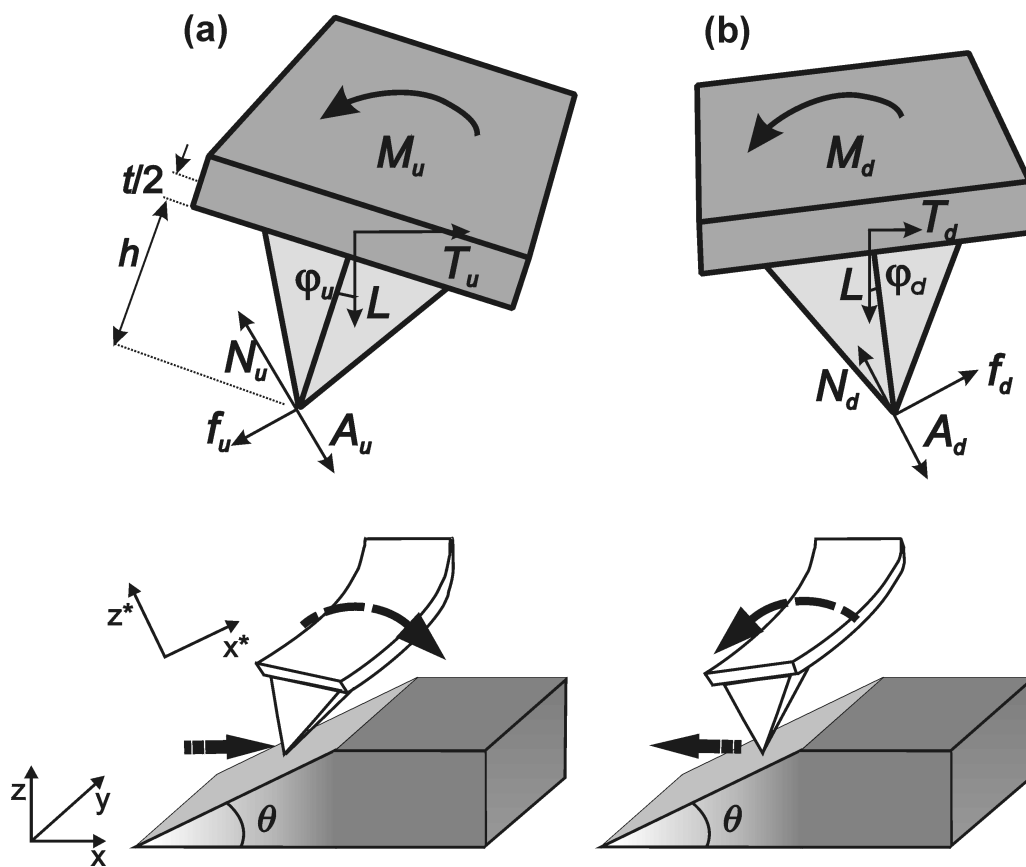
The wedge calibration method was demonstrated to provide access to truly quantitative nanotribological LFM data.<sup>7-9</sup> However, the originally proposed calibration standards (a specially treated SrTiO<sub>3</sub> (305)<sup>4,10</sup> specimen and a silicon calibration grating)<sup>5,11</sup> possess some limitations that restrict the applicability of the method. The SrTiO<sub>3</sub> specimens are suitable only for very sharp probes owing to the small dimensions of the exposed terraces (surfaces exposing (103) and (101) facets) with defined slopes (approx. 10 - 100 nm), while the silicon gratings provide reliable data solely for LFM tips with small cone angles due to the very high slope of the specimen surface ( $\theta = 54^{\circ}44'$ ). Hence for most applications these standards can be considered to be inadequate.

In this Chapter, the fabrication, validation and application of a new, universally applicable standard specimen that overcomes the mentioned limitations and enables one to calibrate all types of LFM probe cantilevers, are described. This calibration platform (specimen + method) thus renders the two-step procedure discussed in Chapter 3 obsolete. Critical tests of the platform regarding the re-positioning of the laser beam on the cantilever, laser spot asymmetry, additional sample tilt, the effect of the tip being located off the central axis of the cantilever, as well as the effect of different feedback loop settings are critically discussed. As shown for oxidized Si(100), thin films of poly(methyl methacrylate) (PMMA), and micropatterned self-assembled monolayers (SAMs) on gold, the calibration of various V-shaped and single beam cantilevers using the wedge method in conjunction with the new universal standard allows one to perform quantitative nanotribology for a wide range of materials and applications.



## 4.2. Wedge calibration method

In the wedge calibration method a cantilever is scanned across a calibration sample with two well-defined slopes (see Scheme 4-1). The friction signal is recorded as a function of the applied load. At a given load, friction and normal forces depend on the direction of motion. The forces applied to the tip on the surface (the applied load  $L$  and the horizontal tractive force  $T$ ), and the torsion momentum  $M$  must be balanced by the adhesion force  $A$  and a reaction force from the surface acting on the tip. This reaction force can be divided into two components, namely a friction force  $f$  parallel to the surface and a second component  $N$  normal to the surface. The subscripts  $u$  and  $d$  denote uphill and downhill scan directions, respectively.



Scheme 4-1. Schematic illustration of cantilever torsion while (a) sliding up and (b) sliding down on a sloped surface (in the  $x$  direction). When sliding across a sloped surface with angle  $\theta$ , the acting forces (applied load  $L$ , horizontal tractive force  $T$ , adhesion force  $A$ , the reaction force from the surface acting on the tip with a component  $N$  in the surface normal direction and a component  $f$  (friction force) parallel to the surface) and torsion momentum  $M$  are in equilibrium and depend on the direction of motion – uphill and downhill, denoted here with subscripts  $u$  and  $d$ , respectively.  $\varphi$  represents the torsion angle of the cantilever, which is proportional to the friction force.  $h$  and  $t$  stand for tip height and cantilever thickness, respectively.

For uphill motion (denoted with subscript  $u$ ) in the  $z^*-x^*$  coordinate we can write:

$$-T_u \sin \theta - L \cos \theta + N_u - A_u = 0 \quad (\text{Eq. 4-1})$$

$$T_u \cos \theta - L \sin \theta - f_u = 0 \quad (\text{Eq. 4-2})$$

Similarly, for the downhill motion (denoted with subscript  $d$ ) we can write:

$$-T_d \sin \theta - L \cos \theta + N_d - A_d = 0 \quad (\text{Eq. 4-3})$$

$$T_d \cos \theta - L \sin \theta + f_d = 0 \quad (\text{Eq. 4-4})$$

Assuming that  $A_u = A_d = A$  and  $f = \mu N$ , where the friction coefficient  $\mu$  is a constant, and that the tip height  $h$  is much larger than the radius of curvature of the tip  $r$  ( $h \gg r$ ), the torsion moment about the tip-surface contact can be expressed as:

$$M_u = T_u \left( h + \frac{t}{2} \right) = \frac{L \sin \theta + \mu(L \cos \theta + A)}{\cos \theta - \mu \sin \theta} \left( h + \frac{t}{2} \right) \quad (\text{Eq. 4-5})$$

and

$$M_d = T_d \left( h + \frac{t}{2} \right) = \frac{L \sin \theta - \mu(L \cos \theta + A)}{\cos \theta + \mu \sin \theta} \left( h + \frac{t}{2} \right) \quad (\text{Eq. 4-6})$$

In the wedge calibration method, the experimentally obtained voltage outputs of the torsion moments  $M_u^V$  and  $M_d^V$  (denoted with superscript  $V$ ) are converted to the corresponding forces  $T_u$  and  $T_d$  using  $T = \alpha M^V = M/(h+t/2)$ , where  $\alpha$  is the friction force calibration factor [nN/V]. This factor is calculated from the relations between measured lateral forces (half width of friction loop  $W^V = (M_u^V - M_d^V)/2$ ) and the friction loop offsets ( $\Delta^V = (M_u^V + M_d^V)/2$ ) for sloped and flat surfaces at a given load (Eq. 4-7 to 4-10). The subscripts  $s$  and  $f$  denote sloped and flat surfaces, respectively.

$$\frac{\mu_s (L + A \cos \theta)}{\cos^2 \theta - \mu_s^2 \sin^2 \theta} = \alpha W_s^V \quad (\text{Eq. 4-7})$$

$$\frac{\mu_s^2 \sin \theta (L \cos \theta + A) + L \sin \theta \cos \theta}{\cos^2 \theta - \mu_s^2 \sin^2 \theta} = \alpha (\Delta_s^V - \Delta_f^V) \quad (\text{Eq. 4-8})$$

$$\sin\theta(L \cos\theta + A) \cdot \mu_s^2 - \frac{\Delta_s^V - \Delta_f^V}{W_s^V} (L + A \cos\theta) \cdot \mu_s + L \sin\theta \cos\theta = 0 \quad (\text{Eq. 4-9})$$

$$\mu_f = \frac{\alpha W_f^V}{(L + A)} \quad (\text{Eq. 4-10})$$

By solving (Eq. 4-9) for  $\mu_s$ , two mathematical solutions are provided (for any given load and adhesion). When substituted into equation (Eq. 4-7) or (Eq. 4-8) these yield correspondingly two values of the friction calibration factor  $\alpha$ . Since  $\alpha$  must be identical for sloped and flat surfaces, we obtain  $\mu_f$  from equation (Eq. 4-10). The physical solution stands for  $\mu_s$ ,  $\mu_f < 1/\text{tg}\theta$ . A more detailed description of the wedge calibration procedure can be found in references 4 and 5.

### 4.3. Fabrication of the universal calibration specimen

The universal friction force calibration sample used in this study was fabricated by FIB in Si(100). As shown in Figure 4-1, the specimen contains several notches (30 and 50  $\mu\text{m}$  wide) with slopes of 20°, 25°, 30° and 35° with respect to the wafer surface. The slopes possess an accuracy of 0.5°, as revealed by AFM topography images (Figure 4-1(c)).

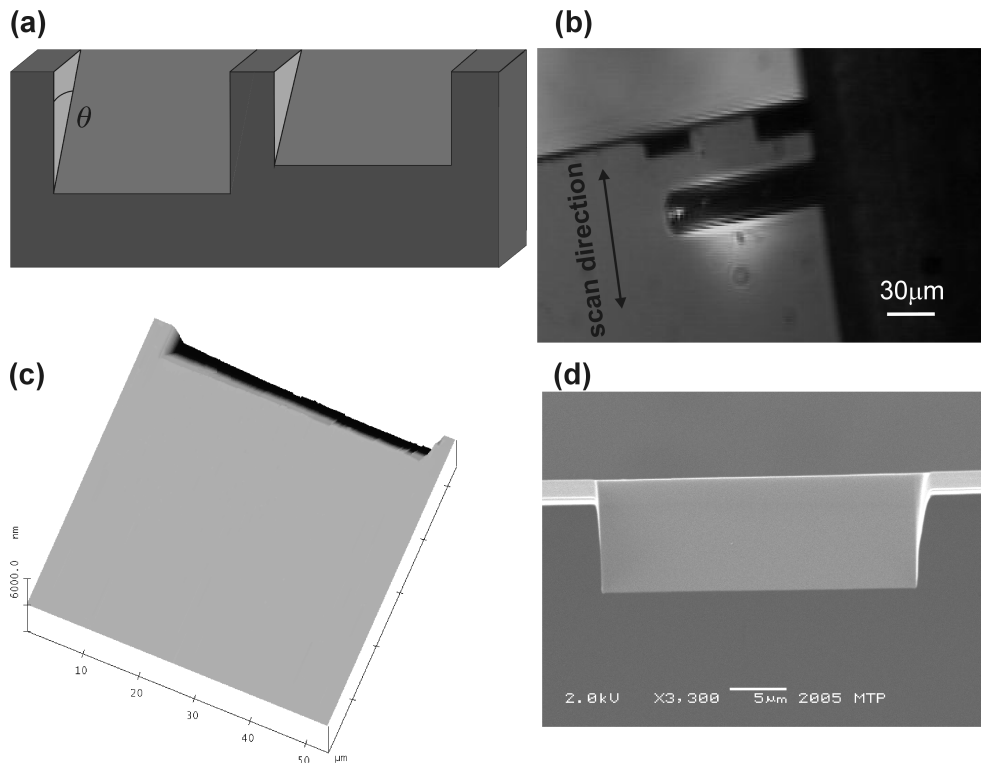


Figure 4-1. (a) Schematic of the lateral force calibration specimen fabricated using FIB milling (not to scale), (b) optical microscopy image of notches with  $\theta = 25^\circ$  and  $30^\circ$  (top view) with a single beam cantilever positioned below the notches, (c) AFM image of a notch with a tilt angle  $\theta = 20^\circ$  (notch width 50  $\mu\text{m}$ ), (d) SEM image (top view) of a notch with a tilt angle  $\theta = 30^\circ$  (notch width 30  $\mu\text{m}$ ).

The spacing and the size of the notches allow for convenient engagement of the LFM tip in the vicinity of a particular notch and the use of large tips, *e.g.* colloidal probe tips, respectively. As discussed in Chapter 3, one of the important criteria for quantitative friction measurements is the presence of a symmetrical tip-sample contact shape. Consequently, this criterion (the presence of a symmetrical tip-sample contact shape on flat and sloped surfaces) is also essential for the applicability of the calibration method discussed here. Hence, LFM probe tips with spherical or spherical conical profile can be utilized. This requirement may not be maintained on too steep surfaces, when the sum of the tip cone angle and surface slope angle is close to  $90^\circ$  (typical  $\text{Si}_3\text{N}_4$  cantilevers possess tips with cone angles of  $35^\circ$ ). Since  $\theta$  is limited  $\leq 35^\circ$  in the new universal standard, the lateral force calibration can be performed routinely for all types<sup>12</sup> of cantilevers with both integrated tips and colloidal probes due to the geometrical parameters of the specimen (large areas of sloped surfaces and low slope angles). Moreover, in contrast to, *e.g.*, the  $\text{SrTiO}_3$  standard mentioned above, the Si(100)-based calibration standard can be cleaned without any damage using several established methods, such as standard wafer cleaning, ultrasonic cleaning in solutions, treatment with strongly oxidizing media, such as “piranha” solution (see Section 4.8.1), or in an oxidizing plasma.

An example of experimental data of friction force calibration on the new specimen obtained by scanning both the sloped and the flat surface perpendicular to the main cantilever axis is shown in Figure 4-2. The white line in the topography image (Figure 4-2(a)) corresponds to the cross-sectional view shown in Figure 4-2(b). The raw friction data (friction loop) are presented in Figure 4-2(e). The horizontal line in the middle of the graph is associated with the zero value of the lateral photodiode difference output, whereas Figures 4-2(c) and 4-2(d) show the difference friction signal and friction loop off-sets, respectively, both for sloped ( $\Delta_s^V$ ) and flat ( $\Delta_f^V$ ) surfaces.

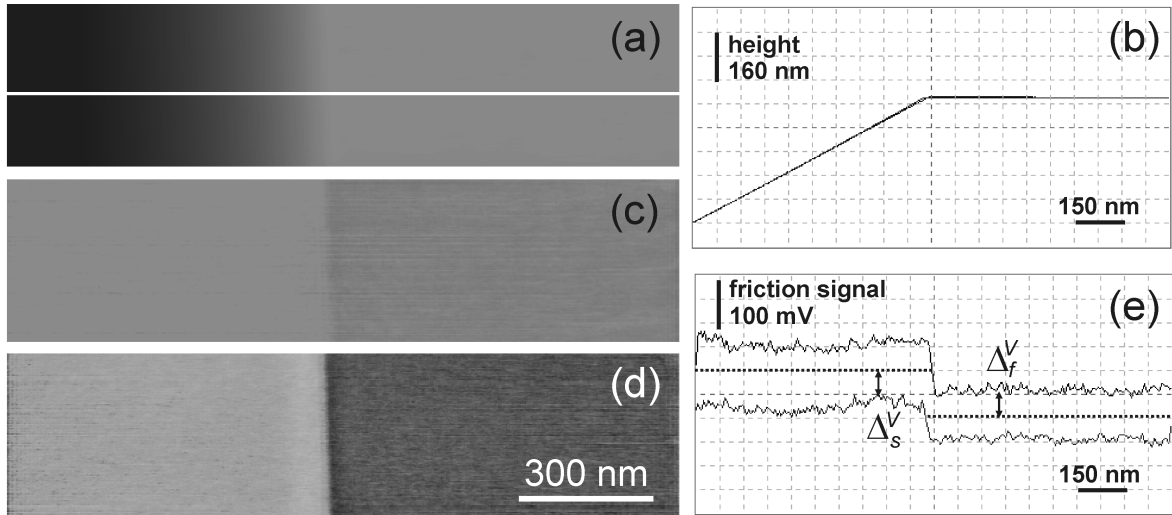


Figure 4-2. Example of experimental data measured with a  $\text{Si}_3\text{N}_4$  tip on both sloped and flat surfaces: (a) topography image (vertical scale from black to white 800 nm), (b) cross-section of topography (vertical scale 800 nm), (c) difference friction image (trace - retrace, vertical scale 0.5 V), (d) off-set of the friction loops (trace + retrace, vertical scale 0.5 V) and (e) friction loop corresponding to cross-section shown in panel (b) (the off-sets for sloped and flat surface,  $\Delta_s^V$  and  $\Delta_f^V$ , respectively, have been marked).

Using the procedure described in the Section 4.2, the calibration factor  $\alpha$  can be conveniently calculated. The largest source of error for the value of  $\alpha$  is the error in the value of the difference of the friction loop off-sets ( $\Delta_s^V - \Delta_f^V$ ), while  $W^V$  and  $A$  contribute only to a negligible extent to  $\delta\alpha$ . Assuming an unrealistically high error of 10% for  $\Delta_s^V - \Delta_f^V$  one can calculate an error of  $\alpha$  of 20%. A more realistic estimate yields an error similar to the observed statistical error of 5%, which is in agreement with the reported statistical error of the wedge method 5 – 10%.

Before discussing the effects of various factors that may affect the accuracy of the wedge calibration method using this universal standard, as well as some quantitative LFM data acquired on a range of relevant materials and systems, the approach is compared with the more traditional two-step calibration approach (described in Chapter 3).

#### 4.4. Comparison of the direct method and the two-step approach

Table 4-1 summarizes the results for the friction calibration factors determined for the V-shaped and single beam cantilevers using the direct (wedge) calibration method (using a notch of  $30^\circ$ ) and the two-step approach with individual normal and lateral cantilever spring constants and photodiode lateral sensitivities. The error analysis was performed as described in the Appendix 4.9.1.

Table 4-1. Comparison of the direct and the two-step calibration approaches for various V-shaped and single beam  $\text{Si}_3\text{N}_4$  cantilevers (normal and lateral spring constants of V-shaped cantilevers were calculated using the Sader method<sup>13</sup>). The errors of the experimentally determined and calculated quantities represent the standard deviation and the results of the corresponding error propagation, respectively.

	V-shaped <sup>*,13</sup>				Single beam <sup>**</sup>			
	A	B	C	D	E	F	G	H
$k_N$ reference lever [N/m]	$0.32 \pm 0.05$	$0.10 \pm 0.01$	$0.18 \pm 0.03$	$0.06 \pm 0.01$	$0.12 \pm 0.02$	$0.95 \pm 0.014$	$0.10 \pm 0.01$	$0.52 \pm 0.08$
$k_N$ calculated [N/m]	$0.31 \pm 0.12$	$0.11 \pm 0.04$	$0.20 \pm 0.08$	$0.05 \pm 0.02$	$0.12 \pm 0.09$	$0.97 \pm 0.73$	$0.06 \pm 0.05$	$0.51 \pm 0.38$
$k_L$ calculated [N/m]	$210 \pm 80$	$230 \pm 90$	$150 \pm 60$	$120 \pm 50$	$180 \pm 160$	$360 \pm 320$	$90 \pm 80$	$180 \pm 160$
$S_L$ [nm/V]	$1.60 \pm 0.24$	$1.60 \pm 0.24$	$1.60 \pm 0.24$	$1.40 \pm 0.21$	$0.82 \pm 0.12$	$0.93 \pm 0.14$	$0.51 \pm 0.08$	$0.55 \pm 0.08$
laser spot aspect ratio	$0.50 \pm 0.05$	$0.50 \pm 0.05$	$0.43 \pm 0.04$	$0.50 \pm 0.05$	$0.45 \pm 0.04$	$0.45 \pm 0.04$	$0.77 \pm 0.08$	$0.77 \pm 0.08$
$\alpha$ exp [nN/mV]	$0.25 \pm 0.03$	$0.08 \pm 0.01$	$0.18 \pm 0.03$	$0.08 \pm 0.01$	$0.25 \pm 0.03$	$0.79 \pm 0.09$	$0.10 \pm 0.01$	$0.21 \pm 0.01$
$\alpha$ cal [nN/mV]	$0.34 \pm 0.18$	$0.37 \pm 0.20$	$0.23 \pm 0.12$	$0.16 \pm 0.08$	$0.14 \pm 0.13$	$0.33 \pm 0.30$	$0.04 \pm 0.04$	$0.10 \pm 0.09$

\* $E=185\text{GPa}$ , \*\* $E=180\text{GPa}$

The friction calibration factors  $\alpha$  determined experimentally differ from the calculated ones, for both types of cantilevers, as shown in Figure 4-3.

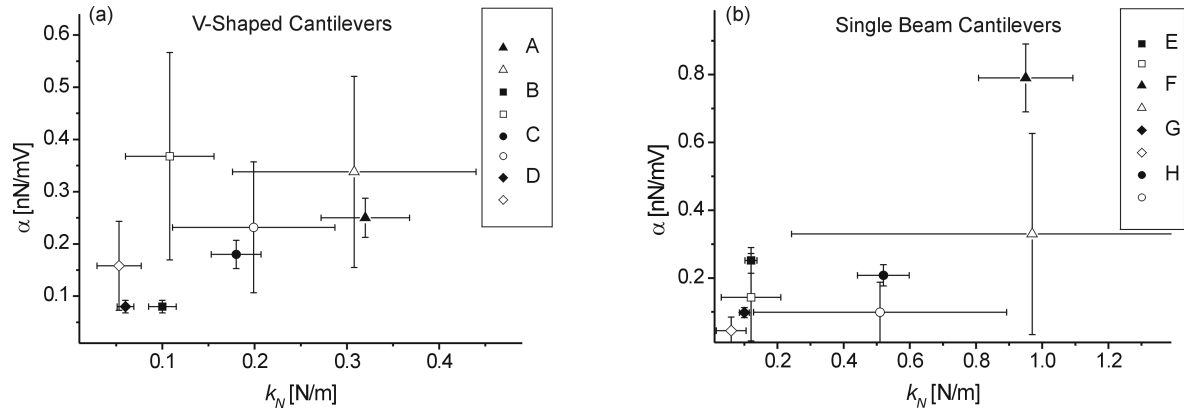


Figure 4-3. Comparison of friction calibration factors determined by the direct (solid symbols) and two-step methods (open symbols) for (a) V-shaped and (b) single beam  $\text{Si}_3\text{N}_4$  cantilevers.

Interestingly, there seems to be a trend that the calculated factors for V-shaped cantilevers are overestimated, whereas for single beam cantilevers the corresponding values are underestimated. This difference would lead to distinctive disagreement between results of measurements on a given sample carried out with cantilevers that possess different geometry, yet are calibrated using the ‘same’ two-step approach. Moreover, due to the uncertainty in the material properties,<sup>14-16</sup> the calculated spring constants  $k_L$  are loaded with large relative errors of 40 - 45% and 30 - 35% (assuming uniform thickness) for V-shaped and single beam cantilevers, respectively. For non-uniform thicknesses of the cantilevers (see Chapter 3) the relative errors can exceed 75 - 90% for single beam cantilevers.

In addition to the inherent errors in the calculated value of  $k_L$ , the lateral photodiode sensitivity  $S_L$ , which is very sensitive to laser intensity fluctuations, interference effects, the position of the laser beam on the cantilever apex, and the thermal stability of the AFM set up, are additional significant sources of error in the two-step calibration approach. Therefore, the final friction calibration factors  $\alpha_i$  cannot be obtained with high accuracy according to this two-step procedure; relative errors  $\delta\alpha_i$  are 45 - 50% and 35 - 40% for V-shaped and single beam cantilevers, respectively. By contrast, the wedge calibration method affords the friction calibration factors with errors of *ca.* 5%. Therefore, the direct method is superior to the two-step method, as discussed above, to provide access to *quantitative* friction forces.

#### 4.5. Discussion of the factors that affect the direct wedge calibration method

Following the discussion of the errors associated with the two-step procedure (see Chapter 3, Section 3.3) and the relatively low error of the wedge calibration method using the new

universally applicable standard, we discuss in the following sections possible factors that may interfere with an accurate calibration using this direct method.

#### 4.5.1. Wedge calibration on differently sloped surfaces

To exclude any possible effect of different slopes (*i.e.* different angles  $\theta$ ) on the calibration factor  $\alpha$ , friction calibration factors  $\alpha(\theta)$  were determined for one of the V-shaped cantilevers by performing experiments with tilt angles  $\theta$  between  $20^\circ$  and  $35^\circ$  for a large spectrum of applied loads. The laser light position on the cantilever was not changed during these experiments. The values of  $\alpha(\theta)$  obtained for different  $\theta$  were identical to within the statistical error of 10% (see Figure 4-4 and error analysis in the Appendix 4.9.1).

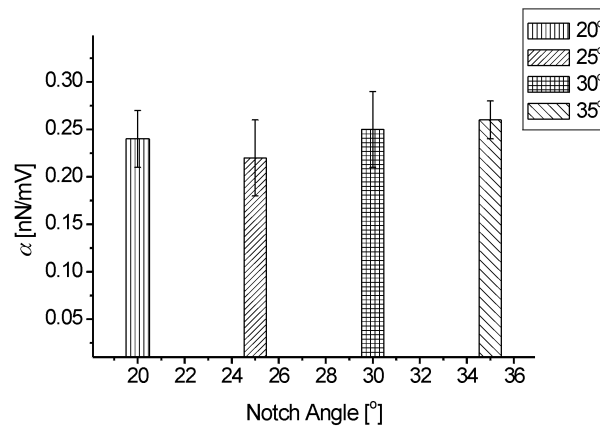


Figure 4-4. Calibration factors of a V-shaped  $\text{Si}_3\text{N}_4$  cantilever ( $k_N = 0.32 \pm 0.05$ ) obtained on notches with different angles.

Reliable calibration factors were obtained for applied loads that exceeded the value of the mean pull-off force by 2 - 3 times. For lower forces significant deviations of  $\alpha$  were observed, while for sufficiently high loads the calibration factors were found to be independent of the applied load (see Figure 4-5). The deviation at low loads may be related to small, not accurately measurable differences in the friction loop off-sets between the sloped and flat surfaces, which possess a large impact on the values of the resulting factors  $\alpha$ .



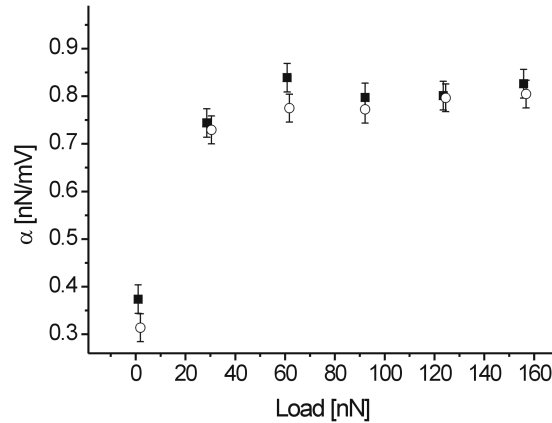


Figure 4-5. Calibration factor  $\alpha$  as a function of applied load obtained for a single beam  $\text{Si}_3\text{N}_4$  cantilever ( $k_N = 0.95 \pm 0.014$ ). For lower forces significant deviations of  $\alpha$  were observed, while for sufficiently high loads the calibration factors were found to be independent of the applied load. The deviation at low loads may be related to small, not accurately measurable, differences in the friction loop off-sets between the sloped and flat surfaces, which possess a large impact on the resulting factors  $\alpha$ .

Individual lateral force signals (trace and retrace) may be convoluted with topography information.<sup>17-20</sup> In addition, they contain signals due to electronic noise, laser intensity fluctuations, laser interference, environmental changes (temperature and relative humidity),<sup>19</sup> and cross-talks effects.<sup>21-24</sup> These signals that all contribute to the lateral signal may vary from scan line to scan line, and may depend on load. By subtracting the corresponding trace and retrace lateral signals, the impact of the factors may be canceled in the difference friction signal. Except for the effect of interference, which will be discussed separately below, the signals will affect primarily the friction loop offsets  $\Delta_s^V$  and  $\Delta_f^V$ , albeit in a similar way. In the wedge calibration method the difference of the friction loop offsets is used ( $\Delta_s^V - \Delta_f^V$ ). Therefore, the signals do not affect the calibration factors, unless the offset difference is very small (applied load close to zero).<sup>25</sup>

#### 4.5.2. Effect of laser light interference

To assess the effect of laser light interference on the accuracy of the calibration procedure, the calibration was performed using three different optical heads that possess lasers with different characteristics. Two of the optical heads are equipped with lasers and optics that exhibit poorer characteristics in terms of intensity, shape and size of the laser beam. Therefore, only a fraction of the incident laser light is reflected off the backside of the cantilever, the other fraction is reflected off the sample surface. Superposition of the reflected light results in interference.<sup>26</sup>

The optical interference was observed more frequently on the sloped surfaces, whereas on the flat surfaces it was usually insignificant. While this effect is subtracted from the difference friction signal, the offset  $\Delta_s^V$  is substantially affected. In our experiment  $\Delta_s^V$  was not a constant value, as normally expected. Instead,  $\Delta_s^V$  was found to vary with the actual tip position on the sloped surface during scanning (see Figure 4-6). The laser with better characteristics did not give rise to significant optical interference effects and thus  $\Delta_s^V$  was a constant value (Figure 4-2).<sup>27</sup> Consequently, the direct calibration procedure discussed in this paper may not be applicable for AFM systems that suffer from laser optics with poor characteristics. However, it should be noted that the difference friction signal (trace – retrace) is *not* affected by the laser interference effect in this case (compare with Figure 4-2(c)).

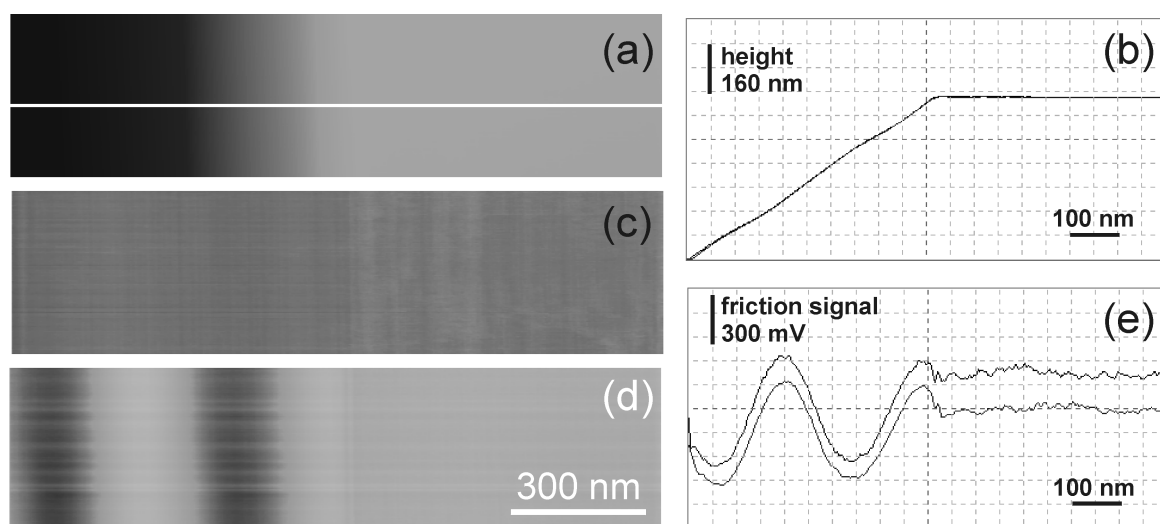


Figure 4-6. Effect of laser beam interference on friction signals measured on both sloped and flat surfaces: (a) topography image (vertical scale 800 nm), (b) cross-section of topography (vertical scale 800 nm), (c) difference friction image (trace - retrace, vertical scale 1.5 V), (d) off-set of the friction loops (trace + retrace, vertical scale 1.5 V) and (e) corresponding friction loop, the off-sets for sloped and flat surface. Strong interference is observed on the sloped surface (in panel (d)), whereas on the flat area the interference is insignificant.

#### 4.5.3. Tip position relative to the cantilever's main axis

Many of the V-shaped  $\text{Si}_3\text{N}_4$  cantilevers possess integrated tips that are, due to alignment problems during the fabrication process, located off the central axis of the cantilever (see Figure 4-7(a) and (b)). It is easy to see that this will be the source of coupling between normal and lateral signals.<sup>4,28,29</sup> In the rest position, an additional momentum (torque) will occur, which is a linear function of the applied load. In the difference friction signal the momentum is subtracted and thus no effect is observed. Similarly, the momentum cancels from the friction loop offsets

calculated in the wedge calibration procedure, as equal momentum will occur due to the tip's off center location, when performing the calibration on both sloped and flat surfaces. No effect of the tip position (for up to 1.5  $\mu\text{m}$  off center position) on the calibration factors was observed in our procedure described, *i.e.* the coupling between the normal and lateral forces was insignificant. However, in the case of strong coupling, as expected for very rough samples and measurements performed under high loads, normal and lateral signals may be affected, as well as the calibration factor.

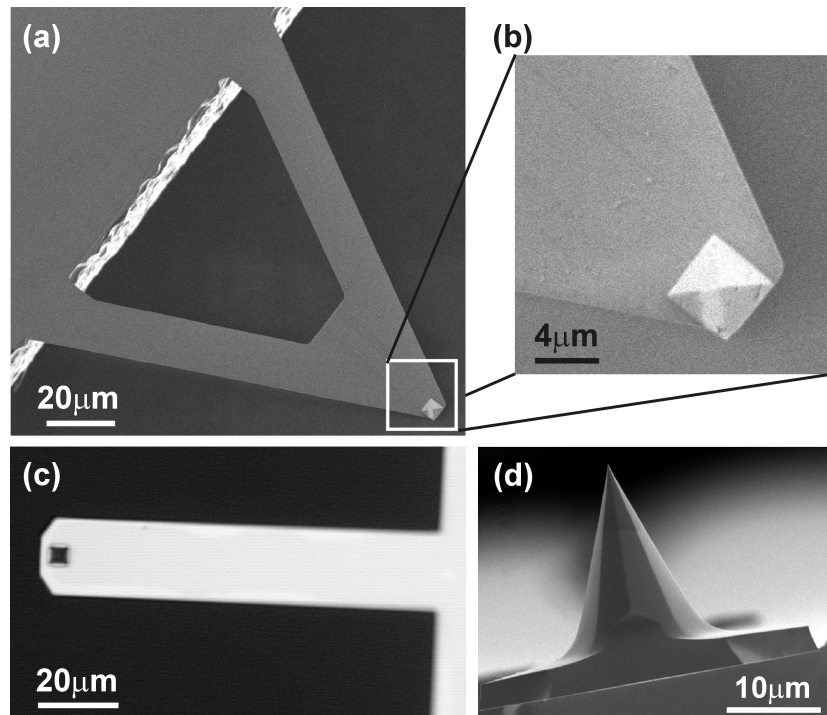


Figure 4-7. SEM images of AFM cantilever-tip assemblies: (a) V-shaped  $\text{Si}_3\text{N}_4$  cantilever with the tip located off the central cantilever axis, (b) close view of the tip from image (a), and single beam (c)  $\text{Si}_3\text{N}_4$  and (d) Si cantilevers with the tips located on the central cantilever axis, respectively. The single beam cantilevers studied here did not show misalignment problems.

#### 4.5.4. Tips with flat apex

Depending on the tip material, the analyzed sample characteristics and the scanning conditions, wear of the AFM tip may occur. To assess the impact of worn tips (with a flattened apex) on the calibration factors, intentionally worn tips with flattened apex were calibrated (Figure 4-8). In this case, the contacting surfaces on the flat and sloped areas of the calibration standard were significantly different (smaller on sloped surface as compared to the flat surface). Therefore, the measured friction loop exhibited a lower value of the half width of friction loop on the sloped surface compared to the flat surface. For a symmetrical apex, *e.g.* spherical tip apex, the opposite was observed (*vide supra*). Moreover, an additional load-dependent momentum is

present in case of a flattened apex, which is *not* subtracted in the calibration procedure. Consequently, the friction coefficients on the sloped and the flat areas  $\mu_s$  and  $\mu_f$ , respectively, obtained from this experimental data will be significantly different due to the contact area difference and the presence of the additional momentum ( $\mu_s > \mu_f$ ). Hence, in this case, the calibration factors obtained will not be reliable.

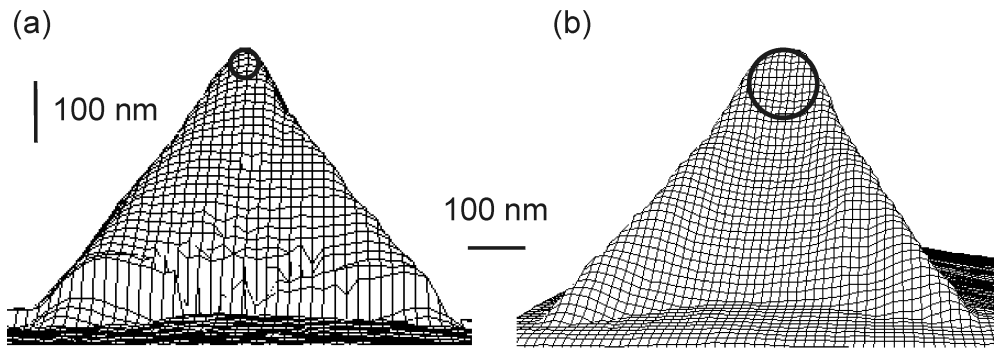


Figure 4-8. Images (obtained by AFM using a calibration grating) of (a) a sharp and (b) a flat tip apex. The tip radii  $r$  determined for (a) and (b) were 25 nm and 60 nm, respectively.

#### 4.5.5. Additional sample tilt

Depending on the design of the AFM, some of the instruments do not possess the option of vertical engagement. Thus an additional sample tilt may be present. This tilt may, in principle, affect the values of the determined calibration factors. Therefore, an experiment of a cantilever calibration on the sample with an added tilt angle of  $+\beta$  and  $-\beta$  was performed. Consequently, the sloped (e.g.  $30^\circ$ ) and flat surfaces had tilt angles of  $(30 + \beta)^\circ$  and  $\beta^\circ$ ,  $(30 - \beta)^\circ$  and  $-\beta^\circ$ , respectively. The applied angle  $\pm \beta$  was in the range  $10 - 15^\circ$ . The friction calibration factors obtained in this experiment were similar to those determined in the absence of the additional tilt to within the error of 20% (Figure 4-9). However, for high accuracy calibration a small sample tilt is required (below  $5^\circ$ ). In all other cases the effect may be eliminated using equations (3) and (4) extended for two differently sloped calibration wedges (Eq. 4-11 to 4-16, Appendix 4.9.2).

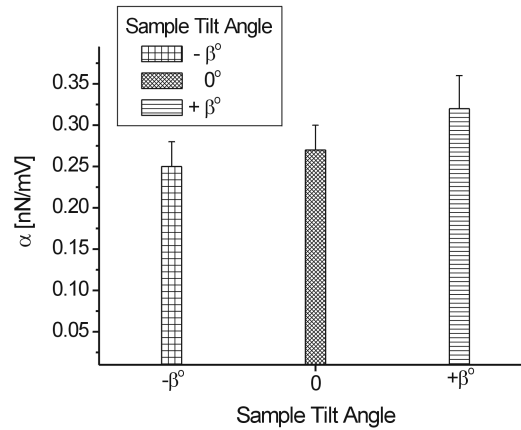


Figure 4-9. Effect of additional sample tilt ( $\beta \sim 10 - 15^\circ$ ) on the calibration factor.

#### 4.5.6. Different feedback settings

It is known that high values of the gain settings of the feedback loop may cause the scanner to oscillate. These oscillations can reduce the measured frictional forces significantly, even without showing up in the deflection and the height signals.<sup>30</sup> An experiment revealing this effect was carried out with gain values below the critical value above which an oscillatory signal was observed. The calibration procedure was performed using different integral (IG) and proportional (PG) gains settings, presented here in arbitrary units: (a) IG = 2, PG = 4, (b) IG = 4, PG = 8, and (c) IG = 6, PG = 12. The calibration factors obtained for the experiments had the same values and did not show any influence of the used range of gains, thus an effect of these on the calibration can be excluded.

#### 4.5.7. Repositioning of the laser beam on the cantilever

It has been shown that both normal and lateral forces strongly depend on the position of the laser beam on the cantilever beam, which determines the measured deflection and torsion angles of the cantilever, as well as the shape and symmetry of the reflected laser beam.<sup>30-33</sup> In a test experiment, the friction calibration factors were determined for the same cantilever before and after re-positioning of the laser beam (four different positions of the laser beam on the cantilever apex and one with the beam moved from the cantilever apex towards its base). The values of the factors  $\alpha$ ,  $\mu$  and  $S_N$  obtained were compared for various laser positions (see Figure 4-10). We observed variations between the calibration factors within the statistical error (5%) for the spot position at the cantilever apex. Only for laser beam positions near the cantilever base,  $\alpha$  and  $S_N$  were found to be significantly higher. Moreover, for all measurements the value of  $\mu$  was similar, indicating that an accurate calibration can still be carried out. However, this result

depends on a reproducible, precise alignment of the laser on the cantilever apex. Poor alignment (see Chapter 3, Figure 3-3) may cause artifacts in recorded friction forces and their calibration.

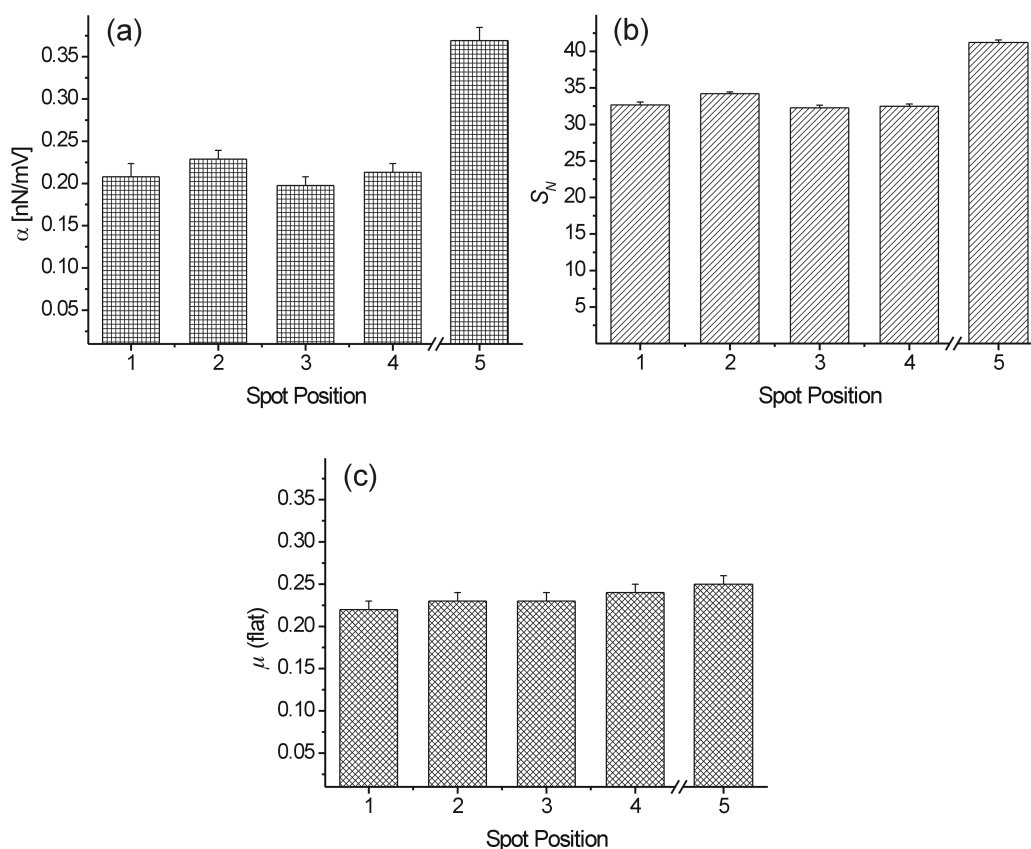


Figure 4-10. Effect of the re-positioning of the laser beam on a single beam cantilever ( $k_N = 0.52 \pm 0.08$ ; spot position 1-4: different positions of the laser spot on the cantilever apex; spot position 5: the beam was moved from the cantilever apex towards its base). (a)  $\alpha$ , (b)  $S_N$ , and (c)  $\mu$  as a function of spot position. A discrepancy up to 5% between the calibration factors was obtained for differently adjusted, yet nominally identical spot positions on the cantilever apex. Only for the laser spot position nearer to the cantilever base (position 5), the values of  $\alpha$  and  $S_N$  were significantly higher. Moreover, for all measurements the value of  $\mu$  was similar, indicating that the position of the laser beam is accounted for in the calibration method.

#### 4.6. Experimental results for nanotribology on Si(100), PMMA and micropatterned SAMs

To demonstrate that the direct wedge calibration method, in conjunction with the new universal standard, allows one to perform quantitative nanotribology for a wide range of materials and applications, the nanotribological properties of various systems were characterized by LFM. The

measurements of friction forces were carried out as a function of normal forces in the elastic contact regime using  $\text{Si}_3\text{N}_4$  as a probe (tip) material.

Figure 4-11 shows the dependence of friction forces vs. normal forces for (a) a PMMA film and (b) oxidized Si(100). The measurements were performed using the same probe tip in 10% RH with a scan velocity of  $6.6 \mu\text{m/s}$ . The friction and normal forces were calibrated after the nanotribological analysis.

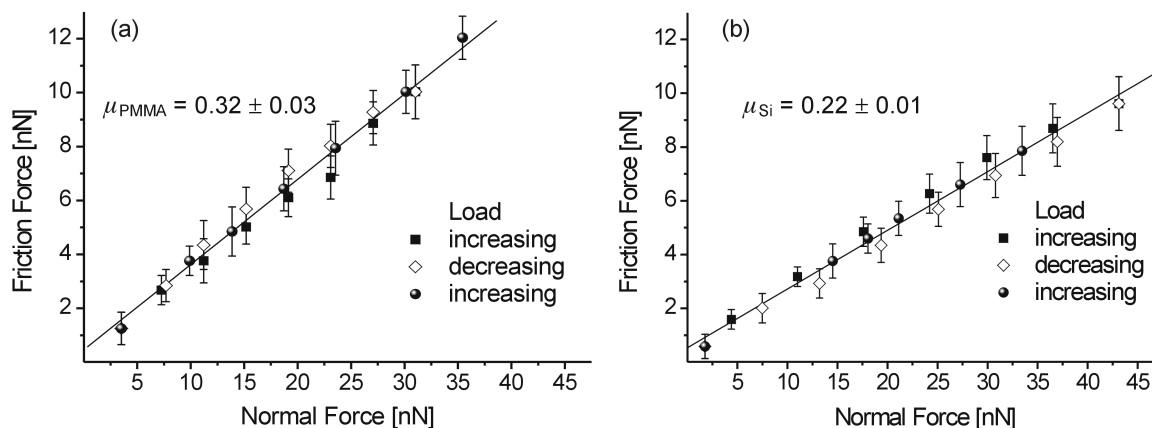


Figure 4-11. Friction force versus normal force for (a) PMMA film (thickness  $125 \pm 5 \text{ nm}$ ) on oxidized Si(100) substrate and (b) oxidized Si(100) measured using the same  $\text{Si}_3\text{N}_4$  tip (scanning velocity  $6.6 \mu\text{m/s}$ ; 10% RH;  $25^\circ\text{C}$ ). The solid lines correspond to linear least squares fits. The error bars indicate the standard deviation ( $n = 128$ ) of the data analyzed for a given normal force.

A linear increase of the friction force signal with increasing normal forces was observed for both tribosystems. There was no detectable hysteresis for data acquired with increasing and decreasing loads, respectively. The friction coefficients, determined from the slopes of linear least squares fits, were  $0.32 \pm 0.03$  and  $0.22 \pm 0.01$  for PMMA and Si(100) samples, respectively. Compared to PMMA films, a reduction of friction forces, as well as friction coefficient, was observed for the oxidized Si(100). The results for the PMMA sample very well correspond to the literature values of macroscopic friction coefficient ( $\mu(\text{PMMA}) = 0.2 - 0.5$ ),<sup>34-39</sup> obtained for various counter bodies and environmental conditions. Also the values of friction coefficient determined for Si(100) are in agreement with previous studies.<sup>40,41</sup>

Finally, two  $\text{Si}_3\text{N}_4$  probes with different cantilever geometry were used for the nanotribological analysis of a micropatterned binary SAM that exposed hydrophilic and hydrophobic headgroups ( $-\text{COOH}$  and  $-\text{CH}_3$ , respectively). The measurements shown in Figures 4-12 and 4-13 were

carried out in controlled environment (50% RH and 25°C). The circular carboxylic acid terminated areas of the micropatterned SAM are clearly recognized as high friction areas in the LFM difference images in Figure 4-12.<sup>42-47</sup>

The effect of increasing load on the contrast in this two component SAM is obvious. With increasing load, the difference friction images show higher contrast between -COOH and -CH<sub>3</sub> head groups. The corresponding friction force distributions reveal that both the difference between the mean friction forces, as well as the peak widths, increase with higher applied force.

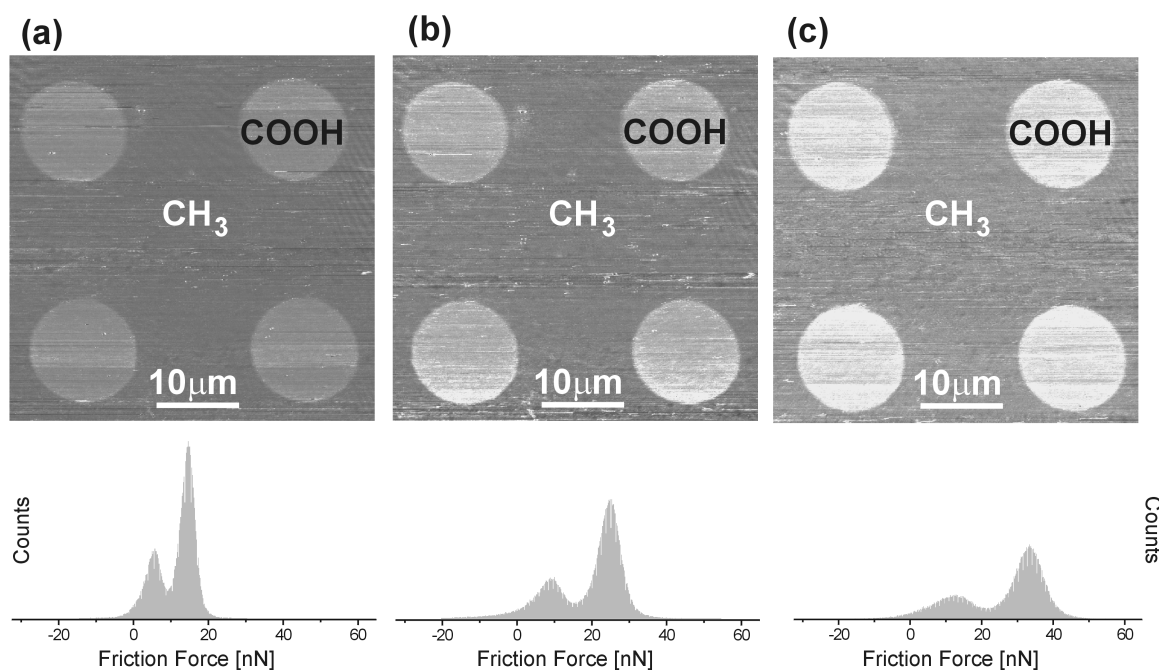


Figure 4-12. Difference friction images and corresponding friction force distribution of binary SAM measured with a Si<sub>3</sub>N<sub>4</sub> tip (single beam cantilever) for different applied loads: (a) 5 nN, (b) 18 nN and (c) 30 nN. Bright and dark colors correspond to high and low friction forces and are attributed to -COOH and -CH<sub>3</sub> headgroups, respectively. The sample was scanned with velocity of 200 μm/s at 50% RH and 25°C.

This observation is due to a significantly higher friction coefficient of the hydrophilic areas compared to the hydrophobic areas. Figure 4-13 shows the friction force as function of load obtained with (a) a V-shaped and (b) a single beam cantilever. The pull-off force for -COOH and -CH<sub>3</sub> groups were 21 nN and 14 nN measured with the V-shaped cantilever and 15 nN and 9 nN measured with the single beam cantilever, respectively. The ratio between the pull-off forces for hydrophobic and hydrophilic groups was about 0.6 for both probes, consistent with the different surface energies and the resulting capillary forces.<sup>48-50</sup>



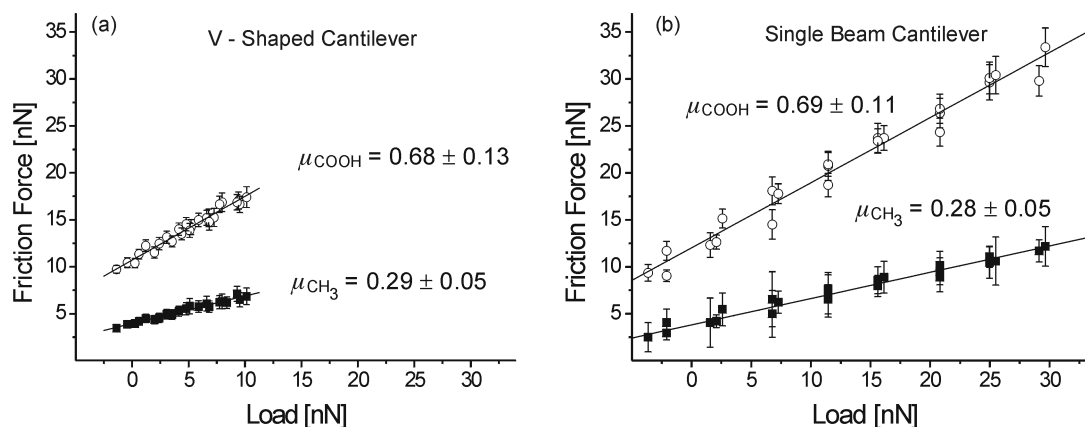


Figure 4-13. Friction force versus load for a micropatterned SAM sample (exposing  $-\text{CH}_3$  and  $-\text{COOH}$  headgroups, respectively) measured using two different  $\text{Si}_3\text{N}_4$  cantilevers: (a) V-shaped and (b) single beam, with scanning velocity of  $40 \mu\text{m/s}$  at 50% RH and  $25^\circ\text{C}$ . The solid lines correspond to linear least squares fits. The error bars indicate the standard deviation ( $n = 128$ ) of the data analyzed for a given load.

The friction coefficients determined with the two cantilever probes with different geometry were identical to within the error ( $\mu_{\text{Si}_3\text{N}_4}(\text{CH}_3) = 0.29 \pm 0.05$  and  $0.28 \pm 0.05$  and  $\mu_{\text{Si}_3\text{N}_4}(\text{COOH}) = 0.68 \pm 0.13$  and  $0.69 \pm 0.11$ , using V-shaped and single beam cantilevers, respectively). Green *et al.*<sup>46</sup> reported similar values of friction coefficients ( $\mu_{\text{Si}_3\text{N}_4}(\text{CH}_3) = 0.34$  and  $\mu_{\text{Si}_3\text{N}_4}(\text{COOH}) = 0.76$ ), which are comparable with microscopic results obtained with zirconia balls ( $\mu(\text{CH}_3) = 0.2 - 0.4$ ).<sup>51</sup>

The results discussed above show that the wedge calibration method in conjunction with the new universal calibration specimen enables one to perform truly quantitative nanotribology. This calibration approach is a convenient, yet robust and precise, method and can be expected to open the pathway to improved fundamental LFM work in the area of tribology. In addition, it allows an improved quantitative compositional mapping and imaging in nanoscience and nanotechnology-related surface characterization (see Chapters 6 and 8) and quantitative comparisons between nano- and microtribology (see Chapter 7).

#### 4.7. Conclusions

A new universal calibration standard was fabricated that allows one to calibrate all types of LFM probe cantilevers *independent* of cantilever geometry and tip radius using the direct wedge calibration method. Compared to friction force calibration factors calculated using standard methods for various V-shaped and single beam cantilevers with errors in excess of 40%, this

direct approach allows one to calculate the calibration factors with an error of *ca.* 5%. As shown, the approach is not affected by an additional small sample tilt, different feedback settings, and a possible tip position off the central cantilever axis. Only laser light interference and non-spherical tip apex shapes must be taken into account. The calibration of V-shaped and single beam cantilevers using the direct wedge calibration method in conjunction with the new universal standard showed *quantitatively identical* results on micropatterned SAMs. Hence it can be concluded that this calibration platform allows one to perform truly quantitative nanotribology for a wide range of materials and applications (see Chapters 6-8), as also demonstrated in this Chapter for oxidized Si(100), thin films of poly(methyl methacrylate), and micropatterned binary self-assembled monolayers on gold.

## 4.8. Experimental

### 4.8.1. Materials and sample preparation

All chemicals were used as received, unless otherwise stated. 16-Mercaptohexadecanoic acid (MHDA,  $\text{HS}(\text{CH}_2)_{15}\text{COOH}$ ), octadecanethiol (ODT,  $\text{CH}_3(\text{CH}_2)_{17}\text{SH}$ ) were purchased from Aldrich, all solvents were purchased from Biosolve. Bare Si(100) wafers with native oxide layer (P/Boron type, thickness  $525 \pm 25\mu\text{m}$ , Okmetic Oyj, Vantaa, Finland) were cleaned prior to the measurements by rinsing thoroughly with chloroform and ethanol, followed by an oxygen-plasma treatment (30 mA, 60 mTorr) using a Plasma Prep II plasma cleaner (SPI Supplies, West Chester, PA) for 10 min. Films of poly(methyl methacrylate) (PMMA, Aldrich,  $M_w = 120\,000$  g/mol) were prepared by spin coating filtered solutions in toluene (conc. 5 wt-%) onto freshly cleaned oxidized Si(100) substrates (Spin Coater P6700, Specialty Coating Systems, Indianapolis, IN). Films were annealed at  $150^\circ\text{C}$  under vacuum for 12 hours.

Micro-contact printed self-assembled monolayers (SAMs) on Au substrates (Metallhandel Schröder GmbH, Lienen, Germany) were prepared by In Yee Phang (Department of Materials Science and Technology of Polymers, University of Twente) according to published procedures.<sup>52</sup> The Au substrates were cleaned in piranha solution (7:3 mixture of concentrated  $\text{H}_2\text{SO}_4$  and 30%  $\text{H}_2\text{O}_2$ ) [*CAUTION! Piranha solutions should be handled with great care in open containers in a fume hood. Piranha is highly corrosive and toxic and potentially explosive.*], followed by rinsing with Milli-Q water. ODT was applied during 60 s using a PDMS stamp (pattern of circular depressions in square geometry; circles: 15  $\mu\text{m}$  diameter with 30  $\mu\text{m}$  center-to-center distance). The patterned SAM obtained was rinsed with ethanol, water and dried in a  $\text{N}_2$  stream. The un-patterned area was backfilled with MHDA by immersion into

an ethanolic solution of MHDA, followed by rinsing with ethanol, water and drying in a N<sub>2</sub> stream.

#### 4.8.2. Fabrication of the universal calibration specimen

The calibration specimen was fabricated in Si(100) using focused ion beam (FIB) milling (NOVA-500, FEI Company, Eindhoven, The Netherlands) (Ga ions, 6.5 nA, 30 kV, beam size 30 μm x 7 μm). A freshly cleaned piece of Si(100) wafer (10 mm x 5 mm) was mounted in the FIB machine with angles of 20°, 25°, 30° and 35° (relative to the wafer surface) with respect to the incident beam. The milling was carried on until the entire material was removed from the beam path. Therefore notches with the specified angles and widths of 30 - 50 μm were obtained (Figure 4-1).

#### 4.8.3. Calibration procedures

The friction force calibration was performed using the wedge approach<sup>4,5</sup> on the newly fabricated universal calibration standard using a NanoScope IIIa (Digital Instruments/Veeco, Santa Barbara, CA) atomic force microscope equipped with a CCD camera. Several V-shaped (Model NP, Veeco Nano Probe, Santa Barbara, CA) and single beam (OMCL-RC800PSA series, Olympus, Tokyo, Japan) Si<sub>3</sub>N<sub>4</sub> cantilevers were tested under different conditions. For each cantilever and particular experiment, friction force data were acquired without changing the laser light position on the cantilever. The data were recorded in the form of images of difference photodiode output signal for trace and retrace (512 × 128 pixels; scan size 2000 nm x 500 nm; slow scan axis disabled; scan velocity 8 μm/s) simultaneously on the sloped, as well as on the flat, areas of the specimen for different externally applied loads (see Figure 4-2, section 4.3). The range of applied loads varied from near zero to 2 - 3 times exceeding the pull-off force. The scanner hysteresis between trace and retrace was corrected using the AFM software. The mean friction forces and mean friction loop offsets for the sloped and the flat surfaces were determined for each applied load from an analysis of the difference and sum images, respectively. The values of the normal spring constants  $k_N$  and tip radii were individually calibrated using the reference lever method<sup>53,54</sup> and a calibration grating (silicon grating TGT1, NT-MDT, Moscow, Russia), respectively.

#### 4.8.4. Lateral force measurements

Quantitative friction analyses on clean Si(100), freshly prepared PMMA films and micropatterned SAM samples were carried out using different V-shaped and single beam Si<sub>3</sub>N<sub>4</sub>

probes. Prior to the measurements the probes were cleaned by immersion in and rinsing with chloroform followed by drying in a stream of nitrogen. Friction data were acquired from images of difference photodiode output signal (simultaneously for trace and retrace) for different normal forces. The normal force is defined as the sum of pull-off force and externally applied load. The relative humidity (%RH) was precisely controlled (10% RH for Si(100) and PMMA, 50% RH for micropatterned SAMs) using mixtures of wet and dry N<sub>2</sub>, as measured by a humidity sensor (SHT15, Sensirion, Switzerland), while the temperature was maintained constant during all measurements (25°C). The calibration of the cantilevers was performed following completion of the measurements to avoid contamination of the probes.

## 4.9. Appendix

### 4.9.1. Error analysis for the wedge calibration method

The error of the experimental calibration factor was calculated from a statistical analysis of 5 - 8 measurements for different applied loads. For the analysis, only  $\alpha$  for higher loads were used, since these were independent of load (see Figure 4-5, section 4.5.1). Usually, the statistical error was in range of 5 - 15%. The range strongly depends on the instrument stability (laser beam stability, thermal equilibration, and electronic noise). These factors that all contribute to the lateral signal may depend on load. The variations of the signal from scan line to scan line due to these factors affect primarily the measured friction loop offsets  $\Delta_s^V$  and  $\Delta_f^V$ . Although, in the wedge calibration method a difference of the friction loop offsets ( $\Delta_s^V - \Delta_f^V$ ) is utilized, those factors contribute to the precision of the determined ( $\Delta_s^V - \Delta_f^V$ ), which possesses a dominating impact on the resulting values of  $\alpha$  (strongly visible at low applied load) and the value of error of  $\alpha$ . The errors can be reduced to below 5%, if the calibration is performed with a well-equilibrated and stable AFM (see Figure 4-5, section 4.5.1).

### 4.9.2. The improved wedge calibration method for specimens with two (non-zero) slopes

In the wedge calibration method for two sloped surfaces, relations between measured lateral forces (half width of friction loop  $W^V = (M_u^V - M_d^V)/2$ ) and the friction loop offsets ( $\Delta^V = (M_u^V + M_d^V)/2$ ) for two sloped surfaces at a given load are used to calculate the friction force calibration factor  $\alpha$  [nN/V] (see Scheme 1). The subscripts 1 and 2 denote two differently sloped surfaces, respectively.

Here  $p$  and  $q$  are defined as follows:

$$p \equiv \frac{W_1^V}{W_2^V} \quad (\text{Eq. 4-11})$$

$$q \equiv \frac{\Delta_1^V - \Delta_2^V}{W_1^V} \quad (\text{Eq. 4-12})$$

From equation (Eq. 4-11) and equations (Eq. 4-7) and (Eq. 4-8) in Section 4.2 we obtain

$$\mu_1 = \frac{-(L + A \cos \theta_1) + \sqrt{(L + A \cos \theta_1)^2 + \kappa^2 \sin^2 2\theta_1}}{2\kappa \sin^2 \theta_1} \quad (\text{Eq. 4-13})$$

$$\kappa = p \frac{\mu_2 (L + A \cos \theta_2)}{\cos^2 \theta_2 - \mu_2^2 \sin^2 \theta_2} \quad (\text{Eq. 4-14})$$

From Eq. (Eq. 4-12), (Eq. 4-7) and (Eq. 4-8) we obtain:

$$2q = \frac{\mu_1^2 \left( L + \frac{A}{\cos \theta_1} \right) + L}{\mu_1 (L + A \cos \theta_1)} \sin 2\theta_1 - \frac{1}{p} \frac{\mu_2^2 \left( L + \frac{A}{\cos \theta_2} \right) + L}{\mu_2 (L + A \cos \theta_2)} \sin 2\theta_2 \quad (\text{Eq. 4-15})$$

The resulting equation (Eq. 4-15) is difficult to invert, but can be solved numerically for the root such that  $0 < \mu_1 < 1$ . With this solution we find the calibration factor:

$$\alpha = \frac{1}{W_1^V} \frac{\mu_1 (L + A \cos \theta_1)}{\cos^2 \theta_1 - \mu_1^2 \sin^2 \theta_1} \quad (\text{Eq. 4-16})$$

#### 4.10. References

- 1 Feiler, A.; Attard, P.; Larson, I. *Rev. Sci. Instrum.* **2000**, *71*, 2746-2750.
- 2 Attard, P. *J. Adhes. Sci. Technol.* **2002**, *16*, 753-791.
- 3 Toikka, G.; Hayes, R. A.; Ralston, J. *J. Adhes. Sci. Technol.* **1997**, *11*, 1479-1489.
- 4 Ogletree, D. F.; Carpick, R. W.; Salmeron, M. *Rev. Sci. Instrum.* **1996**, *67*, 3298-3306.
- 5 Varenberg, M.; Etsion, I.; Halperin, G. *Rev. Sci. Instrum.* **2003**, *74*, 3362-3367.
- 6 Even if the normal force constant is uncertain, the ratio of normal to lateral forces (the friction coefficient) is determined quantitatively using this method.
- 7 Enachescu, M.; van den Oetelaar, R. J. A.; Carpick, R. W.; Ogletree, D. F.; Flipse, C. F. J.; Salmeron, M. *Tribol. Lett.* **1999**, *7*, 73-78.
- 8 Enachescu, M.; Carpick, R. W.; Ogletree, D. F.; Salmeron, M. *J. Appl. Phys.* **2004**, *95*, 7694-7700.
- 9 Carpick, R. W.; Eriksson, M. A. *MRS Bull.* **2004**, *29*, 472-477.
- 10 Sheiko, S. S.; Möller, M.; Reuvekamp, E.; Zandbergen, H. W. *Phys. Rev. B* **1993**, *48*, 5675-5678.
- 11 TGF11, MikroMasch, Tallinn, Estonia.
- 12 Provided that the criterion for quantitative nanotribology measurements (probes with symmetrical tip apex) is maintained, the quantitative lateral force calibration can be performed routinely for all types of probes.
- 13 Sader, J. E. *Rev. Sci. Instrum.* **2003**, *74*, 2438-2443.
- 14 Clifford, C. A.; Seah, M. P. *Nanotechnology* **2005**, *16*, 1666-1680.
- 15 Liu, E.; Blanpain, B.; Celis, J. P. *Wear* **1996**, *192*, 141-150.
- 16 Neumeister, J. M.; Ducker, W. A. *Rev. Sci. Instrum.* **1994**, *65*, 2527-2531.
- 17 Grafström, S.; Ackermann, J.; Hagen, T.; Neumann, R.; Probst, O. *J. Vac. Sci. Technol. B* **1994**, *12*, 1559-1564.
- 18 Grafström, S.; Neitzert, M.; Hagen, T.; Ackermann, J.; Hagen, T.; Neumann, R.; Probst, O.; Wörtge, M. *Nanotechnology* **1993**, *4*, 143-151.
- 19 Podesta, A.; Fantoni, G.; Milani, P. *Rev. Sci. Instrum.* **2004**, *75*, 1228-1242.
- 20 Radmacher, M.; Tillmann, R. W.; Fritz, M.; Gaub, H. E. *Science* **1992**, *257*, 1900-1905.
- 21 Varenberg, M.; Etsion, I.; Halperin, G. *Rev. Sci. Instrum.* **2003**, *74*, 3569-3571.
- 22 Such, M. W.; Kramer, D. E.; Hersam, M. C. *Ultramicroscopy* **2004**, *99*, 189-196.
- 23 Piner, R.; Ruoff, R. S. *Rev. Sci. Instrum.* **2002**, *73*, 3392-3394.
- 24 Fujisawa, S.; Ogiso, H. *Rev. Sci. Instrum.* **2003**, *74*, 5115-5117.
- 25 The variations of the signal that change from scan line to scan line will increase the error of the calibration factor.
- 26 Burnham, N. A.; Chen, X.; Hodges, C. S.; Matei, G. A.; Thoreson, E. J.; Roberts, C. J.; Davies, M. C.; Tandler, S. J. B. *Nanotechnology* **2003**, *14*, 1-6.
- 27 Therefore, all the calibration data presented below were performed using the optical head with better laser characteristics, where only insignificant interference was observed.
- 28 Jeon, S.; Braiman, Y.; Thundat, T. *Rev. Sci. Instrum.* **2004**, *75*, 4841-4844.
- 29 Green, C. P.; Lioe, H.; Cleveland, J. P.; Proksch, R.; Mulvaney, P.; Sader, J. E. *Rev. Sci. Instrum.* **2004**, *75*, 1988-1996.
- 30 Schwarz, U. D.; Köster, P.; Wiesendanger, R. *Rev. Sci. Instrum.* **1996**, *67*, 2560-2567.

- 31 D'Costa, N. P.; Hoh, J. H. *Rev. Sci. Instrum.* **1995**, *66*, 5096-5097.
- 32 Proksch, R.; Schaffer, T. E.; Cleveland, J. P.; Callahan, R. C.; Viani, M. B. *Nanotechnology* **2004**, *15*, 1344-1350.
- 33 Warmack, R. J.; Zheng, X. Y.; Thundat, T.; Allison, D. P. *Rev. Sci. Instrum.* **1994**, *65*, 394-399.
- 34 Bouissou, S.; Petit, J. P.; Barquins, M. *Tribol. Lett.* **1999**, *7*, 61-65.
- 35 He, X. M.; Walter, K. C.; Nastasi, M.; Lee, S. T.; Sun, X. S. *Thin Solid Films* **1999**, *356*, 167-173.
- 36 Khidas, Y.; Ammi, M.; Delannay, R.; Oger, L. *Eur. Phys. J. E* **2003**, *10*, 387-391.
- 37 Li, D. J.; Cui, F. Z.; Gu, H. Q. *Appl. Surf. Sci.* **1999**, *137*, 30-37.
- 38 Nuno, N.; Amabili, M.; Groppetti, R.; Rossi, A. *J. Biomed. Mater. Res.* **2002**, *59*, 191-200.
- 39 Yang, Z.; Dong, B.; Huang, Y.; Liu, L.; Yan, F. Y.; Li, H. L. *Mater. Lett.* **2005**, *59*, 2128-2132.
- 40 Scandella, L.; Meyer, E.; Howald, L.; Lüthi, R.; Guggisberg, M.; Gobrecht, J.; Güntherodt, H. J. *J. Vac. Sci. Technol. B* **1996**, *14*, 1255-1258.
- 41 Qian, L. M.; Tian, F.; Xiao, X. D. *Tribol. Lett.* **2003**, *15*, 169-176.
- 42 Wilbur, J. L.; Biebuyck, H. A.; Macdonald, J. C.; Whitesides, G. M. *Langmuir* **1995**, *11*, 825-831.
- 43 Vezenov, D. V.; Noy, A.; Ashby, P. *J. Adhes. Sci. Technol.* **2005**, *19*, 313-364.
- 44 Vezenov, D. V.; Zhuk, A. V.; Whitesides, G. M.; Lieber, C. M. *J. Am. Chem. Soc.* **2002**, *124*, 10578-10588.
- 45 Noy, A.; Vezenov, D. V.; Lieber, C. M. *Annu. Rev. Mater. Sci.* **1997**, *27*, 381-421.
- 46 Green, J. B. D.; McDermott, M. T.; Porter, M. D.; Siperko, L. M. *J. Phys. Chem.* **1995**, *99*, 10960-10965.
- 47 Frisbie, C. D.; Rozsnyai, L. F.; Noy, A.; Wrighton, M. S.; Lieber, C. M. *Science* **1994**, *265*, 2071-2074.
- 48 Noy, A.; Frisbie, C. D.; Rozsnyai, L. F.; Wrighton, M. S.; Lieber, C. M. *J. Am. Chem. Soc.* **1995**, *117*, 7943-7951.
- 49 van der Vegte, E. W.; Hadziioannou, G. *Langmuir* **1997**, *13*, 4357-4368.
- 50 Weeks, B. L.; Vaughn, M. W.; DeYoreo, J. J. *Langmuir* **2005**, *21*, 8096-8098.
- 51 Nakano, M.; Ishida, T.; Numata, T.; Ando, Y.; Sasaki, S. *Appl. Surf. Sci.* **2005**, *242*, 287-294.
- 52 Xia, Y. N.; Whitesides, G. M. *Angew. Chem.-Int. Edit.* **1998**, *37*, 551-575.
- 53 Tortonese, M.; Kirk, M. *Proc. SPIE* **1997**, *3009*, 53-60.
- 54 Gibson, C. T.; Watson, G. S.; Myhra, S. *Nanotechnology* **1996**, *7*, 259-262.



# Chapter 5

## Development of a high velocity accessory for atomic force microscopy-based friction measurements\*

*In this Chapter, the development of a high velocity accessory for friction force microscopy measurements for velocities up to the mm/s range using a commercial stand-alone atomic force microscope (AFM) is described. The accessory consists of a shear piezo element, which rapidly displaces the sample in the lateral direction, perpendicular to the main axis of the AFM cantilever. Friction forces, which are acquired via conventional optical beam deflection detection, can thus be measured as a function of velocity and load in controlled environment (0 - 40% relative humidity and 0 - 40°C). Using the accessory, a broad range of velocities up to several mm/s can be accessed independent of the lateral scan size up to a maximum scan size of 1000 nm. The device was validated in studies of the velocity dependence of friction forces and friction coefficients on organic [poly(methyl methacrylate)], as well as inorganic [oxidized Si(100)] samples. It was shown that the accessory allows one to bridge the time and length scales from ms to several s and 10's of micrometers to nanometers, respectively, in tribological studies on oxidic ceramics systems and amorphous polymers, as also described in detail in Chapters 7 and 8.*

---

\* Parts of this work were published in the following article: Tocha, E.; Stefański, T.; Schönherr, H.; Vancso, G. J. *Rev. Sci. Instrum.* **2005**, 76, 083704.

## 5.1. Introduction

Micro- and nanotribology receive increasing attention with the on-going trend of miniaturization of moving components in micro- and nanoscale technological devices ranging from magnetic storage systems<sup>1-5</sup> to microelectromechanical systems (MEMS)<sup>6-10</sup> and nanoelectromechanical systems (NEMS).<sup>11,12</sup> For the development of appropriate theories and simulations for applications,<sup>13</sup> it is necessary, as discussed in Chapter 2, to conduct micro- and nanoscale friction measurements at the relevant velocities, *i.e.* mm/s to m/s. Moreover, sliding velocity is one of the parameters in the so-called “friction phase diagrams”,<sup>14-17</sup> determined for confined liquids, lubricants and polymers, which can undergo first-order transitions and become “glassy” depending on the sliding conditions (load, velocity and temperature). Thus, experimental data at high speeds is needed also for the construction of the corresponding phase diagrams.

The surface forces apparatus (SFA)<sup>18,19</sup> and the atomic force microscope (AFM)<sup>20-25</sup> are among the most prominent instruments for performing micro- and nanotribological studies (Chapter 2). While the SFA is limited to mica as a substrate and possesses a limited lateral resolution (several micrometers),<sup>16,26</sup> AFM is suitable to detect friction forces of nanometer-scale contacts of real surfaces with high spatial resolution under pressures of several GPa.<sup>27</sup> However, the velocity range accessible with conventional AFMs is limited to the range of  $\mu\text{m/s}$ , which is insufficient to provide relevant friction force data captured under realistic conditions. High velocities can only be realized at the expense of (pixel) resolution, control of load, and noise.

An approach to circumvent this problem of limited velocities is the combination of an AFM with a high frequency actuator for lateral displacement, *e.g.* a quartz crystal microbalance (QCM).<sup>28,29</sup> In such a combined instrument the sample is vibrated laterally by means of the resonating quartz crystal of the QCM with constant frequency (several MHz) and amplitude (up to 100 nm). However, while velocities up to m/s have been achieved, only a very limited velocity range (three orders of magnitude) can be covered by a single QCM and the resolution is compromised by changing the scan size (to achieve different velocities).<sup>30</sup> Clearly, the use of a more versatile *variable* frequency actuator for lateral displacement would be highly beneficial.

High frequency transducers that oscillate the sample horizontally (with frequencies between tens of kHz and MHz, and amplitudes up to several nm) have also been used in dynamic modes, *e.g.*, the so-called ultrasonic force microscopy,<sup>31,32</sup> local-acceleration microscopy,<sup>33,34</sup> and lateral force modulation.<sup>35-37</sup> These techniques provide information on the relative elasticity and the

viscoelastic shear response; in addition, they allow one to perform high contrast friction imaging.

In this chapter, the development of a variable frequency, high velocity accessory is described for friction force microscopy measurements, covering the velocity range between nm/s and several mm/s, designed for a commercial stand-alone AFM. The design and calibration of the accessory, as well as validation measurements at high velocities, are discussed, followed by a report of novel nanotribology data acquired on thin polymer films and oxidized Si(100).

## 5.2. Experimental setup

### 5.2.1. Instrumental design

The high velocity accessory for AFM friction measurements was designed and developed for commercial stand-alone AFMs, such as a PicoSPM scanning probe microscope (Molecular Imaging, Tempe, USA). In the stand-alone AFM configuration, the sample is immobilized on a support table and the probe tip, which is attached to the xyz piezo tube scanner of the AFM, is raster-scanned during the imaging of the sample. The deflection and the torsion of cantilever are measured by the optical beam deflection method, in which a laser beam is reflected from the end of cantilever to a four-quadrant position sensitive photodiode.

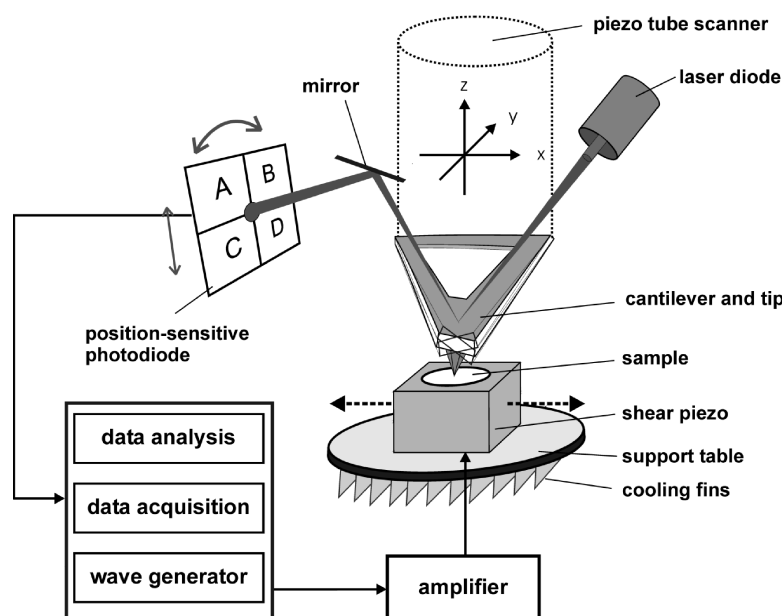


Figure 5-1. Schematic of the high velocity AFM set-up comprised of a commercial stand-alone AFM, the high velocity accessory and peripheral devices for accessory operation, data acquisition and signal processing (the components are not shown to scale). The controller for the xyz piezo tube scanner, as well as the PC and other parts, has been omitted for clarity.

Figure 5-1 shows a schematic diagram of the instrument. The high velocity accessory consists of a fast shear piezo element (PAXZ 012.05.05.xx.255 Shear Piezo, capacity 250 nF, PI Ceramic, Germany), to which the sample is attached. The shear piezo scanner is driven by an amplifier (E-507.K HVPZT Amplifier Module<sup>38</sup> and E-500.00 Controller Basic Chassis 19, Physik Instrumente, Karlsruhe, Germany), fed by an analog output of a National Instruments NI 6070E multifunction data acquisition board (maximum sampling rate 1 MS/s). The lateral photodiode signal is acquired by an analog input of the board with a maximum sampling rate equal to 1.25 MS/s. The wave generation and data acquisition are performed simultaneously, controlled with a conventional PC computer, which is also used for data processing and statistical analysis.

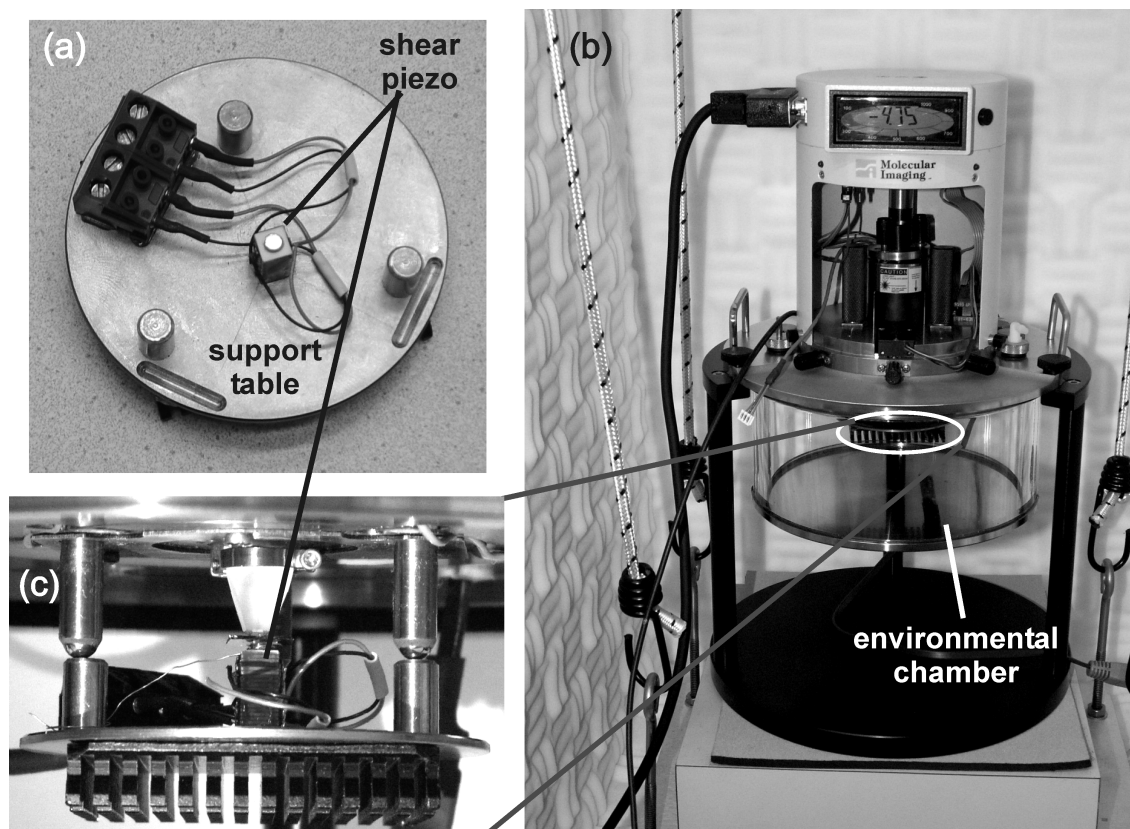


Figure 5-2. Photographs of the high velocity AFM-setup. (a) The high velocity accessory (support table diameter 64 mm). On top of the shear piezo a magnet for sample fixation is attached. (b) The AFM equipped with an environmental chamber, suspended on elastic ropes in an acoustic box. (c) A close view of the high velocity accessory attached to the AFM.

Close-up photographs of the high velocity AFM-setup are shown in Figure 5-2 (a)-(c). The shear piezo scanner is assembled on a support table (Figure 5-2(a)), which is fixed via magnets to the AFM (Figure 5-2(c)). On the top of the shear piezo scanner, a small magnet (surface flux 1500 Gauss, Neodymium Iron body, Nickel plated, model nr. M1219-1, Assentech, UK) is fixed for

convenient sample attachment. The table is further equipped with cooling fins in order to avoid overheating of the shear piezo scanner during operation.

For operation in the high velocity friction measurement mode, both the AFM xyz piezo tube scanner and the high velocity piezo scanner are used simultaneously. The xyz piezo tube scanner works in the z-direction both for feedback control (constant load) and for adjustment of the externally applied load, while the shear piezo scanner is scanning the sample unidirectionally perpendicular to the main cantilever axis. The performance of the feedback loop can be assessed by recording line traces for the height and deflection channels.<sup>39</sup> The angular alignment of the shear piezo relative to the cantilever is performed manually. Using a charge coupled device (CCD) camera, an error of  $\leq 5^\circ$  is typically achieved. This level of possible misalignment has a negligible influence on the scanning velocity (error  $\leq 1\%$ ).

The maximum operational frequency for the high velocity instrument is associated with the performance of the AFM electronics and the accessory. The electronic bandwidth of our AFM for the feedback control is 12 kHz and the cut-off frequency of the photodetector filter is set to 400 kHz. The resonance frequency of the shear piezo is 100 kHz; therefore, the theoretical limit of the shear piezo's operational frequency is  $\leq 50$  kHz.<sup>40</sup> However, the maximum operating frequency of the shear piezo is a function of the maximum output current of the amplifier (50 mA), capacitance of the shear piezo (250 nF) and peak-to-peak drive voltage, and is limited to 1 kHz (for the shear piezo scan size of 1000 nm),<sup>41</sup> which determines in our case the maximum operation frequency for the high velocity instrument. Driving the current set-up with its maximum frequency of 1 kHz and the maximum scan size of 1000 nm, velocities of 2 mm/s can be achieved. Operation of the accessory with the highest possible velocity does not lead to additional noise in the lateral deflection signal when flat samples, such as oxidized Si(100) (see also below), are probed. However, rough surfaces require operation with optimized gain settings of the feedback loop. Moreover, sample mass should be low ( $< 200$  mg), since the addition of mass to the shear piezo scanner necessitates the use of a higher dynamic force that is needed for driving the shear piezo in the “turning points”, where the motion is reversed. For the deceleration and acceleration higher current is required, if the mass is increased. Consequently, this leads to a decrease of the maximum operational frequency.

The high velocity set-up is fully compatible with measurements under environmental control. The limits of operation in high humidity or temperature conditions are given by the piezoceramic material's specifications. Using climate control via the flow of pre-thermostatted nitrogen gas of controlled humidity through an environmental chamber (PicoAPEX, Pyrex glass,

---

MI, Tempe, USA), measurements were carried out in 0 - 40% relative humidity (RH) and temperatures between 0 - 40°C without detectable effect on the piezo performance. For a schematic of the environmental control set-up, see Appendix 5-1 and 5-2. The corresponding parameters were monitored on-line using a humidity sensor (SHT15, Sensirion, Switzerland) placed inside the chamber in the vicinity of a sample (sensor accuracy:  $\pm 2\%$  RH and  $\pm 0.5\%$ °C).

### 5.2.2. Data acquisition

The shear piezo accessory is controlled via a custom-developed software. This software was written in collaboration with T. Stefański (R&D Marine Technology Centre, Gdynia, Poland) in the National Instruments LabVIEW environment to automate signal acquisition, data processing, and driving of the shear piezo with a triangular waveform.<sup>42</sup> The number of generated cycles (trace and retrace), the resolution of the acquired signal, the scan size and the scanning frequency are set manually by the operator. The scan size is automatically transformed using calibration factors (see below) into the required peak-to-peak voltage of the generated waveform (see Appendix 5-3 and 5-4).

The torsion of the cantilever (lateral deflection signal), which is proportional to the friction force between tip and sample, is monitored by a four-quadrant photodiode. The corresponding signal, which is acquired in the time domain, is recorded via the data acquisition board and is processed by the software mentioned. Simultaneously, the deflection signal is recorded in the time domain to monitor the performance of the feedback loop and possible variations in load.

Figure 5-3(a) shows an example of raw lateral deflection signal for several scanning cycles ( $\text{Si}_3\text{N}_4$  tip on oxidized Si(100)). The subsequently captured lateral signals composed of 150 overlapped cycles can be seen in Figure 5-3(b). Several options for statistical analyses are possible for processing the acquired data, including averaging of the measured signal (average trace and retrace signals), calculation of histograms of trace and retrace difference signals (Figure 5-3(c)), as well as separate histograms of trace and retrace signals (Figure 5-3(d)) and the corresponding standard deviations. The typical data analysis of friction force is based on the estimation of one-half of the difference (trace minus retrace) lateral deflection signal averaged over a given (or pre-set) number of scanned lines (cycles) for a given load and velocity. In addition, the lateral difference signal plotted as a function of the cycle number, allows one to quantitatively analyze friction forces as a function of time, *i.e.* scanned line (Appendix 5-5 and 5-6). The variations in load and, assuming constant adhesion, also normal force due to operation of the shear piezo at high velocities are negligible, as shown in Figure 5-3(e). The corresponding

deflection signal shows that the feedback loop holds the load (normal force) constant within an error of  $\pm 40$  pN. This error is insignificant compared to the typically applied variations in load.

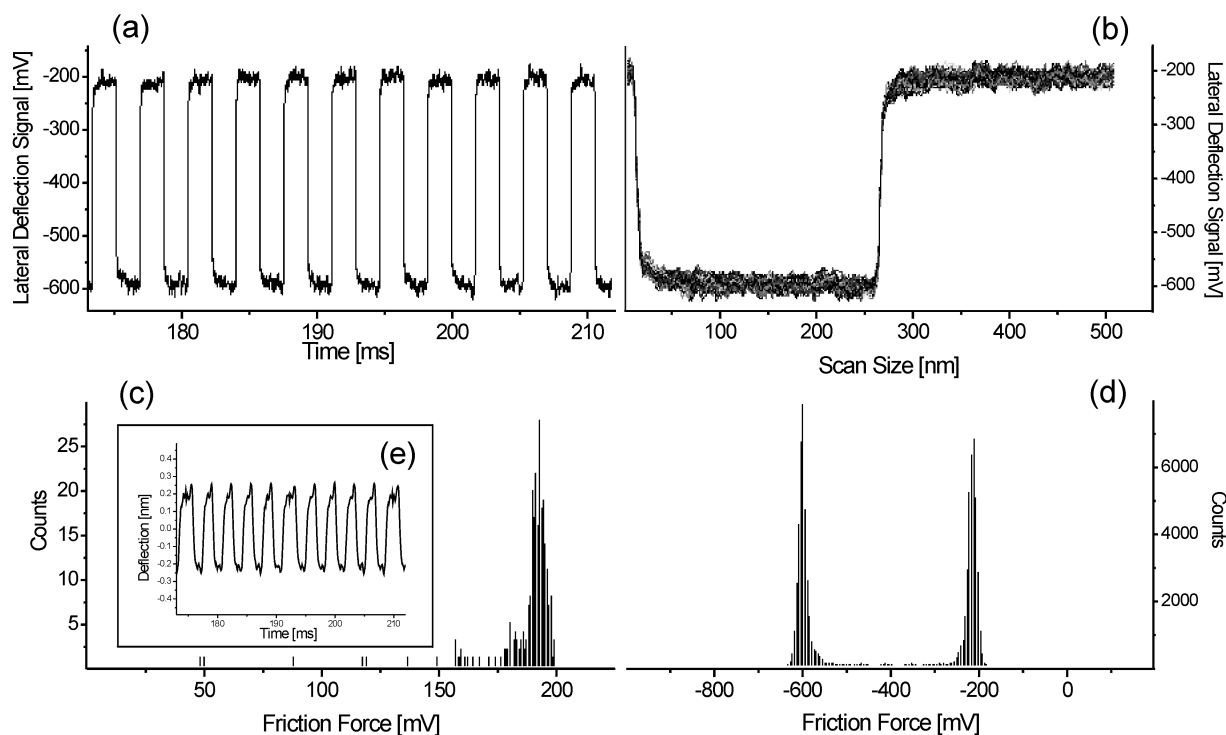


Figure 5-3. Example of friction force microscopy data acquired with the high velocity accessory ( $\text{Si}_3\text{N}_4$  tip vs. oxidized Si(100); scan size 500 nm, scan velocity  $280 \mu\text{m/s}$ ,  $25^\circ\text{C}$ , in  $\text{N}_2$  atmosphere,  $< 5\%$  RH): (a) raw friction signal vs. time for several cycles, (b) overlapped friction signals of 150 cycles, (c) histogram of trace and retrace difference signal, (d) separate histograms of trace and retrace signals, and (e) corresponding deflection (error signal) for measured data.

### 5.2.3. Calibration

The response of the shear piezo scanner displacement to the applied peak-to-peak voltage was calibrated by scanning a reference sample exclusively in x direction using the xyz piezo tube scanner of the AFM (Figure 5-4; the tube scanner's slow scan axis was disabled). The reference sample [polystyrene-*block*-poly(*tert*-butyl acrylate)] consists of two sets of microfabricated lines (spacing: 400 nm and 600 nm, line width *ca.* 100 nm, height  $21 \pm 2$  nm).<sup>43</sup> Scanning the calibration sample simultaneously with both scanners (xyz tube piezo scanner was driven with a frequency of 1 Hz and the shear piezo scanner with significantly lower frequency of 0.01 Hz) resulted in a zigzag pattern (Figure 5-4(c) and 5-4(d)). The slight distortion is related to the non-linearity of the shear piezo scanner.

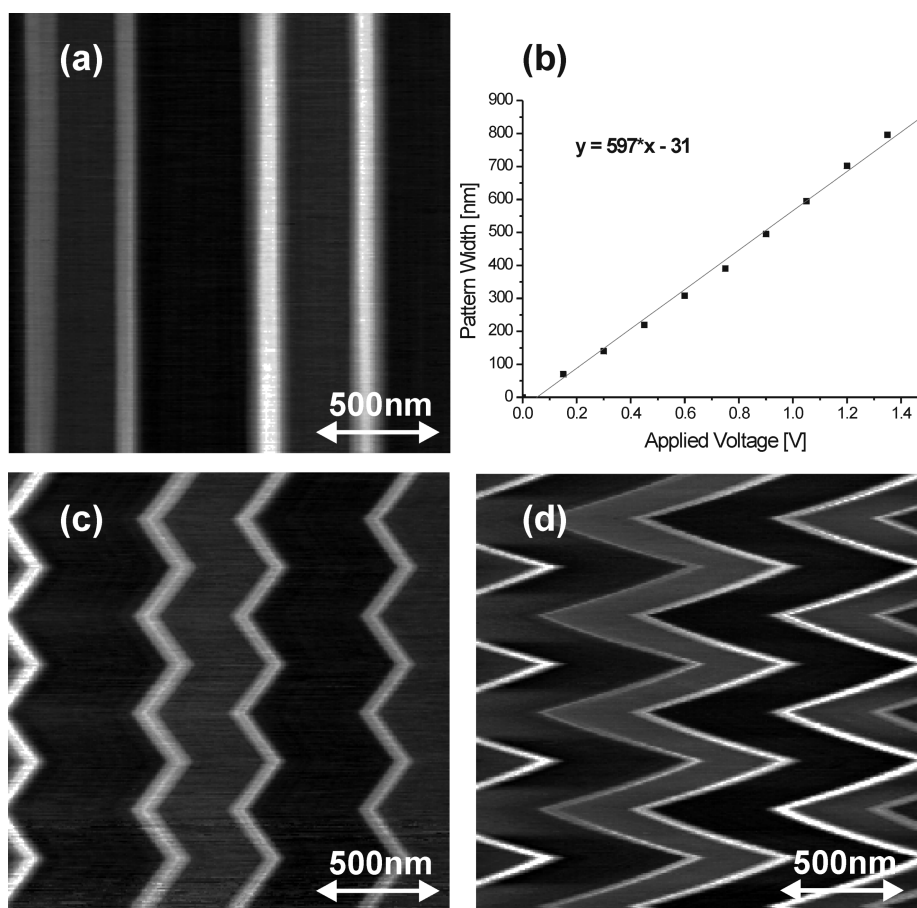


Figure 5-4. AFM height images of a calibration sample with two sets of periodically spaced lines, scanned simultaneously by the xyz piezo tube scanner (frequency 1 Hz, slow scan axis disabled, lateral scan size 2  $\mu\text{m}$ ) and the shear piezo scanner (frequency 0.01 Hz, different shear piezo drive peak-to-peak voltages were applied). The peak-to-peak voltages were: (a)  $U_{p-p} = 0.00$  V, (c)  $U_{p-p} = 0.30$  V and (d)  $U_{p-p} = 1.05$  V. The calibration curve (linear least square fit,  $R^2 = 0.994$ ) of the shear piezo displacement is shown in (b).

The displacement of the shear piezo scanner, which is equal to width of the zigzag pattern, was recorded as a function of the applied voltage. The standard deviation of each measurement point was 2%. Figure 5-4(b) shows the corresponding calibration curve. A linear curve serves as an approximation to the response of the shear piezo scanner on applied voltages in the low-frequency regime.

The response of the shear piezo scanner displacement to the applied voltage for the entire spectrum of frequencies was obtained from the analysis of modified regions in a poly(methyl methacrylate) (PMMA) film on silicon. This film is reproducibly scratched by the scanning probe tip under loads of  $> 40$  nN.<sup>44</sup> For these calibration measurements the sample was scanned with the shear piezo scanner at a fixed amplitude. The position of the tip was changed along the y axis for each frequency from 10 Hz to 100 Hz in increments of 30 Hz and from 100 Hz to 1000



Hz in increments of 100 Hz. Afterwards, the scratched surface was imaged in contact mode with the AFM xyz tube scanner. The displacement of the shear piezo scanner, as deduced from the length of the scratches, did not depend on the applied shear piezo frequency up to 800 Hz, see Figures 5-5 and 5-6. Only for the highest frequencies and larger shear piezo displacements small deviations from the linear trend were observed.

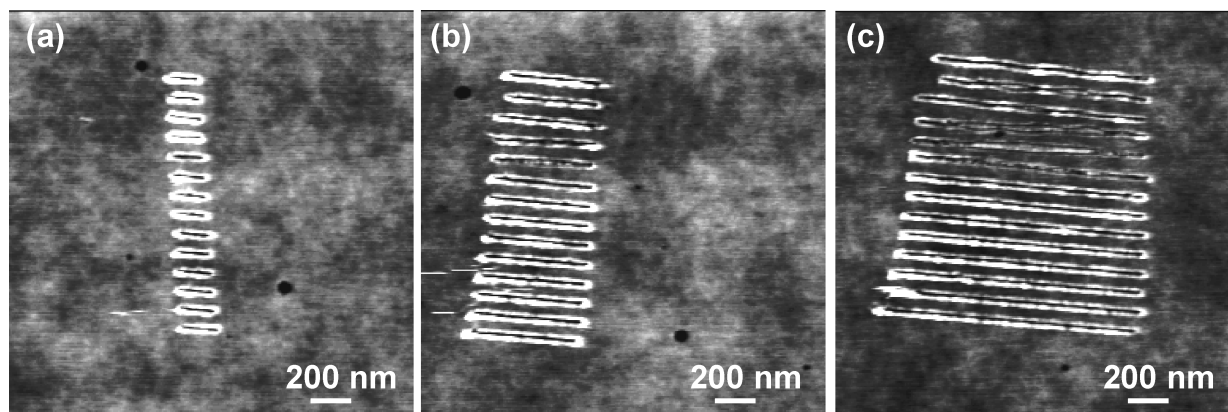


Figure 5-5. AFM topography images of PMMA film after scratching by scanning with the shear piezo under loads of  $> 40$  nN. Different shear piezo peak-to-peak voltages were applied: (a)  $U_{p-p} = 0.39$  V, (b)  $U_{p-p} = 0.98$  V, and (c)  $U_{p-p} = 1.98$  V. The position of the tip was changed along the y axis for each frequency from 10 Hz to 100 Hz in increments of 30 Hz and from 100 Hz to 1000 Hz in increments of 100 Hz.

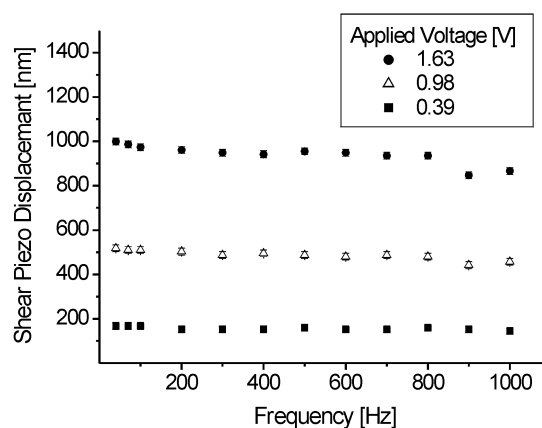


Figure 5-6. Calibration plot of the shear piezo scanner response at various applied voltages for different frequencies, obtained from an analysis of AFM images of a scratched PMMA sample (see Figure 5-5).

The shear piezo calibration was performed over the entire spectrum of temperatures utilized (0 - 40°C), revealing independence from temperature within this range. Using the calibration methods, the velocity is determined with an error below 5%.

### 5.3. Experimental results and discussion

The high velocity set-up was tested on two types of samples that are relevant for the work described in Chapters 7 and 8: spin-coated thin films (film thickness = 450 nm) of PMMA on Si(100) and neat oxidized Si(100) wafers. The friction forces obtained on the polymer film can be expected to depend on scanning velocity (based on time-temperature superposition for polymers),<sup>45,46</sup> while the micro- and nanotribology of oxidized Si(100) is relevant in the context of MEMS and NEMS devices *etc.*<sup>7-10</sup>

Friction force - velocity measurements (scan size of 500 nm) were performed with the AFM equipped with the high velocity accessory on PMMA thin films on oxidized Si(100) using single beam Si cantilevers with a normal spring constant of  $k_N = 0.03$  N/m (CSC38 without reflecting coating, MikroMasch, Tallinn, Estonia). For the measurements on O<sub>2</sub>-plasma cleaned (SPI Supplies, Plasma Prep II; conditions: 5 minutes, 30 mA, 60 mTorr) oxidized Si(100) samples, V-shaped Si<sub>3</sub>N<sub>4</sub> cantilevers with  $k_N = 0.30$  N/m (Model NP, Veeco, Santa Barbara, CA) were used. The spring constants in the normal direction were individually calibrated using the reference lever method.<sup>47</sup>

Each data point represents the mean value of one-half of the difference friction signal calculated from 150 trace and retrace cycles and the error bars correspond to the standard deviation of the data analyzed for a given velocity. The measurements on PMMA were carried out in dry N<sub>2</sub> at temperatures of 5°C and 25°C. A load of 0.2 nN was applied during all measurements. The pull-off force was 1.2 nN independent of the temperature. The Si(100) sample was analyzed in dry N<sub>2</sub> at 25°C.

The friction force vs. velocity data for PMMA displays a broad peak around 200  $\mu\text{m/s}$  at 25°C, as shown in Figure 5-7. Such a behavior is not surprising, as it is known that friction in polymers results from internal viscoelastic dissipation, which is derived from molecular relaxation and is hence rate-dependent.<sup>46</sup> The observed peak can be attributed to the  $\beta$ -relaxation of PMMA (see also Chapter 8), which is the result of the rotation of the  $-(\text{CO})\text{OCH}_3$  side groups around the C-C bonds linking the side groups to the main polymer chain.<sup>48,49</sup> The peak shifts towards lower velocities at reduced temperatures (5°C), which is consistent with the time-temperature superposition for polymers.<sup>45,49-51</sup> In order to correlate the frictional response with known relaxation mechanisms, a conversion from velocity to frequency dependence can be performed using the tip-sample contact length. This procedure is described in detail in Chapter 8.

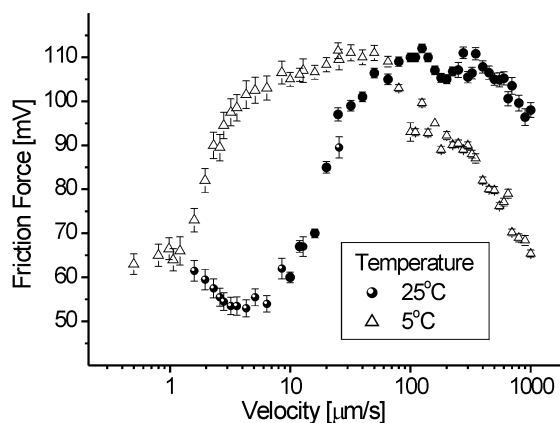


Figure 5-7. Semi-log plot of friction force signal (difference signal) vs. velocity for PMMA film on silicon measured with an oxidized silicon tip in nitrogen atmosphere ( $< 5\%$  RH) at  $5^{\circ}\text{C}$  and  $25^{\circ}\text{C}$ . A load of  $0.2\text{ nN}$  was maintained constant during the measurements. The error bars indicate the standard deviation of the data analyzed for a given velocity ( $n = 150$ ).

A qualitatively similar trend in PMMA friction force - velocity data was reported by Hammerschmidt *et al.*<sup>49</sup> These authors measured the friction force for only four different velocities between  $2$  and  $220\ \mu\text{m/s}$ . A “peak” was observed for measurements at  $25^{\circ}\text{C}$ , which shifted towards higher velocities at increasing temperatures. The scanning velocity was obtained by changing simultaneously both the scan frequency *and* the scan size, thus resolution was compromised.<sup>52</sup> By contrast, using the newly developed high velocity accessory described herein, it is possible to study high velocity nanotribology with high resolution of the friction signal at continuous frequency/velocity values (see Chapter 8).

Figure 5-8(a) shows the friction force – normal force – velocity dependence for oxidized Si(100). Increasing both load and velocity cause an increase in the measured friction force. A linear relation between the friction force and the normal force was observed. However, the friction coefficient, determined from the slopes of linear least-square fits calculated for each velocity, increases up to  $12\ \mu\text{m/s}$  and then remains constant (Figure 5-8(b)). This observation is consistent with reports on microtribology,<sup>53-55</sup> where the friction coefficient has been shown to be independent of velocity in the high velocity regime (from the  $\text{cm/s}$  to the  $\text{m/s}$  range). While the peculiar behavior of exponentially increasing friction force and initially increasing friction coefficient could have been detected and/or analyzed in principle using a conventional AFM, the transition of the slope for friction coefficient vs. velocity plot (Figure 5-8(b)) and the magnitude of friction force at velocities relevant for MEMS applications could not have been addressed in

detail using traditional instruments. Thus, high velocity nanotribology proves to be useful in particular for bridging the gap for time scales between nano- and microtribology.

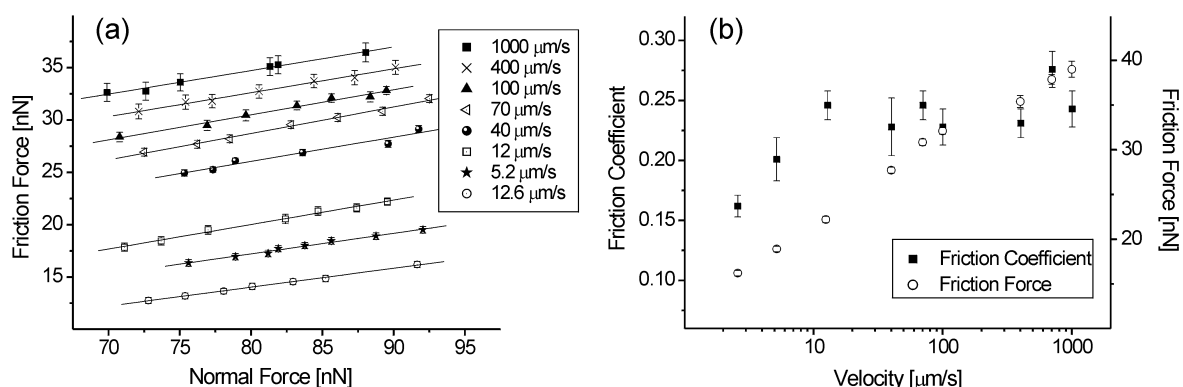


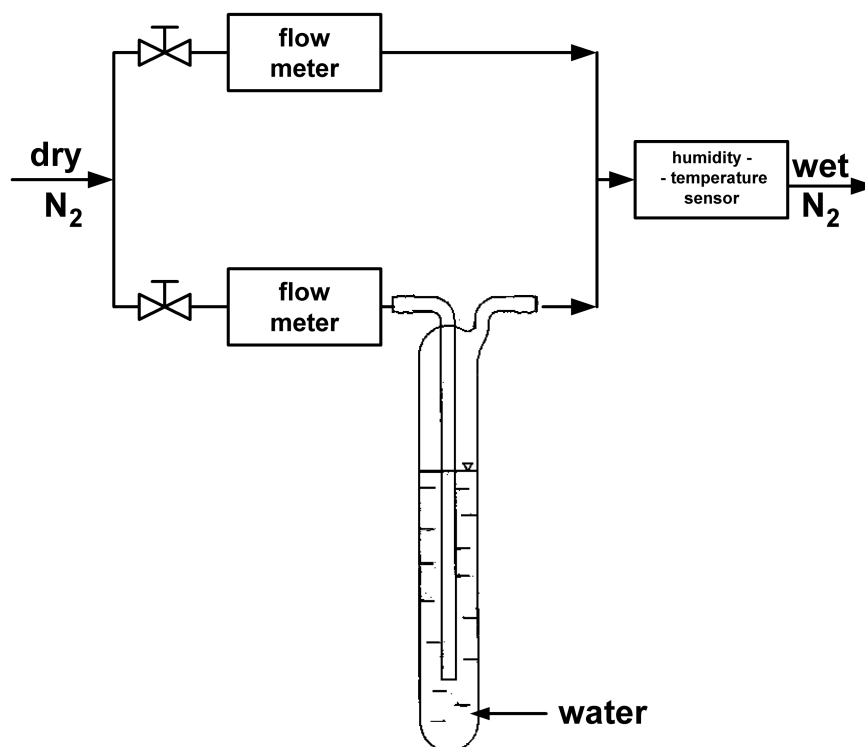
Figure 5-8. (a) Friction force as a function of normal force for oxidized Si(100) measured for several velocities using a  $\text{Si}_3\text{N}_4$  tip. The error bars indicate the standard deviation of the data analyzed for a given velocity and load (90 nN). (b) Friction coefficient for oxidized Si(100) and  $\text{Si}_3\text{N}_4$  tip as a function of velocity. The measurements were performed in nitrogen atmosphere (< 5% RH) at room temperature (25°C).

Our accessory can be improved further by exchanging the driving amplifier with an amplifier with higher linearity, thus the velocity range can increase up to several cm/s. With the application of an additional protective coating on the shear piezo, the range of possible humidity can be increased up to 60% RH and also measurements in liquid (*i.e.*, in a drop of water) are feasible. Finally, two-dimensional friction mapping can be achieved by expanding the software.

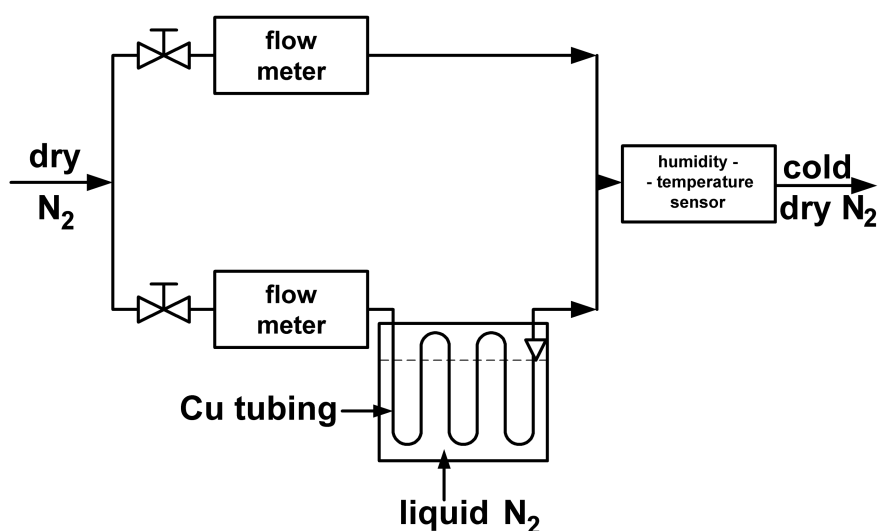
#### 5.4. Conclusions

In this chapter, a high velocity accessory was described for friction force microscopy measurements in controlled environment (0 - 40% RH and 0 - 40°C), developed for a commercial stand-alone AFM. Using the accessory, a broad range of velocities up to several mm/s can be accessed independent of the lateral scan size up to a maximum scan size of 1000 nm with high lateral force signal resolution. This instrument can contribute to bridge the gap between conventional AFM-based low velocity nanotribology and the established field of microtribology, as shown for oxidic ceramics systems in Chapter 7. In addition, it can also provide valuable information across four decades of velocity that becomes essential for the study of viscoelastic systems, as described for amorphous polymers in Chapter 8.

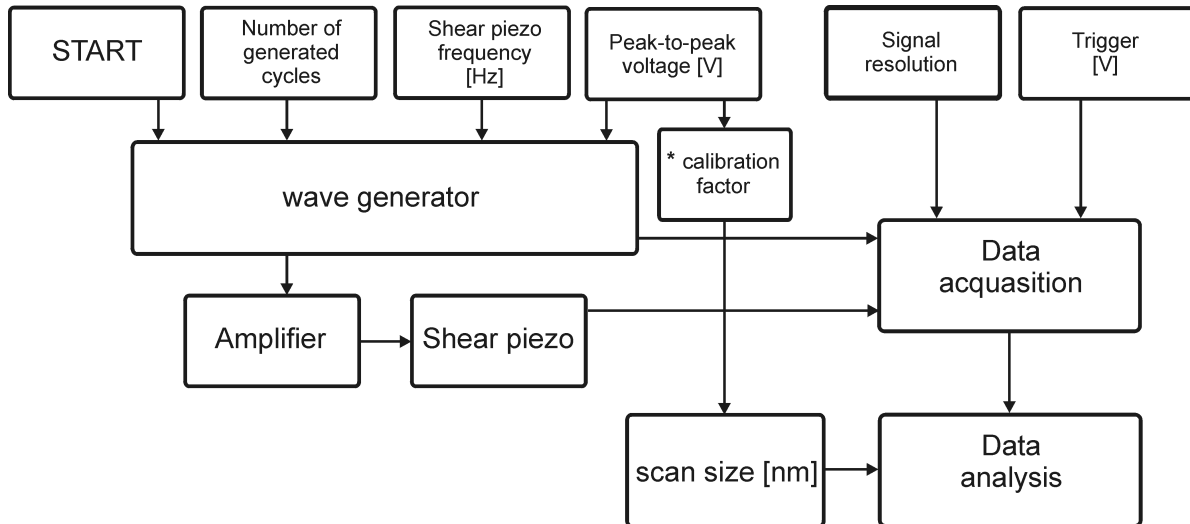
## 5.5. Appendix



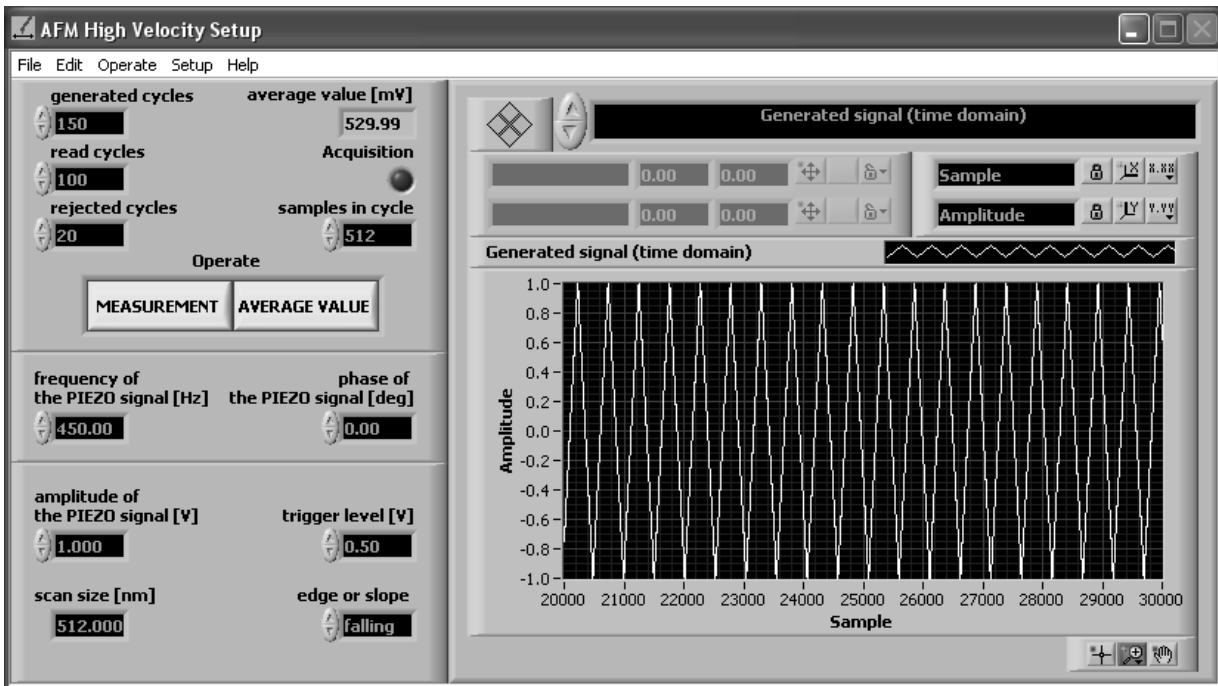
Appendix 5-1. Schematic of the humidity control. The humidity control was performed using mixture of dry/wet N<sub>2</sub> gas adjusted by gas flow meters (flow range 0 – 10 L/min). A humidity sensor was used for monitoring environmental control.



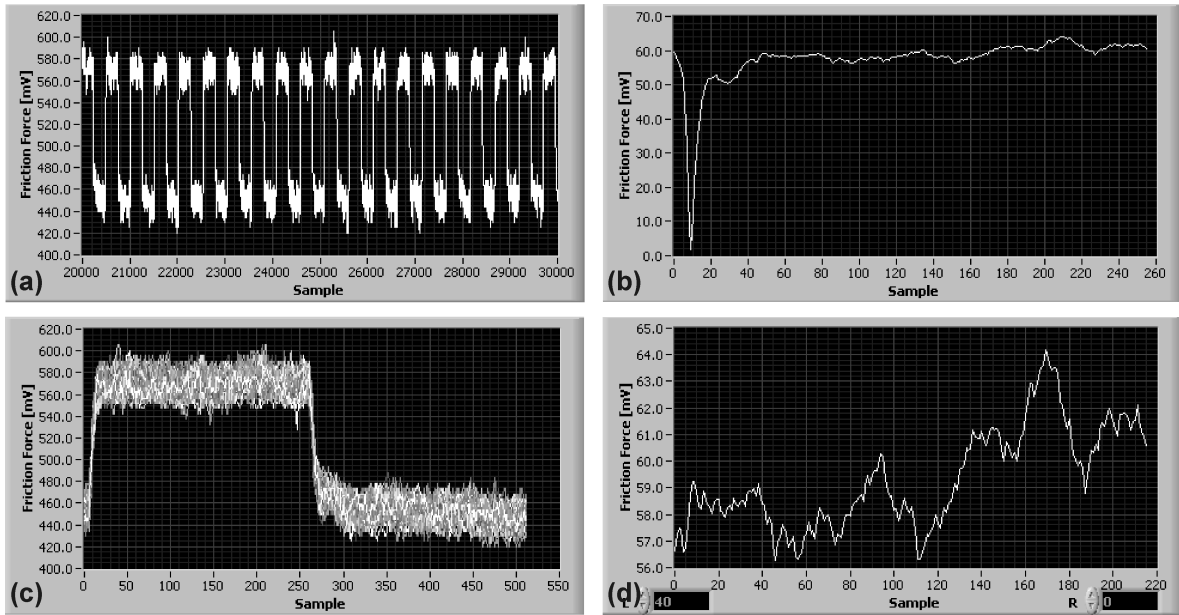
Appendix 5-2. Schematic of the temperature control. The temperature control was achieved using cold/warm dry N<sub>2</sub> gas adjusted by gas flow meters (flow range 0 – 10 L/min). The operating range of temperatures varied from < 0°C to 40°C at dry N<sub>2</sub> conditions. A humidity sensor was used for monitoring environmental control.



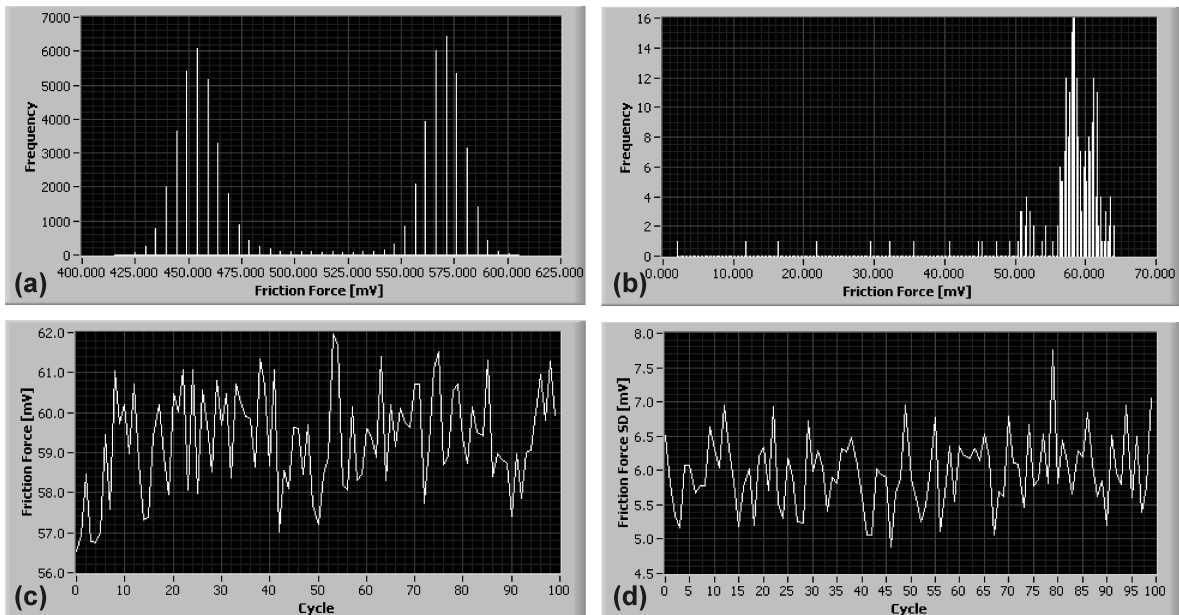
Appendix 5-3. Flow chart diagram of the software for data acquisition and processing.



Appendix 5-4. The front panel of the software for driving the shear piezo, data acquisition and processing.



Appendix 5-5. Data analysis by the software: (a) raw friction signal in the time domain, (b) one-half of the difference friction signal (trace minus retrace) averaged over a given number of scanned lines for a given load and velocity, (c) overlapped friction signals composed of a given number of cycles, (d) averaged one-half of the friction signal (see (b)), after excluding the “turning points”, where the motion is reversed. The values of friction forces in mV can be converted into nN using the method described in Chapter 3.



Appendix 5-6. Statistical analysis by the software: (a) separate histograms of the trace and retrace signals, (b) histogram of the one-half difference friction signal, (c) friction force signal as a function of the cycle number (in the time domain), (d) standard deviation of the one-half of friction force signal as a function of the cycle number. The values of friction forces in mV can be converted into nN using the method described in Chapter 3.

**5.6. References**

- 1 Bull, S. J.; Korsunsky, A. M. *Tribol. Int.* **1998**, *31*, 547-551.
- 2 Lee, S. C.; Polycarpou, A. A. *J. Tribol.-Trans. ASME* **2004**, *126*, 334-341.
- 3 Zhang, H.; Ono, K. *Tribol. Int.* **2003**, *36*, 361-365.
- 4 Li, X. D.; Bhushan, B. *J. Inf. Stor. Process. Syst.* **2001**, *3*, 131-142.
- 5 Tyndall, G. W.; Karis, T. E.; Jhon, M. S. *Tribol. Trans.* **1999**, *42*, 463-470.
- 6 Phinney, L. M.; Lin, G.; Wellman, J.; Garcia, A. *J. Micromech. Microeng.* **2004**, *14*, 927-931.
- 7 Maboudian, R.; Carraro, C. *Annu. Rev. Phys. Chem.* **2004**, *55*, 35-54.
- 8 de Boer, M. P.; Luck, D. L.; Ashurst, W. R.; Maboudian, R.; Corwin, A. D.; Walraven, J. A.; Redmond, J. M. *J. Microelectromech. Syst.* **2004**, *13*, 63-74.
- 9 Patton, S. T.; Zabinski, J. S. *Tribol. Int.* **2002**, *35*, 373-379.
- 10 Wang, W. Y.; Wang, Y. L.; Bao, H. F.; Xiong, B.; Bao, M. H. *Sens. Actuator A-Phys.* **2002**, *97-8*, 486-491.
- 11 Tambe, N. S.; Bhushan, B. *Nanotechnology* **2004**, *15*, 1561-1570.
- 12 Cagin, T.; Che, J. W.; Gardos, M. N.; Fijany, A.; Goddard, W. A. *Nanotechnology* **1999**, *10*, 278-284.
- 13 Persson, B. N. J.; Albohr, O.; Mancosu, F.; Peveri, V.; Samoilov, V.; Sivebaek, I. M. *Wear* **2003**, *254*, 835-851.
- 14 Drummond, C.; Israelachvili, J. *Phys. Rev. E* **2001**, *6304*, 041506.
- 15 Daikhin, L. I.; Urbakh, M. *Phys. Rev. E* **1999**, *59*, 1921-1931.
- 16 Yoshizawa, H.; Chen, Y. L.; Israelachvili, J. *J. Phys. Chem.* **1993**, *97*, 4128-4140.
- 17 Maeda, N.; Chen, N. H.; Tirrell, M.; Israelachvili, J. N. *Science* **2002**, *297*, 379-382.
- 18 Yamada, S.; Israelachvili, J. *J. Phys. Chem. B* **1998**, *102*, 234-244.
- 19 Gao, J. P.; Luedtke, W. D.; Gourdon, D.; Ruths, M.; Israelachvili, J. N.; Landman, U. *J. Phys. Chem. B* **2004**, *108*, 3410-3425.
- 20 Zwörner, O.; Holscher, H.; Schwarz, U. D.; Wiesendanger, R. *Appl. Phys. A-Mater. Sci. Process.* **1998**, *66*, S263-S267.
- 21 Riedo, E.; Pallaci, I.; Boragno, C.; Brune, H. *J. Phys. Chem. B* **2004**, *108*, 5324-5328.
- 22 Riedo, E.; Gnecco, E.; Bennewitz, R.; Meyer, E.; Brune, H. *Phys. Rev. Lett.* **2003**, *91*, 084502.
- 23 Riedo, E.; Levy, F.; Brune, H. *Phys. Rev. Lett.* **2002**, *88*, 185505.
- 24 Gnecco, E.; Bennewitz, R.; Gyalog, T.; Loppacher, C.; Bammerlin, M.; Meyer, E.; Guntherodt, H. J. *Phys. Rev. Lett.* **2000**, *84*, 1172-1175.
- 25 Tocha, E.; Siebelt, N.; Schönherr, H.; Vancso, G. J. *J. Am. Ceram. Soc.* **2005**, *88*, 2498-2503.
- 26 Luengo, G.; Heuberger, M.; Israelachvili, J. *J. Phys. Chem. B* **2000**, *104*, 7944-7950.
- 27 Carpick, R. W.; Salmeron, M. *Chem. Rev.* **1997**, *97*, 1163-1194.
- 28 Lübben, J. F.; Johannsmann, D. *Langmuir* **2004**, *20*, 3698-3703.
- 29 Kim, J. M.; Chang, S. M.; Muramatsu, H. *Appl. Phys. Lett.* **1999**, *74*, 466-468.
- 30 Tip wear and environmental control over a broad range have also not been addressed.
- 31 Scherer, V.; Bhushan, B.; Rabe, U.; Arnold, W. *IEEE Trans. Magn.* **1997**, *33*, 4077-4079.
- 32 Yamanaka, K.; Ogiso, H.; Kolosov, O. *Jpn. J. Appl. Phys. Part 1 - Regul. Pap. Short Notes Rev. Pap.* **1994**, *33*, 3197-3203.



- 
- 33 Oulevey, F.; Burnham, N. A.; Kulik, A. J.; Gallo, P. J.; Gremaud, G.; Benoit, W. *J. Phys. IV* **1996**, *6*, 731-734.
- 34 Burnham, N. A.; Kulik, A. J.; Gremaud, G.; Gallo, P. J.; Oulevey, F. *J. Vac. Sci. Technol. B* **1996**, *14*, 794-799.
- 35 Reinstadtler, M.; Rabe, U.; Scherer, V.; Hartmann, U.; Goldade, A.; Bhushan, B.; Arnold, W. *Appl. Phys. Lett.* **2003**, *82*, 2604-2606.
- 36 Scherer, V.; Arnold, W.; Bhushan, B. *Surf. Interface Anal.* **1999**, *27*, 578-587.
- 37 Yamanaka, K.; Tomita, E. *Jpn. J. Appl. Phys. Part 1 - Regul. Pap. Short Notes Rev. Pap.* **1995**, *34*, 2879-2882.
- 38 Modified version with limited maximum voltage up to  $\pm 250\text{V}$ , 50W.
- 39 In the measurements described in this Chapter, the maximum observed deflection was  $< 2\text{ nm}$ , which is insignificant compared to typically applied loads.
- 40 In principle, for open-loop systems (described in this Chapter), one can operate the piezo even above its resonance frequency. However, at the resonance the amplitudes can become extremely large even for low input signals, which would cause the piezo to break. Additionally, at high frequencies, a phase shift between the input signal and the motion of the piezo will occur. This phase-shift is negligible at relative low frequencies. In case of closed-loop operation, the piezos are typically used below 50% of their resonance frequency due to bandwidth limitations of the electronics.
- 41 The nominal shear piezo displacement is 5000 nm.
- 42 For higher scanning frequencies, due to cut-off of higher frequency components in the spectrum, the waveform will become distorted. Consequently, the acceleration and deceleration parts were excluded from measured frictional signals for further analysis, providing a satisfactory approximation of linear velocity.
- 43 The sample, fabricated according to Vaeth *et al.* (Vaeth, K. M.; Jackman, R. J.; Black, A. J.; Whitesides, G. M.; Jensen, K. F. *Langmuir* **2000**, *16*, 8495-8500) using a capillary force lithography process, was kindly supplied by Dr. Chuanliang Feng (group of Materials Science and Technology of Polymers, University of Twente).
- 44 Pickering, J. P.; Vancso, G. J. *Appl. Surf. Sci.* **1999**, *148*, 147-154.
- 45 Young, R. J.; Lovell, P. A. *Introduction to Polymers*. Chapman & Hall: London, 1991.
- 46 Moore, D. F. *The Friction and Lubrication of Elastomers*. Pergamon Press: Oxford, 1972.
- 47 Tortonese, M.; Kirk, M. *Proc. SPIE* **1997**, *3009*, 53-60.
- 48 Gedde, U. W. *Polymer Physics*. Kluwer Academic Publishers: Dordrecht, 1999.
- 49 Hammerschmidt, J. A.; Gladfelter, W. L.; Haugstad, G. *Macromolecules* **1999**, *32*, 3360-3367.
- 50 Cherry, B. W. *Polymer Surfaces*. Cambridge University Press: Cambridge, 1981.
- 51 Grosch, K. A. *Proc. R. Soc. London Ser. A-Math. Phys. Sci.* **1963**, *274*, 21-39.
- 52 *E.g.* for a scan size of  $1\mu\text{m}^2$  the pixel size is  $2\text{ nm}^2$ , by increasing the scan size to  $100\mu\text{m}^2$ , the resolution decreases 100 times and the pixel size equals  $200\text{ nm}^2$ . In this case, sample homogeneity and roughness may influence the measured friction force data. Moreover, for most commercial AFMs, the highest scanning frequencies have discrete values and cannot be changed continuously.
- 53 Fisher, J.; Dowson, D.; Hamdzah, H.; Lee, H. L. *Wear* **1994**, *175*, 219-225.
- 54 Davim, J. P.; Marques, N. *J. Mater. Process. Technol.* **2004**, *152*, 389-394.
- 55 Pasaribu, H. R.; Sloetjes, J. W.; Schipper, D. J. *Wear* **2003**, *255*, 699-707.
-



# Chapter 6

## Effects of grain size and humidity on nanotribological properties of nanostructured ZrO<sub>2</sub>\*

*In this Chapter, AFM-based nanotribological measurements on advanced ceramic coatings are discussed, which aimed at unraveling the relation of structural factors and the frictional response on nanostructured ZrO<sub>2</sub>. In particular, the nanotribological properties of nanostructured thin films of tetragonal ZrO<sub>2</sub> on oxidized Si(100) were investigated as a function of grain size and relative humidity (RH). The nanostructured ZrO<sub>2</sub> showed a 50% decrease in friction coefficient measured with a Si<sub>3</sub>N<sub>4</sub> tip ( $\mu_{\text{Si}_3\text{N}_4}$ ) compared to oxidized Si(100) in dry nitrogen atmosphere and 40% RH. A maximum of  $\mu_{\text{Si}_3\text{N}_4}$  was observed at ca. 40% RH for both samples, while there were insignificant differences in  $\mu_{\text{Si}_3\text{N}_4}$  for ZrO<sub>2</sub> samples with grain sizes between 12 nm and 30 nm. The good tribological properties open the possibility for nanostructured zirconia to be applied as wear-resistant, low friction coatings on various materials.*

---

\* Parts of this work were published in the following article: Tocha, E.; Siebelt, N.; Schönherr, H.; Vancso, G. J. *J. Am. Ceram. Soc.* **2005**, *88*, 2498-2503.

## 6.1. Introduction

The unique mechanical and tribological properties of nanostructured materials, resulting from large surface to volume ratio, make them interesting not only as bulk materials, but also as coatings. During the last decade, rapidly increasing interest has been directed towards nanocrystalline materials with grain sizes well below 100 nm. With decreasing grain size, the mechanical properties of different (semi)crystalline compounds (including ceramic, metallic and composite materials), such as hardness<sup>1-5</sup> or plasticity,<sup>6,7</sup> as well as tribological properties (wear-resistance and low friction behavior),<sup>5,8-13</sup> can be significantly improved.

Recently special attention has been paid to tough nanostructured zirconia thin films. Numerous preparation techniques can be used to prepare these systems, including physical vapor deposition,<sup>14</sup> sputtering,<sup>15</sup> spraying,<sup>8,10,12,16</sup> plasma-assisted deposition,<sup>17</sup> sol-gel deposition<sup>7,18</sup> and the emulsion precipitation technique.<sup>19,20</sup> In particular, the emulsion precipitation technique offers the advantage of directly coating flat substrates with well-controlled, agglomerate-free, monodisperse zirconia films with grain sizes below 30 nm.<sup>19</sup> These coatings are particularly suitable as wear-resistant, anticorrosive, insulating coatings with low thermal conductivity and relatively large thermal expansion coefficient.<sup>21</sup>

ZrO<sub>2</sub> occurs in three major crystalline polymorphic forms – monoclinic, tetragonal and cubic,<sup>17</sup> depending on temperature and pressure. The monoclinic structure is stable at room temperature and undergoes a reversible martensitic phase transformation at about 1200°C into the tetragonal phase. The transformation from the tetragonal to the monoclinic phase during thermal cycling is accompanied by a volume expansion of 3% to 5%, which can lead to failure by cracking. The metastable tetragonal phase of zirconia at the application temperature can be achieved through control over the dopant content and its distribution<sup>22</sup> or by limiting the grain size to the nanoscale, between 6 nm and 30 nm,<sup>16,23-25</sup> depending on hydrostatic and/or non-hydrostatic stresses present. The metastable tetragonal phase of zirconia stabilized by dopants may transform to the monoclinic phase under the application of stress,<sup>22</sup> for instance introduced by mechanical polishing, ion-bombarding, or electron beam irradiation.<sup>26</sup> The phase transformation is promoted by increasing the average grain size<sup>22,27,28</sup> and has been reported to be always accompanied with microcracking.<sup>22</sup> The transformation of tetragonal nanostructured zirconia was associated with an enlargement of the zirconia nanocrystallites above a critical size.<sup>16</sup>

The phase transformation can affect tribological properties (wear-resistance and friction coefficient), which are determined by plastic deformation, inter-crystalline microfracture, grain

---

fragmentation, and the formation of surface layers.<sup>27</sup> The observation that the wear volume increases with increasing grain size can be attributed to a higher degree of transformation of tetragonal to monoclinic phase, which is accompanied with microcracking.<sup>22,28</sup> Different wear mechanisms were observed for traditional zirconia coatings and nanostructured zirconia.<sup>8,10</sup> The wear mechanism of traditional zirconia in the high load regime (80 N) is mainly brittle fracture, delamination and plastic deformation, while that of nanostructured zirconia is plastic deformation and microcracking. The improvement in wear-resistance of nanostructured zirconia is attributed to an enhancement of mechanical properties, such as increased hardness and plasticity.<sup>12</sup> No significant influence of the grain size on the friction coefficient was observed for grain sizes in the micrometer range.<sup>29</sup> However, it has been shown that friction is reduced for nanostructured zirconia in comparison with traditional zirconia.<sup>8,10,27</sup> Low friction coefficients were observed for pure tetragonal nanostructured zirconia (against a steel ball  $\mu \sim 0.13 - 0.15$  for loads of 0.5 N).<sup>7</sup>

The importance of grain boundaries for the mechanical properties and tribological properties of, *e.g.* ceramics on the one hand and the mentioned development of improved materials with grain sizes in the sub-100 nm regime on the other hand, necessitates the application of characterization techniques that address the underlying physics at the relevant length scale.

In this general context, the potential of atomic force microscopy (AFM) has been realized for topographical, as well as nanotribological measurements.<sup>30</sup> This technique offers the possibility to study tribology down to the nanometer scale, in optimum cases on the single asperity level, as reviewed by Carpick and Salmeron.<sup>31</sup> For single asperity contacts, friction force is proportional to the real area of contact. The sum of the frictional effects occurring at many individual small asperities results in multi-asperity friction, as discussed in Chapter 2. The investigation of “point contact friction” of these small asperities is essential for a fundamental understanding of frictional processes. Despite the success of AFM friction measurements on inorganic, and most notably on organic and polymeric surfaces,<sup>30,32-44</sup> the application of AFM friction analysis to ceramics is limited to very few studies on systems like Ti<sub>3</sub>SiC<sub>2</sub>, MoS<sub>x</sub> or SiC.<sup>45-48</sup>

In this Chapter, the nanotribological properties of ultrathin nanostructured tetragonal ZrO<sub>2</sub> coatings on oxidized Si(100), prepared by the emulsion precipitation technique, as assessed by AFM-based friction force microscopy under full environmental control, are discussed. In addition to validating nanotribology on ceramic coatings by AFM, the effects of grain size and humidity on the friction coefficient were investigated. In comparison with the reference sample

of Si(100) with native oxide layer, ultrathin nanostructured ZrO<sub>2</sub> coatings showed a significantly reduced friction coefficient under all conditions.

## 6.2. Morphology

The morphology and the chemical composition of the film surfaces were characterized first to establish the relevant characteristics of the ultrathin coatings for the subsequent tribological measurements. In particular, the possible effect of the different sintering conditions was investigated.

The morphology of a series of nanocrystalline zirconia samples, prepared by using different sintering conditions, was investigated by intermittent contact TM-AFM. The different sintering conditions (temperatures 600°C - 1000°C, times 3 h - 15 h) resulted in specimens exhibiting different grain sizes in the range of 12 - 30 nm, as shown in the TM-AFM images displayed in Figure 6-1. While the Si(100) substrate appears homogeneous and featureless ( $R_{\text{rms}} = 0.2 \pm 0.1$  nm on a scan size of 300 nm × 300 nm), the ZrO<sub>2</sub> coatings were crack-free and consisted of densely packed and uniformly shaped, homogeneous grains. Agglomerated structures were absent. An average grain size ( $R_{\text{rms}}$  on a scan size of 300 nm × 300 nm) of  $12 \pm 2$  nm ( $R_{\text{rms}} = 0.6 \pm 0.5$  nm),  $20 \pm 3$  nm ( $R_{\text{rms}} = 1.3 \pm 1.0$  nm) and  $30 \pm 4$  nm ( $R_{\text{rms}} = 1.6 \pm 1.3$  nm), was revealed from the quantitative analysis of the TM-AFM images in Figure 6-1(a)-(c), respectively.

The effect of different sintering conditions on grain size is shown in Figure 6-2. The grain size increased monotonically from 12 nm to 20 nm with increasing sintering temperature in the range of 600°C - 1000°C (Figure 6-2(a)). Longer sintering time resulted in more pronounced grain growth, which can be seen in Figure 6-2(b). The films sintered at 1000°C for 3 hours consisted of 20 nm grains, for longer sintering time (10 – 15 hours) the grains reached 30 nm size.

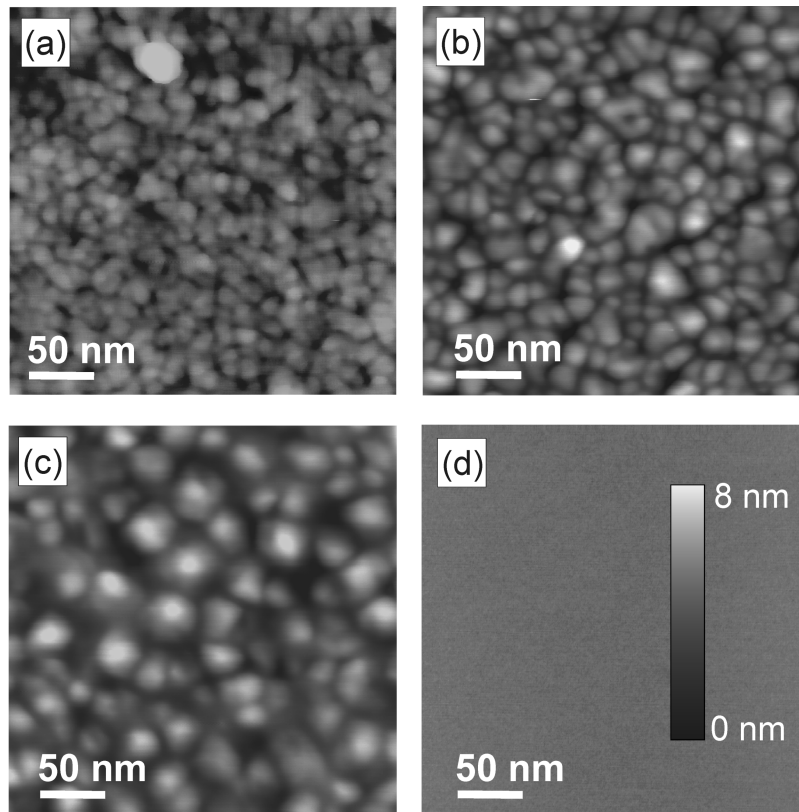


Figure 6-1. TM-AFM height images of nanostructured ZrO<sub>2</sub> coatings on oxidized Si(100) sintered (a) for 3 hours at 600°C, (b) for 3 hours at 1000°C, (c) 10 hours at 1000°C, as well as (d) bare oxidized Si(100). The height (z) scale (see inset in (d)) covers height differences of 8 nm from dark to bright. Average grain sizes were: (a) 12 nm ± 2 nm, (b) 20 nm ± 3 nm, and (c) 30 nm ± 5 nm.

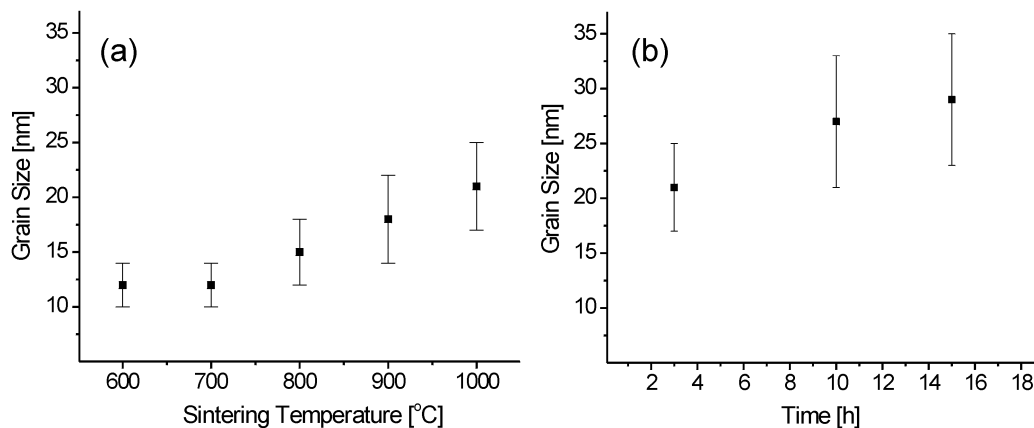


Figure 6-2. Grain size of nanostructured ZrO<sub>2</sub> as a function of (a) sintering temperature (for a sintering time of 3 hours) and (b) sintering time (at a sintering temperature of 1000°C) unveiled by TM-AFM. The data shown is based on the analysis of 100 - 150 measured peak-to-peak intergrain distances for each set of conditions and is expressed as arithmetic mean ± standard deviation  $\sigma$ . The histograms of the grain size distributions of the nanostructured ZrO<sub>2</sub> are shown in Appendix 6-1.

The kinetics of grain growth in nanocrystalline materials has been investigated by several authors<sup>49</sup> and it was found to be similar to the kinetics in conventional materials with micrometer grain size. In general, it is observed that the grain size is increasing with temperature and time.<sup>23,27,50</sup> Our observations are hence in full agreement with the literature.

As reported by Woudenberg *et al.*<sup>19,51</sup> the nanostructured zirconia investigated here exists in the metastable tetragonal phase up to a sintering temperature of 1000°C as a result of the lower surface energy of the tetragonal zirconia.<sup>23-25</sup> During longer annealing times at 1000°C a tetragonal to monoclinic phase transition takes place when the critical grain size is exceeded and in consequence two crystallographic phases may coexist.

### 6.3. Film characterization

The surface atomic composition of freshly cleaned zirconia samples was analyzed by XPS. To assess the effect of removal of organic contaminations the data was acquired as a function of oxygen-plasma cleaning time. The amount of carbon decreased with increasing cleaning time and reached plateau value after 5 minutes. Compared to the theoretical composition, we observed some enrichment in oxygen (Table 6-1).

Table 6-1. Selected XPS data measured on ZrO<sub>2</sub> samples after different oxygen plasma cleaning times.

O <sub>2</sub> -plasma cleaning time [min]	O/Zr ratio	C concentration [atom-%] (error ± 3%)
0	2.3	14.8
5	2.7	7.8
15	2.8	7.6
30	2.8	9.1

Using angle-dependent XPS measurements (30° - 90°) yielding different information depth (*ca.* 5 nm - 10 nm),<sup>52</sup> it was shown that the residual carbon is located at the film surface. The detected carbon is unlikely an airborne contamination, as judged from the significant impact of the plasma treatment time on sample surface composition, and may be a residue of surfactants



from the synthesis.<sup>19</sup> The presence of a thin surface layer (thickness ~ 1 nm) has been observed previously by cross-sectional TEM.<sup>51</sup>

The static contact angles measured with water on the zirconia and oxidized Si(100) samples was smaller than 15°, indicating a strongly hydrophilic, high-energy nature of these samples. During all AFM measurements discussed below, the complete wettability of the samples served as qualitative measure for the absence of contamination.

#### **6.4. Nanotribology – results and discussion**

The nanotribological properties of nanostructured zirconia and oxidized Si(100) were characterized by AFM measurements of friction forces as a function of normal forces in the elastic contact regime using Si<sub>3</sub>N<sub>4</sub> as a probe (tip) material.

Figure 6-3(a) shows the dependence of friction forces on normal forces for both nanostructured zirconia (12 nm grain size) and oxidized Si(100). The measurements were performed in dry atmosphere (< 5% RH) with a scan velocity of 6.6 μm/s. The friction force data were calibrated according to the wedge method described in Chapter 4. There was no hysteresis for data acquired with increasing and decreasing loads, respectively. A linear increase of the friction force with increasing normal forces was observed in the range of applied normal forces. The friction coefficients were determined from the slopes of linear least square fits. Compared to oxidized Si(100), a substantial reduction of friction forces, as well as friction coefficient, was observed for the nanostructured zirconia. The ratio of friction coefficients of the oxidized Si(100) with respect to the nanostructured zirconia was found to be  $2.00 \pm 0.25$ .

For low normal forces, friction force increased non-linearly, which is a result of a non-linear contact area-load dependence. This non-linear dependence may be attributed to the presence of single (or few) asperity contacts. Different power law functions ( $f \sim x^b$ ) were fitted for the data of Si(100) and nanostructured ZrO<sub>2</sub> (see Figure 6-3(b)), with resulting exponents *b* of 0.80 and 0.54, respectively. As described in Chapter 2, for ideal single asperity contacts (between sphere and flat sample), *b* is equal to 2/3 according to Hertz and JKR theories. The higher value of the parameter *b* observed for Si(100) may be attributed to an actual tip apex shape different from the usually parabolic shape, whereas the lower value for ZrO<sub>2</sub> could be related to the contact area-load dependence between nanometer grains and the tip. The measurements were reproduced with different probe tips and using the same probe on different AFM instruments (Digital Instruments multimode AFM (DI) and Molecular Imaging Pico SPM (MI)).

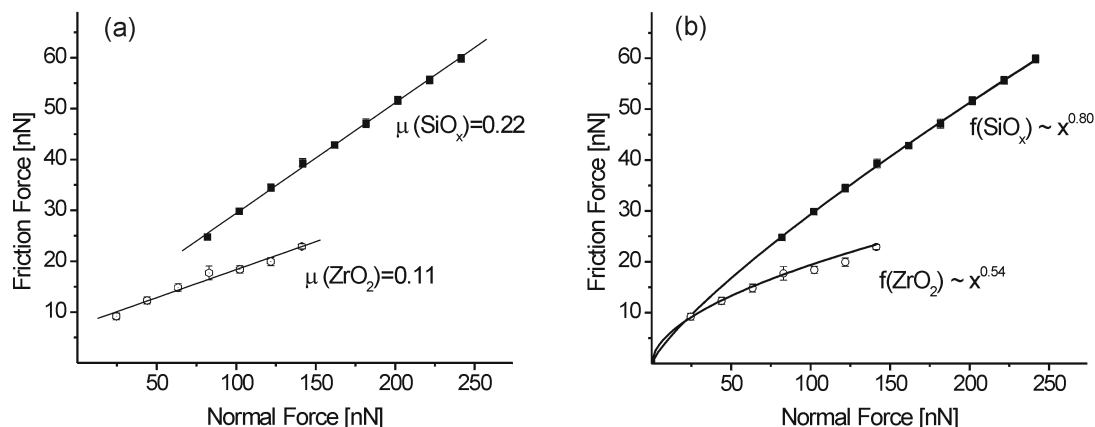


Figure 6-3. Friction force (calibrated differential photodiode output signal) versus normal force data for ZrO<sub>2</sub> and oxidized Si(100) surfaces measured in dry nitrogen atmosphere (< 5% relative humidity); the error bars indicate the standard deviation of the data analyzed for a given normal force): (a) Data fitted using linear least squares fitting. The friction coefficient of oxidized Si(100) is a factor of 2.0 higher compared to the friction coefficient of ZrO<sub>2</sub>. (b) Data fitted to power law functions.

The stability of the probe tips was checked using a calibration grating for quantitative tip shape analysis before and after the tribological measurements (see Chapter 3).<sup>53-55</sup> The samples' high wear-resistance was additionally confirmed using a cantilever with high normal spring constant (1 N/m) with integrated diamond-coated tip. No detectable wear of the sample was observed even after applying loads of 250 nN.

Similar to the friction forces, the pull-off forces recorded on the nanostructured zirconia were also significantly smaller than for the reference Si sample, even though both the nanostructured zirconia samples and oxidized Si(100) are similarly hydrophilic. For this type of samples, even in dry nitrogen atmosphere, there could be some residual water present on a sample surface forming water bridges with the probe tip.<sup>56-59</sup>

The observed difference in friction coefficients between the nanostructured zirconia and oxidized Si(100) may be attributed, in part, to the corrugations present on the nanostructured coating and, in part, to significantly different mechanical properties of the samples, such as hardness. This assertion is supported by reports for various materials showing that a decrease of grain size caused an increase in material hardness.<sup>1-5</sup> Moreover, it was also found that a nanocrystalline morphology might lead to a decrease in friction coefficient.<sup>7,8,10</sup> The contact area between a spherical Si<sub>3</sub>N<sub>4</sub> probe (radius 50 nm) and flat surface, estimated using Hertz theory for a load of 25 nN is 15 nm<sup>2</sup>.<sup>60</sup> In the case of an ideal single asperity contact between the probe and single zirconia grain (12 nm), the area of contact is 3 nm<sup>2</sup>; for a several asperity contact

(few zirconia grains in contact with the probe) the contact area is 4 – 6 nm<sup>2</sup>. With increasing load, the area of contact increases more strongly for the flat sample in comparison with single (several) asperity contact for the nanostructured sample. No significant difference in increased area of contact (which is directly proportional to the friction force)<sup>61</sup> as a function of load was observed for different grain sizes (12, 20 and 30 nm).

A similar set of nanotribology measurements for the nanostructured zirconia with 12 nm grain size and oxidized Si(100) was performed at 40% RH. Under higher humidity conditions the nanostructured zirconia showed again a lower friction coefficient compared to the reference. The ratio of the friction coefficients was again equal to 2. The data were reproduced using different tips showing that for the same probe the ratios of friction coefficients for nanostructured zirconia and the reference sample were the same as for the measurements performed in dry atmosphere. However, for the same sample (nanostructured zirconia or oxidized Si(100)) and different Si<sub>3</sub>N<sub>4</sub> probe tips, the ratio of friction coefficients between measurements performed at dry atmosphere condition and 40% RH varied significantly. This result is likely an effect of different sample-tip contact area caused by tip shape and size, and the formation of capillary water bridges in humid atmosphere.

#### 6.4.1. Effect of humidity

The dependence of friction coefficient of the nanostructured zirconia and oxidized Si(100) samples on humidity was also studied in detail (Figure 6-4). Two distinct regimes were observed for both samples. In the low humidity regime the friction coefficient increased monotonically with increasing humidity, while in the second, high humidity regime, the friction coefficient decreased. A transition between these two regimes (maximum of friction coefficient) is located around 40% RH. These results appear to be characteristic for hydrophilic samples, as for Si(100) and titanium oxide similar behavior was reported.<sup>62-67</sup> The first regime is attributed to an increase in adhesion and thus contact area between Si<sub>3</sub>N<sub>4</sub> probe and hydrophilic sample due to strong capillary forces. The drop in the value of the friction coefficient at higher humidity values likely results from the decreasing capillary pressure for the nanometer-scale AFM tip,<sup>62,63</sup> resulting in a strong decrease in the friction coefficient often attributed to water lubrication effects.<sup>5,29</sup> Moreover, the reduction in the friction coefficient observed for related ZrO<sub>2</sub> systems at high humidity was attributed in a recent study by Basu *et al.*<sup>68</sup> to the formation of a protective lubrication layer (Zr-OH). The formation of such a layer would also contribute to the here observed reduction in friction coefficient.

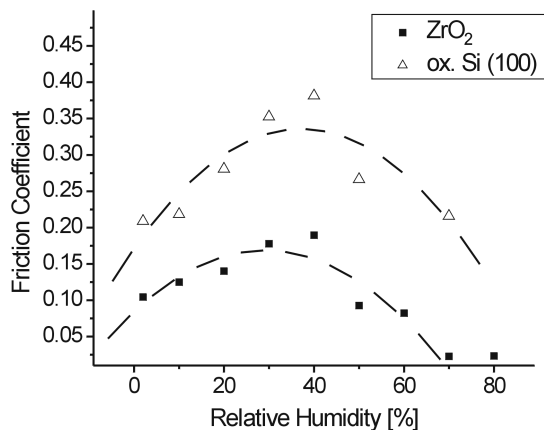


Figure 6-4. Variation of friction coefficient vs. relative humidity for ZrO<sub>2</sub> with 20 nm grain size and oxidized Si(100) samples. Measurements were taken with a Si<sub>3</sub>N<sub>4</sub> tip at a constant velocity of 6.6 μm/s. Each data point has been calculated as the mean value of 20 measurements.

#### 6.4.2. Effect of grain size

Finally, the possible influence of the nanostructure on the friction properties was studied for the nanostructured zirconia with 12 nm, 20 nm and 30 nm grain sizes, sintered at 600°C for 3 h, 1000°C for 3h and 1000°C for 10h, respectively. These measurements were performed in dry atmosphere conditions and 40% RH, respectively. Different tips and different scanning conditions were used (40% RH) in order to exclude any tip shape or time dependent contamination effects. One set of measurements, shown in Figure 6-5(a), was performed for the sequence of samples with increasing grain sizes (from 12 nm to 30 nm). A second set of measurements was carried out for specimens with decreasing grain sizes (from 30 nm to 12 nm). As summarized in Table 6-2, we did not observe any significant dependence of the friction coefficient on the grain size.

It is likely that the grain size (in this range) does not influence the nanotribological properties. This interpretation is in part supported by the quantitative grain size analysis. As shown in Figure 6-5(b)-(d), a clear difference in the grain size distribution could be observed for samples with 12 nm and 20 nm average grain size. Interestingly, the distributions for the samples with average grain size of 20 nm and 30 nm were found to overlap significantly. The insignificant difference in friction coefficients among those samples may thus indicate that no phase transformation from tetragonal to monoclinic phase occurred in the sample sintered at 1000°C for 10 h (30 nm) (see section 6.2.),<sup>51</sup> unless the friction coefficient of the monoclinic phase possesses a similar value compared to the tetragonal phase or unless the effect of larger grain size and the change in the phase canceled each other.

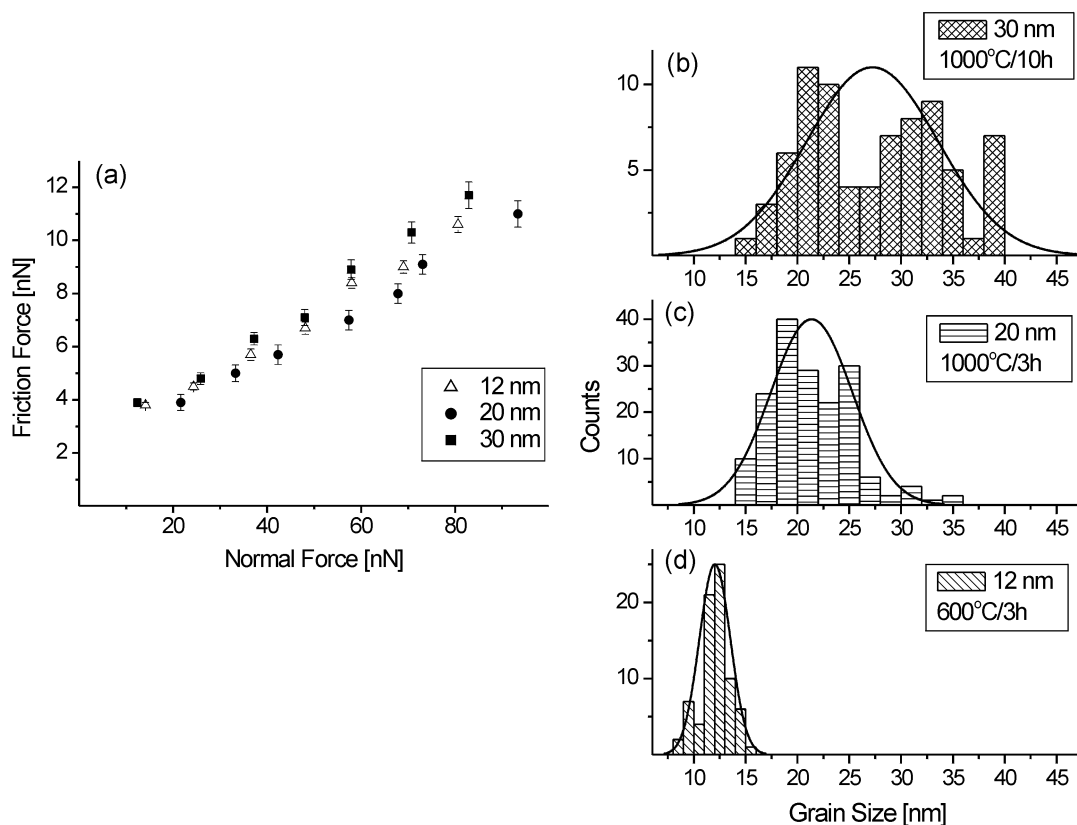


Figure 6-5. (a) Friction force vs. normal force for various grain sizes. Measurements were taken at a constant scan velocity of 6.6  $\mu\text{m/s}$  in dry nitrogen atmosphere. (b) – (d) Histograms of the grain size (solid lines correspond to Gaussian fits): (b) 30 nm, (c) 20 nm, and (d) 12 nm.

Table 6-2. Normalized friction coefficients of nanostructured ZrO<sub>2</sub> samples with different grain size measured with Si<sub>3</sub>N<sub>4</sub> tips. Measurements were taken in dry N<sub>2</sub> atmosphere and 40% RH at a constant velocity of 6.6  $\mu\text{m/s}$ . Samples were scanned in the following order: \*12, 20, and 30 nm, and \*\*30, 20, and 12 nm grain size.

Friction coefficient	Grain Size		
	12 nm	20 nm	30 nm
dry N <sub>2</sub> atmosphere	0.10 ± 0.01	0.13 ± 0.01	0.11 ± 0.01
40% RH*	tip 1	0.19 ± 0.02	0.17 ± 0.02
	tip 2	0.21 ± 0.02	0.17 ± 0.02
40% RH**	tip 1	0.19 ± 0.02	0.17 ± 0.02
	tip 2	0.21 ± 0.02	0.15 ± 0.02

Similar to the present results, wear was reported to be independent of the grain size of sub-micrometer and coarser alumina ceramics in wet environment.<sup>5</sup> This behavior could now be regarded as a more general feature of such oxide ceramics. In dry air, on the other hand, the presently observed absent influence of the grain size on the friction coefficient could be explained by insufficient nanostructural variations in these coatings.

## 6.5. Conclusions

Thin films of nanostructured zirconia on Si(100) showed a lower friction coefficient by a factor of two compared to oxidized Si(100) in dry nitrogen atmosphere and 40% RH, as revealed by AFM-based nanotribology. A pronounced effect of the RH on the friction coefficient was observed and quantified for ZrO<sub>2</sub> and oxidized Si(100). The friction coefficient increased with rising humidity, reached a maximum value for *ca.* 40% RH and then decreased. The increase in friction coefficient could be attributed to the formation of water capillary bridges, whereas at high humidity water may act as a lubricant. No significant difference in friction coefficient was observed among samples with grain sizes between 12 and 30 nm, which is attributed to insignificant differences in mechanical and nanostructural properties of the samples. The good tribological properties open the possibility for nanostructured zirconia to be applied as wear-resistant, low friction coatings on various materials.

## 6.6. Experimental

### 6.6.1. Materials

Dense, 20-50 nm thin nanostructured coatings of ZrO<sub>2</sub> with tetragonal symmetry were prepared in the Inorganic Materials Science group, University of Twente, by N. Siebelt via the modified emulsion precipitation technique, and were spin-coated on Si(100) wafers.<sup>19</sup> Different sintering conditions (temperatures between 600°C and 1000°C; sintering times between 3 and 15 hours; sintering rate: initially 5°C/min and for the last 50°C, 2°C/min) afforded coatings with different grain sizes. As reference samples, bare Si(100) wafers with native oxide layer were used. Prior to the measurements the samples were rinsed thoroughly with chloroform (Biosolve, Westford, MA) and ethanol (Biosolve), and were cleaned by oxygen-plasma (30 mA, 60 mTorr) using a SPI Supplies, Plasma Prep II (West Chester, PA) for 10 min.

### 6.6.2. AFM

**a. Morphology.** The morphology of the samples was revealed by intermittent contact (tapping) mode AFM (TM-AFM) (NanoScope III multimode AFM, Veeco/Digital Instruments, Santa Barbara, CA) using Si probes (type NCH, Nanosensors, Wetzlar, Germany). The tip radii (in the range of 7 - 9 nm) were characterized before and after the measurements using a Au-colloid calibration sample (diameter of the colloids  $13.2 \pm 1.3$  nm) kindly provided by Dr. E. S. Kooij (group of Solid State Physics, University of Twente).<sup>69,70</sup> The quantitative determination of the grain size was based on the statistical analysis of 100 - 150 measured peak to peak inter-grain distances. The results are expressed as arithmetic mean  $\pm$  standard deviation  $\sigma$ .

**b. Nanotribology.** Friction force measurements were performed with a PicoSPM scanning probe microscope (Molecular Imaging (MI), Tempe, AZ) equipped with an environmental chamber (Pyrex glass) using V-shaped Si<sub>3</sub>N<sub>4</sub> cantilevers (Model NP, Veeco Nano Probe, Santa Barbara, CA). The normal spring constants ( $k_N = 0.30 - 0.32$  N/m) and tip radii (in the range of 40 - 70 nm) were individually calibrated using the reference lever method<sup>71</sup> and a calibration grating (silicon grating TGT1, NT-MDT, Moscow, Russia), respectively. The humidity was precisely controlled from dry N<sub>2</sub> conditions to  $80\% \pm 2\%$  RH, as measured by a humidity sensor (SHT15, Sensirion, Zurich, Switzerland), while the temperature was maintained constant during all the measurements (25°C). Friction data in the form of images of differential photodiode output signal for trace and retrace ( $256 \times 256$  pixels; scan size  $1 \mu\text{m}^2$ ; scan velocity  $6.6 \mu\text{m/s}$ ) were acquired simultaneously for different normal forces (normal force is defined as the sum of pull-off force and externally applied load). The normal forces were limited to values  $< 100$  nN to work in the elastic contact regime without detectable tip wear.<sup>61,72</sup> Subsequent to a correction of the scanner hysteresis between trace and retrace using the MI software, the mean friction force  $\pm$  standard deviation  $\sigma$  was determined from an analysis of the difference images, as described by Hammerschmidt *et al.*<sup>73</sup> The wear-resistance of the coatings was tested with a stiff cantilever (1 N/m) comprising an integrated diamond-coated tip (DT-FMR, Nanosensors, Neuchatel, Switzerland). The friction force data were calibrated according to the wedge method described in Chapter 4.

### 6.6.3. X-ray photoelectron spectroscopy (XPS)

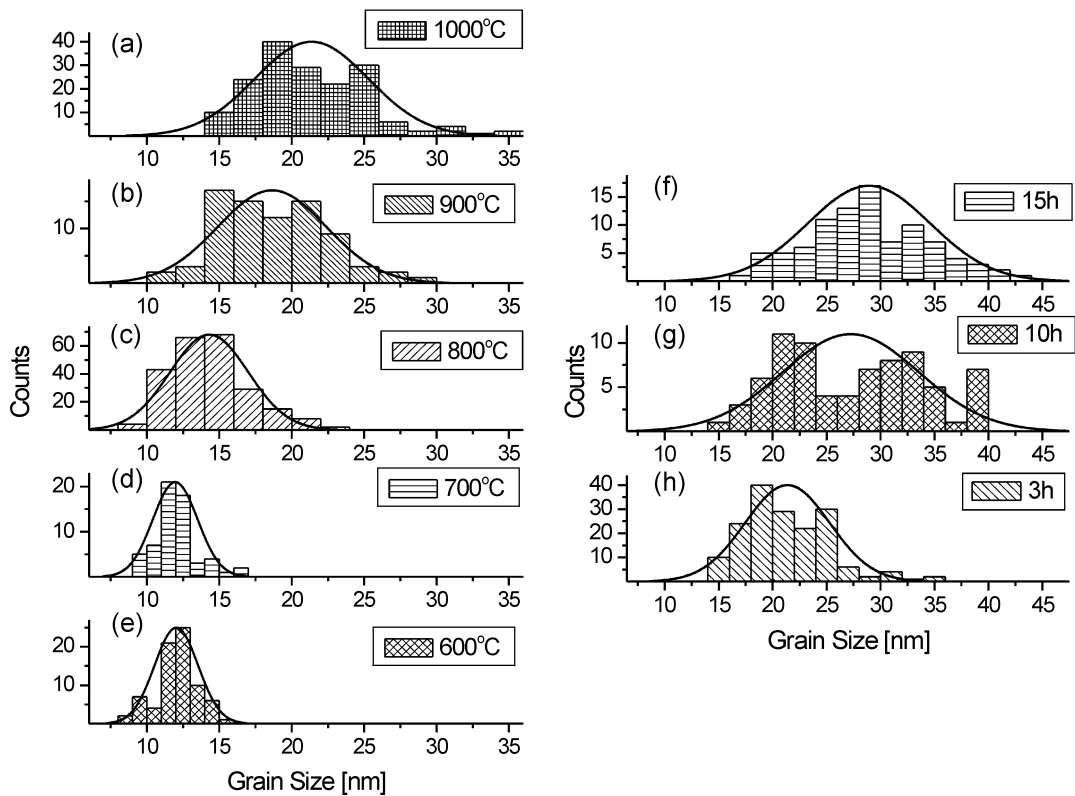
The surface composition of freshly cleaned samples was analyzed by angle-dependent XPS on a PHI Quantum 2000 Scanning ESCA microprobe (Chanhasen, MN). The spectra were recorded at a different take off angles (30°, 45° and 90°) providing different thickness information (*ca.* 5

nm, 7 nm and 10 nm).<sup>52</sup> The atomic concentrations were determined by numerical integration of the relative peak areas in the detailed element scans using the following sensitivity factors:<sup>52</sup> C1s [0.314], O1s [0.733] and Zr3d [2.767].

### **6.6.4. Contact angle measurements**

The values of static contact angles were measured with Millipore water as a probe liquid by using a contact angle microscope (OCA 15plus, Data Physics, Filderstadt, Germany). Contact angles were determined at room temperature and ambient humidity. A set of at least three different locations was taken for each sample.



**6.7. Appendix**

Appendix 6-1. Histograms of grain size of nanostructured ZrO<sub>2</sub> samples sintered at temperatures for various times: (a) - (e) 600°C - 1000°C for 3 h and (f) - (h) 1000°C for 3h - 15 h, as determined by TM-AFM. The data shown are based on the analysis of 100 - 150 measured peak-to-peak intergrain distances for each set of conditions.

---

**6.8. References**

- 1 Chaim, R.; Hefetz, M. *J. Mater. Sci.* **2004**, *39*, 3057-3061.
- 2 Akamatsu, H.; Azuma, K.; Fujiwara, E.; Yatsuzuka, M. *Jpn. J. Appl. Phys. Part 1 - Regul. Pap. Short Notes Rev. Pap.* **2002**, *41*, 399-404.
- 3 Zhang, S.; Fu, Y. Q.; Du, H. J.; Zeng, X. T.; Liu, Y. C. *Surf. Coat. Technol.* **2003**, *162*, 42-48.
- 4 Krell, A. *J. Am. Ceram. Soc.* **1995**, *78*, 1417-1419.
- 5 Krell, A. *Mater. Sci. Eng. A-Struct. Mater. Prop. Microstruct. Process.* **1996**, *209*, 156-163.
- 6 Mayo, M. J. *Mater. Des.* **1993**, *14*, 323-329.
- 7 Chen, Y. X.; Liu, W. M. *J. Am. Ceram. Soc.* **2002**, *85*, 2367-2369.
- 8 Chen, H.; Ding, C. X.; Zhang, P. Y.; La, P. Q.; Lee, S. W. *Surf. Coat. Technol.* **2003**, *173*, 144-149.
- 9 Hahn, H.; Averback, R. S. *J. Am. Ceram. Soc.* **1991**, *74*, 2918-2921.
- 10 Chen, H. A.; Zhang, Y. F.; Ding, C. X. *Wear* **2002**, *253*, 885-893.
- 11 Mukhopadhyay, A. K.; Mai, Y. W. *Wear* **1993**, *162*, 258-268.
- 12 Li, J. F.; Liao, H.; Wang, X. Y.; Normand, B.; Ji, V.; Ding, C. X.; Coddet, C. *Tribol. Int.* **2004**, *37*, 77-84.
- 13 Basu, B.; Lee, J. H.; Kim, D. Y. *J. Am. Ceram. Soc.* **2004**, *87*, 1771-1774.
- 14 Matsumoto, M.; Yamaguchi, N.; Matsubara, H. *Scr. Mater.* **2004**, *50*, 867-871.
- 15 Yashar, P.; Rechner, J.; Wong, M. S.; Sproul, W. D.; Barnett, S. A. *Surf. Coat. Technol.* **1997**, *94-5*, 333-338.
- 16 Chraska, T.; King, A. H.; Berndt, C. C. *Mater. Sci. Eng. A-Struct. Mater. Prop. Microstruct. Process* **2000**, *286*, 169-178.
- 17 Moulzolf, S. C.; Yu, Y.; Frankel, D. J.; Lad, R. J. *J. Vac. Sci. Technol. A-Vac. Surf. Films* **1997**, *15*, 1211-1214.
- 18 Liu, W. M.; Chen, Y. X.; Ye, C. F.; Zhang, P. Y. *Ceram. Int.* **2002**, *28*, 349-354.
- 19 Woudenberg, F. C. M.; Sager, W. F. C.; Sibelt, N. G. M.; Verweij, H. *Adv. Mater.* **2001**, *13*, 514-516.
- 20 Tai, C. Y.; Lee, M. H.; Wu, Y. C. *Chem. Eng. Sci.* **2001**, *56*, 2389-2398.
- 21 Gell, M. *Mater. Sci. Eng. A-Struct. Mater. Prop. Microstruct. Process.* **1995**, *204*, 246-251.
- 22 Basu, B.; Vleugels, J.; Van Der Blest, O. *J. European Ceram. Soc.* **2004**, *24*, 2031-2040.
- 23 Garvie, R. C. *J. Phys. Chem.* **1965**, *69*, 1238-1243.
- 24 Garvie, R. C. *J. Phys. Chem.* **1978**, *82*, 218-224.
- 25 Garvie, R. C.; Goss, M. F. *J. Mater. Sci.* **1986**, *21*, 1253-1257.
- 26 Schofield, M. A.; Aita, C. R.; Rice, P. M.; Gajdardziska-Josifovska, M. *Thin Solid Films* **1998**, *326*, 117-125.
- 27 Gahr, K. H. Z.; Bundschuh, W.; Zimmerlin, B. *Wear* **1993**, *162*, 269-279.
- 28 He, Y. J.; Winnubst, A. J. A.; Burggraaf, A. J.; Verweij, H.; vanderVarst, P. G. T.; deWith, G. J. *European Ceram. Soc.* **1997**, *17*, 1371-1380.
- 29 Krell, A.; Klaffke, D. *J. Am. Ceram. Soc.* **1996**, *79*, 1139-1146.
- 30 Schönherr, H.; Vancso, G. J. *Mater. Sci. Eng. C-Biomimetic Supramol. Syst.* **1999**, *8-9*, 243-249.
- 31 Carpick, R. W.; Salmeron, M. *Chem. Rev.* **1997**, *97*, 1163-1194.
- 32 Pearce, R.; Vancso, G. J. *Polymer* **1998**, *39*, 6743-6746.

- 
- 33 Schönherr, H.; Kenis, P. J. A.; Engbersen, J. F. J.; Harkema, S.; Hulst, R.; Reinhoudt, D. N.; Vancso, G. J. *Langmuir* **1998**, *14*, 2801-2809.
- 34 Schönherr, H.; Vancso, G. J. *Macromolecules* **1997**, *30*, 6391-6394.
- 35 Smith, P. F.; Nisman, R.; Ng, C.; Vancso, G. J. *Polym. Bull.* **1994**, *33*, 459-464.
- 36 Mougin, K.; Castelein, G.; Haidara, H. *Tribol. Lett.* **2004**, *17*, 11-17.
- 37 Noy, A.; Frisbie, C. D.; Rozsnyai, L. F.; Wrighton, M. S.; Lieber, C. M. *J. Am. Chem. Soc.* **1995**, *117*, 7943-7951.
- 38 Marti, A.; Hahner, G.; Spencer, N. D. *Langmuir* **1995**, *11*, 4632-4635.
- 39 Lio, A.; Charych, D. H.; Salmeron, M. *J. Phys. Chem. B* **1997**, *101*, 3800-3805.
- 40 Liu, Y. H.; Evans, D. F.; Song, Q.; Grainger, D. W. *Langmuir* **1996**, *12*, 1235-1244.
- 41 Xiao, X. D.; Hu, J.; Charych, D. H.; Salmeron, M. *Langmuir* **1996**, *12*, 235-237.
- 42 Ge, S. R.; Takahara, A.; Kajiyama, T. *Langmuir* **1995**, *11*, 1341-1346.
- 43 Liu, Y. H.; Wu, T.; Evans, D. F. *Langmuir* **1994**, *10*, 2241-2245.
- 44 Overney, R. M.; Meyer, E.; Frommer, J.; Brodbeck, D.; Luthi, R.; Howald, L.; Guntherodt, H. J.; Fujihira, M.; Takano, H.; Gotoh, Y. *Nature* **1992**, *359*, 133-135.
- 45 Zhang, X. L.; Celis, J. P. *Appl. Surf. Sci.* **2003**, *206*, 110-118.
- 46 Myhra, S.; Summers, J. W. B.; Kisi, E. H. *Mater. Lett.* **1999**, *39*, 6-11.
- 47 Crossley, A.; Kisi, E. H.; Summers, J. W. B.; Myhra, S. *J. Phys. D-Appl. Phys.* **1999**, *32*, 632-638.
- 48 Sundararajan, S.; Bhushan, B. *Wear* **1998**, *217*, 251-261.
- 49 Vassen, R.; Stover, D. *J. Mater. Process. Technol.* **1999**, *93*, 77-84.
- 50 Northwood, D. O.; Alpas, A. T. *Nanostruct. Mater.* **1998**, *10*, 777-793.
- 51 Woudenberg, F. C. M. *Nanostructured Oxide Coatings via Emulsion Precipitation*. Ph.D. Thesis, University of Twente, Enschede, 2001.
- 52 Wagner, C. D.; Riggs, W. M.; Davis, L. E.; Moulder, J. F. *Handbook of X-ray Photoelectron Spectroscopy*. Eden Prairie: Minnesota, 1979.
- 53 Montelius, L.; Tegenfeldt, J. O. *Appl. Phys. Lett.* **1993**, *62*, 2628-2630.
- 54 Bykov, V.; Gologanov, A.; Shevyakov, V. *Appl. Phys. A-Mater. Sci. Process.* **1998**, *66*, 499-502.
- 55 Atamny, F.; Baiker, A. *Surf. Sci.* **1995**, *323*, L314-L318.
- 56 Riedo, E.; Pallaci, I.; Boragno, C.; Brune, H. *J. Phys. Chem. B* **2004**, *108*, 5324-5328.
- 57 Patton, S. T.; Cowan, W. D.; Eapen, K. C.; Zabinski, J. S. *Tribol. Lett.* **2000**, *9*, 199-209.
- 58 Chilamakuri, S. K.; Bhushan, B. *J. Appl. Phys.* **1999**, *86*, 4649-4656.
- 59 Bocquet, L.; Charlaix, E.; Ciliberto, S.; Crassous, J. *Nature* **1998**, *396*, 735-737.
- 60 Hertz, H. *J. Reine Angew. Math.* **1882**, *92*, 156-171.
- 61 Schwarz, U. D.; Zwörner, O.; Köster, P.; Wiesendanger, R. *Phys. Rev. B* **1997**, *56*, 6987-6996.
- 62 Xiao, X. D.; Qian, L. M. *Langmuir* **2000**, *16*, 8153-8158.
- 63 Qian, L. M.; Tian, F.; Xiao, X. D. *Tribol. Lett.* **2003**, *15*, 169-176.
- 64 Bhushan, B.; Dandavate, C. *J. Appl. Phys.* **2000**, *87*, 1201-1210.
- 65 Sirghi, L. *Appl. Phys. Lett.* **2003**, *82*, 3755-3757.
- 66 Sirghi, L.; Aoki, T.; Hatanaka, Y. *Surf. Rev. Lett.* **2003**, *10*, 345-349.
- 67 Scherge, M.; Li, X.; Schaefer, J. A. *Tribol. Lett.* **1999**, *6*, 215-220.
-

- 68 Basu, B.; Vitchev, R. G.; Vleugels, J.; Celis, J. P.; van der Biest, O. *Acta Mater.* **2000**, *48*, 2461-2471.
- 69 Xu, S.; Arnsdorf, M. F. *J. Microsc.-Oxf.* **1997**, *187*, 43-53.
- 70 Xu, S.; Arnsdorf, M. F. *J. Microsc.-Oxf.* **1994**, *173*, 199-210.
- 71 Tortonese, M.; Kirk, M. *Proc. SPIE* **1997**, *3009*, 53-60.
- 72 Schwarz, U. D.; Zwörner, O.; Köster, P.; Wiesendanger, P. *Phys. Rev. B* **1997**, *56*, 6997-7000.
- 73 Hammerschmidt, J. A.; Gladfelter, W. L.; Haugstad, G. *Macromolecules* **1999**, *32*, 3360-3367.

# Chapter 7

## Nano- and microtribology of low friction wear-resistant ceramics: From micro- to nanotribology

*In this Chapter, the tribological properties of CuO doped 3Y-TZP ceramics worn by alumina balls in pin-on-disc experiments are discussed. The changes in morphology and friction coefficient in and outside the corresponding pin-on-disc wear tracks were analyzed by AFM for a broad range of velocities (6 - 500  $\mu\text{m/s}$ ). During the initial sliding the layer of surface contaminations was removed and wear of high asperities occurred, as inferred from decreasing values of rms roughness measured in the wear tracks. The friction coefficient  $\mu_{\text{Si}_3\text{N}_4}^{\text{nano}}$  determined on these modified flattened areas by AFM was significantly higher compared to the value of  $\mu_{\text{Si}_3\text{N}_4}^{\text{micro}}$  determined on the micrometer scale in pin-on-disc experiments. Longer sliding resulted in values of  $\mu_{\text{Si}_3\text{N}_4}^{\text{nano}}$  that were comparable with  $\mu_{\text{Si}_3\text{N}_4}^{\text{micro}}$  ( $\mu_{\text{Si}_3\text{N}_4} \approx 0.30$ ). Thus, AFM provides evidence for the presence of a soft layer in the wear tracks that was generated during sliding in the pin-on-disc tests. These data form the basis for complementary nano- and microtribology analyses and the bridging of the gap of length and time scales.*

## 7.1. Introduction

As discussed in Chapter 2, friction force has contributions from different phenomena, such as wear-less friction, plastic deformation of asperities, lateral forces to move debris particles, viscous forces and ploughing terms.<sup>1</sup> To understand the complex behavior of real contacts and to ultimately be able to design high performance materials based on first principles, it is desirable to learn about the properties of single asperity interfacial friction and the energy dissipation at the fundamental level.<sup>2,3</sup> Based on this understanding and, *e.g.*, the understanding of plastic deformation of smaller asperities etc., multiasperity friction and the role of different mechanisms can be addressed. Until now, it was practically impossible to bridge the various length and times scales between nanotribology and microtribology.<sup>4</sup> Some of the instrumental and technical limitations have been successfully overcome, as described in Chapters 3, 4 and 5 of this Thesis. Hence previously unattainable data can now be acquired.

For technological applications materials that exhibit a low friction coefficient ( $\leq 0.2$ ) and high wear-resistance (wear rate  $< 10^{-6} \text{ mm}^3\text{N}^{-1}\text{m}^{-1}$ ) are required.<sup>5</sup> Liquid lubrication (mainly based on organic materials) is the most widely used method to reduce the interfacial shear strength resulting in low friction systems.<sup>6</sup> However, for some applications, such as those in high temperature, in cryogenic environment and in high vacuum, liquid lubricants do not function properly or can be a source of contamination.<sup>7</sup> In these applications dry sliding is used. Here friction can be reduced by creating a weak interface between two opposing surfaces that are made of a hard material that supports the normal load. This can be realized by using a thin layer of soft material (solid lubricant) to provide easy shear.<sup>8</sup> Solid lubrication is obtained either by covering the surface with a thin layer of soft material (graphite,  $\text{MoS}_2$  and  $\text{CF}_x$ )<sup>9-14</sup> or by a self-lubricating composite,<sup>15,16</sup> in which a second phase composed of soft particles is embedded in the base material. Due to the high contact pressure during sliding a soft interfacial layer is generated. The friction properties of these layered systems depend critically on the thickness of the layer formed. When the layer is very thin, the interaction is dominated by the contact of the slider asperities with the substrate, thus the friction coefficient is equivalent to the value for the substrate without the layer. For thick layers, the coefficient of friction is similar to the bulk value of the layer material used.

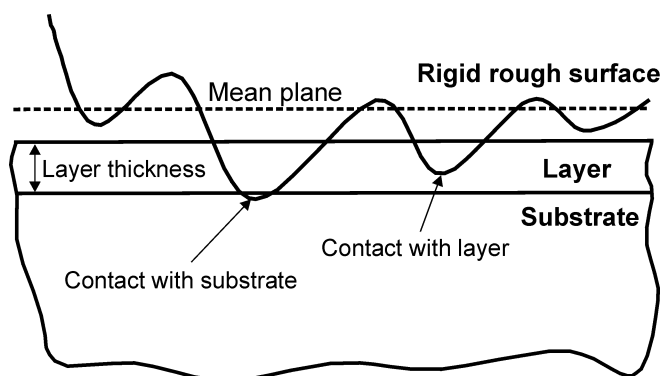


Figure 7-1. Schematic model for layered systems (after reference 17).

Self-lubricating composites have been reported for metals and ceramics.<sup>16,18-20</sup> A reduction of friction was observed for alumina and zirconia systems doped with CuO sliding against alumina.<sup>15,21,22</sup> The experimental results showed that an addition of 8 mol% of CuO to 3 mol% yttria-stabilized tetragonal zirconia (3Y-TZP) reduced the friction coefficient from  $\sim 0.7$  to  $\leq 0.3$ . Combined transmission electron microscopy (TEM) and energy dispersive X-ray (EDX) analysis of the doped 3Y-TZP revealed crystalline zirconia grains of several hundred nanometers and crystalline Cu-rich phases among the zirconia grains. Nanoindentation tests performed on the wear tracks, where low friction was observed, showed a significantly reduced hardness of 6 GPa as compared to the bulk value of 14 GPa.<sup>17,21</sup>

To explain these results, Pasaribu *et al.*<sup>23</sup> proposed a deterministic friction model for layered systems. In this model, the rough surface is represented by a distribution of spherically shaped asperities with different radii and heights. The contributions of both adhesion and ploughing to friction are taken into account by a summation of the resistance to motion experienced by each asperity in elastic, elastic-plastic and plastic contact. Using this model, the value of the microscopic friction coefficient can be successfully predicted for a known (or assumed) thickness of the soft layer and the percentage of the layer coverage on the wear track. This calculated value leads to *quantitative* agreement with the experimental data. Even though the model can successfully predict the macroscopic friction coefficient, the mechanism responsible for the formation of this layer remains unknown to date.

To obtain a better understanding of the processes that occur during sliding of an alumina ball on CuO doped 3Y-TZP ceramics, the wear tracks obtained in such microtribological experiments were investigated by AFM for various sliding distances. In addition, the nanotribological properties of the wear track and the third body (*i.e.* the layer) formed in the pin-on-disc measurements were investigated for a broad range of scanning velocities, thus aiming at bridging across the length and time scales of nano- and microtribology.

## 7.2. Morphology of 3Y-TZP doped with CuO

To investigate and characterize the previously observed formation of a third body layer in the wear tracks, the morphology of 3Y-TZP specimens doped with 8 mol% CuO was characterized using scanning electron and atomic force microscopy. Several wear tracks were generated in microtribology tests with different sliding distances (Figure 7.2).

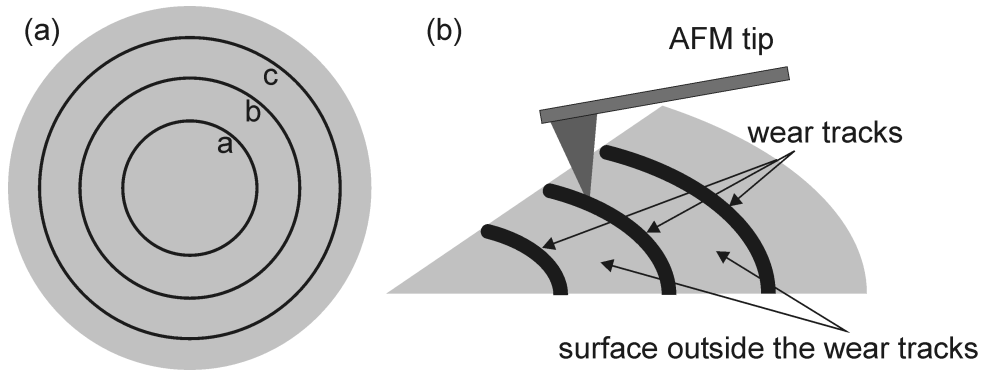


Figure 7-2. (a) Schematic of a pin-on-disc sample with wear tracks a, b and c for different sliding distances. (b) Schematic of AFM experiment on the wear track (not to scale).

Figure 7-3 shows SEM images taken on a sample worn for 300 meters (track C). The wear track (Figure 7-3(b)) appeared smoother as compared to the area outside the wear track (Figure 7-3(c)). Several holes up to 30  $\mu\text{m}$  in diameter were evenly distributed on the surface that appeared heterogeneous on the micrometer scale.

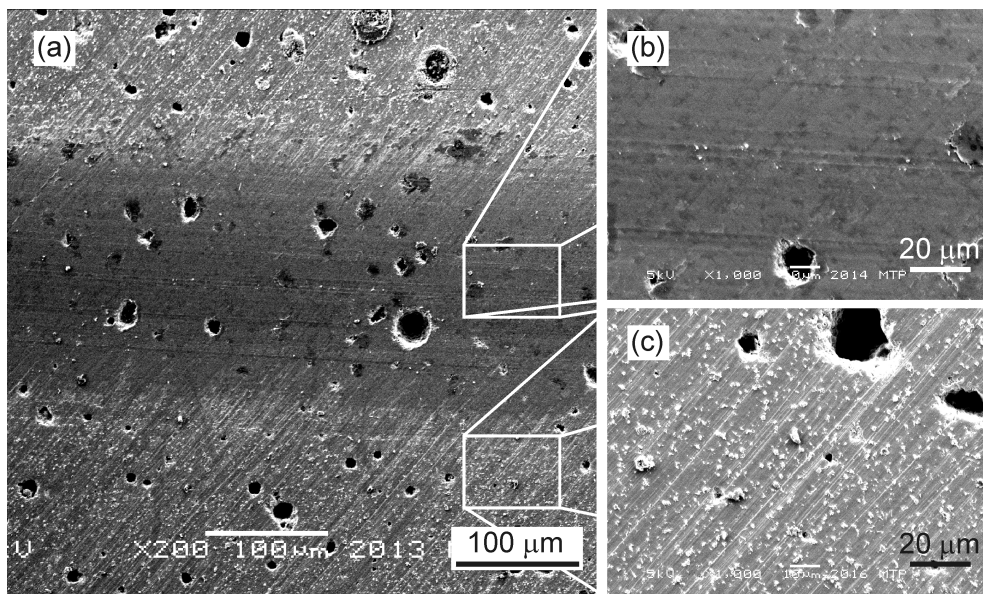


Figure 7-3. SEM images of (a) wear track in 3Y-TZP sample doped with 8 mol% CuO after sliding with an  $\alpha\text{-Al}_2\text{O}_3$  ball for 300 m (track C). Panels (b) and (c) show enlarged views of areas inside and outside the track, respectively.



The surface in the wear tracks and the area outside the wear tracks were also analyzed using AFM to obtain a more detailed view of the morphological features. Figure 7-4 shows the topography of a center part in track C (300 m). The diagonal scratches in the image (Figure 7-4(a)) are a result of the polishing (compare also with Figure 7-3), whereas the vertical lines originated from wear in the microtribology test. Several particles of a few micrometer diameter were present on the surface. The particles are likely debris of the wear process. The surface was rough with peak-to-valley height differences of 200 nm (rms roughness  $R_{\text{rms}} = 58 \pm 3$  nm), see Figure 7-4(c). Locally, the surface in the wear track was apparently plastically deformed during sliding and large smooth areas were found (Figure 7-4(b)).

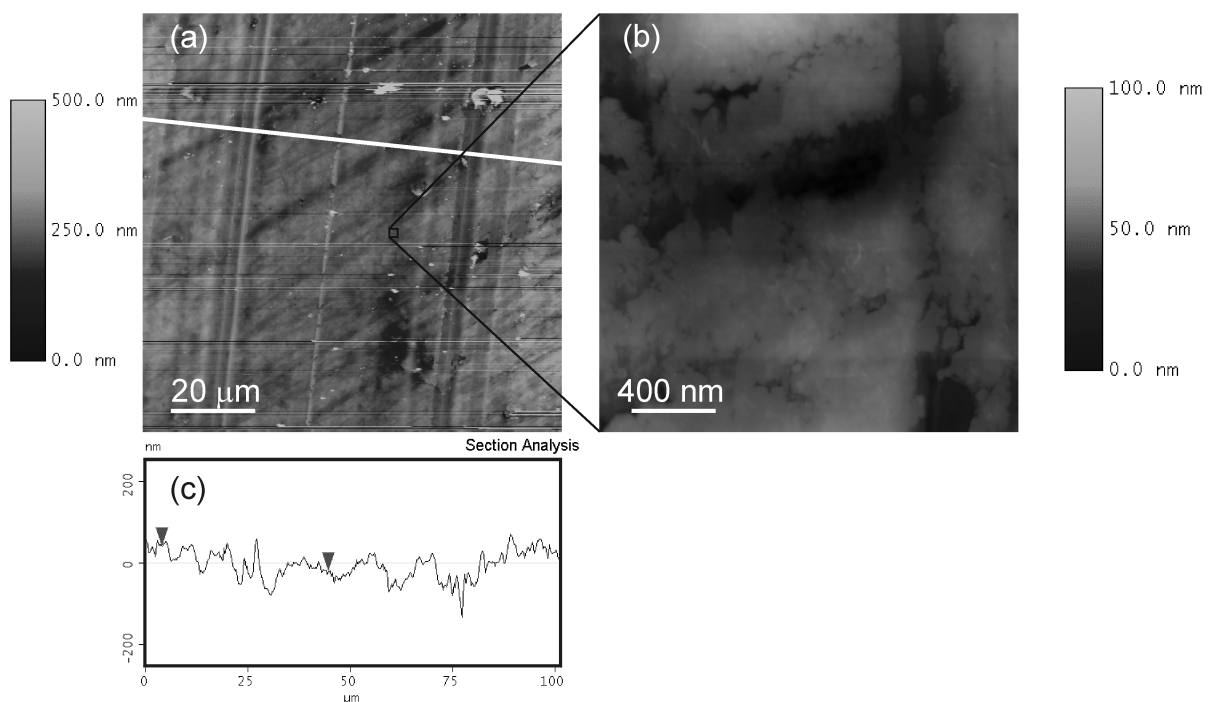


Figure 7-4. (a), (b) Tapping mode (TM)-AFM height images of a center part in track C after 300 meter of sliding and (c) cross-section of image (a) along the white line.

The tracks obtained for different sliding distances were subsequently analyzed to follow the morphological changes during sliding in the pin-on-disc experiment (Figure 7-5). Already after 20 meters of sliding the surface was flattened locally, see Figure 7-5(a). For sliding distances of 30 m and 300 m larger smooth areas were observed, which were very likely generated by plastic deformation (Figure 7-5(b) and (c)). The coverage of the plastically deformed areas increased in time.

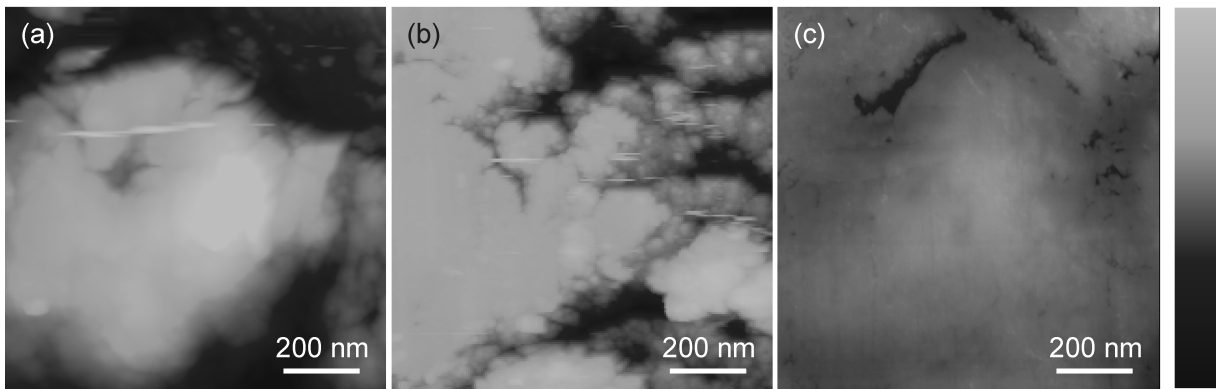


Figure 7-5. Contact mode AFM images of wear tracks for different sliding distances: (a) 20 m (track A), (b) 30 m (track B), and (c) 300 m (track C), respectively. The corresponding height ( $z$ ) scales cover height differences from dark to bright of 250 nm (for (a) and (b)), and 100 nm (for (c)), respectively. The corresponding roughnesses were (a)  $R_{\text{rms}} = 56 \pm 2$  nm, (b)  $R_{\text{rms}} = 52 \pm 2$  nm, and (c)  $R_{\text{rms}} = 6.0 \pm 0.5$  nm.

### 7.3. Microtribology of 3Y-TZP doped with CuO

The microtribological properties, as well as the formation of the third body layer of CuO doped 3Y-TZP samples were investigated using an  $\alpha\text{-Al}_2\text{O}_3$  ball in a pin-on-disc tribometer. Different tracks were generated for various sliding distances. Figure 7-6 shows the measured friction coefficients as a function of sliding distance for various tracks.

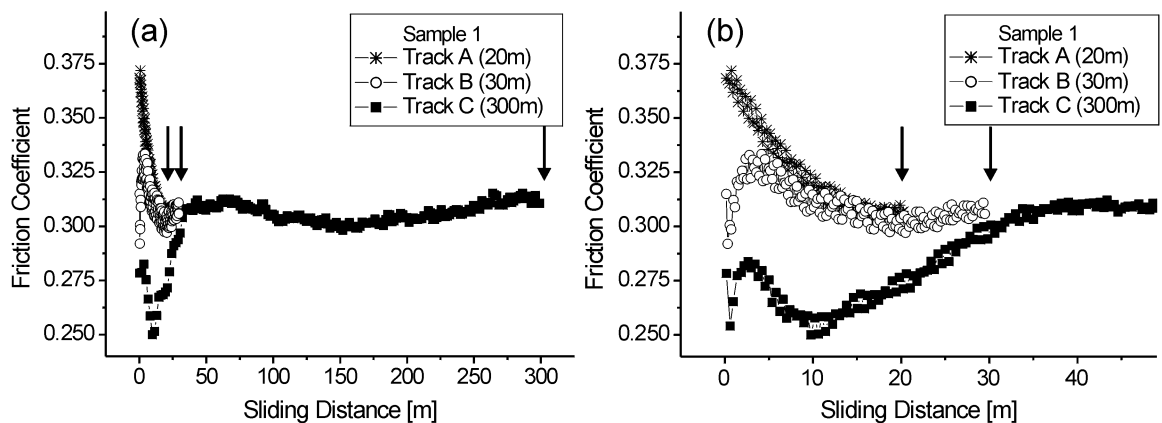


Figure 7-6. Coefficient of friction as a function of sliding distance for 3Y-TZP sample doped with 8 mol% CuO measured against an  $\alpha\text{-Al}_2\text{O}_3$  ball using a pin-on-disc tribometer (normal load 5 N, velocity  $5 \times 10^4 \mu\text{m/s}$ , 40% RH,  $25^\circ\text{C}$ ). Plot (b) is a magnified section of (a) showing the friction coefficient for the initial sliding distances. The arrows mark the end of each of these experiments.

The initial value of  $\mu_{\alpha\text{-Al}_2\text{O}_3}^{\text{micro}}$  varied between 0.25 – 0.35, after sliding for 100 meters the friction coefficient reached a steady state value of approximately 0.30 – 0.40. The initially low

$\mu_{\alpha\text{-Al}_2\text{O}_3}^{\text{micro}}$  is attributed to the presence of contaminations resulting in lubrication of the contacting surfaces.<sup>24</sup> The initial part of the plot was observed to be somewhat different for various nominally identical samples (see *e.g.* Appendix 7-1). As compared to the pure 3Y-TZP system ( $\mu_{\alpha\text{-Al}_2\text{O}_3}^{\text{micro}} = 0.7$ ),<sup>17</sup> a significant reduction in friction coefficient was observed.<sup>17</sup> In reference 21, Pasaribu, Sloetjes and Schipper reported that the surface was deformed plastically during sliding and that an interfacial layer was generated in the contact area (so-called third body formation).<sup>25</sup> The low friction behavior was associated with the presence of this thin layer that was shown to possess significantly lower hardness ( $H \cong 6$  GPa) than the bulk sample ( $H \cong 14$  GPa). Using these values and the model by Pasaribu *et al.* (see Chapter 6 in reference 17), the value of the microscopic friction coefficient can be successfully determined for known thickness of the soft layer and the percentage of the layer coverage on the wear track.

#### **7.4. Nanotribology of 3Y-TZP doped with CuO**

Using AFM the tribology on nanometer length scales was analyzed. Besides the locally resolved differences in tribological behavior, the attention was focused on analyzing the tribological properties of selected areas.

Simultaneous mapping of topography and friction force revealed that the wear tracks show an inhomogeneous friction on the nanometer scale in some areas (see Figure 7-7). Higher friction forces were measured in depressions, whereas smooth areas showed low friction forces. Most likely this result could be a consequence of local variations in the tip-sample interface caused by variable film thickness of the third body formed in the wear track. Whereas areas with a thicker film showed already the described effect of this soft layer, the areas that appeared lower in height in AFM images did not yet lead to a reduction of friction as the soft layer was here presumably too thin (compare Figure 7-1).

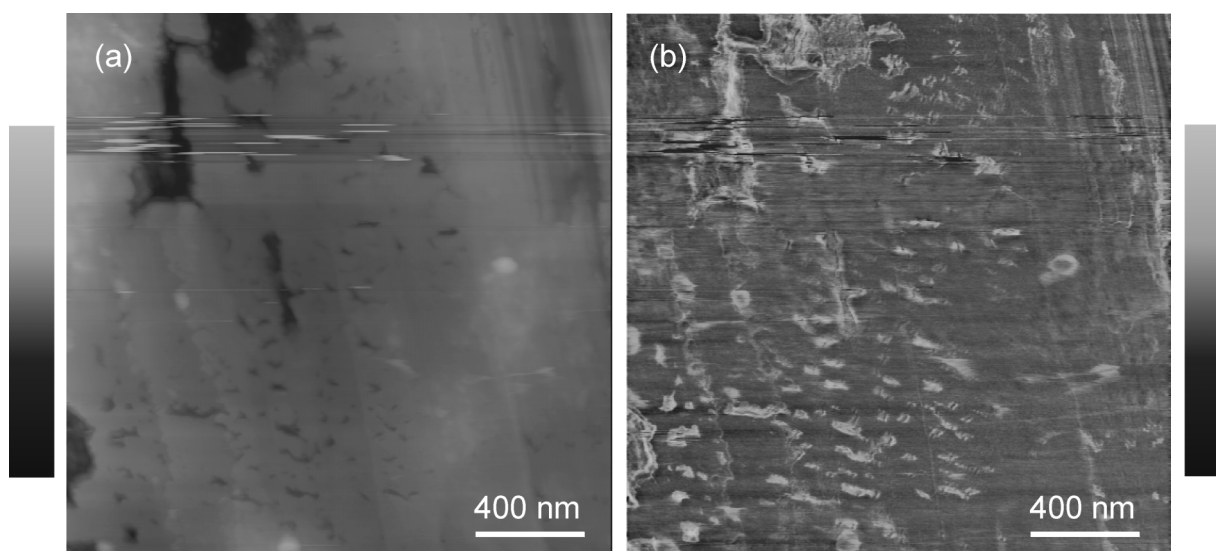


Figure 7-7. Contact mode AFM images of wear track C (300 m) using a  $\text{Si}_3\text{N}_4$  tip: (a) topography, the height (z) scale covers height differences of 100 nm from dark to bright; (b) friction force map, the vertical scale covers friction differences of 40 nN from dark to bright (load 0 nN, adhesion force  $22.6 \text{ nN} \pm 1.2 \text{ nN}$ , velocity  $6.1 \mu\text{m/s}$ , 40% RH,  $25^\circ\text{C}$ ).

Further nanotribological analyses were performed on the flat areas, which did not show pronounced contrast in friction force maps for a given load (Figure 7-8). These smooth regions are the contact areas of the ceramic with the alumina ball.

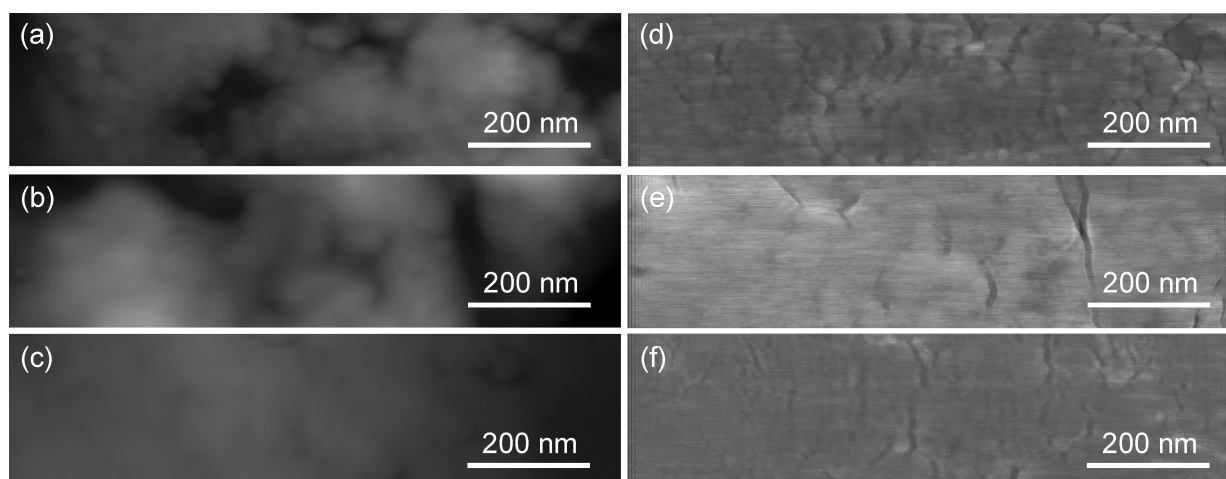


Figure 7-8. Contact mode AFM images of wear tracks in 3Y-TZP sample doped with 8 mol% CuO (after sliding with an  $\alpha\text{-Al}_2\text{O}_3$  ball for different distances in pin-on-disc tribometer) using a  $\text{Si}_3\text{N}_4$  tip [(a) – (c) topography and (d) – (f) corresponding friction maps, for sliding distances of: (a), (d) 20 m (track A), (b), (e) 30 m (track B), and (c), (f) 300 m (track C), respectively]. The height scale in (a) – (c) covers height differences of 100 nm from dark to bright, the vertical scale in (d) – (f) covers friction differences of 30 nN from dark to bright [load 0 nN, adhesion force (d)  $12 \text{ nN} \pm 2 \text{ nN}$ , (e)  $13.5 \pm 1.5 \text{ nN}$ , and (f)  $22.6 \text{ nN} \pm 1.2 \text{ nN}$ , velocity  $6.1 \mu\text{m/s}$ , 40% RH,  $25^\circ\text{C}$ ].

Using AFM, friction forces were measured as a function of normal force in the wear-less regime using  $\text{Si}_3\text{N}_4$  as probe (tip) material. The same environmental conditions were maintained as for the pin-on-disc experiment (40% RH and  $25^\circ\text{C}$ ). The average contact pressures to 1.2 GPa were in the same range as the values in the microtribology test (1 GPa). However, the tip-sample contact length of  $\sim 7$  nm (tip radius of 50 nm) was significantly smaller as compared to  $100\ \mu\text{m}$  -  $200\ \mu\text{m}$  in the pin-on-disc experiments for a ball with a radius of 5 mm.

Figure 7-9 shows the dependence of friction forces on normal forces for track B (length of sliding = 30 m) measured at a scan velocity of  $6.1\ \mu\text{m/s}$ . The friction force data were calibrated according to the wedge method described in Chapter 4. A linear increase of the friction force with increasing normal forces was observed in the range of applied normal forces. The friction coefficient was determined from the slope of a linear least square fit. There was no hysteresis for the data acquired with increasing and decreasing loads, respectively.

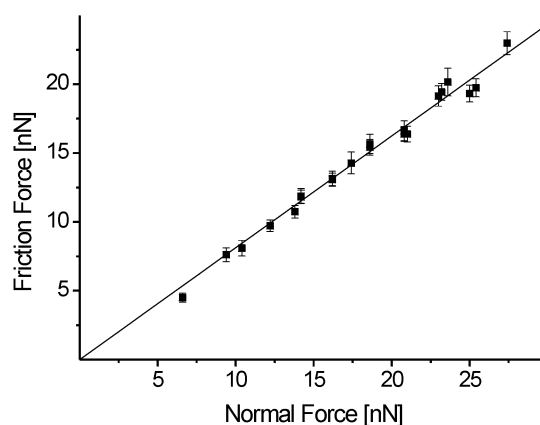


Figure 7-9. Friction force (calibrated difference photodiode output signal) versus normal force data for track B (30 m) measured in 40% RH at  $25^\circ\text{C}$  with velocity of  $6.1\ \mu\text{m/s}$ ; the error bars indicate the standard deviation ( $n = 128$ ) of the data analyzed for a given normal force.

Data acquired in different locations of similar morphological appearance were found to show consistent results (Table 7-1).

Table 7-1. Friction coefficient of wear tracks and area outside the tracks measured at different locations using a Si<sub>3</sub>N<sub>4</sub> tip (velocity 6.1 μm/s, 40% RH, 25°C).

Location #	Outside tracks	Track A, sliding distance 20 m	Track B, sliding distance 30 m	Track C, sliding distance 300 m
1	0.50	0.73	0.91	0.29
2	0.55	0.81	0.80	0.25
3	0.49	0.63	0.86	0.37
Average value $\mu_{\text{Si}_3\text{N}_4}^{\text{nano}}$	<b>0.51</b>	<b>0.72</b>	<b>0.85</b>	<b>0.30</b>
Standard deviation	0.03	0.08	0.06	0.03

Figure 7-10(a) shows the friction coefficients  $\mu_{\text{Si}_3\text{N}_4}^{\text{nano}}$  for various sliding distances. The friction coefficients measured on the wear track after 20 m and 30 m of sliding, respectively, were significantly higher than the value for the area outside the wear tracks. As revealed in the microtribology test, the surface layer of the sample (contamination and/or a thin soft layer that may be generated during polishing) is removed by wear during the initial sliding. Thus, the areas in the track may possess different properties as compared to areas outside the track resulting in different values of the friction coefficients.

After longer sliding distances (300 m), the friction coefficient decreases to a value of 0.30. Moreover, the low friction behavior vanishes after O<sub>2</sub>-plasma treatment (see Figure 7-10(b)). The friction coefficient increases nearly by a factor of 2. By contrast, the modification by the O<sub>2</sub>-plasma did not affect  $\mu_{\text{Si}_3\text{N}_4}^{\text{nano}}$  for the other areas to within the experimental error. These observations may indicate that the surface composition of track C was different, as compared to the other tracks and the outside area. Since all components of the sample are likely in the highest oxidation state (ZrO<sub>2</sub>, Y<sub>2</sub>O<sub>3</sub>, and CuO), the oxidation of the surface may be excluded. Alternatively, the mechanism of surface modification by the O<sub>2</sub>-plasma treatment could be attributed to sputtering and concomitant roughening of the top layer of the track C. Thus, these

results may indicate that during sliding an interfacial layer with low shear strength was generated.

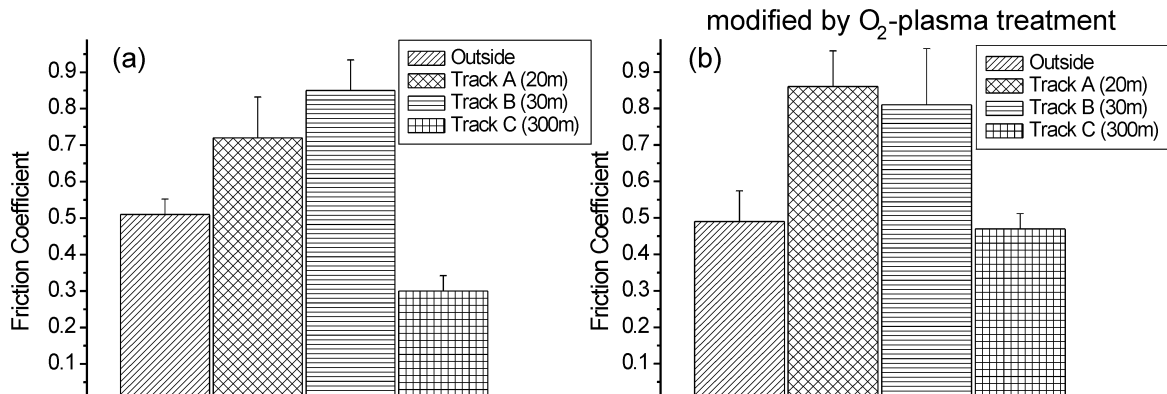


Figure 7-10. Friction coefficient  $\mu_{\text{Si}_3\text{N}_4}^{\text{nano}}$  of (a) sample analyzed directly after pin-on-disc measurements without any additional treatment, (b) sample analyzed after pin-on-disc test and subsequent modification for 10 min in an O<sub>2</sub>-plasma. The measurements were performed with a Si<sub>3</sub>N<sub>4</sub> tip using AFM (velocity 6.1  $\mu\text{m/s}$ , 40% RH, 25°C).

$\mu_{\text{Si}_3\text{N}_4}^{\text{nano}}$  in the area outside the wear tracks was constant, as shown in Figure 7.10(a) and (b). However, differences in friction coefficient were observed for different samples. This observation is attributed to varying surface contaminations for samples subjected to different storage conditions.

The velocity dependence of  $\mu_{\text{Si}_3\text{N}_4}^{\text{nano}}$  was determined using the high velocity AFM described in Chapter 5. Velocities close to the values used in the pin-on-disc experiments were obtained. Figure 7-11 shows the friction coefficient as a function of velocity for track D (sliding distance of 100 m) measured with a Si<sub>3</sub>N<sub>4</sub> tip. In the range of the attainable velocities (between 6  $\mu\text{m/s}$  and 500  $\mu\text{m/s}$ ),  $\mu_{\text{Si}_3\text{N}_4}^{\text{nano}}$  was *independent* of velocity. Higher velocities were inaccessible due to too high sample mass and the sample roughness (see also Chapter 5). Similarly, for oxidized Si(100) and nanostructured zirconia (see Chapter 6), no dependence of  $\mu_{\text{Si}_3\text{N}_4}^{\text{nano}}$  on velocity was revealed in the range of 10  $\mu\text{m/s}$  to 1 mm/s (see Chapter 5, Figure 5-8, and Appendix 7-2).

These data are also qualitatively in agreement with microtribology experiments, where the friction coefficient for the 3Y-TZP doped with CuO was also found to be independent of velocity in the range of 0.05 m/s to 0.5 m/s.<sup>21</sup>

We assume that the friction coefficient will be also independent of velocities for the range of velocities between those that can be probed by AFM and those that can be accessed by pin-on-

disc experiments ( $\mu\text{m/s}$  - 0.5 m/s). Based on this assumption the values obtained on the nanometer scale with a velocity of 6 - 500  $\mu\text{m/s}$  can be directly compared with the values measured using the pin-on-disc tribometer with  $5 \times 10^4 \mu\text{m/s}$ .

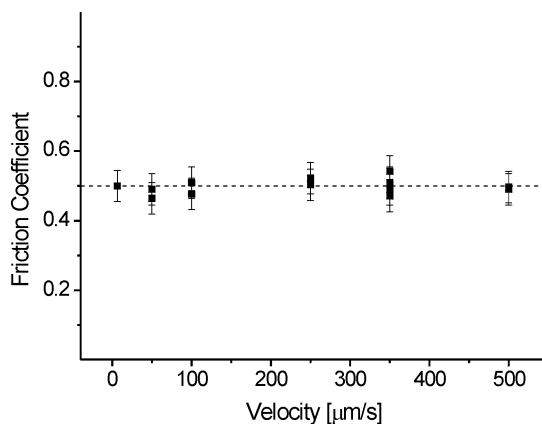


Figure 7-11. Friction coefficient vs. velocity for track D (sliding distance of 100 m) measured with  $\text{Si}_3\text{N}_4$  tip using the high velocity AFM described in Chapter 5 (40% RH, 25°C).

## 7.5. Comparative discussion of micro- and nanotribology on CuO doped 3Y-TZP

Complementary nano- and microtribology measurements on CuO doped 3Y-TZP require experiments with identical counter surfaces. As described in Chapter 3, we attempted to coat AFM probes with  $\alpha\text{-Al}_2\text{O}_3$ . However, the coating was not optimized and could not be applied in our studies.

In order to provide a basis for comparison of the nano- and microtribology in this Chapter, a CuO doped 3Y-TZP sample was first probed with an  $\alpha\text{-Al}_2\text{O}_3$  ball (to generate the third body layer) and then on the same track with a  $\text{Si}_3\text{N}_4$  ball (Figure 7-12). In this experiment, the friction coefficient of the  $\text{Si}_3\text{N}_4$  slider ( $\mu_{\text{Si}_3\text{N}_4}^{\text{micro}}$ ) maintained the same value as the  $\alpha\text{-Al}_2\text{O}_3$  slider during the first several meters of sliding. After sliding for a distance of *ca.* 4 meters, the friction coefficient increased rapidly. This increase in  $\mu_{\text{Si}_3\text{N}_4}^{\text{micro}}$  coincided with the onset of severe wear of the ball. Direct wear-less testing of 3Y-TZP/CuO with a  $\text{Si}_3\text{N}_4$  ball was impossible as severe wear was observed for all sliding distances and loads (see Appendix 7-3). Based on these observations we assume that  $\mu_{\text{Si}_3\text{N}_4}^{\text{micro}}$  and  $\mu_{\alpha\text{-Al}_2\text{O}_3}^{\text{micro}}$  measured on the wear track are very similar (in the absence of wear).



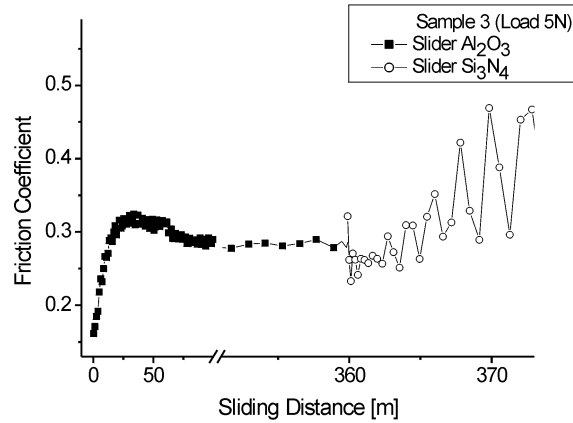


Figure 7-12. Coefficient of friction as a function of sliding distance measured using various balls.  $\mu$  was measured with an  $\alpha$ - $\text{Al}_2\text{O}_3$  ball for 360 meters. After sliding for 360 meters, the ball was exchanged against a  $\text{Si}_3\text{N}_4$  ball (velocity 0.05 m/s, 40% RH, 25°C).

In Figures 7-13, the friction coefficients  $\mu_{\text{Si}_3\text{N}_4}^{\text{nano}}$  and  $\mu_{\alpha\text{-Al}_2\text{O}_3}^{\text{micro}}$  are compared for various sliding distances. As expected, the areas outside the wear tracks for different samples deviate significantly. For short sliding distances of 20 – 30 meters, the smooth areas analyzed on the nanometer scale are regions where the contamination layer was removed and the highest asperities were worn.  $\mu_{\text{Si}_3\text{N}_4}^{\text{nano}}$  of 0.70 – 0.85 was significantly higher compared to  $\mu_{\alpha\text{-Al}_2\text{O}_3}^{\text{micro}}$  of 0.33. It was also higher than measured for undoped 3Y-TZP ( $\mu_{\text{Si}_3\text{N}_4}^{\text{nano}} = 0.5$ ).<sup>26</sup> However, for long sliding distances (> 100 m) very similar values of  $\mu_{\alpha\text{-Al}_2\text{O}_3}^{\text{micro}}$  and  $\mu_{\text{Si}_3\text{N}_4}^{\text{nano}}$  were observed.

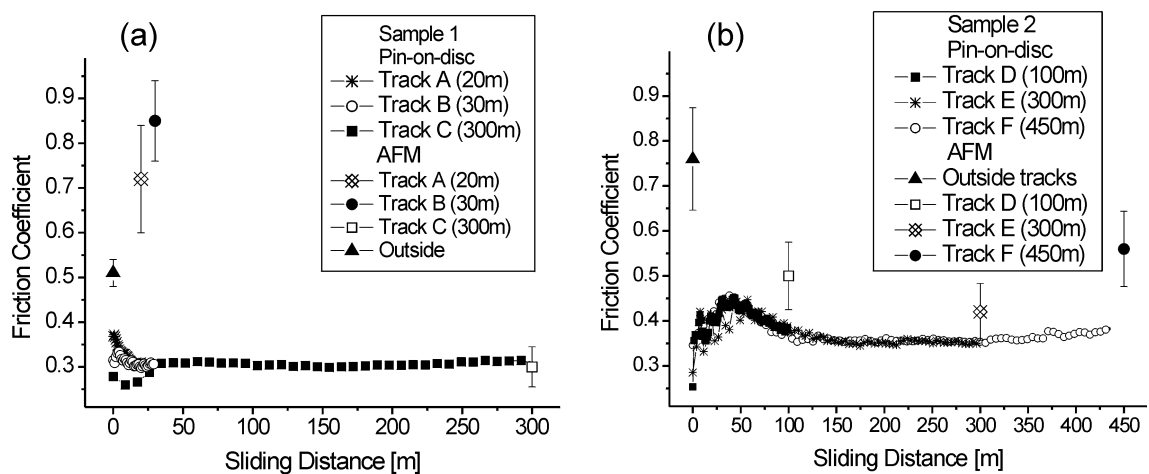


Figure 7-13. Comparison of nano- and microtribology for two individual CuO doped 3Y-TZP specimens. Friction coefficients vs. sliding distance measured by AFM using  $\text{Si}_3\text{N}_4$  tips and by a pin-on-disc tribometer against an  $\alpha$ - $\text{Al}_2\text{O}_3$  ball (40% RH, 25°C).

The nanotribological properties of the analyzed selected areas for various sliding distances are in agreement with the presence of the soft layer. Since the areas do not show local variations in friction force, it is assumed that the generated layer in these regions is continuous. For short sliding distances of 20 – 30 meters (track A and B), the soft layer on these areas is very thin and the contact is dominated by the contact of the AFM tip (single/few asperity) with the underlying 3Y-TZP, see Figure 7-14(a). By contrast, the large scale multiasperity contact of the alumina ball in the pin-on-disc experiments on this heterogeneous and rough sample is already dominated by the contact of the ball with the soft layer. Consequently, we observe  $\mu^{\text{nano}} > \mu^{\text{micro}}$  for measurements on wear tracks with short sliding distances.

Longer sliding resulted in values of nanometer scale friction coefficient comparable with the micrometer scale. This result is consistent with a layer thickness in those smooth areas that is sufficient to provide low friction behavior for the single/few asperity contact (Figure 7-14(b)). In addition, the modification of the surface of track C using O<sub>2</sub>-plasma treatment (Figure 7-10(b)), which caused a significant increase of friction coefficient after treatment, suggests a surface chemical difference between those tracks (presence of the soft layer on track of 300 m sliding distance). For long sliding distance of 450 m (track F),  $\mu_{\text{Si}_3\text{N}_4}^{\text{nano}}$  is slightly higher than  $\mu_{\alpha\text{-Al}_2\text{O}_3}^{\text{micro}}$ . The increase in the friction coefficient can be due to different reasons: (i) an increase in layer thickness above the critical value resulting in friction coefficient similar to the bulk value of the layer material used, or (ii) wear of the soft layer accompanied with significant increase in roughness. The first situation (i) is predicted by the model for layer thickness above 1  $\mu\text{m}$ .<sup>23</sup> The second case was observed experimentally for the microscopic friction coefficient for sliding distances above 1000 m. Since, the roughness of track for 300 m and 450 m sliding distance (track E and F, respectively) was practically the same, we can exclude (ii) as a reason of increase in  $\mu_{\text{Si}_3\text{N}_4}^{\text{nano}}$  in respect to  $\mu_{\alpha\text{-Al}_2\text{O}_3}^{\text{micro}}$ . Most probably the higher friction coefficient is caused by an increase in the layer thickness, as described by the model (Figure 7-14(c)). However, the critical layer thickness for this single/few asperity contact may be thinner than the value calculated for rough surfaces.

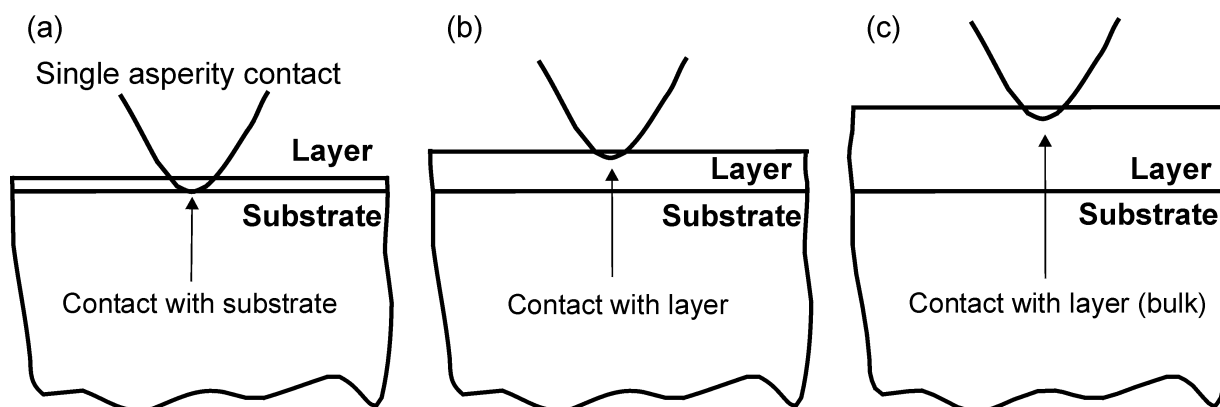


Figure 7-14. Schematic of a single asperity contact with layered system for different layer thickness: (a) thin layer, (b) layer with intermediate thickness, and (c) thick layer (bulk).

The excellent agreement between  $\mu_{\text{Si}_3\text{N}_4}^{\text{nano}}$  and  $\mu_{\alpha\text{-Al}_2\text{O}_3}^{\text{micro}}$  for sliding distances of 100 – 300 m shown above could be a coincidence as the values of  $\mu_{\text{Si}_3\text{N}_4}^{\text{nano}}$  are most likely overestimated due to humidity effects. As described in Chapters 2 and 6, the friction coefficient as determined by AFM was observed to depend critically on the relative humidity. For nanostructured  $\text{ZrO}_2$  an increase in  $\mu^{\text{nano}}$  by a factor of 2 was observed when the %RH was changed from < 5% (dry nitrogen conditions) to 40% RH. This increase was attributed to the formation of capillary forces in humid environment. The maximum coefficient of friction was observed for a value of 40% RH. By contrast, differences of friction coefficients as function of humidity in microtribology are small.<sup>27</sup>

Hence, the real  $\mu_{\text{Si}_3\text{N}_4}^{\text{nano}}$  of the smooth areas tested is very likely smaller than  $\mu_{\alpha\text{-Al}_2\text{O}_3}^{\text{micro}}$ . A lower value of friction coefficient would in fact be expected for friction in absence of ploughing ( $\mu^{\text{nano}}$ ) as compared to the normal friction ( $\mu^{\text{micro}}$ ) (see Chapter 2).

The mechanism of the soft layer formation is still unclear and more analysis need to be carried out, including the characterization of the morphology and nanotribology on compositionally heterogeneous areas of the wear tracks using  $\alpha\text{-Al}_2\text{O}_3$ -coated AFM probes for different sliding distances. The complementary analysis of nano- and microtribology should also include the extensive study of the humidity effects and the quantification of the friction coefficient over the entire velocity range up to 0.05 m/s.

## 7.6. Concluding remarks

In this Chapter we focused on performing complementary nano- and microtribology measurements on CuO doped 3Y-TZP ceramics. Using the quantitative nanotribology analysis

and the newly developed high velocity AFM (Chapters 3 - 5) the gap between nano- and microtribology in terms of length and time scales was considerably narrowed. In particular, the effect of velocity on friction coefficient and a soft layer formation during sliding on different length scales were studied. The observed trends in friction coefficients determined on the nanometer scale by AFM are in agreement with data acquired using a pin-on-disc tribometer on the micrometer scale. During the initial sliding in pin-on-disc experiments the layer of surface contaminations is removed and wear of high asperities occurs. The friction coefficient determined by AFM on these modified flattened areas is significantly higher compared to the value determined on the micrometer scale for sliding distances below 30  $\mu\text{m}$ . This behavior is attributed to (i) humidity effects and (ii) the biased sampling of the surface properties due to a non-representative selection of smooth areas for the nanometer scale analysis. For sliding distances  $> 100 \mu\text{m}$  very similar values of  $\mu_{\alpha\text{-Al}_2\text{O}_3}^{\text{micro}}$  (which we assume to be of similar value of  $\mu_{\text{Si}_3\text{N}_4}^{\text{micro}}$ ) and  $\mu_{\text{Si}_3\text{N}_4}^{\text{nano}}$  were observed. This observation may indicate that during sliding an interfacial layer with low shear strength is generated and that the AFM measurements were performed on this layer. While these results do not provide a complete explanation of process of layer formation, they represent the first report of bridged nano- and microtribological analysis of a compositionally heterogeneous low friction, low wear ceramic material and confirm some of the key assumptions for the model by Pasaribu *et al.*<sup>17,23</sup>

## 7.7. Experimental

### 7.7.1. Materials and sample preparation

Dense 3Y-TZP samples (94 - 95%) were prepared from commercial materials in the Inorganic Materials Science group, University of Twente, by Dr. R. Ran. Several 3Y-TZP samples doped with 8 mol% CuO were prepared, named here with numbers from 1 to 3. Appropriate amounts of 3Y-TZP (TZ3Y, Tosoh, Japan) and CuO (Aldrich, Germany) powders were mixed by wet-milling for 24 hours in a polyethylene bottle using ethanol (Biosolve, Westford, MA) and zirconia balls as milling media. The milled suspension was oven-dried for 24 hours at 80°C and subsequently for 8 hours at 120°C. The dry cake was ground lightly in a plastic mortar and then sieved through a 180  $\mu\text{m}$  sieve. Green compact discs of the composite powder with a diameter of 50 mm and a thickness of around 5 mm were prepared by uniaxial pressing at 30 MPa followed by isostatic pressing at 400 MPa. These discs were sintered for 8 hours in stagnant air at 1500°C. The heating and cooling rate used during sintering were both 2°C/min. The sintered

discs were polished to a centerline surface roughness ( $R_a$ ) of 0.1  $\mu\text{m}$  using diamond paste. The polished discs were ultrasonically cleaned in ethanol and then annealed at 850  $^{\circ}\text{C}$  for 2 hours.

Prior to the pin-on-disc measurements the samples were ultrasonically cleaned for 20 min in ethanol (Biosolve) and subsequently annealed for 20 min at 120 $^{\circ}\text{C}$ . Some samples were ultrasonically cleaned for 20 min in ethanol (Biosolve) and were then treated by oxygen-plasma (30 mA, 60 mTorr) using a SPI Supplies, Plasma Prep II (West Chester, PA) for 10 min.

### 7.7.2. AFM

**a. Morphology.** The morphology of the samples was revealed by intermittent contact (tapping) mode AFM (TM-AFM) (NanoScope III multimode AFM, Veeco/Digital Instruments, Santa Barbara, CA) using Si probes (type NCH, Nanosensors, Wetzlar, Germany).

**b. Nanotribology.** Friction force measurements were performed using a NanoScope IIIa (Digital Instruments/Veeco, Santa Barbara, CA) atomic force microscope enclosed in an environmental glovebox. The normal spring constants of V-shaped  $\text{Si}_3\text{N}_4$  cantilevers (Model NP, Veeco Nano Probe, Santa Barbara, CA) ( $k_N = 0.20 - 0.22 \text{ N/m}$ ) and tip radii (in the range of 40 – 70 nm) were individually calibrated using the reference lever method<sup>28</sup> and a calibration grating (silicon grating TGT1, NT-MDT, Moscow, Russia), respectively. The humidity of 40%  $\pm$  2% relative humidity (RH) was precisely controlled using mixture of wet and dry  $\text{N}_2$  gas, as measured by a humidity sensor (SHT15, Sensirion, Zurich, Switzerland), while the temperature was maintained constant during all measurements (25 $^{\circ}\text{C}$ ). Friction data in the form of images of differential photodiode output signal for trace and retrace (512  $\times$  128 pixels; scan size 1000 nm  $\times$  250 nm; scan velocity 6.1  $\mu\text{m/s}$ ) were acquired simultaneously for different normal forces (normal force is defined as the sum of pull-off force and externally applied load). The normal forces were limited to values  $< 100 \text{ nN}$  to work in the elastic contact regime without detectable tip wear.<sup>29,30</sup> Subsequent to a correction of the scanner hysteresis between trace and retrace using the Digital Instruments software, the mean friction force  $\pm$  standard deviation  $\sigma$  was determined from an analysis of the difference images, as described in reference 31. The friction force data were calibrated according to the wedge method described in Chapter 4.<sup>32</sup>

Friction coefficient - velocity measurements (scan size of 250 nm) were performed with a stand alone AFM (Molecular Imaging, Tempe, USA) equipped with the newly developed high velocity accessory (Chapter 5). The lateral photodiode output signal, which was acquired in the time domain, was recorded via the data acquisition board and was processed by the software described in Chapter 5. Each data point represents the mean value of one-half of the difference

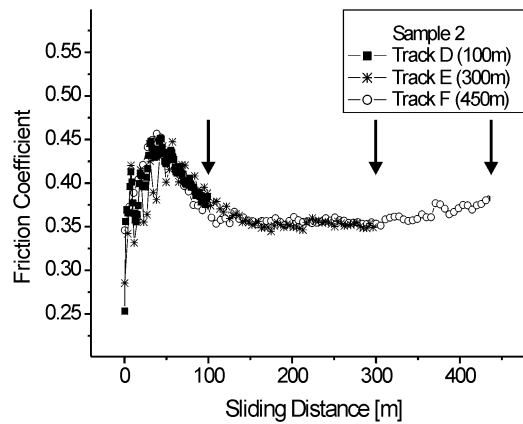
---

friction signal calculated from 150 trace and retrace cycles and the error bars correspond to the standard deviation of the data analyzed for a given load and velocity. The climate control (40%  $\pm$  2% RH and temperature 25°C) was performed via the flow of nitrogen gas of controlled humidity through an environmental chamber (PicoAPEX, Pyrex glass, MI, Tempe, USA) as measured by a humidity sensor (SHT15, Sensirion, Switzerland).

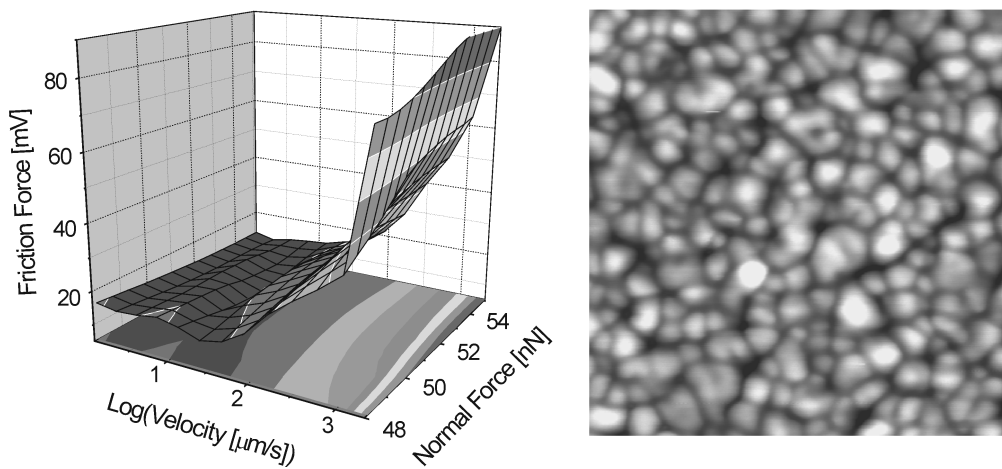
### *7.7.3. Pin-on-disc measurements*

The dry sliding tests were performed using a pin-on-disc tribometer (CSEM, Switzerland) by Dr. Richard Pasaribu in the Tribology group, University of Twente. The instrument was placed in a climate chamber to maintain testing conditions (40% RH). Commercially available 10 mm diameter  $\alpha$ -Al<sub>2</sub>O<sub>3</sub> balls (AKP50, Sumitomo, Japan) with a crystallite size of 0.1 – 0.3  $\mu$ m, and Si<sub>3</sub>N<sub>4</sub> balls (HPSN, GIMEX technische keramiek BV, Geldermalsen, the Netherlands) were used as counter surface. Sliding tests were conducted with load of 5 N (unless differently specified) and velocity of 0.05 m/s for different sliding distance (up to 450 m).

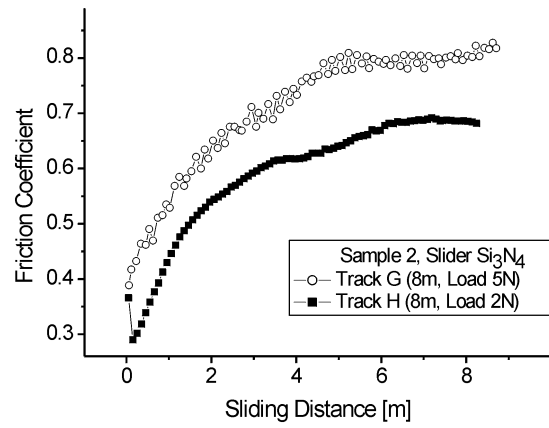
## 7.8. Appendix



Appendix 7-1. Coefficient of friction as a function of sliding distance for 3Y-TZP doped with 8 mol% CuO measured against an  $\alpha$ -Al<sub>2</sub>O<sub>3</sub> ball using a pin-on-disc tribometer (normal load 5 N, velocity  $5 \times 10^4$   $\mu\text{m/s}$ , 40% RH, 25°C).



Appendix 7-2. (left) Three-dimensional plot of friction force vs. normal force vs. logarithm of velocity for nanostructured zirconia (grain size of 20 nm) measured using AFM with Si<sub>3</sub>N<sub>4</sub> tip. (right) TM-AFM topography image of nanostructured zirconia with the grain size of 20 nm.



Appendix 7-3. Coefficient of friction as a function of sliding distance measured with a Si<sub>3</sub>N<sub>4</sub> ball on sample 2 using the pin-on-disc tribometer (velocity 0.05 m/s, 40% RH, 25°C).



## 7.9. References

- 1 Meyer, E.; Overney, R. M.; Dransfeld, K.; Gyalog, T. *Nanoscience: Friction and Rheology on the Nanometer Scale*. World Scientific: Singapore, 1998.
- 2 Carpick, R. W.; Salmeron, M. *Chem. Rev.* **1997**, *97*, 1163-1194.
- 3 Czichos, H. *Meccanica* **2001**, *36*, 605-615.
- 4 Iordanoff, I.; Berthier, Y.; Descartes, S.; Heshmat, H. *J. Tribol.-Trans. ASME* **2002**, *124*, 725-735.
- 5 Czichos, H.; Klaffke, D.; Santner, E.; Woydt, M. *Wear* **1995**, *190*, 155-161.
- 6 Fox, N. J.; Tyrer, B.; Stachowiak, G. W. *Tribol. Lett.* **2004**, *16*, 275-281.
- 7 Sliney, H. E. *Tribol. Int.* **1982**, *15*, 303-314.
- 8 Bowden, F. P.; Tabor, D. *Friction and Lubrication of Solids, Part I*. Clarendon Press: Oxford, 1950.
- 9 Chhowalla, M.; Amaratunga, G. A. J. *Nature* **2000**, *407*, 164-167.
- 10 Grossiord, C.; Martin, J. M.; Le Mogne, T.; Palermo, T. *Tribol. Lett.* **1999**, *6*, 171-179.
- 11 Koskinen, J.; Ronkainen, H.; Hirvonen, J. P.; Lappalainen, R.; Pischow, K. A. *Diam. Relat. Mat.* **1995**, *4*, 843-847.
- 12 Rapoport, L.; Bilik, Y.; Feldman, Y.; Homyonfer, M.; Cohen, S. R.; Tenne, R. *Nature* **1997**, *387*, 791-793.
- 13 Singer, I. L. *Langmuir* **1996**, *12*, 4486-4491.
- 14 Vlcek, B. L.; Sargent, B. L.; Lauer, J. L. *Lubric. Eng.* **1993**, *49*, 463-471.
- 15 Kerkwijk, B.; Garcia, M.; van Zyl, W. E.; Winnubst, L.; Mulder, E. J.; Schipper, D. J.; Verweij, H. *Wear* **2004**, *256*, 182-189.
- 16 Renevier, N. M.; Lobiondo, N.; Fox, V. C.; Teer, D. G.; Hampshire, J. *Surf. Coat. Technol.* **2000**, *123*, 84-91.
- 17 Pasaribu, H. R. Friction and wear of zirconia and alumina ceramics doped with CuO. Ph.D. Thesis, University of Twente, Enschede, 2005.
- 18 Alexeyev, N.; Jahanmir, S. *Wear* **1993**, *166*, 41-48.
- 19 Alexeyev, N.; Jahanmir, S. *Wear* **1993**, *166*, 49-54.
- 20 Wang, Y.; Worzala, F. J.; Lefkow, A. R. *Wear* **1993**, *167*, 23-31.
- 21 Pasaribu, H. R.; Sloetjes, J. W.; Schipper, D. J. *Wear* **2003**, *255*, 699-707.
- 22 Winnubst, A. J. A.; Ran, S.; Wiratha, K. W.; Blank, D. H. A.; Pasaribu, H. R.; Sloetjes, J. W.; Schipper, D. J. In *Euro Ceramics VIII, PTS 1-3*, 2004; Key Engineering Materials; Vol. 264-268, p 809-812.
- 23 Pasaribu, H. R.; Schipper, D. J. *Tribol. Lett.* **2004**, *17*, 967-976.
- 24 Cleaning with ethanol and temperature treatment may only partly remove a contamination layer from the surface.
- 25 Singer, I. L.; Dvorak, S. D.; Wahl, K. J.; Scharf, T. W. *J. Vac. Sci. Technol. A* **2003**, *21*, S232-S240.
- 26 It was reported in reference 17 that a very thin soft layer could also be generated during polishing. Thus the determined value of friction coefficient may be influenced/reduced by the presence of the layer. An accurate value of  $\mu_{\text{Si}_3\text{N}_4^{\text{nano}}}$  could be obtained by measuring nanotribological properties on the wear track of 3Y-TZP that will be cleaned in situ during the microtribology test.
- 27 Pasaribu, H. R.; Reuver, K. M.; Schipper, D. J.; Ran, S.; Wiratha, K. W.; Winnubst, A. J. A.; Blank, D. H. A. *Int. J. Refract. Met. Hard Mat.* **2005**, *23*, 386-390.
- 28 Tortonese, M.; Kirk, M. *Proc. SPIE* **1997**, *3009*, 53-60.

- 29 Schwarz, U. D.; Zwörner, O.; Köster, P.; Wiesendanger, R. *Phys. Rev. B* **1997**, *56*, 6987-6996.
- 30 Schwarz, U. D.; Zwörner, O.; Köster, P.; Wiesendanger, P. *Phys. Rev. B* **1997**, *56*, 6997-7000.
- 31 Hammerschmidt, J. A.; Gladfelter, W. L.; Haugstad, G. *Macromolecules* **1999**, *32*, 3360-3367.
- 32 Tocha, E.; Schönherr, H.; Vancso, G. J. *Langmuir* **2006**, *22*, 2340-2350.

# Chapter 8

## Tribology from the nano- to the mesoscale: Probing polymer relaxations at the surface of PMMA films by high velocity AFM

*The advancement in the understanding of friction on polymer film surfaces on the molecular scale, and in particular the study of relaxation processes using atomic force microscopy (AFM), have been hampered until recently by the limited choice of experimental methods. In this Chapter the first comprehensive AFM study of relaxations of poly(methyl methacrylate) (PMMA) is presented. The broad range of scanning velocities accessible using the newly developed high velocity accessory (Chapter 5), temperature control, as well as tips with widely different radii, allowed us to cover a frequency range from 1 to  $10^7$  Hz. Friction data acquired at different temperatures and velocities were corrected for the effect of tip-sample contact pressure and were successfully shifted to yield one mastercurve. The  $\alpha$  and  $\beta$  relaxation processes of PMMA were identified in the Hz and MHz regime, respectively ( $T_{ref} = 26^\circ\text{C}$ ). The activation energies of the relaxation processes ( $E_a^\alpha \sim 110$  kJ/mol and  $E_a^\beta \sim 35$  kJ/mol) were found to be significantly lower than the reported bulk values and the relaxation frequencies of the processes were noticeably higher compared to the bulk. These results are consistent with the existence of an increased free volume at the polymer surface and indicate a significantly higher mobility of the macromolecules at the film surface.*

## 8.1. Introduction

In polymer films the structural, material, and transport properties become increasingly dominated by interfacial, conformational, and dimensional constraints, when the thickness is reduced to the sub-100 nm scale.<sup>1-3</sup> For such ultrathin films, depending on the thickness, the glass transition temperature,<sup>4-12</sup> crystallization kinetics and degree of crystallinity,<sup>13-19</sup> phase behavior,<sup>20-22</sup> morphology,<sup>23</sup> permeability,<sup>24</sup> electrical properties,<sup>25</sup> moisture absorption,<sup>26</sup> or dewetting<sup>27</sup> may be altered. In addition, rheological gradients near the interfaces can lead to a behavior that deviates from the bulk. Relaxation properties can be influenced and enhanced conformational stability may be achieved through control of the interfacial conditions, molecular weight, crosslinking density, and film thickness.<sup>3,28</sup> On the nanoscale, precise material engineering is only possible with an understanding of the polymer dynamics near interfaces. Hence, the characterization and control of interfacial boundary layers become increasingly important for nanotechnological applications, such as nano-electromechanical systems (NEMS) for terabit thermomechanical storage, protective coatings, adhesives and lubricants that rely on very specific relaxation and transition properties in sub-100 nm systems.<sup>29-31</sup>

In this context, particular emphasis is given to the (local) probing of molecular dynamics near the glass transition using different methods, such as spectroscopic ellipsometry,<sup>7</sup> X-ray reflectivity,<sup>11</sup> positron annihilation lifetime spectroscopy,<sup>4</sup> Brillouin scattering,<sup>32</sup> single molecule fluorescence life time detection<sup>12,33-36</sup> and surface plasmon resonance.<sup>10,37</sup>

A relatively new family of techniques for probing polymer relaxations is scanning probe microscopy. Among others, normal amplitude<sup>38-41</sup> and shear modulation force microscopy,<sup>2,3</sup> as well as lateral force microscopy can be employed.<sup>1,42-47</sup> Scanning probe microscopy (SPM) with lateral force sensitivity provides not only measurements of friction forces at single asperity contacts, but also the ability to image nanoscale morphologies and thereby to assess the onset of wear or plastic deformation. Thus, these methods are of particular importance for studies of thin polymer films and for characterizing differences between surface and bulk behavior.

Dynamic friction on polymers has a large contribution from internal viscoelastic dissipation, which is ultimately related to polymer relaxation.<sup>48</sup> From macroscopic tribological experiments it is known that the velocity-dependence of friction force in absence of plastic deformation is very similar to the rate-dependence of  $\tan(\delta) = E''/E'$ , which is the ratio of the dynamic storage modulus  $E'$  and the dynamic loss modulus  $E''$ .<sup>49</sup> This relationship generally displays several broad peaks corresponding to different classes of molecular relaxations labeled  $\alpha$ ,  $\beta$ ,  $\gamma$  and  $\delta$ .

These relaxation processes are ascribed to the glass-rubber transition and different rotations of side groups, respectively. The temperature at which the polymer undergoes the transformation from the rubbery state to the glassy state is known as the glass transition temperature ( $T_g$ ).<sup>50,51</sup> Dramatic changes in various material properties are associated with this transition, *e.g.* when the temperature is increased above  $T_g$ , the elastic modulus decreases by several orders of magnitude. The variation of rate (time) and temperature causes similar effects in polymer relaxation processes. For viscoelastic properties the interplay between relaxation time and temperature is well-known.<sup>44,52-54</sup> The time-temperature superposition principle states that the same molecular relaxation requires longer time at lower temperatures. For instance, a polymer, which displays rubbery characteristics under a given set of testing conditions, can be induced to show glassy behavior by either reducing the temperature (to below  $T_g$ ) or by increasing the testing rate (or frequency). According to the time-temperature superposition principle (higher  $T \Leftrightarrow$  lower frequency), the  $\tan(\delta)$  can be reduced to a master curve at an arbitrary chosen reference temperature  $T_o$ , by multiplying the velocity (or frequency) data with the Williams-Landel-Ferry (WLF) shift factor  $a_T$ .<sup>55</sup> The Arrhenius relationship

$$\ln a_T = \frac{E_a}{R} \left( \frac{1}{T} - \frac{1}{T_o} \right) \quad (\text{Eq. 8-1})$$

between the shift factor  $a_T$  and the temperature  $T$ , and the activation energy  $E_a$ , is commonly used to analyze relaxation phenomena below  $T_g$ . The activation energies represent the potential barrier that is continuously overcome, *e.g.* for the rotation of dipolar moieties in macromolecules.

Since dynamic friction on polymers has a large contribution from internal viscoelastic dissipation, *i.e.* molecular relaxations, it can be expected that the time-temperature superposition principle also holds for friction. Thus, also in steady sliding friction experiments, friction data recorded as a function of velocity and temperature can be rescaled and superimposed according to the time-temperature principle.

The correlation between the friction response (measured for different scanning velocities) in AFM experiments and relaxation processes can be achieved by a comparison of the corresponding data with data measured for bulk polymers. Essential is here the conversion of scanning velocity to frequency dependence (time scale). Using the tip-sample contact length (the contact diameter), which determines the time the tip interacts with a point of polymer surface,

velocity can be converted to frequency by simple division of the velocity by this contact length.<sup>44,56</sup>

In general, the dependence of polymer relaxations on various parameters can be schematically captured in the form of  $\tan(\delta)$  - frequency or  $\tan(\delta)$  - temperature diagrams (Figure 8-1). In the friction force vs. frequency relation, the bell-shape curve characteristic for a relaxation with maximum at  $f_0$  (relaxation frequency) is shifted to lower frequency values for increasing pressure or scanning with a sharper probe (at constant velocity). By contrast, increasing the temperature or using tips with large radii (at constant velocity) result in a shift to higher frequency values.

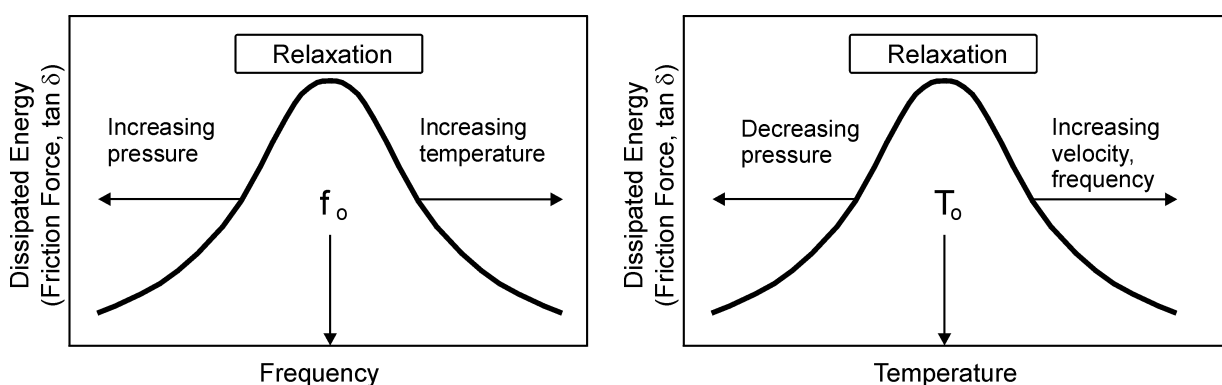


Figure 8-1. Schematic diagrams of a relaxation probed in a friction force – frequency (left) and a friction force – temperature experiment (right) on a polymer.

Comparisons of surface  $E_a$  to the corresponding values measured in the bulk have provided until now only very limited insight into the mobility of macromolecules near a free surface. Several authors have used lateral force microscopy to examine the time-temperature principle in polymer films. Examples include polystyrene (PS),<sup>38,42,57</sup> poly(methyl methacrylate) (PMMA),<sup>44</sup> and polypropylene (PP).<sup>58</sup> The corresponding Arrhenius activation energies determined for these films from the empirical shift factors were significantly lower<sup>38,42,44</sup> or similar<sup>57,58</sup> to the bulk values for the corresponding  $\alpha$  and  $\beta$  relaxations. In fact Kajiyama *et al.*<sup>38,59</sup> reported for PS higher molecular mobility at the surface ( $E_a = 230$  kJ/mol), whereas Overney *et al.*<sup>43</sup> reported a similar activation energy ( $E_a = 335 - 376$  kJ/mol) as compared to the bulk value ( $E_a = 360 - 880$  kJ/mol).<sup>49</sup>

Hammerschmidt *et al.*<sup>44</sup> measured the friction force between a Si tip and a PMMA surface for only four different velocities between 2 and 220  $\mu\text{m/s}$ .<sup>60</sup> A “peak” was observed for measurements at 25°C, which shifted towards higher velocities at increasing temperatures. This “peak” was attributed to the  $\beta$  relaxation process. These authors also reported a lower activation

energy as compared to the bulk values (50 kJ/mol vs. 71 – 96 kJ/mol). However, this process occurred at a similar temperature and a similar frequency as in the bulk, which is inconsistent with the concluded higher mobility at the surface. Since the few AFM studies published to date report results that are in some cases ambiguous, incomplete, or even contradictory, we can conclude that relatively little is understood about relaxations at the polymer/air interface studied by AFM.

In addition to some debatable interpretation of experimental approaches and data, the shortcomings mentioned are also due to technical limitations. Higher velocities up to 200  $\mu\text{m/s}$  were to date only realized at the expense of (pixel) resolution<sup>44</sup> and noise in SPM friction experiments, which may significantly affect the friction response as reported in reference 61. An approach to circumvent this problem of limited velocities has been described in Chapter 5 of this Thesis.<sup>62</sup> Furthermore, several issues, such as the pressure dependence of relaxations or the plastic deformation of polymers, have not been addressed satisfactorily in the literature so far.

As described in Chapter 2, friction force arises from two mechanisms, namely an interfacial adhesion and a deformation component. Consequently, the intrinsic rheological properties are coupled with external tribological attributes, such as wear or ploughing.<sup>63</sup> Moreover, it is known from pressure-volume-temperature (PVT) diagrams that the free volume of polymers decreases at elevated hydrostatic pressures and hence  $T_g$  of the polymer increases.<sup>64,65</sup> Therefore, in AFM (or LFM) the measured relaxation processes can vary depending on the corresponding experimental conditions.<sup>66</sup>

Dinelli *et al.*<sup>1</sup> analyzed friction forces of PS as a function of temperature for different loads using AFM. The critical temperature for which a significant increase of friction forces occurred was assigned to the apparent  $T_g$ . A decrease in the apparent glass transition temperature was reported for increasing pressure, which is in contradiction to the PVT diagrams. This increase in friction force (apparent  $T_g$ ) was also accompanied with plastic deformations and ploughing, which is an additional component of friction and could influence the observations. By contrast, an elevation in the apparent glass transition temperature for PS was reported by Schmidt *et al.*<sup>67,68</sup> This finding was attributed to a reduction of the free volume in the polymer due to large compressive stress beneath the sliding probe.<sup>67,68</sup> For PP, Gracias *et al.*<sup>58</sup> reported a  $T_g$  that was 20°C higher for sharp probe as compared to large probe due to large pressure, in accordance with PVT data.

The proper quantitative analysis of surface relaxation phenomena using SPM, which includes the effects of plastic deformations and pressure, has not been established. This is of particular

---

importance for friction force measured in temperature scans across  $T_g$ , when the material properties, such as *e.g.* Young's modulus, will change significantly and thereby cause a significant increase of tip sample contact area. Additionally, the scratch resistance will also decrease, thus easier ploughing above  $T_g$  will increase the measured friction force and will thus affect the results. Furthermore, typical temperature control is achieved by heating the bottom of a sample, while the measurements are carried out with a cold tip. This will influence results of thick films (above 500 nm).<sup>69</sup> A method that avoids this difficulty, by increasing or decreasing ambient temperature using heated or cooled gas, is described in Chapter 5.

In this Chapter, relaxations of PMMA as a model amorphous polymer, are examined quantitatively by high velocity AFM over a broad range of frequencies (1 Hz to  $10^7$  Hz) using distinctive velocity (up to 1 mm/s) and temperature (from  $-3^\circ\text{C}$  to  $26^\circ\text{C}$ ) ranges, as well as probe tips with different radii (20 nm to 870 nm). The macromolecular relaxations at the surface of  $\sim 125$  nm thick films were probed as a function of sliding speed and temperature. Via the identification of surface relaxations and the quantitative estimation of the surface activation energies using the time-temperature superposition principle, differences between surface and reported bulk behavior was sought.

## 8.2. Nanotribology on PMMA films

The relaxation processes in bulk PMMA are well characterized using a variety of techniques, including dielectric<sup>70,71</sup> and dynamic mechanical analyses,<sup>72-74</sup> NMR spectroscopy,<sup>75</sup> positron annihilation,<sup>76</sup> and fluorescence spectroscopy.<sup>74</sup> In PMMA the highest relaxation temperature, the  $\alpha$  relaxation, is the glass transition temperature ( $T_g = 95 - 110^\circ\text{C}$ ,  $E_a^\alpha = 334 - 460$  kJ/mol)<sup>49</sup> and is ascribed to long-range conformational changes of the polymer backbone (see Figure 8-2). The secondary  $\beta$ ,  $\gamma$ , and  $\delta$  relaxations are attributed to the side chain motions of the ester group and rotations of the methyl groups attached to the main chain and side chain, with characteristic relaxation temperatures  $T_\beta = 10 - 40^\circ\text{C}$ ,  $T_\gamma = -100 - -170^\circ\text{C}$ , and  $T_\delta = -180^\circ\text{C}$ , and activation energies  $E_a^\beta = 71 - 96$  kJ/mol,  $E_a^\gamma = 10 - 29$  kJ/mol,  $E_a^\delta = 3$  kJ/mol, respectively.<sup>49,74,77</sup> In PMMA, the dynamics of the ester group ( $\beta$ -relaxation) may be coupled with main chain motions ( $\alpha$ -relaxation).<sup>71</sup> The overlap of the bell-shape curves characteristic for the  $\alpha$  and  $\beta$  relaxations has been observed at a frequency of about  $10^4$  Hz at  $50^\circ\text{C}$  in bulk mechanical studies.<sup>49</sup> An additional small relaxation band in PMMA was observed due to presence of absorbed water that also affected the  $\alpha$ -relaxation due to its plasticizing effect.<sup>49</sup>



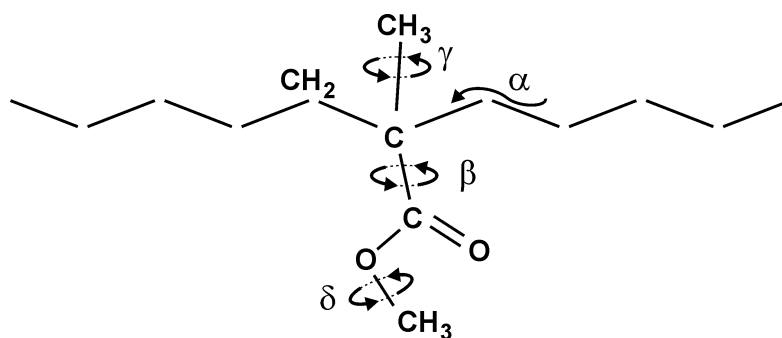


Figure 8-2. Schematic of the relaxations in PMMA.

We investigated PMMA films on oxidized silicon with a thickness of 125 nm. Films of this thickness were reported to show a  $T_g$  similar to the bulk values, as determined by ellipsometry and scanning thermal microscopy-based indentation measurements.<sup>78-80</sup> However, recent studies using fluorescence spectroscopic techniques showed a distribution of  $T_g$  near the interfaces.<sup>81,82</sup> The origins of the perturbations near the free surface and substrate interfaces differ. Near the free surface, enhanced segmental mobility and a reduced  $T_g$  have been observed.<sup>81</sup> At the substrate interface, the mobility depends on interaction of macromolecules with the substrate. No differences were observed for the dynamics of PS on glass. By contrast, an increase in  $T_g$  compared to the bulk  $T_g$  was found for PMMA on silica. This increase was attributed to attractive hydrogen bonding interactions.<sup>81,82</sup> Consequently,  $T_g$ -nanoconfinement effects in ultrathin films (< 100 nm) are induced by the presence of the free surface and the substrate interface that both modify the relevant polymer dynamics in their vicinity.<sup>12,83</sup>

For supported PS films it was shown that the distance over which a diminishing level of enhanced mobility extends into the film is several tens of nanometers from the surface.<sup>81</sup> For thick supported PMMA film, the interfacial effects perturb  $T_g$  values over a length scale of 100 nm.<sup>82</sup>

### 8.2.1. Effect of temperature

Variable temperature friction force vs. velocity measurements were conducted using the high velocity AFM set-up described in Chapter 5 in order to unveil possible surface relaxation processes. Figure 8-3 shows a plot of friction force vs. velocity for a PMMA film (thickness of 125 nm) on oxidized silicon measured with an oxidized silicon tip ( $R = 150$  nm) in dry nitrogen atmosphere (< 5% RH) at various temperatures between 5°C and 26°C. In these experiments no hysteresis was observed for data captured with increasing and for data recorded with decreasing velocity. Each data point was measured at different positions on the sample to prevent any influence of plastic deformation on the measured data. The sample was additionally imaged

using contact mode AFM following the completion of the tribological measurements to assess potential sample deformation. Only for low velocity scans ( $< 1 \mu\text{m/s}$ ), ploughing of the tip into sample surface was occasionally detected.<sup>84</sup> At a temperature of  $26^\circ\text{C}$  the friction force decreased with increasing velocity. For  $20^\circ\text{C}$  temperature a clear minimum in friction force was observed at  $40 \mu\text{m/s}$ . This minimum shifted to lower velocity with decreasing temperature. These results are consistent with the time-temperature superposition principle, which states that the same molecular relaxation requires longer time at a lower temperature.

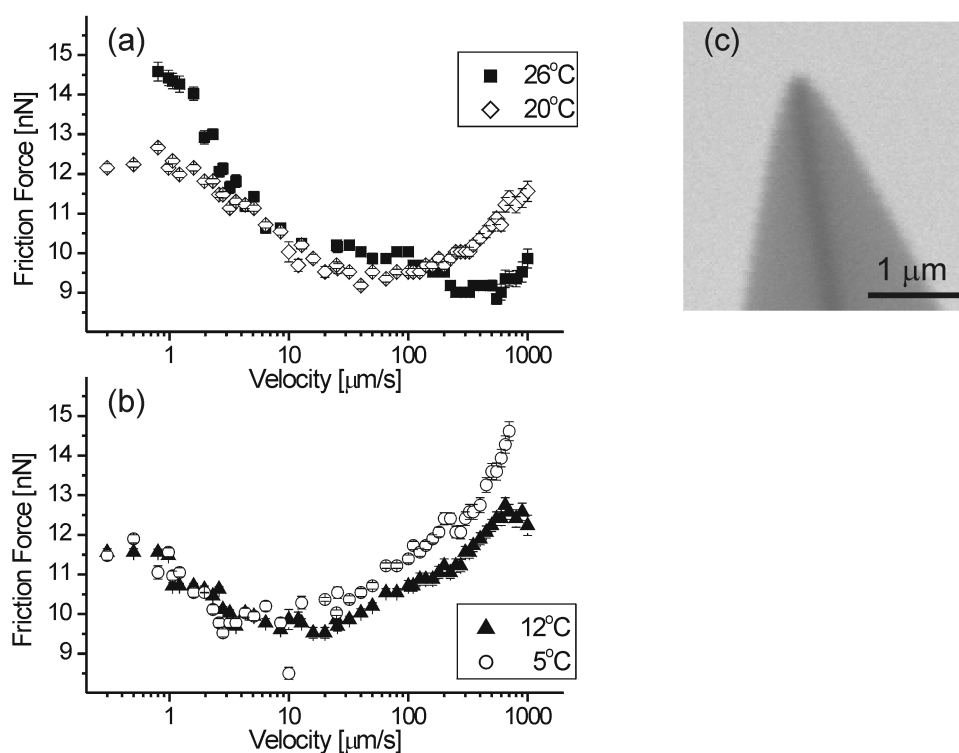


Figure 8-3. Semi-log plot of friction force vs. velocity for PMMA film on oxidized silicon (thickness 125 nm) measured with an oxidized silicon tip ( $R = 150 \text{ nm}$ ) in nitrogen atmosphere ( $< 5\% \text{ RH}$ ) at various temperatures: (a)  $26^\circ\text{C}$  and  $20^\circ\text{C}$ , (b)  $12^\circ\text{C}$  and  $5^\circ\text{C}$ . A load of 2 nN was maintained constant during the measurements. The error bars indicate the standard deviation of the data analyzed for a given velocity ( $n = 150$ ). (c) SEM image of the Si tip with radius  $R = 150 \text{ nm}$ .

The data in Figure 8-3 were shifted by a factor  $a_T$  to produce a master curve. The reference temperature was chosen as  $26^\circ\text{C}$ . Figure 8-4 shows the resulting master curve and the corresponding Arrhenius plot of  $\log(a_T)$  vs. inverse temperature. From the linear fit, an activation energy of  $60 \pm 5 \text{ kJ/mol}$  was calculated (Eq. 8-1). The error corresponds to  $\pm 2$  times the standard deviation of the slope for the linear fit.

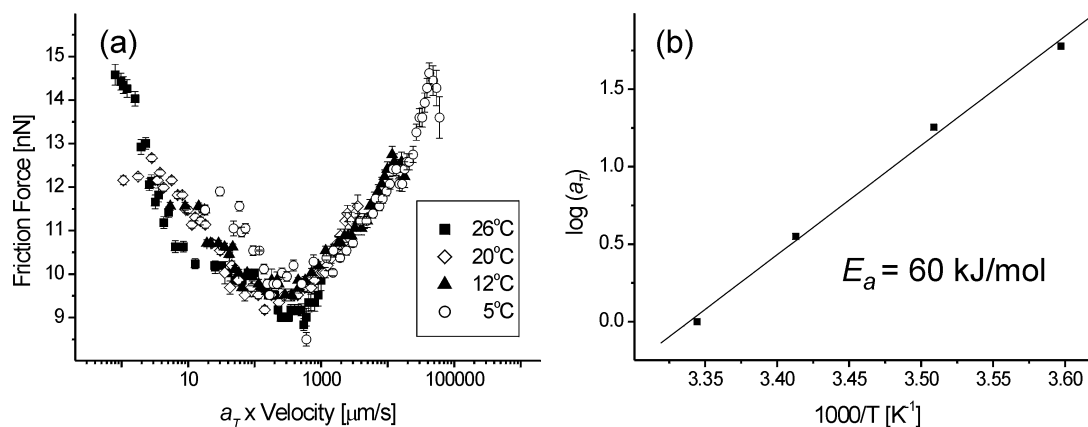


Figure 8-4. (a) Master curve of friction force vs. velocity data for PMMA (Figure 8-3) shifted to  $T_0 = 26^\circ\text{C}$ . (b) Arrhenius plot of log shift factor  $a_T$  vs. inverse temperature with linear fit (correlation coefficient  $R = 0.99$ ).

### 8.2.2. Effect of different tip radii

As already mentioned in the introduction, tips with different radii will result in different tip-sample contact lengths when identical scanning velocities are used. Thereby the time the tip affects a given point of the polymer surface differs, thus different frequencies can be accessed (as also described in detail in Section 8.3). The friction force response was therefore investigated using different tip radii.

Figure 8-5(a) displays a semi-log plot of friction force vs. velocity for a PMMA sample measured using the same conditions as Figure 8-3(a), except for the significantly increased tip radius ( $R = 870$  nm) (see Figure 8-5(b)). The friction force monotonically decreased with increasing velocity at  $26^\circ\text{C}$ . At  $10^\circ\text{C}$ , a similar trend was observed, albeit with lower values. At a temperature of  $-3^\circ\text{C}$ , a constant friction force, which was independent of velocity, was observed.

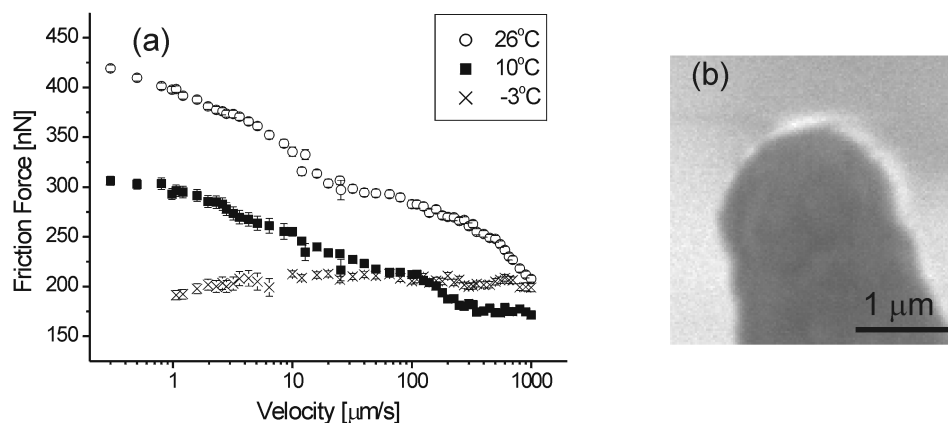


Figure 8-5. Semi-log plot of friction force vs. velocity for PMMA film on oxidized silicon (thickness 125 nm) measured with an oxidized silicon tip ( $R = 870$  nm) in nitrogen atmosphere ( $< 5\%$  RH) at various temperatures. A load of 2 nN was maintained constant during the measurements. The error bars indicate the standard deviation of the data analyzed for a given velocity ( $n = 150$ ).

A master curve of the data shown in Figure 8-5 was constructed according to the time-temperature superposition principle by shifting the data to 26°C. An activation energy of  $110 \pm 10$  kJ/mol was qualitatively estimated. This is higher than the  $E_a$  obtained in Section 8.2.1 (with a probe of 150 nm tip radius).

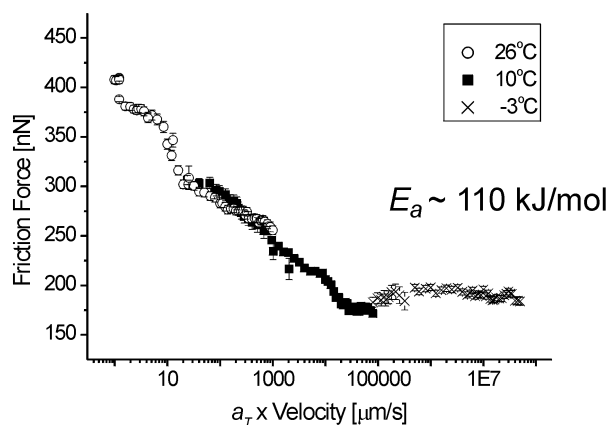


Figure 8-6. Master curve of friction force vs. velocity data for PMMA (Figure 8-5) shifted to 26°C.

The friction force vs. velocity data for PMMA obtained using a sharp tip (20 nm radius) displayed a broad peak around 200  $\mu\text{m/s}$  at 25°C, as shown in Figure 8-7. The peak shifted towards lower velocities at reduced temperatures (5°C), in accordance with the time-temperature principle.

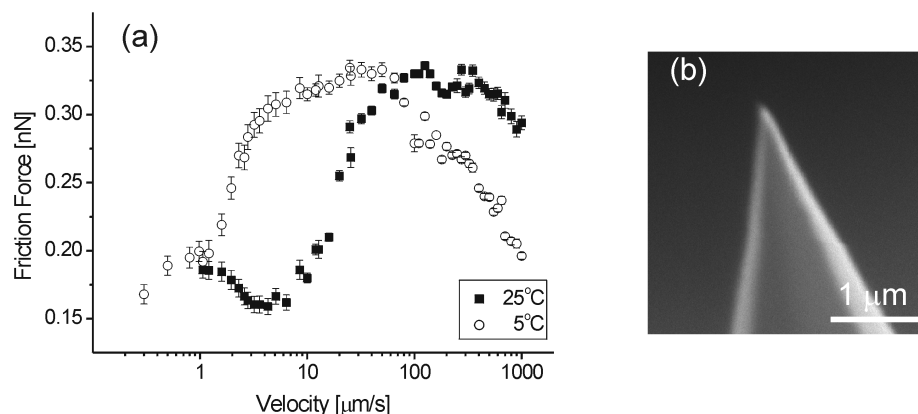


Figure 8-7. (a) Semi-log plot of friction force vs. velocity for PMMA film on oxidized silicon (thickness 125 nm) measured with an oxidized silicon tip ( $R = 20$  nm) in nitrogen atmosphere ( $< 5\%$  RH) at various temperatures: 25°C and 5°C. A load of 0.2 nN was maintained constant during the measurements. The error bars indicate the standard deviation of the data analyzed for a given velocity ( $n = 150$ ). (b) SEM image of the Si tip with radius  $R = 20$  nm.

A corresponding activation energy of 35 kJ/mol for this relaxation was estimated from the Arrhenius dependence shifted to 25°C. Due to the insufficient number of data points, this value can be considered to be a qualitative indication only.

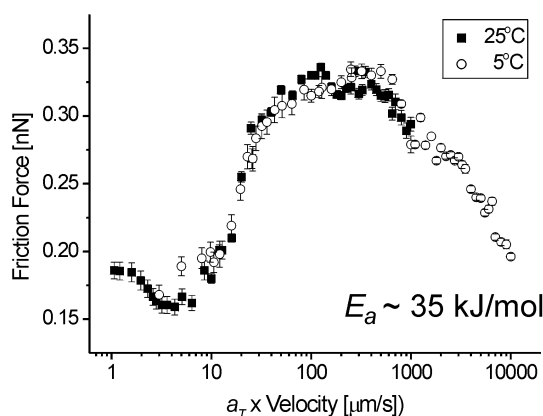


Figure 8-8. Master curve of friction force vs. velocity data for PMMA (Figure 8-7) shifted to 25°C. The estimated activation energy is 35 kJ/mol.

These three different values of activation energy imply that different relaxation processes were probed. Knowing the characteristic  $T$ , rate, and  $E_a$  of the bulk relaxations of PMMA (Section 8.2), we can exclude the presence of the  $\gamma$  and  $\delta$  relaxations. These relaxations are usually inaccessible by dielectric and dynamic mechanical methods due to their low characteristics temperatures. Therefore, we can expect the presence of the  $\alpha$  and/or the  $\beta$  relaxation. The shape

of the friction force velocity curve obtained using the tip with radius of 150 nm, may suggest that parts of two bell-shape curves characteristic for different relaxations coincide. However, the correlation of the results is only possible after conversion of the velocity to the frequency scale, as described in the next section.

### 8.3. Conversion of scanning velocity to frequency

The scan velocity was converted to frequency by dividing velocity values with the value of the contact diameter ( $2a$ ) that was calculated using the JKR theory<sup>85,86</sup> (see Chapter 2, Section 2.3.2). Corresponding contact lengths of 150 nm, 40 nm and 8 nm were calculated for probes with radii of 870 nm, 150 nm, and 20 nm, respectively. The friction force data obtained using different probes at 26°C were normalized by division by the contact area to yield shear strength (friction force per unit area) and were subsequently plotted as a function of frequency (Figure 8-9). The value of the shear strength is very similar to the reported 10 MPa for PMMA films (thickness 200 nm).<sup>56</sup>

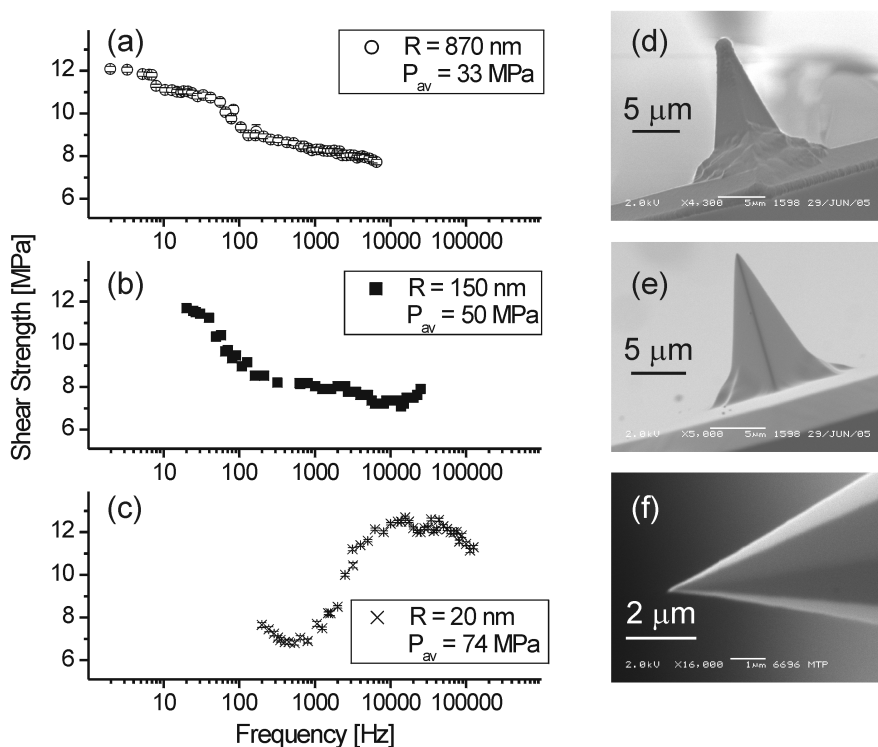


Figure 8-9. Effect of different tip radii on shear strength vs. frequency for PMMA film on oxidized silicon (thickness 125 nm) measured in nitrogen atmosphere (< 5% RH) at 26°C (tip radii: (a) 870 nm, (b) 150 nm, and (c) 20 nm). Loads of 2 nN, 2 nN, and 0.2 nN, respectively, were maintained constant during the measurements. The error bars indicate the standard deviation of the data analyzed for a given velocity ( $n = 150$ ). SEM images of the tips with radii ((d)  $R = 870$  nm, (e) 150 nm, and (f) 20 nm).

It becomes evident that a large range of frequencies from Hz to MHz was probed using tips with different radii. Low frequencies were accessed in experiments with large tip radii, whereas high frequencies were characterized using sharp probes. Two different relaxations can be distinguished by combining the different results, see Figure 8-9(a)-(c). At low frequency only a part of the relaxation curve is visible, whereas at  $10^5$  Hz a typical bell-shape curve is identified. The peak (Figure 8-9(c)) seems to be shifted to lower frequencies, in comparison with the results shown in (a) and (b). This phenomenon could be associated with the tip pressure effect and is discussed in the next section (see also Appendix 8-1).

#### **8.4. Effect of sample-tip contact pressure on relaxation processes**

The effect of the pressure, which was applied by the AFM tip on the surface, on the sample relaxation was investigated using V-shaped  $\text{Si}_3\text{N}_4$  cantilevers<sup>87</sup> at 26°C. This temperature is significantly below the bulk  $T_g$  of 109°C (as determined from differential scanning calorimetry (DSC)). Friction force – velocity measurements were performed for applied loads of 0 nN and 4 nN (Figure 8-10(a)), resulting in different average contact pressures of 84 MPa and 92 MPa, respectively, as calculated using the JKR theory (Chapter 2).

In both cases, broad peaks were observed. For 4 nN load, and the height of the peak was elevated compared to the data obtained at lower load due to the increase in tip sample contact area (for single asperity friction force is proportional to the real contact area, as described in Chapter 2). The peak was also shifted horizontally to lower velocities. This observation is ascribed to the effect of the contact pressure exerted by the tip, which hinders locally the motion of the chain and rotation of the side groups. Thus, the relaxation shifts to lower frequencies, which is similar to the effect observed with decreasing temperature (Figure 8-1). In a control experiment the absence of ploughing or wear was confirmed.

This observation is consistent with PVT diagrams and results reported by Gracias *et al.*<sup>58</sup> They observed a shift of  $T_g$  towards higher temperatures in SPM experiments on polypropylene for measurements performed with constant force with sharp tips (radius  $\sim 50$  nm) as compared to blunt tip (radius  $\sim 1000$  nm).<sup>58</sup> Based on the given arguments, it is assumed that the horizontal shift in the friction force - velocity dependence is caused by the tip sample pressure effect. The pressure exerted acts in a similar manner as hydrostatic pressure and changes the relaxation response locally in the tip - sample contact area.

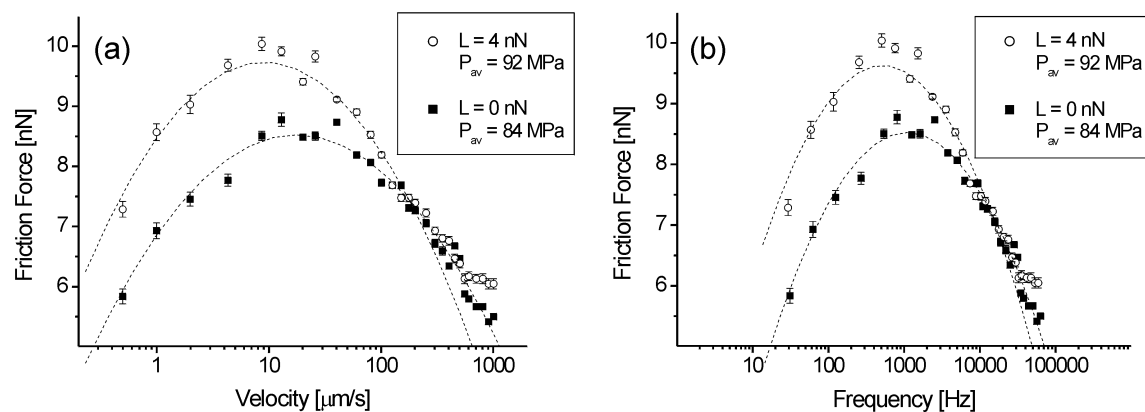


Figure 8-10. Effect of different contact pressure on friction force vs. (a) velocity, and (b) frequency for PMMA films on oxidized silicon (thickness 125 nm) measured with a  $\text{Si}_3\text{N}_4$  tip ( $R = 35$  nm) in nitrogen atmosphere ( $< 5\%$  RH) at  $26^\circ\text{C}$ . The error bars indicate the standard deviation of the data ( $n = 150$ ) analyzed for a given velocity. The transformation of velocity to frequency was performed using the procedure introduced in the previous section.

There is a second factor that may cause a horizontal shift of the friction force – frequency curve that was recognized with increasing pressure (applied load). In addition to the direct effect of the contact pressure of the tip, the concomitant increase of the tip sample contact length needs to be considered. Both effects shift the curve horizontally to lower frequencies. However, the increase in the contact length has a much less pronounced effect on the shift as compared to the pressure effect (below 1% of the total shift using tip of 35 nm radius vs. a 16% increase in pressure accounting for  $> 99\%$  of the shift).

The influence of pressure on the relaxation temperature was estimated from the value of the activation energy, assuming a value of 35 kJ/mol (tip with 20 nm radius). The approximated increase of the relaxation temperature of  $0.5^\circ\text{C}/\text{MPa}$  is in good agreement with the effect of hydrostatic pressure ( $\sim 0.35^\circ\text{C}/\text{MPa}$ ).<sup>77,88</sup> Therefore, an increase as high as  $20^\circ\text{C}$  can be expected for the same relaxation probed with the sharp tip ( $R = 20$  nm), as compared to the large tip ( $R = 870$  nm) at the same applied force.

### 8.5. Construction of a mastercurve for observed surface relaxations via the time-temperature superposition principle

The combined shear strength vs. frequency plot, *i.e.* the overall master curve at  $26^\circ\text{C}$  covering a large range of probed frequencies, obtained in experiments with tips with different radii is displayed in Figure 8-9. In this plot the effect of pressure variation has been corrected according



to the previous section. When compared to bulk relaxations (the frequency is a mirror image vs. y-axis of temperature dependence  $f \leftrightarrow -T$ ), two relaxations can be distinguished: one of lower frequency (higher temperature) and one of higher frequency (lower temperature). These relaxations are attributed to the  $\alpha$  and the  $\beta$  processes, respectively.

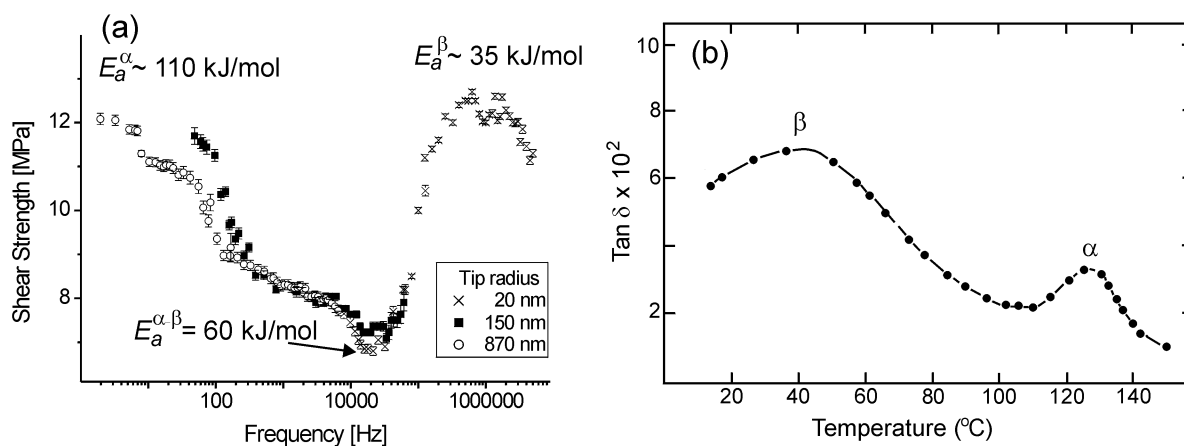


Figure 8-11. (a) Combined shear strength vs. frequency relation for PMMA film obtained using three different tip radii at 26 $^\circ\text{C}$ . The data are corrected for the effect of pressure. (b) Temperature dependence of the dielectric loss tangent at 28 Hz for conventional PMMA (after reference 49).

We assigned the observed peak in the MHz range to the  $\beta$ -relaxation of PMMA, which is the result of the rotation of the  $-(\text{CO})\text{OCH}_3$  side groups around the C-C bonds linking the side groups to the main polymer chain.<sup>77</sup> The value of the corresponding activation energy of  $\sim 35$  kJ/mol is significantly lower than the bulk value (71 – 96 kJ/mol) determined by mechanical and dielectric methods.<sup>49</sup> Furthermore, the frequency of the  $\beta$ -relaxation is significantly higher ( $10^6$  Hz) than the frequency detected in bulk measurements (10 – 100 Hz) at room temperature. Both the higher frequency and lower activation energy indicate greater free volume<sup>89</sup> and correspondingly higher mobility at the polymer surface.

A qualitatively similar trend for  $E_a$  in PMMA friction force - velocity data was reported by Hammerschmidt *et al.*<sup>44</sup> However, *the corresponding temperatures and frequencies were very similar to the bulk values*. These authors measured the friction force for only four different velocities between 2 and 220  $\mu\text{m/s}$ .<sup>90</sup> The highest value observed for measurements at 25 $^\circ\text{C}$  was ascribed to the  $\beta$ -relaxation with an activation energy of 50 kJ/mol, which is also lower than the bulk value. On the other hand, the frequency and temperature of the relaxation were similar to the bulk values ( $f = 2000$  Hz,  $T = 50^\circ\text{C}$ ), which is in contradiction with the concluded higher mobility at the surface and is also in disagreement with the data reported here.

The part of the relaxation curve detected at lower frequencies ( $1 - 10^4$  Hz) is attributed to the  $\alpha$ -transition. From the changing slope of the curve, the maximum can be anticipated at around 1 Hz. The curve is expected to possess a bell shape. However, due to increasing ploughing and plastic deformation it was impossible to measure the bend at low velocities (frequencies). This additional component to friction force is known to change the shape of the relaxation curve.<sup>66</sup> The estimated activation energy of 110 kJ/mol observed is significantly lower than the bulk value (334 – 460 kJ/mol) and the relaxation frequency is noticeably higher compared to the bulk ( $f = 1$  Hz,  $T = 26^\circ\text{C}$  and  $f = 1$  Hz,  $T = 100^\circ\text{C}$ , respectively).<sup>49</sup> The overlap of curves characteristic for the  $\alpha$  and  $\beta$  relaxations is observed at a frequency of about  $2 \times 10^4$  Hz at  $26^\circ\text{C}$ , which is noticeably lower in temperature in comparison with bulk mechanical studies ( $f = 2 \times 10^4$  Hz,  $T = 50^\circ\text{C}$ ).<sup>49</sup> The determined activation energy of 60 kJ/mol is influenced by both  $\alpha$  and  $\beta$  processes due to their different activation energies and shift factors. Thus the resultant shift factor (activation energy) will be a superposition of  $\alpha$  and  $\beta$  processes. These observations of low activation energies and higher relaxation frequencies are consistent with the reported greater free volume at the polymer/air interface.<sup>91</sup> This important result could be obtained due to the large range of frequencies available in the new high velocity AFM approach described earlier, as well as the calibration protocols developed in this Thesis. In addition, AFM tips with widely different radii were exploited to extend the range of frequencies probed by altering the length of the tip-sample contact in a predetermined way. This combined approach of a high velocity actuator and control of tip-sample contact length allowed us to probe the  $\alpha$  and the  $\beta$  relaxations of PMMA at  $26^\circ\text{C}$ , which is significantly below the bulk  $T_g$ .<sup>92</sup> For PMMA a fully consistent picture has emerged, in which significantly lowered activation barriers and increased frequencies coincide, as expected based on the time-temperature superposition principle. Local pressure effects were found to match with trends observed in bulk PVT measurements. In addition to providing new insight into the surface relaxations of PMMA, the work reported in this Chapter demonstrates that such studies and the crossing of length scales of tip-sample contact area from the meso- to the nanoscale are feasible for a wide range of polymeric systems.

## 8.6. Conclusions

Using the newly developed high velocity accessory with temperature control described in Chapter 5 and tips with different radii it was possible to study surface relaxations of PMMA in a broad range of frequencies ( $1 - 10^7$  Hz) quantitatively. The characteristic curves for the  $\alpha$  and the  $\beta$  relaxations, as well as the overlap of the curves, were detected at  $26^\circ\text{C}$  using tips with

radius of 870 nm, 20 nm, and 150 nm, respectively. The activation energies of the relaxation processes were significantly lower and the observed relaxation frequencies were noticeably higher compared to the corresponding bulk values. These results indicate a greater free volume at the polymer surface and a higher molecular mobility at the polymer/air interface. Moreover, it was confirmed that the tip sample pressure acts in a similar way as hydrostatic pressure, *i.e.* it changes locally the relaxation response. The new high velocity AFM technique developed in this Thesis allows one to examine polymer surface dynamics and to characterize differences between surface and bulk behavior. With the advanced understanding of molecular relaxation processes in thin polymer films, the control of interfacial boundary layers will become possible, which will enable precise material engineering that is important for future nanotechnological applications.

## 8.7. Experimental

### 8.7.1. Materials and sample preparation

All chemicals were used as received, unless otherwise stated. All solvents were purchased from Biosolve. Films of poly(methyl methacrylate) (PMMA, Aldrich,  $M_w = 120\,000$  g/mol) with thickness of 125 nm were prepared by spin coating filtered solutions in toluene (conc. 5 wt-%) onto freshly cleaned oxidized Si(100) substrates (Spin Coater P6700, Specialty Coating Systems, Indianapolis, IN). Bare Si(100) wafers with native oxide layer (P/Boron type, thickness  $525 \pm 25$   $\mu\text{m}$ , Okmetic Oyj, Vantaa, Finland) were cleaned prior to spin coating by rinsing them thoroughly with chloroform and ethanol, followed by an oxygen-plasma treatment (30 mA, 60 mTorr) using a Plasma Prep II plasma cleaner (SPI Supplies, West Chester, PA) for 10 min. PMMA films were annealed at 150°C under vacuum for 12 hours.

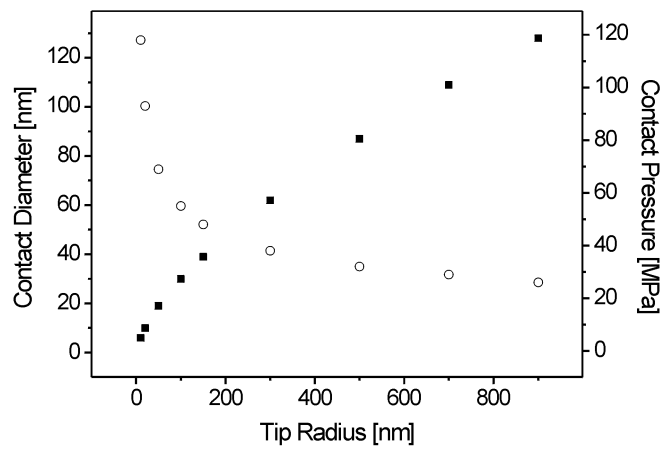
### 8.7.2. Lateral force measurements

Quantitative friction analyses on freshly prepared PMMA films were carried out using Si and Si<sub>3</sub>N<sub>4</sub> probes with different tip radii: 20 nm (Si cantilever with  $k_N = 0.03$  N/m (CSC38 without reflective coating, MikroMasch, Tallinn, Estonia)), 150 nm (Si cantilever with  $k_N = 0.69$  N/m (custom made without reflective coating, kind gift of NanoWorld Services GmbH, Erlangen, Germany)), 870 nm (Si cantilever with  $k_N = 0.30$  N/m (custom made without reflective coating, kind gift of NanoWorld AG, Neuchatel, Switzerland)), and V-shaped Si<sub>3</sub>N<sub>4</sub> cantilever with  $k_N = 0.30$  N/m (Model NP, Veeco, Santa Barbara, CA). Prior to the measurements the probes were

cleaned by immersion in and rinsing with chloroform followed by drying in a stream of nitrogen.

Friction force - velocity measurements (scan size of 500 nm) were performed with a stand alone AFM (Molecular Imaging, Tempe, USA) equipped with the high velocity accessory developed (Chapter 5) on PMMA thin films (thickness  $125 \pm 5$  nm) on oxidized Si(100). The lateral photodiode output signal, which was acquired in the time domain, was recorded via the data acquisition board and was processed by the software described in Chapter 5. Each data point represents the mean value of one-half of the difference friction signal calculated from 150 trace and retrace cycles and the error bars correspond to the standard deviation of the data analyzed for a given load and velocity. The normal force is defined as the sum of pull-off force and externally applied load. The climate control ( $< 5\%$  relative humidity (RH) and temperatures between  $-3^{\circ}\text{C}$  and  $26^{\circ}\text{C}$ ) was performed via the flow of pre-thermostatted nitrogen gas of controlled humidity through an environmental chamber (PicoAPEX, Pyrex glass, MI, Tempe, USA) as measured by a humidity sensor (SHT15, Sensirion, Switzerland). The calibration of the cantilevers was performed using the method described in Chapter 3. The dimensions of the cantilevers and tip radii were obtained from scanning electron microscopy (SEM) images (JSM 5600 LV, Jeol, Tokyo, Japan operated at 2 kV) by Clemens Padberg (Department of Materials Science and Technology of Polymers, University of Twente).

## 8.8. Appendix



Appendix 8-1. The effect of tip radii on contact diameter (solid squares) and average contact pressure (open circles) with a flat surface, calculated using JKR theory (Chapter 2, Section 2.3.2) for an applied load of 0 nN and a work of adhesion of 0.08 J.

**8.9. References**

- 1 Dinelli, F.; Buenviaje, C.; Overney, R. M. *J. Chem. Phys.* **2000**, *113*, 2043-2048.
- 2 Overney, R. M.; Buenviaje, C.; Luginbuhl, R.; Dinelli, F. *J. Therm. Anal.* **2000**, *59*, 205-225.
- 3 Sills, S.; Overney, R. M.; Chau, W.; Lee, V. Y.; Miller, R. D.; Frommer, J. *J. Chem. Phys.* **2004**, *120*, 5334-5338.
- 4 DeMaggio, G. B.; Frieze, W. E.; Gidley, D. W.; Zhu, M.; Hristov, H. A.; Yee, A. F. *Phys. Rev. Lett.* **1997**, *78*, 1524-1527.
- 5 Forrest, J. A.; Mattsson, J. *Phys. Rev. E* **2000**, *61*, R53-R56.
- 6 Jones, R. A. L. *Curr. Opin. Colloid Interface Sci.* **1999**, *4*, 153-158.
- 7 Keddie, J. L.; Jones, R. A. L.; Cory, R. A. *Europhys. Lett.* **1994**, *27*, 59-64.
- 8 Keddie, J. L.; Jones, R. A. L.; Cory, R. A. *Faraday Discuss.* **1994**, 219-230.
- 9 Kim, J. H.; Jang, J.; Zin, W. C. *Langmuir* **2001**, *17*, 2703-2710.
- 10 Prucker, O.; Christian, S.; Bock, H.; Ruhe, J.; Frank, C. W.; Knoll, W. *Macromol. Chem. Phys.* **1998**, *199*, 1435-1444.
- 11 vanZanten, J. H.; Wallace, W. E.; Wu, W. L. *Phys. Rev. E* **1996**, *53*, R2053-R2056.
- 12 Tomczak, N. Single Light Emitters in the Confinement of Polymers. Ph.D. thesis, University of Twente, Enschede, 2005.
- 13 Despotopoulou, M. M.; Frank, C. W.; Miller, R. D.; Rabolt, J. F. *Macromolecules* **1996**, *29*, 5797-5804.
- 14 Despotopoulou, M. M.; Frank, C. W.; Miller, R. D.; Rabolt, J. F. *Macromolecules* **1995**, *28*, 6687-6688.
- 15 Despotopoulou, M. M.; Miller, R. D.; Rabolt, J. F.; Frank, C. W. *J. Polym. Sci. Pt. B-Polym. Phys.* **1996**, *34*, 2335-2349.
- 16 Sawamura, S.; Miyaji, H.; Izumi, K.; Sutton, S. J.; Miyamoto, Y. *J. Phys. Soc. Jpn.* **1998**, *67*, 3338-3341.
- 17 Sutton, S. J.; Izumi, K.; Miyaji, H.; Miyamoto, Y.; Miyashita, S. *J. Mater. Sci.* **1997**, *32*, 5621-5627.
- 18 Schönherr, H.; Frank, C. W. *Macromolecules* **2003**, *36*, 1188-1198.
- 19 Schönherr, H.; Frank, C. W. *Macromolecules* **2003**, *36*, 1199-1208.
- 20 Meuse, C. W.; Yang, X. Z.; Yang, D. C.; Hsu, S. L. *Macromolecules* **1992**, *25*, 925-932.
- 21 Krausch, G.; Dai, C. A.; Kramer, E. J.; Marko, J. F.; Bates, F. S. *Macromolecules* **1993**, *26*, 5566-5571.
- 22 Tao, H. J.; Meuse, C. W.; Yang, X. Z.; Macknight, W. J.; Hsu, S. L. *Macromolecules* **1994**, *27*, 7146-7151.
- 23 Fasolka, M. J.; Banerjee, P.; Mayes, A. M.; Pickett, G.; Balazs, A. C. *Macromolecules* **2000**, *33*, 5702-5712.
- 24 Pfromm, P. H.; Koros, W. J. *Polymer* **1995**, *36*, 2379-2387.
- 25 Liang, T.; Makita, Y.; Kimura, S. *Polymer* **2001**, *42*, 4867-4872.
- 26 Tan, N. C. B.; Wu, W. L.; Wallace, W. E.; Davis, G. T. *J. Polym. Sci. Pt. B-Polym. Phys.* **1998**, *36*, 155-162.
- 27 Reiter, G. *Europhys. Lett.* **1993**, *23*, 579-584.
- 28 Maeda, N.; Chen, N. H.; Tirrell, M.; Israelachvili, J. N. *Science* **2002**, *297*, 379-382.
- 29 Sills, S.; Overney, R. M.; Gotsmann, B.; Frommer, J. *Tribol. Lett.* **2005**, *19*, 9-15.

- 
- 30 Dürig, U.; Cross, G.; Despont, M.; Drechsler, U.; Häberle, W.; Lutwyche, M. I.; Rothuizen, H.; Stutz, R.; Widmer, R.; Vettiger, P.; Binnig, G. K.; King, W. P.; Goodson, K. E. *Tribol. Lett.* **2000**, *9*, 25-32.
- 31 Lutwyche, M. I.; Despont, M.; Drechsler, U.; Dürig, U.; Häberle, W.; Rothuizen, H.; Stutz, R.; Widmer, R.; Binnig, G. K.; Vettiger, P. *Appl. Phys. Lett.* **2000**, *77*, 3299-3301.
- 32 Hall, D. B.; Hooker, J. C.; Torkelson, J. M. *Macromolecules* **1997**, *30*, 667-669.
- 33 Tomczak, N.; Vallee, R. A. L.; van Dijk, E.; Garcia-Parajo, M.; Kuipers, L.; van Hulst, N. F.; Vancso, G. J. *Eur. Polym. J.* **2004**, *40*, 1001-1011.
- 34 Vallee, R. A. L.; Tomczak, N.; Kuipers, L.; Vancso, G. J.; van Hulst, N. F. *Chem. Phys. Lett.* **2004**, *384*, 5-8.
- 35 Vallee, R. A. L.; Tomczak, N.; Kuipers, L.; Vancso, G. J.; van Hulst, N. F. *Phys. Rev. Lett.* **2003**, *91*, 038301.
- 36 Vallee, R.; Tomczak, N.; Gersen, H.; van Dijk, E.; Garcia-Parajo, M. F.; Vancso, G. J.; van Hulst, N. F. *Chem. Phys. Lett.* **2001**, *348*, 161-167.
- 37 Bailey, L. E.; Kambhampati, D.; Kanazawa, K. K.; Knoll, W.; Frank, C. W. *Langmuir* **2002**, *18*, 479-489.
- 38 Kajiyama, T.; Tanaka, K.; Takahara, A. *Macromolecules* **1997**, *30*, 280-285.
- 39 Sills, S.; Fong, H.; Buenviaje, C.; Sarikaya, M.; Overney, R. M. *J. Appl. Phys.* **2005**, *98*.
- 40 Kajiyama, T.; Tanaka, K.; Takahara, A. *Polymer* **1998**, *39*, 4665-4673.
- 41 Satomi, N.; Tanaka, K.; Takahara, A.; Kajiyama, T. *Macromolecules* **2001**, *34*, 6420-6423.
- 42 Tanaka, K.; Takahara, A.; Kajiyama, T. *Macromolecules* **1997**, *30*, 6626-6632.
- 43 Sills, S.; Gray, T.; Overney, R. M. *J. Chem. Phys.* **2005**, *123*, 134902.
- 44 Hammerschmidt, J. A.; Gladfelter, W. L.; Haugstad, G. *Macromolecules* **1999**, *32*, 3360-3367.
- 45 Hammerschmidt, J. A.; Moasser, B.; Gladfelter, W. L.; Haugstad, G.; Jones, R. R. *Macromolecules* **1996**, *29*, 8996-8998.
- 46 Haugstad, G.; Gladfelter, W. L.; Jones, R. R. *Langmuir* **1998**, *14*, 3944-3953.
- 47 Haugstad, G.; Gladfelter, W. L.; Weberg, E. B.; Weberg, R. T.; Weatherill, T. D.; Jones, R. R. *Mater. Sci. Eng. C-Biomimetic Mater. Sens. Syst.* **1995**, *3*, 85-89.
- 48 Aklonis, J. J.; MacKnight, W. J. *Introduction to Polymer Viscoelasticity*. Wiley: New York, 1983.
- 49 McCrum, N. G.; Read, B. E.; Williams, G. *Anelastic and Dielectric Effects in Polymeric Solids*. John Wiley & Sons: London, 1967.
- 50 Flory, P. J. *Statistical Mechanics of Chain Molecules*. Interscience Publishers: New York, 1969.
- 51 Sperling, L. H. *Introduction to Physical Polymer Science*. John Wiley & Sons: New York, 1985.
- 52 Young, R. J.; Lovell, P. A. *Introduction to Polymers*. Chapman & Hall: London, 1991.
- 53 Cherry, B. W. *Polymer Surfaces*. Cambridge University Press: Cambridge, 1981.
- 54 Grosch, K. A. *Proc. R. Soc. London Ser. A-Math. Phys. Sci.* **1963**, *274*, 21-39.
- 55 Ferry, J. D. *Viscoelastic Properties of Polymers*. Wiley & Sons: New York, 1980.
- 56 Briscoe, B.; Smith, A. C. *J. Phys. D: Appl. Phys.* **1982**, *15*, 579-594.
- 57 Sills, S.; Overney, R. M. *Phys. Rev. Lett.* **2003**, *91*, 095501.
- 58 Gracias, D. H.; Zhang, D.; Lianos, L.; Ibach, W.; Shen, Y. R.; Somorjai, G. A. *Chem. Phys.* **1999**, *245*, 277-284.
- 59 Kajiyama, T.; Tanaka, K. I.; Takahara, A. *Macromol. Symp.* **2003**, *192*, 265-270.
- 60 E.g. for a scan size of  $1 \mu\text{m}^2$  the pixel size is  $2 \text{nm}^2$ , by increasing the scan size to  $100 \mu\text{m}^2$ , the resolution decreases 100 times and the pixel size equals  $200 \text{nm}^2$ . In this case, sample homogeneity and roughness may influence the measured friction force data.
- 61 Wang, X. P.; Tsui, O. K. C.; Xiao, X. D. *Langmuir* **2002**, *18*, 7066-7072.
-

- 
- 62 Tocha, E.; Stefański, T.; Schönherr, H.; Vancso, G. J. *Rev. Sci. Instrum.* **2005**, *76*, 083704.
- 63 Niederberger, S.; Gracias, D. H.; Komvopoulos, K.; Somorjai, G. A. *J. Appl. Phys.* **2000**, *87*, 3143-3150.
- 64 Schmidt, M.; Maurer, F. H. J. *J. Polym. Sci. Pt. B-Polym. Phys.* **1998**, *36*, 1061-1080.
- 65 Zoller, P.; Walsh, D. J. *Standard Pressure-Volume-Temperature Data for Polymers*. Technomic Publishing Co. Inc., Lancaster: 1995.
- 66 Grosch, K. A. *Proc. Roy. Soc. London, Ser. A* **1963**, *274*, 21-39.
- 67 Schmidt, R. H.; Haugstad, G.; Gladfelter, W. L. *Langmuir* **2003**, *19*, 10390-10398.
- 68 Schmidt, R. H.; Haugstad, G.; Gladfelter, W. L. *Langmuir* **1999**, *15*, 317-321.
- 69 Schönherr, H.; Bailey, L. E.; Frank, C. W. *Langmuir* **2002**, *18*, 490-498.
- 70 Ardi, M. S.; Dick, W.; Kubat, J. *Colloid Polym. Sci.* **1993**, *271*, 739-747.
- 71 Bergman, R.; Alvarez, F.; Alegria, A.; Colmenero, J. *J. Chem. Phys.* **1998**, *109*, 7546-7555.
- 72 Sane, S. B.; Knauss, W. G. *Mech. Time-Depend. Mater.* **2001**, *5*, 293-324.
- 73 Sane, S. B.; Knauss, W. G. *Mech. Time-Depend. Mater.* **2001**, *5*, 325-343.
- 74 de Deus, J. F.; Souza, G. P.; Corradini, W. A.; Atvars, T. D. Z.; Akcelrud, L. *Macromolecules* **2004**, *37*, 6938-6944.
- 75 Schmidt-Rohr, K.; Kulik, A. S.; Beckham, H. W.; Ohlemacher, A.; Pawelzik, U.; Boeffel, C.; Spiess, W. *Macromolecules* **1994**, *27*, 4733-4745.
- 76 Dubek, G.; Lupke, T.; Stejny, J.; Alam, M. A.; Arnold, M. *Macromolecules* **2000**, *33*, 990.
- 77 Gedde, U. W. *Polymer Physics*. Kluwer Academic Publishers: Dordrecht, 1999.
- 78 Fryer, D. S.; Peters, R. D.; Kim, E. J.; Tomaszewski, J. E.; de Pablo, J. J.; Nealey, P. F.; White, C. C.; Wu, W. L. *Macromolecules* **2001**, *34*, 5627-5634.
- 79 Fryer, D. S.; Nealey, P. F.; de Pablo, J. J. *J. Vac. Sci. Technol. B* **2000**, *18*, 3376-3380.
- 80 Fryer, D. S.; Nealey, P. F.; de Pablo, J. J. *Macromolecules* **2000**, *33*, 6439-6447.
- 81 Ellison, C. J.; Torkelson, J. M. *Nat. Mater.* **2003**, *2*, 695-700.
- 82 Priestley, R. D.; Ellison, C. J.; Broadbelt, L. J.; Torkelson, J. M. *Science* **2005**, *309*, 456-459.
- 83 Tomczak, N.; Vallee, R. A. L.; van Dijk, E.; Kuipers, L.; van Hulst, N. F.; Vancso, G. J. *J. Am. Chem. Soc.* **2004**, *126*, 4748-4749.
- 84 At low scanning velocities small deviation from the applied load was possible due to scanner drift.
- 85 Johnson, K. L. *Proc. R. Soc. London Ser. A-Math. Phys. Eng. Sci.* **1997**, *453*, 163-179.
- 86 Johnson, K. L. *Langmuir* **1996**, *12*, 4510-4513.
- 87 Friction force on polymers has a large contribution from internal viscoelastic dissipation. Thus, the results obtained using Si and Si<sub>3</sub>N<sub>4</sub> probes are anticipated to be similar.
- 88 Schmidt, M.; Maurer, F. H. J. *Macromolecules* **2000**, *33*, 3879-3891.
- 89 The free volume of a polymer is the unoccupied space (vacancies) available for segmental motion.
- 90 The scanning velocity was obtained by changing simultaneously both the scan frequency and the scan size, thus resolution was compromised.
- 91 Mansfield, K. F.; Theodorou, D. N. *Macromolecules* **1991**, *24*, 6283-6294.
- 92 The central advantage of this method, as compared to the friction force studies carried out at variable temperature only, is that significant artifacts due to changes in the materials properties (Young's modulus, adhesion, scratch resistance) associated with the glass transition can be circumvented.
-



# Outlook

The complexity of nanotribology brings many challenges in studying and accordingly understanding the underlying processes, mechanisms and phenomena. Despite the significant success of using new experimental methods, such as AFM and SFA, as well as new computational methods, to analyze friction processes on the nanometer scale and thereby to contribute to an improved understanding of various aspects of tribology, the gap of time and length scales between nano- and microtribology still exists. This gap is evident considering the time and length scales involved in the different experimental techniques compared to the corresponding parameters in molecular dynamic simulations of nanometer scale friction. In addition, each experimental method possesses its own intrinsic limitations and drawbacks (see Chapter 2).

In this Thesis the development of the necessary platform for quantitative nanotribology by AFM at high velocities was described that overcomes some of the previously existing instrumental obstacles, such as the limited range of velocities.<sup>1,2</sup> As shown, this platform allows one to quantitatively study the effects of environment, nanostructure and velocity on friction for different types of materials.<sup>3</sup> The developed platform contributed significantly to narrow the gap of time and length scales between nano- and microtribology, however, the scan velocity must be increased by at least 2 decades to entirely close this gap.

For complementary nano- and microtribology measurements, it is further necessary to use the same probe (tip) material to correlate the corresponding processes as assessed in AFM and pin-on-disc tests, respectively. This can be realized by modifying AFM tips. Future work should address the refinement of tip coating procedures, in which various inorganic materials are deposited in a highly controlled manner onto AFM probe tips. In Chapter 3, PLD was shown to be a suitable method for coating AFM tips. The deposited  $\gamma$ -Al<sub>2</sub>O<sub>3</sub> coating improved the tips' wear resistance and hence stability. The optimization of the coating process to yield a pure  $\alpha$ -Al<sub>2</sub>O<sub>3</sub> coating is expected to result in even higher stability. The improvement of wear-resistance of AFM tips will hence open the possibility to study nanotribology of hard materials, for example ceramics, which are also used as artificial hips.

Apart from experimental studies of nanotribology, the related phenomena need to be simulated and modeled. In Chapter 5 it was shown that friction force increased linearly vs. logarithm of

velocity for Si(100). By contrast, the friction coefficient was independent of velocity above velocities of 12  $\mu\text{m/s}$ . Understanding of this phenomenon requires an in depth understanding of the fundamentals of atomic scale friction on these materials, as well as of the influence of environment on the friction force and the friction coefficient. Modeling and systematic studies of single asperity friction over a broad range of velocities is believed to provide understanding of fundamental aspects of friction and the mechanisms of energy dissipation.

The viscoelastic dissipation in polymer thin films determines their nanotechnological applications.<sup>4,5</sup> Correspondingly tailored materials properties are relevant for many technological applications, such as MEMS, NEMS, as well as nanocomposites, coatings, nanolithography, and data storage devices (“Millipede”).<sup>6-10</sup> The studies of the time-temperature superposition principle of relaxation processes in PMMA films showed significant differences of macromolecular dynamics at the surface as compared to the bulk (Chapter 8). Taking advantage of high lateral resolution of AFM it would be advantageous to perform laterally resolved two-dimensional friction force *mapping* as a function of velocity and to probe local inhomogeneities at polymer surfaces. Ultimately these studies could be extended studies of heterogeneous systems (*i.e.* polymer blends and block copolymers films). This mapping will allow one to obtain detailed understanding of molecular-level processes at the polymer surface, which will provide a new approach to engineered materials.

In this context it is important to point out that the high velocity accessory described in Chapter 5 has not reached the technical limits and can be further improved. The range of accessible velocities can be increased by exchanging the driving amplifier with a high power amplifier. The estimated limit of velocity for this particular shear piezo is *ca.* 0.1 m/s, which does not establish the ultimate fundamental limit of this method. In principle, velocities of  $>$  m/s are accessible with different designs of the piezo scanner.

Going one step further, it appears to be also feasible to perform nanotribological measurements at high velocities *in liquid media* using an improved high velocity accessory. By implementing protective coatings on the shear piezo measurements of friction in liquid (*e.g.* water) could be realized and promise to provide insight into lubrication phenomena, such as the transition of boundary to hydrodynamic lubrication.<sup>11,12</sup> This approach, which could provide high velocity friction information complementary to SFA data, will be of particular importance in characterization of bio-lubricants (*e.g.* hyaluronic acid, carboxymethyl cellulose fluids, silicone fluids, synovial fluid, polymer brushes *etc.*)<sup>13-18</sup> under high pressures and could provide new incentives for the development of functional implants.

---

**References**

- 1 Tocha, E.; Schönherr, H.; Vancso, G. J. *Langmuir* **2006**, *22*, 2340-2350.
- 2 Tocha, E.; Stefański, T.; Schönherr, H.; Vancso, G. J. *Rev. Sci. Instrum.* **2005**, *76*, 083704.
- 3 Tocha, E.; Siebelt, N.; Schönherr, H.; Vancso, G. J. *J. Am. Ceram. Soc.* **2005**, *88*, 2498-2503.
- 4 Priestley, R. D.; Ellison, C. J.; Broadbelt, L. J.; Torkelson, J. M. *Science* **2005**, *309*, 456-459.
- 5 Ellison, C. J.; Torkelson, J. M. *Nat. Mater.* **2003**, *2*, 695-700.
- 6 Vettiger, P.; Brugger, J.; Despont, M.; Drechsler, U.; Dürig, U.; Häberle, W.; Lutwyche, M.; Rothuizen, H.; Stutz, R.; Widmer, R.; Binnig, G. *Microelectron. Eng.* **1999**, *46*, 11-17.
- 7 Dürig, U.; Cross, G.; Despont, M.; Drechsler, U.; Häberle, W.; Lutwyche, M. I.; Rothuizen, H.; Stutz, R.; Widmer, R.; Vettiger, P.; Binnig, G. K.; King, W. P.; Goodson, K. E. *Tribol. Lett.* **2000**, *9*, 25-32.
- 8 Lutwyche, M. I.; Despont, M.; Drechsler, U.; Dürig, U.; Häberle, W.; Rothuizen, H.; Stutz, R.; Widmer, R.; Binnig, G. K.; Vettiger, P. *Appl. Phys. Lett.* **2000**, *77*, 3299-3301.
- 9 Granick, S.; Kumar, S. K.; Amis, E. J.; Antonietti, M.; Balazs, A. C.; Chakraborty, A. K.; Grest, G. S.; Hawker, C.; Janmey, P.; Kramer, E. J.; Nuzzo, R.; Russell, T. P.; Safinya, C. R. *J. Polym. Sci. Pt. B-Polym. Phys.* **2003**, *41*, 2755-2793.
- 10 Lyuksyutov, S. F.; Vaia, R. A.; Paramonov, P. B.; Juhl, S.; Waterhouse, L.; Ralich, R. M.; Sigalov, G.; Sancaktar, E. *Nat. Mater.* **2003**, *2*, 468-472.
- 11 Braun, O. M.; Naumovets, A. G. *Surf. Sci. Rep.* **2006**, *60*, 79-158.
- 12 Zhang, C. H. *Tribol. Int.* **2005**, *38*, 443-448.
- 13 Brown, S. S.; Clarke, I. C. *Tribol. Trans.* **2006**, *49*, 72-78.
- 14 Raviv, U.; Giasson, S.; Kampf, N.; Gohy, J. F.; Jerome, R.; Klein, J. *Nature* **2003**, *425*, 163-165.
- 15 Scholes, S. C.; Unsworth, A. *Proc. Inst. Mech. Eng. Part H-J. Eng. Med.* **2000**, *214*, 49-57.
- 16 Zhu, Y. X.; Granick, S. *Macromolecules* **2003**, *36*, 973-976.
- 17 Muller, M.; Lee, S.; Spikes, H. A.; Spencer, N. D. *Tribol. Lett.* **2003**, *15*, 395-405.
- 18 Pasche, S.; De Paul, S. M.; Voros, J.; Spencer, N. D.; Textor, M. *Langmuir* **2003**, *19*, 9216-9225.



# Summary

The aim of the work described in this Thesis was to develop the necessary platform for quantitative nanotribology by atomic force microscopy at relevant length and time scales and thereby to contribute to bridge the gap between complementary nano- and microtribology. The primary focus was centered on the development of a nanotribology platform that included reliable quantification procedures for friction force measurements and the extension of the range of scanning velocities to 2 mm/s with full environmental control, as well as on the investigation of relevant tribological phenomena on the nanometer scale. The effects of nanostructure, environment and velocity on friction were revealed for different types of samples, ranging from ceramics to polymers, that are important for various types of applications, *e.g.* advanced coatings.

Chapter 2 provided an overview of modern concepts of tribology. The aspects summarized ranged from single asperity to multi asperity friction, including energy dissipation processes, interfacial friction, atomic scale friction, friction anisotropy, velocity dependence, as well as effects of chemistry and environment. Both experimental and computational results were reviewed and instruments for micro- and nanotribology were discussed.

The most important issues for quantitative friction force measurements, including friction force calibration, tip apex characterization, and tip stability, as well as critical tests using a variety of LFM probes, were discussed in Chapter 3. In particular, the frequently applied two-step calibration method for friction quantification was experimentally tested and its accuracy was estimated. The crucial parameters that limit this accuracy were identified. As shown, this method may be highly inaccurate for the calibration of Si<sub>3</sub>N<sub>4</sub> cantilevers due to the inherent errors in the calculation of  $k_L$  originating from poorly defined materials properties and insufficient precision in determination of the value of cantilever thickness. Moreover, the lateral photodiode sensitivity  $S_L$  was found to be an additional significant source of error in the two-step calibration approach. Therefore, the final friction calibration factors  $\alpha_i$  could not be obtained with high accuracy according to this procedure; relative errors  $\delta\alpha_i$  were 45 - 50% and 35 - 40% for V-shaped and single beam cantilevers, respectively. Finally, the wear-resistance of different tips was investigated and a method for improving the tip stability, by applying wear-resistant Al<sub>2</sub>O<sub>3</sub> coatings by pulsed laser deposition, was developed.

In Chapter 4, a new calibration standard that allows one to calibrate all types of LFM probe cantilevers independent of cantilever geometry and tip radius using a direct calibration method

(the wedge calibration method, as originally introduced by Ogletree, Carpick, and Salmeron *Rev. Sci. Instrum.* **1996**, *67*, 3298 - 3306 and later improved by Varenberg, Etsion, and Halperin *Rev. Sci. Instrum.* **2003**, *74*, 3362-3367) was fabricated. The application of this standard specimen enables accurate determination of the calibration factors with an error of *ca.* 5%. This overcomes the limitations of the two-step friction force calibration procedures discussed in Chapter 3. As shown for oxidized Si(100), thin films of poly(methyl methacrylate) (PMMA), and micropatterned self-assembled monolayers (SAMs) on gold, the calibration of various V-shaped and single beam cantilevers using the wedge method in conjunction with the new universally applicable standard allowed us to perform quantitative nanotribology for a wide range of materials and applications.

The development of a high velocity accessory for friction force microscopy measurements in controlled environment (0 - 40% RH and 0 - 40°C) for a commercial stand-alone atomic force microscope (AFM) was described in Chapter 5. Using the accessory, a broad range of velocities up to several mm/s can be accessed independent of the lateral scan size up to a maximum scan size of 1000 nm with high lateral force signal resolution. The design and calibration of the accessory, as well as validation measurements at high velocities, were discussed. The device was validated in studies of the velocity dependence of friction forces and friction coefficients on organic [PMMA], as well as inorganic [oxidized Si(100)] samples. It was shown that the accessory allows one to bridge the time and length scales from ms to several s and tens of micrometers to nanometers, respectively, in tribological studies on oxidic ceramics systems and amorphous polymers, as also described in Chapters 7 and 8.

AFM-based nanotribological measurements on advanced ceramic coatings, which were aimed at unraveling the relation of structural factors and the frictional response, were discussed in Chapter 6. In particular, the nanotribological properties of nanostructured thin films of tetragonal ZrO<sub>2</sub> on oxidized Si(100) were investigated as a function of grain size and relative humidity (RH). The nanostructured ZrO<sub>2</sub> showed a 50% decrease in friction coefficient  $\mu_{\text{Si}_3\text{N}_4}$  compared to oxidized Si(100) in dry nitrogen atmosphere and 40% RH. A maximum of  $\mu_{\text{Si}_3\text{N}_4}$  was observed at *ca.* 40% RH for both samples. No significant difference in friction coefficient was revealed among samples with grain sizes between 12 and 30 nm, which was attributed to insignificant differences in mechanical and nanostructural properties of the samples.

In Chapter 7 we focused on performing complementary nano- and microtribology measurements of 3Y-TZP ceramics doped with 8 mol% CuO. The process of soft layer formation as reported by Pasaribu (Ph.D. Thesis, University of Twente, Enschede 2005) was studied at different length

scales as a function of sliding distance of specimens previously subjected to pin-on-disc tests against  $\text{Al}_2\text{O}_3$  balls. A sharp decrease in friction coefficient measured using AFM with  $\text{Si}_3\text{N}_4$  tips ( $\mu_{\text{Si}_3\text{N}_4}^{\text{nano}}$ ) for wear tracks with sliding distances above 100  $\mu\text{m}$  was observed. For these wear tracks, similar values of  $\mu_{\text{Si}_3\text{N}_4}^{\text{nano}}$  and  $\mu_{\text{Si}_3\text{N}_4}^{\text{micro}}$  were revealed, under the same environmental conditions (40% RH, 26°C). These results are consistent with the formation of a soft layer generated during sliding, which reduces the friction coefficient.

In Chapter 8 the first comprehensive AFM study of surface relaxations of PMMA was presented. The broad range of scanning velocities (up to 1 mm/s) accessible using the newly developed high velocity accessory (Chapter 5), temperature control (from -3°C to 26°C), as well as tips with widely different radii (20 nm to 870 nm), allowed us to cover a frequency range from 1 to  $10^7$  Hz. Friction data acquired at different temperatures and velocities were corrected for the effect of tip-sample contact pressure and were successfully shifted to yield one mastercurve. The  $\alpha$  and  $\beta$  relaxation processes of PMMA were identified in the Hz and MHz regime, respectively ( $T_{\text{ref}} = 26^\circ\text{C}$ ). The activation energies of the surface relaxation processes ( $E_a^\alpha \sim 110$  kJ/mol and  $E_a^\beta \sim 35$  kJ/mol) were found to be significantly lower with respect to reported bulk values and the relaxation frequencies of the processes were noticeably higher compared to the bulk. These results are consistent with the existence of an increased free volume at the polymer surface and indicate a significantly higher mobility of the macromolecules at the film surface.

As shown in this Thesis effects of nanostructure, confinement, environment and velocity on nanoscale friction can now be addressed and quantitatively determined for a wide range of materials. Expanding on instrumental, as well as technical advances, the necessary platform for quantitative nanotribology by AFM has been developed and enables one to tackle previously inaccessible phenomena in nanotribology at relevant length and time scales. Ultimately, the advances summarized in this Thesis may contribute to bridge the gap between complementary nano- and microtribology and thus to enable the development of a fundamental understanding of friction based on first principles.





# Samenvatting

De doelstelling van het in dit proefschrift beschreven werk was het ontwikkelen van een op atomic force microscopy (AFM) gebaseerd platform voor kwantitatieve nanotribologie op relevante tijd- en lengteschalen, om daarmee een brug te slaan tussen de complementaire nano- en microtribologie. De nadruk lag enerzijds op de ontwikkeling van een nanotribologisch platform met een betrouwbare kwantitatieve procedure voor het meten van wrijvingskrachten en het uitbreiden van het bereik van scansnelheden tot 2 mm/s onder volledig gecontroleerde omstandigheden, en anderzijds op het bestuderen van relevante tribologische processen op nanometerschaal. De invloed van nanostructuur, omgevingsparameters en scansnelheid op wrijving zijn bepaald voor verscheidene klassen van monsters, zoals keramische en polymere materialen, die van belang zijn in toepassingen zoals bijvoorbeeld geavanceerde coatings.

Hoofdstuk 2 geeft een overzicht van de huidige concepten in de tribologie. De hier genoemde aspecten lopen uiteen van wrijving met single asperity (enkelvoudig contactvlak) tot multi asperity (meervoudige contactvlakken), waarbij energiedissipatie-processen, grensvlakwrijving, wrijving op atomaire schaal, anisotrope wrijving en snelheidsafhankelijkheid van wrijving aan bod komen, maar ook chemische en omgevingseffecten. Experimentele resultaten, simulaties en instrumenten voor micro- en nanotribologie worden besproken.

De belangrijkste onderwerpen voor kwantitatieve wrijvingskrachtmetingen worden in Hoofdstuk 3 besproken, waarbij onder meer het kalibreren van de wrijvingskracht de karakterisatie van de tip apex, tip stabiliteit en kritieke testen van verschillende types van lateral force microscopy (LFM) probes toegelicht worden. De voor het kwantificeren van wrijving vaak gebruikte twee-staps kalibratiemethode werd experimenteel getest en de nauwkeurigheid werd geëvalueerd. Cruciale factoren die de nauwkeurigheid beperken zijn geïdentificeerd. Gedemonstreerd werd dat de hierboven genoemde methode zeer onnauwkeurig is voor de calibratie van  $\text{Si}_3\text{N}_4$  cantilevers ten gevolge van de inherente fouten in de berekening van  $k_L$ , wat door de slecht gedefinieerde materiaaleigenschappen en onvoldoende nauwkeurigheid in de bepaling van de dikte van de cantilever werd veroorzaakt. Daarnaast werd aangetoond dat de kalibratie van de laterale gevoeligheid van de fotodiode  $S_L$  een significante bron voor fouten is in de twee-staps kalibratiebenadering. Vandaar dat de uiteindelijke wrijvings-kalibratiefactor  $\alpha_1$  niet nauwkeurig bepaald kon worden met deze methode; relatieve fouten  $\delta\alpha_1$  waren 45 - 50% en

35 - 40% voor respectievelijk V-vormige en single beam cantilevers. Tenslotte werd de slijtvastheid van verschillende tips onderzocht en werd een methode ontwikkeld voor het verbeteren van tip stabiliteit, waarbij met gepulste laser depositie een slijtvaste Al<sub>2</sub>O<sub>3</sub> coating werd aangebracht op een tip.

Hoofdstuk 4 beschrijft een nieuwe kalibratiestandaard die het kalibreren van alle types LFM probe cantilevers, onafhankelijk van de geometrie van de cantilever en tip straal, mogelijk maakt door gebruik te maken van een directe kalibratiemethode (de wedge kalibratiemethode, geïntroduceerd door Ogletree, Carpick, en Salmeron *Rev. Sci. Instrum.* **1996**, *67*, 3298 - 3306 en later verbeterd door Varenberg, Etsion, en Halperin *Rev. Sci. Instrum.* **2003**, *74*, 3362-3367). Het gebruik van deze standaard maakt een nauwkeurige bepaling van de kalibratiefactoren met een fout van *ca.* 5% mogelijk. Dit is een verbetering ten opzichte van de beperkingen van de twee-staps kalibratiemethode voor wrijvingskrachten zoals beschreven in Hoofdstuk 3. Zoals werd gedemonstreerd op geoxideerd Si(100), poly(methyl methacrylaat) (PMMA) en voor microgestructureerde self assembled monolayers (SAMs) op goud, was het mogelijk om verschillende V-vormige en single beam cantilevers te kalibreren met behulp van de combinatie van de wedge-methode en de nieuwe, universeel toepasbare standaard, waardoor kwantitatieve nanotribologische metingen gedaan konden worden aan een groot aantal materialen voor een groot aantal toepassingen.

De ontwikkeling van een accessoire voor het bereiken van hoge scansnelheden voor wrijvingskrachtmicroscopie metingen in een gecontroleerde omgeving (0 - 40% RH en 0 - 40°C) dat gebruikt kan worden in een commerciële stand-alone AFM is beschreven in Hoofdstuk 5. Door gebruik te maken van dit accessoire kan een groot bereik van nm/s tot enkele mm/s worden bestreken met een hoge laterale krachtsignaal resolutie, onafhankelijk van de laterale scangrootte en tot een maximale scangrootte van 1000 nm. Het ontwerp en het kalibreren van dit accessoire en de evaluatie van metingen uitgevoerd bij hoge scansnelheden worden hier besproken. Het instrument werd gevalideerd door studies naar de snelheidsafhankelijkheid van de wrijvingskrachten en wrijvingscoëfficiënten op organische (PMMA) en anorganische (geoxideerde Si(100)) oppervlakken. Uit tribologische studies aan geoxideerde keramische en amorfe polymere materialen, zoals beschreven in Hoofdstuk 7 en 8, volgde dat het accessoire het mogelijk maakt om tijd- en lengteschalen te overbruggen van respectievelijk milliseconden tot enkele seconden en van tientallen micrometers tot nanometers.

AFM gebaseerde nanotribologische metingen aan geavanceerde keramische coatings, gericht op het ophelderen van de correlatie tussen structuurfactoren en wrijvingsrespons, worden

besproken in Hoofdstuk 6. Met name de nanotribologische eigenschappen van nanogestructureerde dunne lagen van tetragonale  $ZrO_2$  op geoxideerd Si(100) werden onderzocht als functie van de korrelgrootte en de relatieve vochtigheid (RH). Het nanogestructureerde  $ZrO_2$  vertoonde een afname van 50% in de wrijvingscoëfficiënt  $\mu_{Si_3N_4}$  vergeleken met geoxideerd Si(100) onder een droge stikstofatmosfeer en bij 40% RH. Er werd een maximum gevonden voor  $\mu_{Si_3N_4}$  bij *ca.* 40% RH voor beide samples. Er werd geen significant verschil in wrijvingscoëfficiënt gevonden voor monsters met korrelgroottes tussen 12 en 30 nm, wat toegeschreven werd aan niet-significante verschillen in mechanische eigenschappen en nanostructuur van de monsters.

Hoofdstuk 7 concentreert zich op de beschrijving van complementaire nano- en microtribologische metingen aan met 8 mol% CuO gedoopte 3Y-TZP keramische materialen. Het proces waarbij dunne zachte lagen gevormd worden, zoals beschreven door Pasaribu (Proefschrift, UT, Enschede 2005), werd bestudeerd op verschillende lengteschalen als functie van de afstand waarover verschuiving plaatsvond van monsters die daarvoor pin-on-disc tests met een  $Al_2O_3$  kogel hadden ondergaan. Een scherpe afname in de wrijvingscoëfficiënt werd waargenomen door middel van AFM met  $Si_3N_4$  tips ( $\mu_{Si_3N_4}^{nano}$ ) voor slijtagesporen met afschuifafstanden van meer dan 100 m. Voor deze slijtagesporen werden vergelijkbare waarden voor  $\mu_{Si_3N_4}^{nano}$  and  $\mu_{Si_3N_4}^{micro}$  gevonden onder identieke omstandigheden (40% RH, 26°C). Deze resultaten kunnen worden verklaard door de vorming van een dunne zachte laag tijdens het schuifproces, wat de wrijvingscoëfficiënt reduceert.

In Hoofdstuk 8 wordt een niet eerder in de literatuur beschreven, uitgebreide AFM studie aan oppervlakterelaxaties van PMMA gepresenteerd. Het grote bereik van scansnelheden (tot 1 mm/s) dat toegankelijk was met het nieuw ontwikkelde hoge scansnelheids-accessoire (Hoofdstuk 5), gecombineerd met een gecontroleerde temperatuur (van -3°C tot 26°C) en de beschikbaarheid van tips met zeer verschillende radii (20 nm tot 870 nm), heeft ons in staat gesteld om een frequentiebereik van 1 tot  $10^7$  Hz te bestrijken. Wrijvingsdata, verkregen bij verschillende temperaturen en snelheden, werden gecorrigeerd voor de invloed van tip-monster druk en zijn succesvol teruggebracht tot één mastercurve. De  $\alpha$ - en  $\beta$ -relaxatieprocessen van PMMA zijn vastgesteld op respectievelijk Hz en MHz schaal ( $T_{ref} = 26^\circ C$ ). Er is aangetoond dat de activeringsenergieën van de relaxatieprocessen ( $E_a^\alpha \sim 110$  kJ/mol en  $E_a^\beta \sim 35$  kJ/mol) aan het polymeeroppervlak significant lager zijn dan gerapporteerde waarden in bulk en dat de bijbehorende frequenties significant hoger zijn dan in bulk. Deze resultaten tonen het bestaan

van extra vrij volume aan het oppervlak van het polymeer aan en duiden daarmee op een significant hogere mobiliteit van de macromoleculen aan het polymeer-lucht grensvlak.

In dit proefschrift is aangetoond dat het nu mogelijk is om de invloeden van nanostructuur, ruimtelijke beperkingen, omgevingsvariabelen en scansnelheid op de wrijving op nanoschaal te bestuderen en kwantitatief te bepalen voor een groot aantal verschillende klassen van materialen. Door verder in te gaan op instrumentele en technische vooruitgangen is het benodigde, AFM gebaseerde platform voor kwantitatieve nanotribologie ontwikkeld, dat het mogelijk maakt om tot dusverre niet-toegankelijke processen in nanotribologie te onderzoeken op de relevante tijd- en lengteschalen. Uiteindelijk dragen de ontwikkelingen die in dit proefschrift beschreven zijn bij aan het overbruggen van de kloof tussen de complementaire nano- en microtribologie en daardoor aan het verkrijgen van een fundamenteel inzicht in wrijving en de onderliggende principes.

## Acknowledgments

First of all I would like to thank my promotor, Prof. Julius Vancso for giving me the opportunity to work in your group. I am grateful for your guidance and scientific support. You gave me possibilities to develop myself enormously, both scientifically and personally. I am very happy that our co-operation is further continued within a new project.

My sincerest appreciation goes to my daily supervisor Dr. Holger Schönherr. Through your words: “Even if I know, I will not tell you. You have to find it by yourself.” - you forced me to become an independent researcher. The beginning was hard for both of us with quite some friction and wear. However, in time, our collaboration became better and better. Thanks to you this challenging project ended successfully. You were a great source of motivation and ideas. I am grateful for your enthusiasm, patience and for correcting my papers and Thesis.

I would like to express my heartfelt gratitude to Ing. Clemens Padberg for your great spirit, constant help with computers, SEM measurements, fruitful discussions and always being there when I needed you. I want to thank Dr. Mark Hempenius for your help in the lab and all the chemistry related issues. Special thanks to Cindy, Geneviève, Gerda, Karin and Thelma for your help with all the paperwork, nice chats and making coffee for my monthly project meetings. I also thank Zlata for her assistance.

I owe my appreciation to the following collaborators who made it possible to perform the various studies reported in this dissertation. In particular, I would like to express my gratitude to people involved in the STW project: Prof. Dave Blank, Prof. Dik Schipper, Dr. Louis Winnubst, Dr. Rihard Passaribu, Richard Ran, Jan-Willem Sloetjes, Wika Wiratha, Mieke Luiten and Natasha Siebelt. I am extremely grateful to Tomek Stefański for the software development for the high velocity accessory. The following people deserve my sincere thanks Dr. Guus Rijnders, Dr. Sybolt Harkema and Joska Broekmaat for PLD and XRD measurements. I also would like to thank Nina Dziomkina for high-resolution SEM measurements. Stefan Lutter (NanoWord AG, Neuchatel, Switzerland) and Christoph Richter (NanoWord Services GmbH, Erlangen, Germany) are acknowledged for kindly providing me the AFM probes with large radii.

Thanks for the good times in MTP to all of you: Alex, Anika, Attila, Barbara, Beáta, Béla, Chuanliang, Denis, Dorota, Douwe-Wiebe, Edmondo, Elske, Eugenia, Ewelina, Fabiane, Geerten, Giorgio, Henrik, Hong, Igor, In Yee, Ivan, Janet, Jason, Jing, Joost, Joris, Lanti, Leon, Léon, Marcin, Mária, Marina, Menno, Monika, Monique, Nikodem, Nina, Oya, Qi, Ramon, Renaud, Sandra, Shan, Shuying, Steffi, Szczepan, Thomas, Willem-Jan, Yujie, and everyone

## Acknowledgments

---

that I forgot to mention. I have enjoyed working with you as well as many good parties. I also appreciate all nice moments with members of other groups: PBM, RBT, STEP and tribology.

I am grateful to Joost, Joris, Mark, and Monique for their devoted help to translate the summary into Dutch. I would like to say special thanks to the paranimpfen: Dorota and Monique for being my good friends and sharing together the good and difficult moments.

Jestem niezmiernie wdzięczna mojej rodzinie za przeogromne wsparcie i pomoc. Szczególne podziękowania kieruję do Alicji za wykonanie profesjonalnego rysunku na okładkę.

Na końcu pragnę podziękować mojemu wspaniałemu mężowi za jego troskliwą opiekę w trakcie pisania tej rozprawy. Dziękuję Ci za odwagę bycia przy mnie przez ten ostatni rok. Bez Ciebie nie dałabym rady tego dokonać.

## Curriculum Vitae

Ewa Agnieszka Tocha was born on July 5, 1976 in Gdynia, Poland. After graduating from the High School (Liceum No. III, Gdańsk, Poland) in 1995, she continued her studies at the Technical Physics Faculty at the Technical University of Gdańsk. In 2001, she obtained her Master Degree (with distinction) with the thesis "Nano- and micro-phase separation in linear and cross-linked segmented polyurethanes", completed in cooperation with the Materials Science and Technology of Polymers group at the University of Twente (Enschede, The Netherlands) where she worked during a 5-months Socrates grant. Thereafter, she joined the same group to pursue her Ph.D. degree under the supervision of Prof. Dr. G.J. Vancso. The aim and the results of her project, "Bridging length and time scales by AFM-based nanotribology: Applications to nanostructured ceramics and polymer surfaces" are described in this Thesis. Starting from February 13<sup>th</sup>, 2006, she is working in the same group as a postdoctoral researcher.

## Publications

**Tocha, E.;** Schönherr, H.; Vancso, G.J. "Quantitative nanotribology by AFM: A novel universal calibration platform" *Langmuir* **2006**, *22*, 2340-2350.

**Tocha, E.;** Stefański, T.; Schönherr, H.; Vancso, G.J. "Development of a high velocity accessory for atomic force microscopy-based friction measurements" *Rev. Sci. Instrum.* **2005**, *76*, 083704.

**Tocha, E.;** Siebelt, N.; Schönherr, H.; Vancso, G.J. "Influence of grain size and humidity on the nanotribological properties of wear-resistant nanostructured ZrO<sub>2</sub> coatings: An atomic force microscopy study" *J. Am. Ceram. Soc.* **2005**, *88*, 2498-2503.

**Tocha, E.;** Janik, H.; Dębowski, M.; Vancso, G.J. "Morphology of polyurethanes revisited by complementary AFM and TEM" *J. Macromol. Sci.-Phys.* **2002**, *B41*, 1291-1304.

**Tocha, E.;** Schönherr, H.; Vancso, G.J. "Probing polymer relaxations at the surface of PMMA films by high velocity AFM" *In preparation*.

**Tocha, E.;** Pasaribu, H.R.; Schönherr, H.; Schipper, D.J.; Vancso, G.J. "Nano- and microtribology of low friction wear-resistant ceramics: From micro- to nanotribology" *In preparation*.

